Statistical lifetime modeling of FeNiCr alloys for high temperature corrosion in waste to energy plants and metal dusting in syngas production plants

Sheyla Herminia Camperos Guevara

▶ To cite this version:

Sheyla Herminia Camperos Guevara. Statistical lifetime modeling of FeNiCr alloys for high temperature corrosion in waste to energy plants and metal dusting in syngas production plants. Materials. Institut National Polytechnique de Toulouse - INPT, 2016. English. NNT : 2016INPT0013 . tel-04236703

HAL Id: tel-04236703
https://theses.hal.science/tel-04236703

Submitted on 11 Oct 2023

THÈSE

En vue de l'obtention du

DOCTORAT DE L'UNIVERSITÉ DE TOULOUSE

Délivré par :
Institut National Polytechnique de Toulouse (INP Toulouse)

Discipline ou spécialité :
Science et Génie des Matériaux

Présentée et soutenue par :
Mme SHEYLA HERMINIA CAMPEROS GUEVARA
le mercredi 20 janvier 2016

Titre :

STATISTICAL LIFETIME MODELING OF FeNiCr ALLOYS FOR HIGH-TEMPERATURE CORROSION IN WASTE TO ENERGY PLANTS AND METAL DUSTING IN SYNGAS PRODUCTION PLANTS

Ecole doctorale :
Sciences de la Matière (SDM)

Unité de recherche :
Centre Interuniversitaire de Recherche et d'Ingénierie des Matériaux (C.I.R.I.M.A.T.)

Directeur(s) de Thèse :
M. DANIEL MONCEAU
M. JEAN-MICHEL BROSSARD

Rapporteurs :
M. MICHAEL SPIEGEL, SALZGITTER MANNESMANN FORSCHUNG
M. NIGEL SIMMS, CRANFIELD UNIVERSITY BEDFORD

Membre(s) du jury :
M. MICHEL VILASI, UNIVERSITE DE LORRAINE, Président
M. DANIEL MONCEAU, INP TOULOUSE, Membre
M. FRANÇOIS ROPITAL, IFPEN, Membre

Acknowledgements

The culmination of three years' work, 20 January, 2016 will go down as one of the most important days in my life. It is almost impossible to get to this point by oneself and therefore at this point I would like to take some time to thank the people who were there for me when thinks got tough.

My directors and advisors Dr. Daniel MONCEAU and Dr. Jean Michel BROSSARD who have been an absolute fount of knowledge and patience during the last three years. Thank you for helping me acclimatize, especially in the beginning, to a way to work that was not similar to that of mine. Thank you for your patience with my far-from-perfect French during all these years. The critical thought and detailed oriented mindedness encouraged by them I am sure will help me to succeed in my professional path.

The members of my jury: Dr. Michael Spiegle, Dr. Nigel Simms, Dr. Michel Vilasi, Dr. Mehdi Salem, Dr. François Ropital, Dr. Christel Augustin, Dr. Sébastien Doublet and Dr Aurélie ROUAIX for accepting to be a part of my jury and taking the time to go over this dissertation. I really appreciate their patience in reviewing a dissertation written in a foreign language and foreign English. Their critique of this study has been most informative and I expect a good number of their suggestions to be implemented in the future.

Dr. Pascal Floquet for having me oriented with his technical knowledge about statistics. My workteam Fares MAAD, Emmanuel Schaal, Aurelien Fabas for being cool to me and always be disposed to share. Remi CHAVROT for his help and availability to discuss new and interesting scientific approaches.

A special thanks to my dear friends Aneesha Varguesse and Koenraad.Theuwissen for being there, helping to adapt to a new culture and language. My sincere thanks to my dear friend Pauline Audigie, for her invaluable support, kindness, open-mindedness and friendship. Without them I would not have been able to understand a lot of french jokes and expressions. I learned a lot from this atmosphere while their cheerfulness and their encouragement have bolstered me numerous times over the last three years. They have come to mean a lot to me and I consider them my family away from home.

My oxidation team Charlotte Dupressoire, Aurelien Fabas, Franck Nozahic, my friends and colleagues at CIRIMAT, whom I passed many excellent and fun-filled moments, both at the lab and outside.

My husband for his infinite patience and good energy and for his unconditional support and love, always encouraging me to meet my goals. My brother and sister who have always got my back. My parents who are physically so far away from me but always close to me in spirit, their support and encouragement have been unfailing and I hope I have done them proud.

The SCAPAC project and FUNDAYACUCHO for the financial aid to this project..

Abstract

Over the last decades, the corrosion control of alloys exposed to severe and complex conditions in industrial applications has been a great challenge. Currently, corrosion costs are increasing and preventive strategies have become an important industrial demand. The SCAPAC project funded by the French National Research Agency has proposed to study the corrosion for two separate processes: Steam Methane Reforming (SMR) and Waste to Energy (WtE). Although the operating conditions of both processes are different, the modeling approaches can be similar. Metallic components in the SMR process are subjected to metal dusting corrosion, which is a catastrophic form of damage that affects alloys exposed to highly carburising gases ($a_C>1$) at high temperatures (400–800 °C).[1]. Likewise, metallic components in the Waste to Energy (WtE) process are subjected to high temperature corrosion under deposit that takes place in equipment exposed to atmospheres with high content of corrosive products of combustion.

Metal dusting corrosion is considered as a critical phenomenon that has led to worldwide material loss for 50 years. A basic understanding of the degradation mechanisms is available. However, the effect of some process parameters is still not well understood in current literature and requires further study. Otherwise for high temperature corrosion, a considerable amount of literature has been published over the last few decades and the mechanisms are well documented. Also many materials and coatings have been developed. However, the material performance in different environments has not been sufficiently well understood to define suitable criteria for lifetime prediction models regarding operating conditions, due to the high complexity of the corrosion phenomena involved. Literature research in both fields revealed modeling approaches in different kinds of complex conditions and applications. Nevertheless, there are no lifetime models currently available in the open literature for commercial materials that consider a wide range of conditions and the relative weight of the variables involved in the corrosion processes.

This dissertation presents a methodology to develop lifetime prediction models to evaluate materials performance under metal dusting and high-temperature corrosion conditions. Two databases were created to integrate experimental results from the SCAPAC project, as well as results from literature to enable sufficient amount of data for modeling. The databases allowed analyzing approximately 4000 corrosion rates by different statistical methods over different scenarios. The Principal Component Analysis (PCA) methodology was performed to identify the key parameters to create lifetime prediction models using Multiple Linear Regressions (MLR).

For metal dusting corrosion, two models were obtained to explain the incubation times (IT) and the kinetic of Pit Depth Growth (PDGr). IT showed high dependency on the alloy composition while the PDGr showed high correlations with the atmosphere composition and total pressure. For high-temperature corrosion, three models were obtained in the thermal gradient scenario for three families of alloys: low alloyed steels, Fe/Ni-based high temperature alloys and Ni-based alloys, showing agreeable results. TFlue gas and TMetal were confirmed as 1st order parameters on fireside corrosion. It was also shown that the relative weight of the variables varies with the family of alloys. The statistical models in both cases were compared with experimental and theoretical results showing good agreement with experimental findings, which allows performing a first lifetime assessment of materials under defined conditions.

Contents

INTRODUCTION

The economic growth of any region depends on its natural resources and productive activities, but also on the infrastructure that accounts for goods processing. Industrial installations are affected by deterioration and degradation mechanisms. Corrosion is a worldwide issue that strongly affects natural and industrial environments.[1] It is a pernicious problem that impairs the efficiency of the industrial processes and the lifetime of the infrastructure assets.

Over the years, the corrosion control of alloys exposed to severe and complex conditions has been a great challenge for industrial facilities. Currently, corrosion costs are increasing and preventive strategies have become the main industrial demand. The SCAPAC project funded by French National Research Agency is proposed for two separate processes: Steam Methane Reforming (SMR) and Waste to Energy (WtE). Metallic components in the Steam Methane Reforming process are subjected to metal dusting corrosion, which is a catastrophic form of damage that affects alloys exposed to highly carburizing gases (carbon activity $a_C > 1$) at intermediate temperatures (400–800 °C). Metal dusting corrosion is considered a critical phenomenon that has led to worldwide material loss for 50 years. A basic understanding of the degradation mechanisms is available. However, the effect of some process parameters is still not well understood in current literature and requires further study.

Likewise, metallic components in the Waste to Energy (WtE) process are subjected to high-temperature corrosion that takes place in equipment exposed to atmospheres with high content of corrosive products of combustion. A considerable amount of literature has been published on this subject, and the mechanisms are well documented. Also, many materials and coatings have been developed to resist the damage. However, the material performance in different environments has not been sufficiently well understood to define suitable criteria for lifetime prediction models regarding operating conditions.

Literature research in both fields revealed modeling approaches in different kinds of complex conditions and applications. Nevertheless, there are no lifetime models currently available in literature for commercial materials that consider a wide range of conditions, and the relative weight of the variables involved in the corrosion processes. Although the operational conditions of both processes are different, the application of preventive strategies through predictive modeling approaches can be similar.

A predictive model is based on a number of predictors, which are variable factors that are likely to influence future behavior or results. In predictive modeling, data are collected for the relevant predictors, a statistical model is formulated, and the model makes predictions that are validated with additional data available. Predictive modeling is used widely in information technology (IT), customer relationship management (CRM), planning, management, engineering, change management, material's selection, lifetime assessment, maintenance scheduling.

This dissertation presents a methodology to develop lifetime predictive models to evaluate materials performance under metal dusting corrosion and high-temperature corrosion. Two databases were created to integrate experimental results from the project, as well as results from literature to enable sufficient amount of data for modeling. The databases allowed analyzing over 4000 corrosion rates by different statistical methods over different scenarios. The Principal Component Analysis (PCA) methodology was performed to identify the key parameters for modeling the corrosion mechanisms. Statistical outcomes were explained by experimental and theoretical results in order to build a lifetime prediction model by Multiple Linear Regression (MLR) that corresponds with experimental findings, in a defined scenario.

Now, coming to the definition of the objective of this study; it may be broadly classified under two divisions, one concerning a way to determine the parameters that play the most significant role in metal dusting corrosion and high-temperature corrosion under deposits and the other, to create lifetime prediction models for materials subject to both mechanisms under different scenarios.

Chapter 1 will commence with a description of Steam Methane Reforming (SMR) and Waste to Energy (WtE) processes. This will be followed by a discussion of the mechanisms proposed for metal dusting corrosion and high-temperature corrosion under deposits in the literature review. The goal here was to summarize the effect of the different parameters on the corrosion mechanisms, according to experimental findings by the authors.

Chapter 2 will describe the experimental set-up, database construction procedure and statistical tools used to analyze all the information contained in the databases. Two statistical tools will be exploited in this study:

- Principal component analysis (PCA) - This was utilized to aid in the analysis of the mainly used parameters in experimental studies to determine the parameters that were the most crucial for the corrosion mechanisms.

- Multiple Linear Regression (MLR) - This was employed for modeling the corrosion kinetics to determine, quantitatively, the relative weight of the different parameters on corrosion rates.

Chapter 3 will discuss the results obtained from the statistical analysis to determine the key parameters for modeling the kinetics of metal dusting corrosion. This will be followed by the classification of scenarios considered according to output parameters and family of materials. Finally, six models will be proposed for each possible scenario. The results of modeling will be discussed regarding various data available in literature and experimental data from the SCAPAC project.

Chapter 4 will discuss the results obtained from the statistical analysis to determine the most significant parameters for modeling the kinetics of high-temperature corrosion under deposits. This will be followed by the classification of scenarios considered according to atmosphere conditions and family of materials. Lastly, six models will be suggested for each possible scenario. The results of modeling will be compared with experimental data available in literature and experimental data from this project.

Chapter 5 will consist in the application of the models in lifetime prediction of materials subjected to metal dusting corrosion and to high-temperature corrosion under deposits. This will be followed by plotting the variation of the corrosion rates as a function of the main parameters resulted from modeling procedures. For both mechanisms, the first set of analyses will be performed by scheming the estimate lifetime of materials under defined conditions. The second set of analyses will be performed by plotting corrosion maps as it allowed for a better interpretation of the variation of the corrosion rates with the main affecting parameters.

Chapter 1. Literature Review

Contents

I Chapter 1. Literature Review

Corrosion of metals can be defined as the destructive attack of a metal through interaction with its environment. All metals and alloys can be subject to corrosion even the nobles metals, such as gold, are subject to corrosive attack in some environments. The corrosion is a natural process. Most metals are not thermodynamically stable in the metallic form; they corrode to return to the more stable forms that are normally found in ores, such as oxides. [2] Like other natural hazards, corrosion can cause dangerous and expensive damage to everything from vehicles, home appliances, to pipelines, and industrials assets. However, there are time-proven methods to prevent and control corrosion that can reduce or eliminate its impact on human safety, the economy, and the environment.

The science of *corrosion prevention and control* is highly complex, by the fact that corrosion takes different forms and is affected by numerous outside factors. Corrosion professionals must understand the effects of environmental conditions, required lifetime of the structure or component, appropriate mitigation methods; and other considerations before determining the specific corrosion problem and specifying an effective solution. [3]

Uniform corrosion is characterized by corrosive attack over the entire surface area, or a large fraction of the total area. The breakdown of protective layers or microstructural degradation below coating systems on structures often lead to this form of corrosion. General thinning and microstructural evolution of the substrate take place until failure. In the context of the present study *high-temperature corrosion* mechanism can be included in this category. [4]

Localized corrosion is defined as the selective removal of metal by corrosion at zones on a metal surface in contact with corrosive environment. It usually takes place when small local sites are attacked at a much higher rate than the rest of the surface. Localized corrosion can cause more damage than any other form of corrosion. Pitting corrosion is a localized form of corrosion by which cavities or "holes" are produced in the material, it is considered to be more dangerous than uniform corrosion damage. Pits can create stress raisers zones and it is more difficult to detect, predict and design against. A small, narrow pit with minimal overall metal loss can lead to the failure of an entire engineering system. However, pitting corrosion can be even more dangerous when it becomes generalized as the case of *metal dusting*, extensive areas with large metal wastage in the form of pits leads to catastrophic failure. [4,5]

The first step in effective control and prevention of *high-temperature corrosion* and *metal dusting* corrosion, in certain industrial units is to understand the mechanisms involved, how to detect them, how and why they occur and the factors that govern the processes and add complexity to the equation.

I.2 Metal Dusting

Metal dusting is a catastrophic form of corrosion in environments of carburizing gases, high carbon activities ($a_C > 1$), and very low oxygen partial pressures at elevated temperatures 400-800°C. [6–8] The deposition of carbon from the carbon supersaturated atmosphere disintegrates the metal surface producing powdery carbon, metal particles, carbides and oxides. Corrosion can be in the form of pitting and general metal wastage. This form of corrosion affects iron, low and high alloy steels, Ni-based and Co-based alloys used in structural components in the heat treating industry when oil residue mixes with gases used during heat treating to form gases that are kinetically favorable for metal dusting attack. Oil refineries experience metal dusting attack in hydro-dealkylation and catalyst re-generation processes. Also in the steel industry in blast furnaces and nuclear plants that employ carbon dioxide (CO_2) for cooling, the recycle-gas loop equipment of coal gasification units, fired heaters handling hydrocarbons at high-temperatures and metallic interconnects used in solid oxide fuel cells. [9]

Equipment in processes that use synthesis gas containing varying contents of hydrogen (H_2), carbon monoxide (CO), steam - methane (CH_4) and water vapor (H_2O) is susceptible to metal dusting. [9] Figure I.1 shows a diagram of the steam-methane reforming process used to produce hydrogen. Metal dusting is found in the inside tubes containing syngas downstream the reforming furnace in the heat recovery zone where temperatures start to decrease producing temperature gradients in carburizing atmospheres favorable for metal dusting.

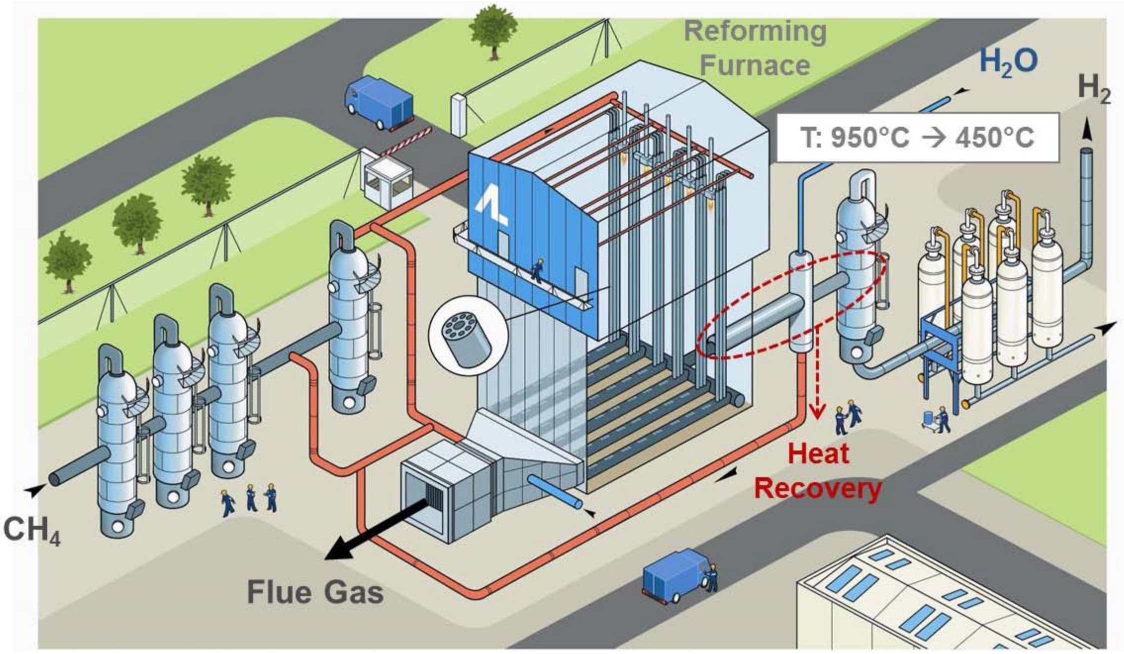

Figure I.1. Schematic representation of the Steam-methane reforming process[1]

Thermogravimetric experiments performed by Grabke et al. [7] at 650°C in a $CO\text{-}H_2\text{-}H_2O$ atmosphere at different carbon activities for iron and low alloys steels showed that at $a_C \leq 1.1$ metal dusting did not occur but at values $a_C > 1.3$ higher carbon content is reached and the mass gain accelerates indicating metal dusting. When the thermodynamic activity exceeds unity, concurrent reactions at the gas-metal interface can cause the formation of coke and carbon deposition. Metal dusting corrosion in CO or CH_4 containing environments can lead to the transfer of carbon to the metal surface thru the following reactions (1,2,3). [8,10]

$$CO + H_2 \leftrightarrow C + H_2O \qquad \textbf{Reaction 1}$$

$$2CO \leftrightarrow C + CO_2 \qquad \textbf{Reaction 2}$$

$$CH_4 \leftrightarrow C + 2H_2 \qquad \textbf{Reaction 3}$$

$$H_2O \leftrightarrow H_2 + 1/2O_2 \qquad \textbf{Reaction 4}$$

---

[1] Source : Air Liquide – Creative Oxygen https://www.airliquide.com

In most of the studies reviewed, CO has been used as the main carbon provider since reaction 1 has the fastest kinetics. Grabke et al.[11] have determined that the carburization in CH_4-H_2 is much slower than in CO-H_2. As the carbon activity is the driving force for metal dusting, for syngas mixtures CO-H_2-H_2O obtained from methane conversion, it can be calculated from reaction 1 and equation (1). Syngas also contains CO_2 and other authors have calculated the carbon activity from the Boudouard reaction 2 through equation (2).[7] However the steady state carbon activity established in non-equilibrium atmospheres on the metal surface is determined by the faster kinetics which is reaction 1.[8,12] And the oxygen partial pressure for the CO-H_2-H_2O mixture results from the reaction 4 and it can be calculated through equation (4).[13]

$$a_C = K_1 \frac{pCO \times pH_2}{pH_2O} \qquad \textbf{Equation 1}$$

$$a_C = K_2 \frac{(pCO)^2}{pCO_2} \qquad \textbf{Equation 2}$$

$$a_C = K_3 \frac{pCH_4}{pH_2} \qquad \textbf{Equation 3}$$

$$pO_2 = K_4 \left(\frac{pH_2O}{pH_2}\right)^2 \qquad \textbf{Equation 4}$$

Additionally metal dusting has been observed under conditions where carbon activity calculated from reaction 2 is $a_C < 1$ and according to reaction 1 is $a_C > 1$ making activity calculation with reaction 1 more reliable. In such cases where metal dusting is observed in processes that involve hydrocarbons and H_2, carbon activity may be calculated from reaction 3 through equation (3). However methane is rather inert at intermediate temperature but may cause metal dusting at about 1000°C.[12]

Young et al [6] have proposed that metal dusting mechanisms can be classified into two types: one for iron and ferritic alloys, where iron carbide forms at the surface and the other for nickel and their alloys where no carbide is formed. Both mechanisms produce coke which consists of carbon filaments and graphite particle containing metal-rich particles inside.

I.2.1 Metal dusting of iron and low alloy steels

Metal dusting for iron and ferritic alloys starts with the transfer of C within the metal surface from the gas atmosphere ($a_C > 1$ in the gas atmosphere) which leads to carburization. No formation of protective scale is expected because iron or low alloy steels do not oxidize under metal dusting conditions. But formation of cementite Fe_3C at the metal surface could act as a barrier for further carbon ingress. After formation of Fe_3C, the carbon oversaturated atmosphere generates the deposition of graphite decreasing the carbon activity on the cementite to $a_C = 1$. This causes Fe_3C dissociation according to reaction 5.

$$Fe_3C \leftrightarrow 3Fe + C \qquad \textbf{Reaction 5}$$

Figure I.2 shows schematically that the carbon atoms are attached to the basal planes of graphite which grow into the cementite which is known to be a carbon diffuser.[6] Iron atoms from cementite intercalate into graphite and diffuse through the interspace between graphite planes and agglomerate to small particles, whose act as catalysts for further carbon deposition and coke formation. This mechanism is in agreement with the proposals of Grabke, [7,12] Chun [10] and Pippel. [14]

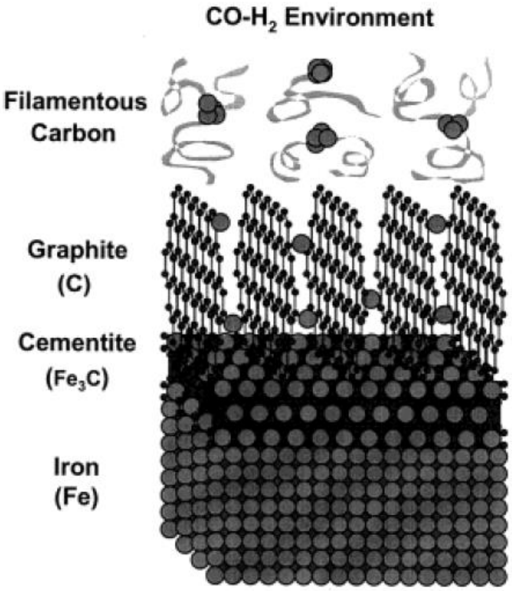

Figure I.2. Schematic representation of metal dusting mechanism of iron at the atomic level [10]

I.2.2 Metal dusting of iron - nickel alloys

Grabke and coworkers [7] have studied metal dusting in Fe-Ni alloys. These alloys are not oxidized in metal dusting atmospheres, because low oxygen pressures do not favor the formation of Fe-oxides and Ni-oxides, hence carburization and metal dusting are possible. Their analysis showed that carbon deposition decreases with increasing Ni content in binary Fe-Ni alloys as well as the metal content in the corrosion product from Fe-30%Ni. These results are in agreement with Zhang and Young [15] findings, where thermogravimetric analysis showed that increasing the nickel content in the alloy decreased the initial rate of carbon uptake. This decrease was approximately linear with nickel concentration up to about 60–70%. Only slight decreases were achieved by further nickel additions. The carbon uptake rate of pure nickel was very small, only about 1% that of pure iron. A uniform Fe_3C scale is formed on pure iron. On ferritic Fe–5%Ni a layer with mixed structures of Fe_3C and α-Fe is developed. Small amounts of Fe_3C was developed at the surface of an austenite layer grown on two-phase ($\alpha + \gamma$) Fe–10%Ni and no carbide appeared at nickel content above 10%. [6,15]

I.2.3 Metal dusting of nickel and Ni-based alloys

For nickel, Ni-base alloys and steels with Ni/Fe > 2/3 another mechanism applies that does not involve the intermediate formation of Fe_3C. After carbon oversaturation of the metal phase, follows graphite growth into the metal phase. Disintegration of the metal results from the growth of graphite oriented perpendicular to the surface, whereas graphite with basal planes parallel to the metal surface seems harmless which indicates that metal dusting attack on Ni is strongly dependent on the surface orientation and the way of epitaxial deposition of graphite. [10,12] Ni-atoms migrate through the graphite layer by intercalation and diffusion and agglomerate into particles in the outer reaction zone (coke layer). In comparison to iron in the case of nickel; the metal particles are much bigger and are not covered by a graphitic envelope which means that Ni particles are less active catalysts for the carbon deposition. [14,16]

I.2.4 Effect of the alloying elements on metal dusting

I.2.4.1 Effect of chromium

Metal oxides induce protection by limiting carbon diffusion into the base metal. Thus alloy resistance to metal dusting is maximized by formation of a dense, well adherent oxide layer which avoid access of carbonaceous gases to the meal substrate.[12] For the temperature range of metal dusting (400°C-800°C), a chromia - layer is the protective scale generally used even when literature studies also deal with alumina layers. Increasing temperature promotes the oxidation of chromia forming steels and Ni-base alloys so metal dusting rates are suppressed by oxide formation at temperatures $T > 650°C$ but also because of carbon activity decreasing at temperatures beyond 700°C. However in the heat recovery process in Syngas plants the temperature will decrease what makes high alloys steels most susceptible to metal dusting in the temperature range 500- 650°C, where generally no protective Cr-rich scale is formed. Also the oxide layer should be thermodynamically and physically stable under the prevailing environmental conditions and during the process. The causes of oxide instability usually are defects in the oxide layer or the oxide carbides that are chemically reduced by gas. [12]

Grabke et al [12] has proposed a mechanism in presence of chromia protective scale, which starts with the local attack at defects of the scale, allowing carbon transfer from the carburizing atmosphere to the metal substrate that allows the dissolution of carbon within the metal. The dissolved carbon diffuses inward and causes precipitation of stable carbides, mainly $M_{23}C_6$. After the precipitation of the carbides, depending on the composition of the matrix, the disintegration of the material starts, either by formation of instable cementite for low alloy steels or by inward internal growth of graphite for high alloy steels and Ni-base alloys. The metal particles that come from disintegration, depending on the composition of the matrix, act as catalyst for carbon deposition and coke arises from the growing pit. The surface around a growing pit is covered by a protective oxide layer, but that cannot stop the pit growth since the scale is already undermined.

Under metal dusting conditions the alloys are exposed to a competition between the process of formation of a chromia layer and the diffusion process of carbon into the metal. If the first process comes earlier, the alloy will be protected for longer time by the Cr-rich scale but if the second process prevails, an unstable scale is formed and metal dusting starts and spreads rapidly. [12]

The formation of stable Cr-oxide layer need to be favored by high Cr-content in the alloy, because at temperatures < 700°C, even steels with enough Cr-content (> 12% for ferritics and > 17% for austenitics) do not form chromia layers. [12] Also if the scale is damaged either by spalling due to thermal cycling or by marring the surface when scratching the coke from the surface, self-healing of the chromia layer is essential to prevent carbon attack.[17] The self-healing process is promoted by high chromium concentration, high diffusivity of chromium in the metal towards the surface and surface modification by cold working to increase the diffusion of chromium. Klower et al.[17] experiments at 650°C showed that Fe-Ni-Cr alloys suffered high metal dusting rates after short periods of time whereas Ni-base alloys were generally less susceptible to metal dusting but their effect was dependent on their Cr-content. Alloy 600H with Cr-content of 16% suffered metal loss rates similar to those of iron base alloys and Ni-base alloys with Cr-contents > 25% showed no significant evidence of metal dusting after 1000 hours of exposure, these findings reveals the presence of a dense chromia scale that protect the alloy substrate from the penetration of carbon.

Later Grabke et al.[18] tested several 9-20%Cr alloys in the temperature range 500-600°C that showed the important effect of the presence of easy-diffusion paths for fast formation or healing of protective Cr-rich oxide scale against metal dusting. Such easy diffusion paths are provided by a fine-grain microstructure which is capable of rapidly supplying chromium to the surface. The surface cold working (polishing, grinding, machining, sand blasting) increases dislocation density, and hence diffusion through dislocations pipes of Cr to the surface. Therefore more resistance to metal dusting is promoted.

I.2.4.2 Effect of aluminum and silicon

Al and Si form stable oxides Al_2O_3 and SiO_2 at the low oxygen potentials of typical dusting atmospheres. It was shown that solubility of carbon in Al_2O_3 at 1000°C is negligible.[6] However the decline in temperature to the metal dusting range compromises this stability.[19]

Al and Si are added to form continuous protective layers. However, when concentrations are too low at metal dusting temperature range, they will form internal oxides which are detrimental for corrosion resistance, therefore a less stable oxide eventually will not be enough to protect against metal dusting. [19]

I.2.4.3 Effect of copper

Copper is shown to be noncatalytic to carbon deposition from gas atmospheres, and owing to its extremely low solubility for carbon, it is inert to the metal dusting. [20] Several authors have studied its effect on the metal dusting behavior. Zhang [20] investigated the weight changes of Ni-Cu alloys after carburization and it was concluded that increasing the alloy Cu content decreased the rate of carbon deposition. Similar results were reported by Nishiyama [21] who studied binary alloys from 1-70%Cu-Ni and concluded that almost 20% of Cu is needed to avoid carbon deposition. He also performed metal dusting tests using transition metals which suggest that noble metals such as Cu, Ag, and Pt have good resistance against metal dusting. There is neither coke formation nor change mass in Cu-specimen after exposure in a simulated synthetic gas at 650°C. As Cu does not protect by formation of an oxide scale, the element has a “Surfactant-Mediated Suppression” role against metal dusting which is explained in terms of atomistic interaction of CO with transition-metal surfaces by electronic structure analyses.

Later Zhang and Young [22] evaluated the effect of copper on alloys 304SS, 310S and 800H. Cu content of up to 10% in 304SS show no effect in metal wastage rates but at 20%Cu the alloy dusted even faster. Cu contents of up to 10% in 310SS suppressed dusting but at 20% it shows even higher wastage rates. In the alloy 800H the variants of Cu content shows the same rates which are slightly lower than the original alloy. It is concluded that copper additions at appropriate levels can provide significant protection against carbon deposition and consequently dusting problems if the alloy is fully austenitic and large amounts of Cu-rich phases are avoided. Its positive effect for ferritic alloys is not evident.

I.2.5 Effect of the environment

I.2.5.1 Effect of temperature

Young et al.[6] expose that temperature affects both sides of the dusting process: the driving force for reactions is the gas phase supersaturation with carbon. The kinetics of degradation is controlled by the rates of internal oxidation and diffusion of carbon. Since dusting can occur only when carbon activities $a_C > 1$, it is interesting to study how equilibrium constants for reactions 1, 2 and 3 vary with temperature as shown in Figure I.3. The synthesis gas (reaction1) and Boudouard reaction (reaction 2) are exothermic and produce increasing carbon activities as the temperature is lowered and the hydrocarbon cracking reaction (reaction 3) is endothermic and leads to $a_C > 1$ at high-temperature. Nevertheless the reaction 1 has the fastest kinetics and therefore deposition of carbon will be higher in the interval (400°C - 600°C°) at high a_C. However there is confusion in literature related to the effect of temperature on metal dusting because of the way in which a_C varies with temperature and gas composition in $CO/H_2/H_2O$ mixtures.

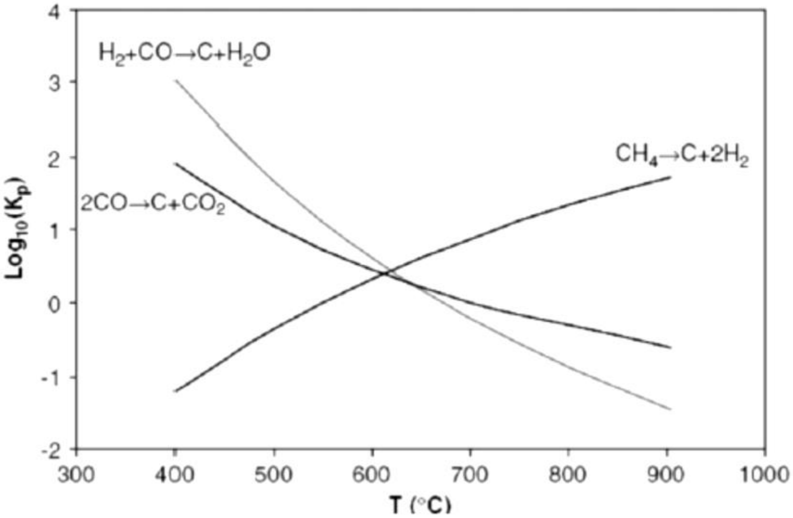

Figure I.3. Equilibrium constants for gas phase carbon producing reactions.[6]

Muller Lorenz [23] and Grabke [12] showed in Figure I.4 that metal dusting rates of several alloys increase with temperature up to 600°C, in spite a_C decreases when temperature increases, according to kinetics reactions in controlled atmospheres of $CO/H_2/H_2O$ where the activities can be quantified. This is due to the fact that diffusion and reaction kinetics involved in metal dusting are thermally activated. Therefore, the correlations between dusting rates and temperature and a_C are not directly proportional.

Chun et al. [24] showed the temperature dependence of the corrosion rate of iron in a $50CO{:}50H_2$ gas mixture in Figure I.5 and gave a microstructural explanation. In the case of iron (Figure I.5a), three regimes can be distinguished, corrosion rate increases up to a maximum observed around 575°C, above this temperature corrosion rate decreases until 723 °C where it becomes independent of temperature. In the first regime, the competition between the growth of Fe_3C and its dissociation determines the overall metal dusting rate. In the second regime, the decrease in the corrosion rate can be explained considering that nucleation of metal particles by cementite decomposition is related to the chemical potential difference of carbon between cementite and graphite (μ_C - μ_C*), this difference decreases with increase in temperature. Therefore it could explain the decrease of corrosion rate when temperature rises. In the third regime above 723°C, iron undergoes from BCC structure to the FCC structure. The latter has considerably higher solubility for carbon therefore the dissolution and diffusion of carbon in the austenite phase prevent surface carbide formation.[10] On the other hand, from the point of view of the gas atmosphere conditions, even when activities of carbon cannot be controlled because of the absence of H_2O, in the first regime the dusting rates increase with temperature but qualitatively it is known that simultaneously a_C decreases, in the second regime the contrary happens up to 723°C and in the third regime a_C goes down with rates. This means that in such atmospheres neither the correlation between dusting rates and a_C values is directly proportional.

In the case of nickel, corrosion rate increases up to a maximum around 600°C, above this temperature corrosion rate becomes independent of temperature in the 600-1050°C range. Nickel does not form carbides, metal dusting corrosion of nickel depends on the composition of the gas. Figure I.5b shows a slight increase in corrosion rate with temperature up to 600 °C, beyond this temperature it becomes independent. In this study, Chun et al. [10] exposes that in the absence of surface carbide, dusting rates do not show temperature dependence because the activation energy for the rate-limiting step (growth of Fe_3C) is negligible. The most likely rate-limiting step is the diffusion of Fe or Ni through graphite.

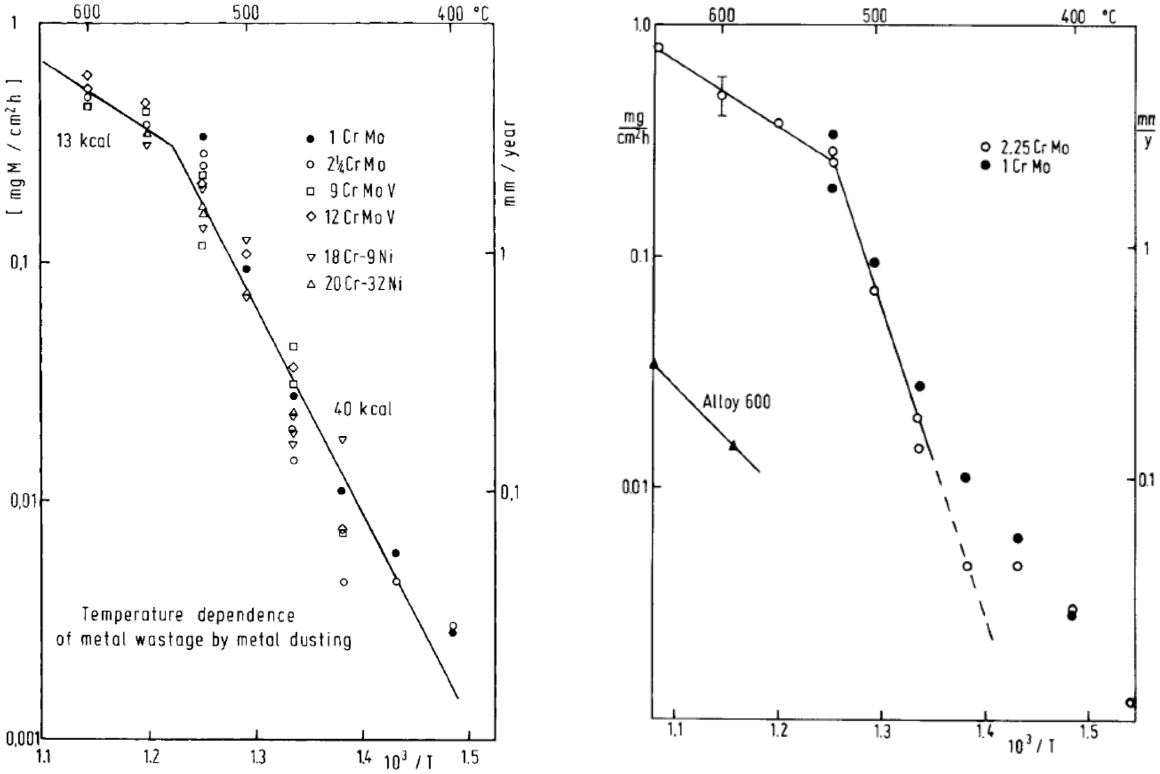

a)

b)

Figure I.4. Arrhenius diagram of metal wastage rates by metal dusting in $H_2/CO/H_2O$ atmospheres [23] a) Different steels b) Two low alloys and Ni-base 600.

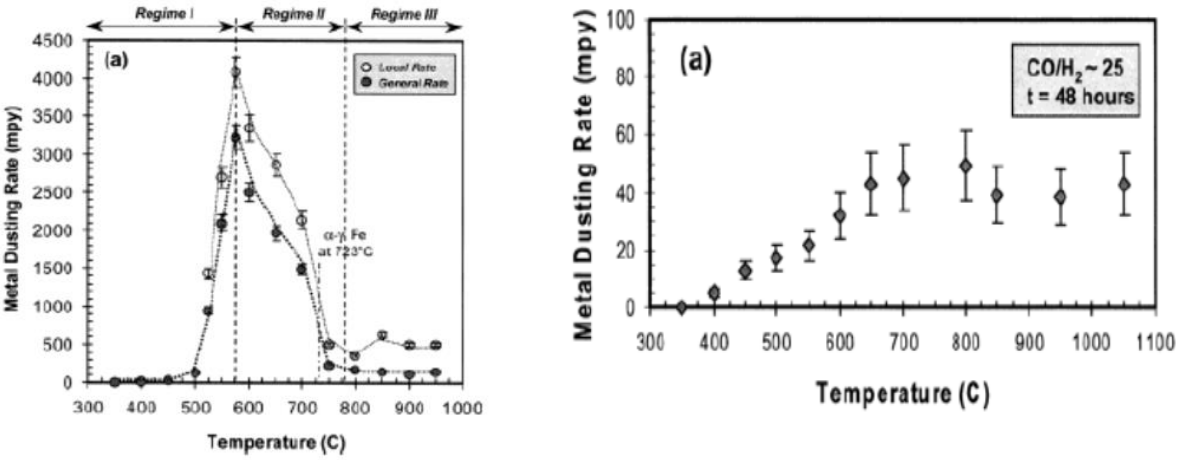

a)

b)

Figure I.5. b) Temperature dependence of iron in $CO/H_2 \approx 1$ mixture b) Temperature dependence of nickel in $CO/H_2 \approx 25$ mixture. [10]

I.2.5.2 Effect of gas composition

The dependence of coking and dusting rates on the composition of $CO/H_2/H_2O$ has been studied by several authors. Grabke et al. [25] curves for the mass gain vs. time at different pCO, pH_2, and pH_2O show clear dependence on the partial pressures: its rate is proportional to pCO and pH_2 and inversely proportional to pH_2O. Thus, the equation (5) is valid for reaction 1 where μ is the coking rate.

$$\mu \propto \frac{pCO \times pH_2}{pH_2O} \qquad \textbf{Equation 5}$$

Muller Lorenz et al.[23] measured coking rates at 650°C varying partial pressures shown in Figure I.6a, it indicates that coking rates increase with partial pressure of CO. However, Yin et al. [26]shows a significant increase of carbon uptake for both steel and pure iron, increasing 0.25 to 0.5 atm of pCO, some smaller increase was observed between 0.5 and 0.68 and finally rates decreased with further increase of pCO up to 0.9 atm, reaching the steady-state carbon uptake at a maximum value of 0.68atm.

Muller Lorenz [23] also measured the metal wastage at the same conditions and showed that the process is dependent on the partial pressures of CO an H_2 and independent on H_2O. The maximum rate was observed at about $CO/H_2 \approx 1$ which indicates that the rate of metal wastage in the high-temperature range is proportional to the product pCO x pH_2. These results are consistent with Chun [24] experiments shown in Figure I.6b which indicates that the general corrosion rate is more or less independent of the gas composition in region A and go through a maximum in region B, at the $CO/H_2 \approx 1$ composition. The forward rate of reaction 1 should be proportional to the product of the concentrations of CO and H_2.

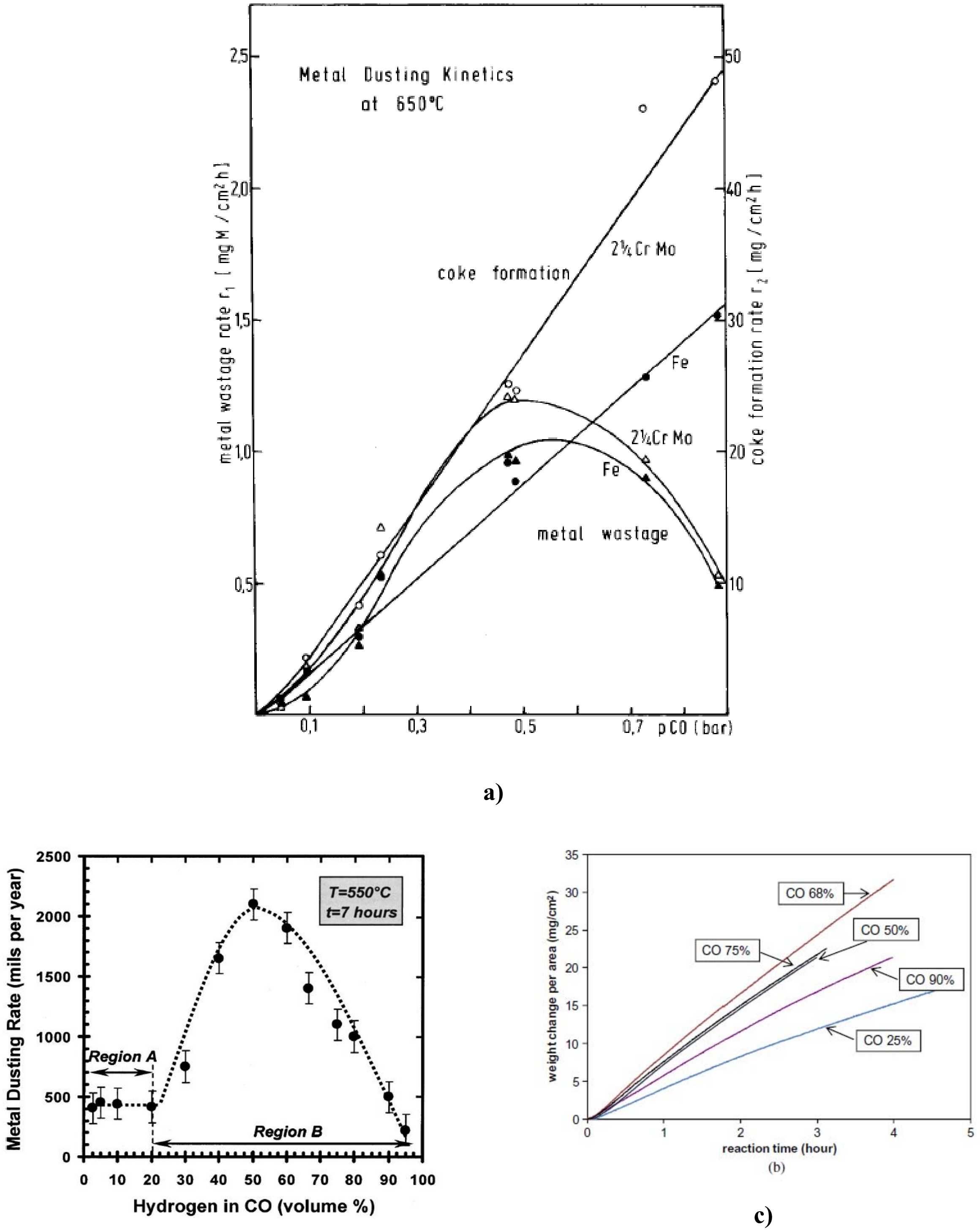

a)

b)

c)

Figure I.6. a) Dependence of metal wastage rate and coking rate on Fe and 2 ¼ Cr-1Mosteel in various $H_2/CO/H_2O$ mixtures at 650°C. [23] **b) Metal dusting corrosion rate of iron as a function of H_2 content in CO at 550°C for 7 h.** [24]**c) Coking rate of iron at $a_C = 4.5$.** [26]

I.2.5.3 Effect of pressure

Levi et al. [27]studied the effect of pressure on the "metal dusting" on stainless steel TP 316. They found that for a given pressure the pit depth increases with temperature and for a given temperature the pit depth increases with pressure (Figure I.7). In this study the effect of the temperature is consistent with previous studies. [10,23] However further experiments at high pressures are necessary to elucidate the effect of pressure on the carbon activity that causes the increase of the attack by "metal dusting".

I.2.5.4 Effect of mechanical stress

Usually in industrial installations certain components such as reactors and tubes are submitted to different levels of pressure. This condition creates a state of biaxial stress in the materials which is certainly harmful for equipment in service. In the case of metal dusting, the pits might act as stress risers leading to cracks and hence failures. [4] Also these stresses can degrade the oxide protective layers on the surface of the materials, accelerating the attack. No systematic studies deal with this specific subject. Most of metal dusting experiments undergo no mechanical stress, however this is a limitation to reproduce industrial conditions in laboratory, and therefore further studies involving considering mechanical stress would be useful.

I.2.5.5 Effect of gas velocity

More data is required to discuss the effect of gas rates on metal dusting. Most laboratory experiments are performed under low gas rates, smaller than those observed in industrial conditions.

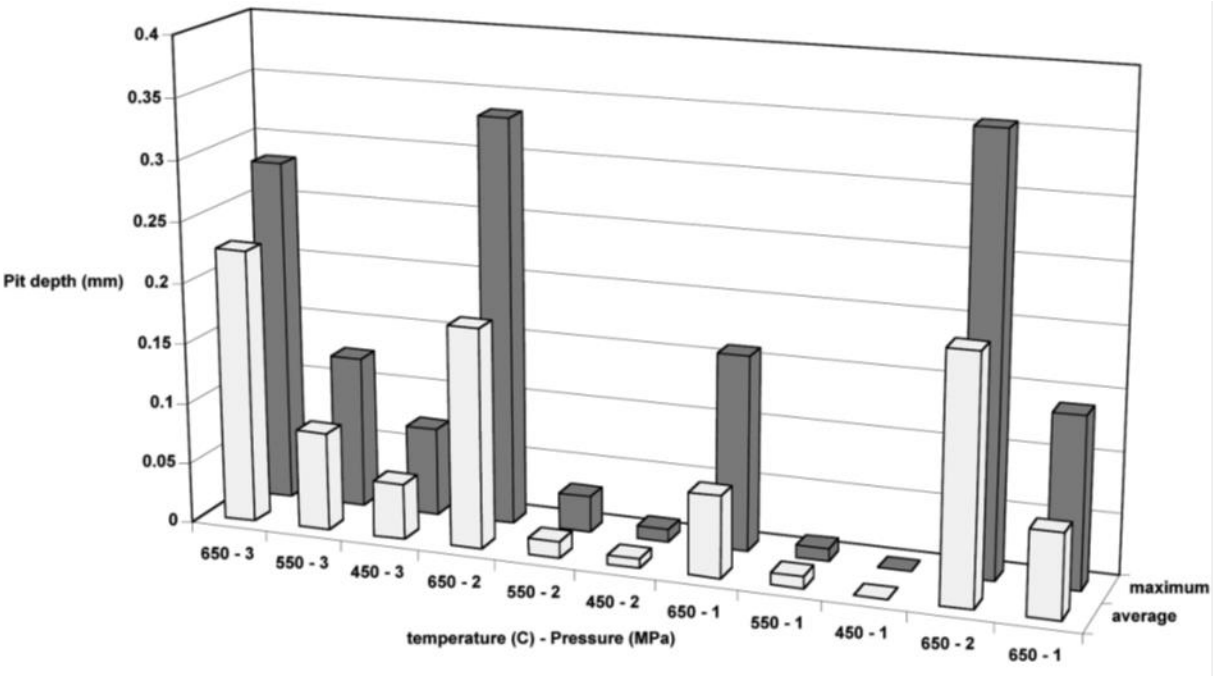

Figure I.7. Graphical representation of the average and maximum pit depths between 1 and 3 Mpa at 450° to 650°C.[27]

I.2.6 Kinetics modeling of metal dusting

In the last decades several models have been proposed by different authors using different approaches. Young et al. [6] studied the kinetics of metal dusting in iron and some ferritic steels where iron carbides like cementite (Fe_3C) form at the surface and is surmounted by coke. Measurements of the average scale thickness as a function of time at 680°C in a gas of CO-26%H_2-6%H_2O and $a_C = 2.9$ is shown in Figure I.8. It clearly shows that the cementite scale continues to thicken throughout the reaction. For this to happen, a_C must be higher than the value required to stabilize Fe_3C. For temperatures lower than 764°C this value is higher than 1, this means that carbon supersaturated gas penetrates the porous coke. As a consequence the scale thickness increases with reaction time as a result of solid state diffusion and simultaneously the cementite is consumed at the surface as material is removed as dust. Young et al.[6] proposed a model represented by equation (6) that describes the growth kinetics of the cementite layer mentioned above. In the equation (6) the constant k_p is the parabolic rate constant for scaling evaluated from Wagner's theory (7) with D_C the carbon diffusion coefficient in cementite and a_c', a_c'' the boundary values at the metal-scale and scale-gas interfaces and k_d is the linear rate constant for cementite scale loss. At constant rate, the solution of the equation (6) is a final constant thickness $X = \frac{k_p}{k_d}$ when $\frac{d_x}{d_t} = 0$.

The measurement of k_p under defined carbon activity conditions leads to the calculation of D_C which corresponds with estimates made by other authors cited by Young in his article [6] validating that the rate of cementite scale growth is controlled by solid state diffusion. In this model the kinetics estimations are limited to the evaluation of the cementite layer under one single temperature and gas composition. However the metal dusting goes further with temperature gradients and more complex alloy systems.

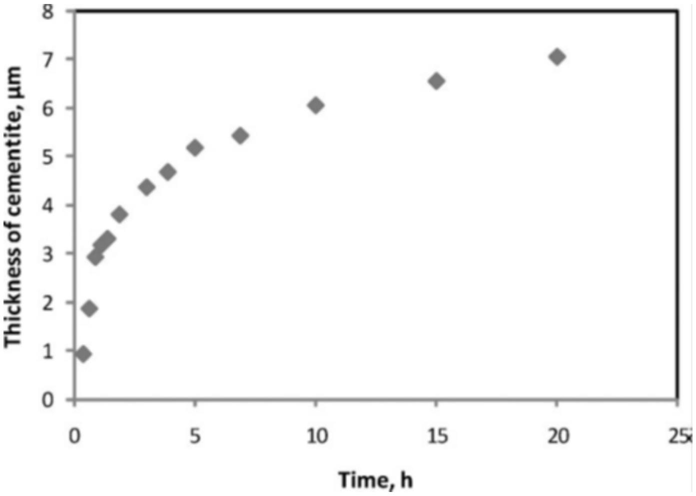

$$\frac{dX}{dt} = \frac{k_p}{X} - k_d \qquad \textbf{Equation 6}$$

$$k_p = \int_{a_c'}^{a_c''} D_c \, d \ln a_c \qquad \textbf{Equation 7}$$

Figure I.8. Measurements of cementite scale thickness represented in the model (equation (6))

Yin [26] evaluated the reaction of 2¼Cr-1Mo and pure iron at 650°C in CO-H_2-H_2O gas, varying *pCO* and nominal a_C which is calculated assuming equilibrium of the synthesis gas reaction. After an incubation period a cementite scale grew, covered by a graphite deposit containing cementite particles. It was concluded that both iron and steel were initially protected against dusting by a marginally stable surface oxide scale, once disappeared the oxide layer, carbon uptake followed linear kinetics at rates which varied with gas composition but did not correlate with the carbon activity. Based on these experimental results Yin et al.[26] presented a simple kinetics model abandoning the application of the equilibrium approximation and considering reactions 1, 2 and the carbon gasification process by reaction 6. The same approach was offered by Young et al. [8] previously. All contribute to carbon production (1, 2) and removal (6). Assuming their reverse reactions negligible the model is described by equation (8).

$$C + 2H_2 \leftrightarrow CH_4 \qquad \textbf{Reaction 6}$$

$$r = \mathbf{k_1\, pCOp}H_2 + \mathbf{k_2\, p^2CO} - \mathbf{k_2 p^2}H_2 \qquad \textbf{Equation 8}$$

Where, ***r*** represents carbon deposition rate and ***k₁, k₂, k₃*** represent the reaction rate constants for reactions 1, 2 and 6 from left to right. The values of ***r*** were calculated from the straight line portions of the carbon uptake kinetics plots and individual rate constants k_i deduced from the experimental results. The experimental data and the rates calculated from equation (7) are compared for both iron and steel with reasonable agreement. Comparison of the corresponding rate constant values for pure iron, steel and nickel from the study, [8] shows that all three reactions are fastest on steel, intermediate for iron and slowest on nickel. These results indicate that the relative contribution of the carbon gasification reaction changes with the substrate. This model may be appropriate to assess the influence of the gas composition on the kinetics of carbon uptake during metal dusting. However, it does not allow predicting the material lifetime, as it considers neither the mass loss caused by metal dusting nor the material chemical composition. Even for evaluating the effect of the gas composition, it takes into account only the linear zone without considering the incubation time that is usually longer for high performance alloys.

Albertsen [28] evaluated the mechanisms of pitting corrosion in the Ni-based alloys 602 and 693, submitted to 4 years' plant-exposed to syngas at 540°C and 35 bar total pressure. In this study, it is concluded that pitting corrosion attack starts when carbon diffuses into the bulk of the alloys after the breakdown of the protective Cr_2O_3-Al_2O_3 oxide layer which provides an effective barrier against carbon diffusion during the incubation time. The corrosion pits then grow by process of internal carburization and oxidation in which carbides, oxides and graphite form separately within an approximately 30 µm thick belt shown in Figure I.9a. The oxidation of internal Cr_3C_2 carbides is associated with large volume changes which result in the buildup of high mechanical stresses in the white zone and eventually, to the complete disintegration of the original alloy into a layered pit microstructure consisting of Ni + Fe and $Cr_2O_3 + Al_2O_3$ + graphite.

All these microstructural changes have been rationalized through a detailed model represented by equation (9) that describes by the physical reactions involved.

$$SSCR = \frac{dx_1}{dt} = \frac{k_1}{x_{CZ}} = \frac{\alpha}{\beta}\,\frac{D_c}{C_{Cr}^0}\frac{C_C^i}{Z_{Cr}}\frac{1}{X_{CZ}} \qquad \textbf{Equation 9}$$

Where SSCR is the steady state corrosion rate indicated in Figure I.9b, α and β are the stoichiometric coefficients of $Cr_\alpha C_\beta$ specie, D_C is the coefficient of diffusion of carbon in the alloy, C_C^i is the molar concentration of carbon at the interface between the carburized region and the substrate of the alloy, C_{Cr}^0 is the molar concentration of chromium in the alloy, Z_{Cr} is the mole fraction of chromium associated with the specie $Cr_\alpha C_\beta$ and X_{CZ} is the thickness of the carburized area.

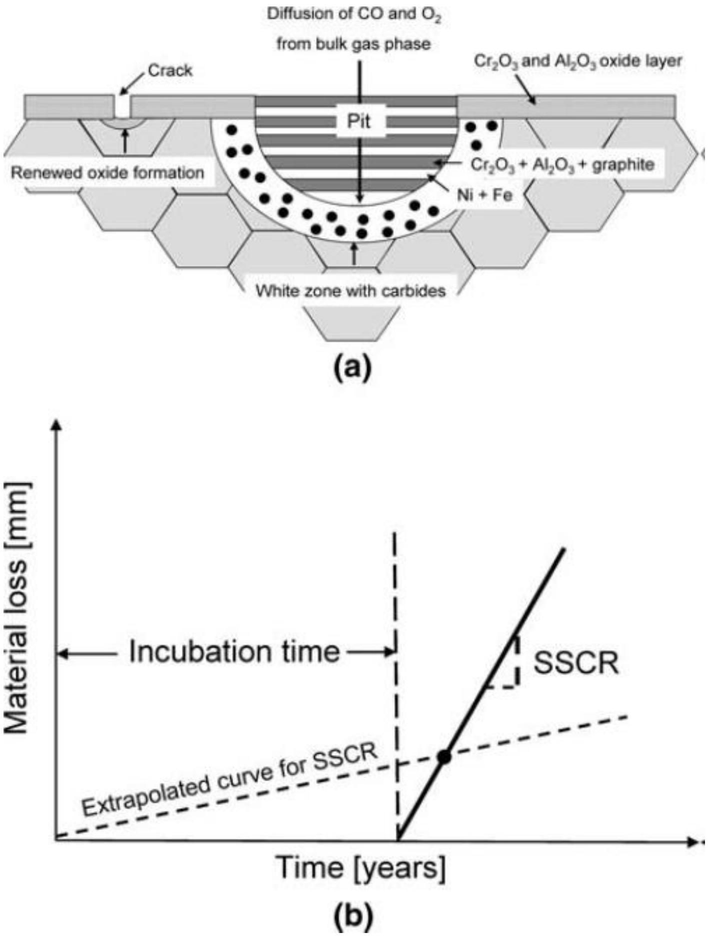

Figure I.9. Model by Albertsen for high-temperature pitting corrosion in Ni-based alloys proposed. a) Pit formation and associated carbide precipitation within the white zone after the breakdown of protective layer. b) Corrosion kinetics as observed during and after incubation period when carbon starts to penetrate into bulk of materials.[28]

The model allows predicting corrosion rates in different materials and operational conditions. However, the influence of the different operational parameters such as gas composition and its variation during the exposition period cannot be elucidated. The approach is essentially metallurgical, it is required to characterize the final pit resulting from the exposition period to calculate the corrosion rate without considering the incubation time, the calculated corrosion rate corresponds to the regime after incubation time, additionally the model does not show if the growth kinetics of the pit is associated with a known kinetics law.

Baker et al.[29,30] evaluated different commercial alloys at 621 °C in CO-H_2-H_2O gas, this study showed that the kinetics of mass loss and pit depth growth can be fitted with a linear combination of the alloy element concentrations. Baker established linear models for the mass loss rate (MLr) (10) and the pit depth growth rate (PDGr) (11) as a function of the chemical composition of the different commercial alloys, using different approaches that show good agreement. The pit depth (local attack) is greater than the average thickness loss calculated from the mass loss (general attack). Therefore, the measurement of the pit depth is more conservative for estimating material lifetime. This model can be useful for materials selection nevertheless the estimations can only be made under the specific validity domain shown in the study.

$$\log MLr = (Ni + Co) + 72.4\,Si + 43.4\,Al + 41.3\,Ti + 10.2\,Cr + 6.2\,(Mo + W) - 1.3\,Fe$$ **Equation 10**

$$\log PDGr = (Ni + Co) + 23.7Si + 30Al + 30.9Ti + 3Cr + 4.8(Mo + W) - 1.9Fe$$ **Equation 11**

In the equations (10) and (11) the elements are expressed in weigth percentage (wt.%). These models are consistent with a positive effect of Ni and Co in the matrix and a negative effect of Fe. They also show the positive effect of protective oxide forming elements (Al, Cr, Si) and carbide forming elements (Ti, Mo, W).

Table I.1 shows the summary of the models found in literature focused in the kinetics of metal dustings. The authors have proposed different modeling approaches for a variety of validity domains with advantages as well as limitations for their further application.

Table I.1. Summary of kinetics models for metal dusting corrosion

Author	Material	Magnitude	Equation	Validity domain
Young [6]	Pure Iron 2 ¼ Cr – 1Mo	• Fe_3C thickness	5 and 6	T= 680°C $p_{Internal}$= 1 atm 68%CO–26%H_2–6%H_2O a_C = 3
Yin [26]	Pure Iron Pure Nickel 2 ¼ Cr – 1Mo	• Mass gain (carbon uptake)	7	T= 650°C $p_{Internal}$= 1 atm %CO = 25- 90 a_C = 2,35 - 16
Albertsen [28]	602, 693	• Pit depth growth	8	Operational conditions Syngas plant
Baker [29,30]	754, TD, 600, 758, 400, 693, 602CA, 625, 625, 601, 690, C-276, 671, 617, 263, 825, DS, 330, 803, 864, 800, 800HT, 956	• Mass loss • Pit depth growth	9 and 10	T= 621°C $p_{Internal}$= 1 atm 70%CO-25%H_2-0.8%H_2O-4%CO_2 a_C = 58

According to experimental results reported in literature (Table I.1), the main parameters that affect metal dusting kinetics are the temperature, the total pressure and the gas phase composition. Regarding the alloy composition, higher ratios of Fe/Ni (wt.%) seem to be detrimental to the alloy resistance and the alloying elements such as Cr, Al, Si and Cu contribute to metal dusting resistance. Other factors like gas rates, grain orientation, grain size, surface finish and cold working are reported to have certain influence on metal dusting. However further studies are needed regards to these parameters.

Metal dusting degradation has been measured using several parameters such as: Fe_3C thickness, the carbon uptake by mass gain and the material loss by mass loss and pit depth. Unlike the incubation periods which are reported by very few authors.

I.3 High-temperature corrosion

The process, which involves solid waste for the production of energy, is named waste to energy (WtE). WtE is a process, which recovers energy contains in high-temperature flue-gas resulting from the waste materials combustion.[31] Figure I.10 illustrates how the process works.[31] Solid waste is unloaded from collection trucks and placed in a waste storage bunker (1). An overhead crane is used to lift waste fuel into a combustion chamber to be burned (2). Calories from combustion flue-gas flow are transfer to heat exchangers tube to convert water to steam in boiler tubes (3). The remaining bottom ash is collected and taken to a landfill (4). The steam is then transported from the boilers to a turbine generator to produce electricity (5) and the remaining fly ash particles are captured by a filtering system where more than 99% of particles matter is removed to avoid pollution. [31]

The tubular water boilers are generally used for steam and hot water generation from the energy potential of hot flue-gases that come from combustion of waste. The steam or hot water is generally produced in tube bundles or platen located in the flue-gas path (6). Special attention is required in boiler design and steam parameters of WtE facilities because, while the selection of high-temperatures and pressures increases boiler efficiency, these conditions favor corrosion problems, especially at the superheater surfaces and the evaporator.[32,33] Also, the high proportion of ash in flue-gas causes high fouling of the heat transfer surfaces, leading to a decline in heat transfer and severe corrosion [34] As the ash and the flue-gas contain high concentrations of alkaline metals (Na, K, etc) heavy metals (Pb, Zn, etc) chlorides and sulfates which adhere on the material surface exposed to combustion gas, severe corrosion is caused by ash deposits melting at 300-500°C. [35,36]

The combustion chamber, the waterwalls of the first blank passes, and the superheater are the boiler components most susceptible of corrosion (Figure I.11). Corrosion of boiler tubes is caused by the chemical attack of flue-gas and ash particles from the furnace. The superheater tube corrosion is either due to gaseous chloride attack and deposits containing chloride salts (active oxidation) or a combination of molten chlorides and molten sulfates.[,37,38] Table I.2 shows typical temperatures conditions in corrosion sensitive areas in WtE boilers.

Ash particles present in flue-gas and sootblowers cleaning system can cause erosion, which is the abrasion of surface material. Erosion appears mostly in the area of high flue gas velocity or gas redirection. Tube wear is caused by a combination of corrosion and erosion. [39] As the corrosion products form a layer on the pipe surface (oxide layer), they act as a protective layer and slow down corrosion but if this protective layer wears out through cracks, spalling or erosion, the metallic surface reappears and the entire process starts anew.

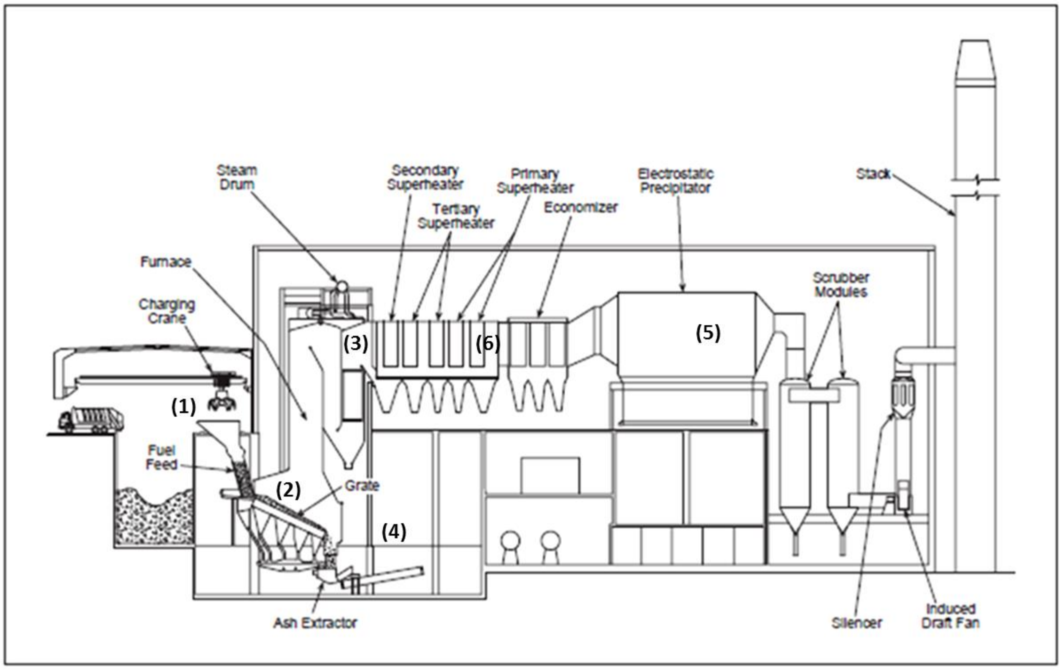

Figure I.10. Waste to energy process diagram. European mass burning power plant [31]

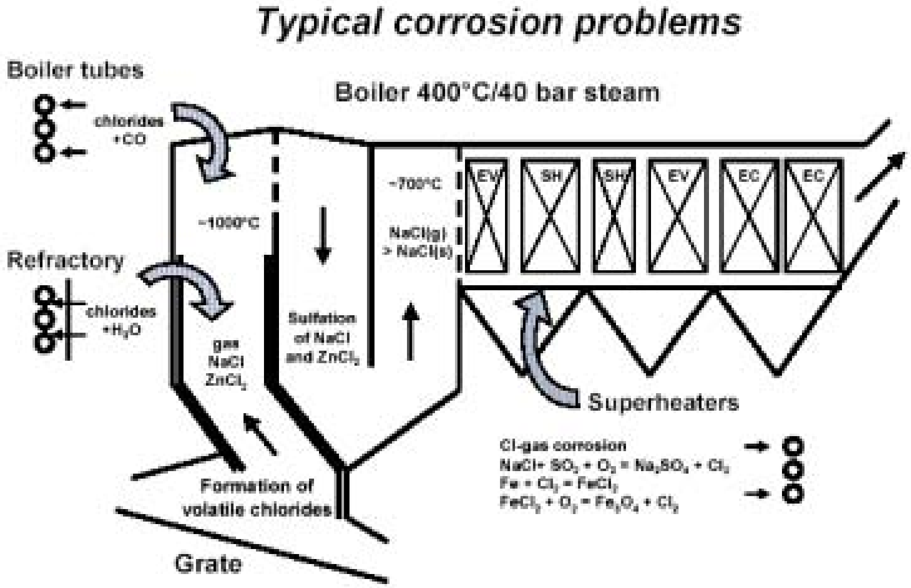

Figure I.11. Corrosion sensitive areas in a WtE Unit [37]

Table I.2. Boiler parts and temperature levels [40]

Boiler part	Steam System	T_{Metal} (°C)	T_{Gas} (°C)
Waterwall	Evaporator (~265°C)	~200 – 300°C	~1000 – 800°C
Screen Tubes	Evaporator (~265°C)	~200 – 300°C	~800 – 700°C
Superheater	Steam (~400°C)	~400 – 530°C	~700 – 600°C

Corrosion rates in WtE boilers is reported to be higher than in boilers combusting fossil fuels that operate at higher temperatures, [41] due to the heterogeneous nature of the municipal waste which makes difficult to maintain the uniform combustion conditions required in the steam boilers but also to its variable chlorine, alkali and heavy metals contents. High-temperature corrosion in WtE boilers could causes 70% of shutdowns approximately and corrosion maintenance costs can reach to a third of the annual maintenance budget and might be as high as 10% of the annual turnover.[37]

The characteristics of the fuel also can cause incomplete combustion, increasing CO levels and occasional heat flux peak on the waterwall produced by flame impingement, [37] High-temperatures of metal surface, either due to high radiation fluxes to the wall or inadequate transfer of heat to the water/steam result in the melting point of deposits and acceleration of the corrosion rate. Furthermore, the temperature gradient between gas temperature and the metal surface determines the condensation of vapor species, rate of deposition and the composition of deposits. [42–44]

Coherent consideration of the corrosion process is difficult, as several parameters interact simultaneously: physical, chemical, operating conditions, metallurgical and crystallographic. Corrosion is often the summative or increased effect of specific parameters which are not critical when taken individually. [45] Therefore the influence of each parameter must be analyzed separately and their relative contribution in the global corrosion processes must be elucidated considering their possible variations caused by the interaction with others parameters involved in the process.

I.3.1 Effect of the environment

I.3.1.1 Effect of the temperature

Both metal and flue gas temperatures are important parameters affecting corrosion in waste-fired boilers. Flue gas temperatures at heat exchanger location determine the types of volatile species that can be transported in the gas, as well as the maximum temperature of any deposits. Tube metal temperatures determine the minimum temperature of such deposits, and thus have a decisive influence on corrosion mechanisms and corrosion rate. [38]

The metal temperature generates the high-temperature reactions and activates melting of deposits to enhance the corrosive process, as shown in Figure I.12. Numerous studies have been performed under isothermal conditions and demonstrated that wastage rate increase with metal temperature. Nevertheless these tests do not consider the effect of flue gas temperature.

The gas temperature determines the composition of the deposits and influences the deposition rate. The temperature gradient at the corrosion interface is the driving force for condensing and diffusion of gas constituents such as alkali and heavy metal chlorides. Figure I.13 shows that corrosion rates increase with metal temperature (1/T) for a given flue gas temperature and with flue gas temperature for a given metal temperature. [38]

Brossard et al.[46] also showed that corrosion rate increases with flue-gas temperature for a given metal temperature, as shown in Figure I.14. It is observed that the mechanism and kinetics are different for temperatures lower than 650°C and temperatures higher than 650°C for a given deposit composition. At $T_{\text{flue gas}}$ < 650°C no molten salts were observed and corrosion mechanism was assumed to be mainly controlled by gas phase attack while at $T_{\text{flue gas}} > 650°C$, fused phases were detected which confirms molten salts corrosion mechanism.

This is consistent with real conditions in WtE facilities, where significant differences can be observed between corrosion rates in heat exchangers for a given steam temperature at different flue gas temperature and corrosion rates for a given flue gas temperature at different steam temperature. [47]

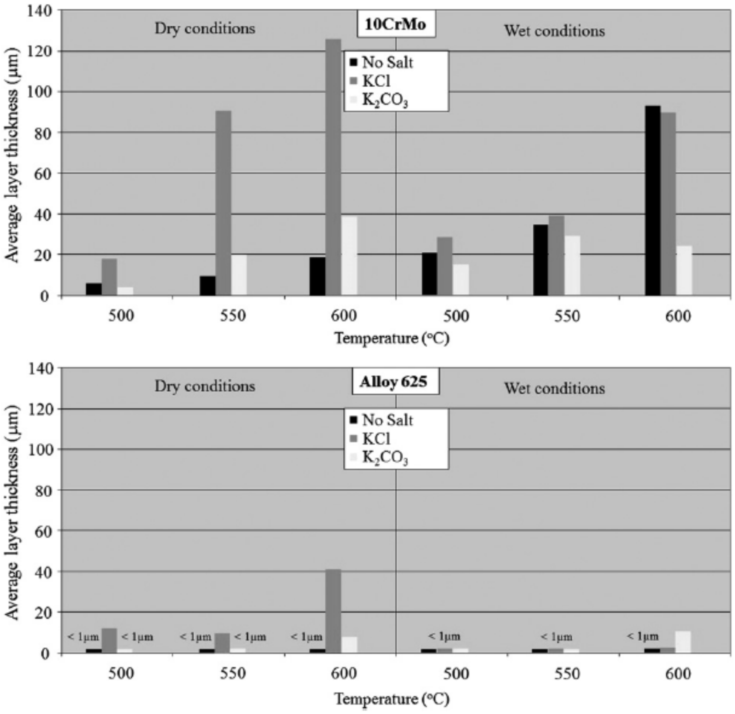

Figure I.12. High-temperature corrosion of superheater steels by KCl and K_2CO_3 under dry and wet conditions. [38]

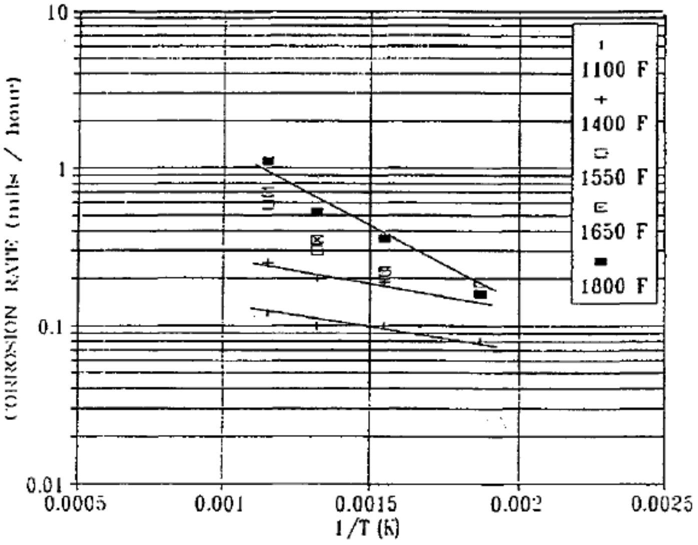

Figure I.13. Corrosion rates of carbon steel in municipal solid waste combustors as a function of metal temperature at different gas temperatures. [38]

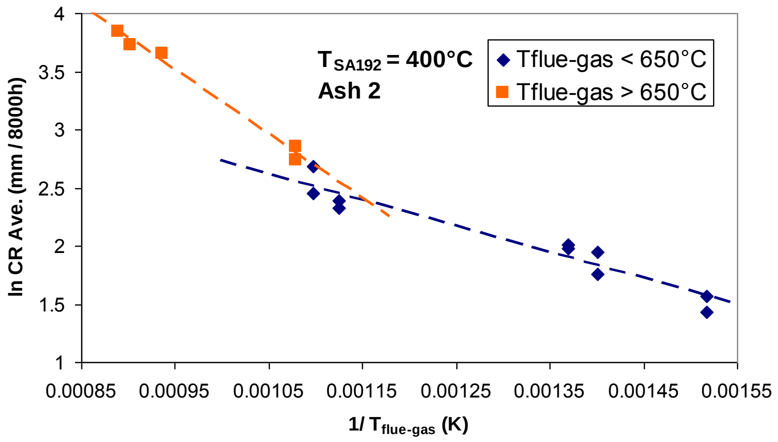

Figure I.14. Arrhenius plots of corrosion rates as a function of flue gas temperature for a given metal temperature at [46]

Waldman et al.[48] also quantified the effect of flue gas and metal temperature on corrosion rates in WtE boilers measured by cooled probe as shown in Figure I.15. Some authors also claim that a large temperature gradient increases the concentration of chlorides within an area in which the eutectics melt, accelerating corrosion.[49] However, this indicator must be considered carefully because significant differences can be observed for a given temperature gradient, at low and high flue gas temperature areas.

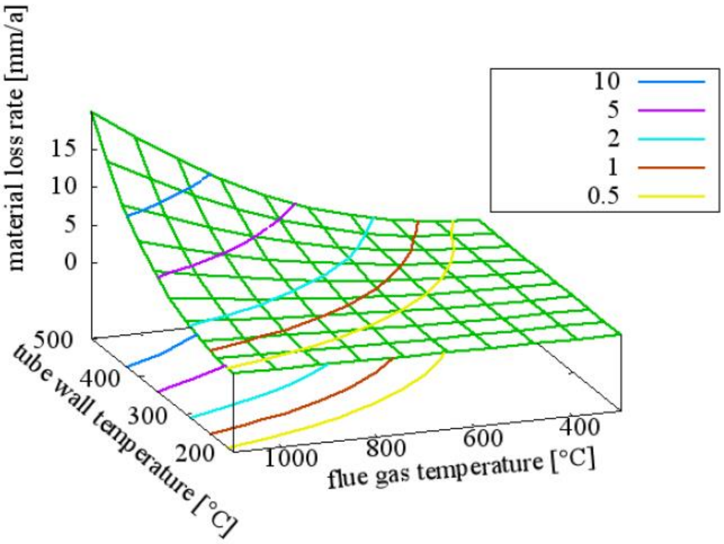

Figure I.15. 3D plot: Corrosion rate as a function of flue gas temperature and metal temperature. [48]

I.3.1.2 Effect of the flue-gas composition

Combustion of waste produces flue-gas and ash particles (aerosols and solid particles). [50] The gas composition depends on the composition of waste and combustion conditions (O_2, temperature) which change with time and depends on the country. The flue-gas composition is not constant throughout the facility; it depends on local injections of air and the gas temperature which vary according to the location. [51,52] Table I.3 shows an example of gas phase composition at the combustion chamber.

Table I.3. Gas composition in the different parts of an incinerator. [52]

Zone	O_2 [a]	H_2O [a]	CO_2 [a]	HCl [b]	SO_2 [b]	HF [b]	CO [b]
Lower ($T_{Flue-Gas}$>1000°C)	6			40-1650	90-200	10-40	>1000
Higher (combustion chamber- superheaters) (700°C < $T_{Flue-Gas}$ < 900°C)	8-10	15	9-12	600-1200	90-130	<20	20-40

[a] *(vol%),* [b] *(ppm)*

Carbon dioxide (CO_2), sulfur dioxide (SO_2) and water vapor (H_2O) present in the flue-gas come from the combustion of organic matter and moisture waste. Hydrogen chloride (HCl) comes from chlorine release in different type of biomass residues [34] or plastics (PVC) [53]. HCl and SO_2 are considered corrosive agents from average levels of 500 ppm and 50 ppm, respectively. [51]

In general, oxidizing conditions by excess of oxygen O_2 tend to limit corrosion.[54,55] The positive effect of oxygen in delaying corrosion has been demonstrated in simulated incineration atmospheres [56,57] as shown in Figure I.16. Water vapor (H_2O) content in the combustion atmosphere can cause a similar corrosion-suppressing effect. [56,58] Nakagawa et al.[59] studied the behavior of carbon steel and type 347H below deposits (NaCl-KCl) under oxidizing and reducing conditions and found a severe corrosion attack in the reducing gas with HCl and H_2O as H_2O acts as an oxidant in molten chlorides, while in the oxidizing atmosphere with H_2O and the highest level of HCl the corrosion rate decreased for all the temperature tested. However the results from two laboratory tests appear to negate that reducing conditions are more damaging than oxidizing conditions. [60,61] This inconsistency can be explained by the fact that reducing conditions raise the vapor pressure of alkali chlorides and thus enhance their formation and deposition but, that once formed; these deposits are more corrosive under oxidizing conditions. This suggests that alternating oxidizing/reducing atmospheres from unstable combustion conditions may promote especially rapid attack.[53] Besides Ruh and Spiegel [55] also showed recently that water vapor seems to reduce the corrosion rate in oxidizing conditions. It can be concluded that both oxidizing and reducing atmospheres are damaging depending on the composition of the gas and characteristics of the deposits but the effect of water vapor can vary according to the type of atmosphere.

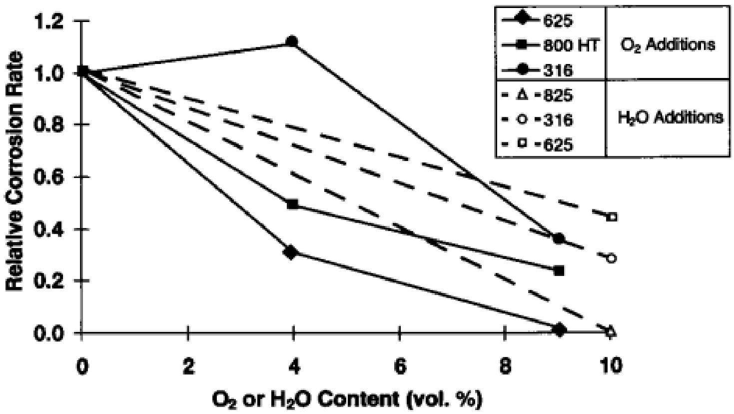

Figure I.16. Effect of O_2 or H_2O on corrosion in MSW incineration environments [56]

The effect of HCl and SO_2 has been studied extensively and the principal findings indicates: a) there is a strong corrosive effect of HCl, in low alloy steels, [37,]b) corrosion increases with temperatures (flue-gas and metal) [37,]and c) the combined effect of HCl and SO_2 in the gas may retard corrosion in low alloy steels. [37] Grabke et al [62] studied the individual effect of HCl and SO_2 in the active oxidation of steels below deposits. SO_2 in the gas causes a minor increase of active corrosion by sulfation of alkali chlorides in deposit and formation of sulfide at metal / oxide interface that limit chloride volatilisation. Corrosion was strongly enhanced by the presence of HCl. Higher concentrations of HCl rather than SO_2 in the gas also might cause the transformation of melted sulfates in the deposits into volatile chlorides which increase active oxidation. [62] However, in the presence of balanced concentrations of HCl and SO_2 in the atmosphere, the corrosion caused by HCl was reduced by the presence of SO_2. These results correspond with the findings of Krause [63] which added sulfur to the waste and the chloride content of the deposits decreased significantly as well as the corrosion rate in carbon steel and austenitic stainless steel.

Also Spiegel et al. [64] studied the influence of gas phase composition on the hot corrosion of steels and Ni-based alloys beneath a (Ca-Na-K)-sulfate mixture containing $PbSO_4$ and $ZnSO_4$. With the addition of SO_2, the corrosion of every alloy increased. The relatively poor behavior of Ni-based alloys under these conditions is due to the higher solubility of NiO rather than Fe_2O_3 in the form of sulfates. With the addition of HCl corrosion rates increased on the Fe-based alloys, due to the presence of more precipitates in the melt. The solubility of the oxides was enhanced by the presence of HCl in the gas phase. For the Ni-based alloys, the mass loss was lesser than for Fe-based alloys but also increased with the HCl addition to the atmosphere. However, in comparison to the SO_2 containing gas, mass loss was less. Thus in this study it seems that Ni-based alloys were more affected by the SO_2 than by the HCl. In the presence of both HCl and SO_2 in the gas, the mass loss was delayed in comparison to only HCl-containing gas for low alloy steels which corresponds with Grabke et al. [62] observations, while the mass loss of Ni-based alloys was increased. Thus, the Ni-containing alloys were relatively more attacked than the Fe-based materials. Therefore, the effect of the HCl and SO_2 individually or combined, depends on the alloy system under study.

I.3.1.3 Effect of the composition of deposits

I.3.1.3.1 Deposit - induced corrosion

During combustion of waste highly corrosive species are released, such as Cl_2 , HCl, SO_x, HBr, alkali metals (Na, K) and heavy metals (Zn, Pb).[65,66] These elements can condensate and form with fly ash deposits on the tubes and interact with the metal oxide scale. Such gases also can influence the corrosion of boiler tubes when the volatilized salt chlorides, sulfates, fly ash and others are deposited on the boiler tubes during cooling. Therefore the presence of chlorides in deposits generates corrosion in three ways: [36]

- The presence of chlorine in most cases limits the formation of the protective oxide layer and causes accelerated attack by active oxidation.
- Presence of chlorinated species in the deposit and at the metal/oxide interface causes a reaction similar to gas phase/active oxidation. Gaseous chlorine may be generated from the sulfation of alkali chlorides or reaction between the chlorides and the metal oxide.
- The chloride in the deposits may form low-temperature melting eutectics (mixture characterized by the lowest possible melting point), which may flux (dissolve) the oxide layer.

Grabke, [62] Viklund [36] and Albina [37] agree in the description of the mechanism of active oxidation as follows:

a) Formation of chlorine at the scale surface, from the oxidation of HCl according to the Deacon reaction (reaction 7) [67] or from the reaction of chlorides such as NaCl with the oxides of the scale (reaction 8). In the case of high-temperature alloys (high Cr and Ni) the process is similar to that with Fe but reactions take place within the chromium oxide scale (reaction 9).

$$2HCl_{(g)} + \frac{1}{2}O_{2(g)} \rightarrow Cl_{2(g)} + H_2O_{(g)} \qquad \textbf{Reaction 7}$$

$$2NaCl_{(g)} + Fe_2O_{3(s)} + \frac{1}{2}O_2 \rightarrow Na_2Fe_2O_{4(s)} + Cl_{2(g)} \qquad \textbf{Reaction 8}$$

$$4NaCl_{(g)} + Cr_2O_{3(s)} + \frac{5}{2}O_2 \rightarrow 2Na_2CrO_{4(s)} + 2Cl_{2(g)} \qquad \textbf{Reaction 9}$$

b) Penetration of chlorine into the scale to the oxide/metal interface: chlorine penetrates the oxide and reaches the metal, under enough chlorine partial pressure and low oxygen partial pressure; the formed metallic chlorides are stable.

c) Formation of chlorides on the metal surface components: gaseous Cl_2 (present up to 600°C) (reactions 10, 11, 12) or HCl (present above 600°C) (reaction 13) diffuses through the oxide layer presumably through the pores and any cracks of the oxide scale, thus allowing metal chlorides to be formed at the metal/oxide interface. Several volatile solids and gaseous chlorides can form at the interface oxide/metal. At 600°C, the Gibbs free energies of formation of the different metal chlorides indicate that $CrCl_2$ has the highest negative value (–286 kJ/mole) followed by $FeCl_2$ (–232 kJ/mol) and $NiCl_2$ (–174.2 kJ/mole) which points out that Ni is less reactive than Fe and Cr.

$$Fe_{(s)} + Cl_{2(g)} \rightarrow FeCl_{2(s)} \qquad \textbf{Reaction 10}$$

$$Cr_{(s)} + Cl_{2(g)} \rightarrow CrCl_{2(s)} \qquad \textbf{Reaction 11}$$

$$Ni_{(s)} + Cl_{2(g)} \rightarrow NiCl_{2(s)} \qquad \textbf{Reaction 12}$$

$$Fe + 2HCl = FeCl_2 + H_2 \qquad \textbf{Reaction 13}$$

d) Diffusion of chlorides outward: the solid chlorides formed at the interface have considerable equilibrium vapor pressures and sublimate continuously (reactions 14, 15, 16). The gaseous metal chlorides diffuse outwards toward the gas/oxide interface i.e. down their activity gradient to regions with higher oxygen partial pressure.

$$FeCl_{2(s)} \rightarrow FeCl_{2(g)} \qquad \textbf{Reaction 14}$$

$$CrCl_{2(s)} \rightarrow CrCl_{2(g)} \qquad \textbf{Reaction 15}$$

$$NiCl_{2(s)} \rightarrow NiCl_{2(g)} \qquad \textbf{Reaction 16}$$

e) At high pO_2, the gaseous metal chlorides react with oxygen to form solid oxides and release gaseous chlorine (reactions 17-21). The volatile Cr-chlorides are oxidized closer to the metal surface than Fe-and Ni-chlorides, since Cr-chloride is converted into oxide at lower oxygen partial pressure than Fe-oxides and Ni-oxides which need significantly higher oxygen to oxidize. These oxides are porous and non-protective.

One fraction of the chlorine released diffuses to the gas and another fraction goes back through the oxide/deposit interface to react with the metal at the oxide/metal interface and start the cycle again.

$$3FeCl_{2(g)} + 2O_2 \rightarrow Fe_3O_{4(s)} + 3Cl_{2(g)} \qquad \textbf{Reaction 17}$$

$$2FeCl_{2(g)} + \frac{3}{2}O_2 \rightarrow Fe_2O_{3(s)} + 2Cl_{2(g)} \qquad \textbf{Reaction 18}$$

$$2CrCl_{2(g)} + \frac{1}{2}O_2 \rightarrow Cr_2O_{3(s)} + 2Cl_{2(g)} \qquad \textbf{Reaction 19}$$

$$2CrCl_{3(g)} + \frac{3}{2}O_2 \rightarrow Cr_2O_{3(s)} + 3Cl_{2(g)} \qquad \textbf{Reaction 20}$$

$$NiCl_{2(g)} + O_2 \rightarrow NiO_{(s)} + Cl_{2(g)} \qquad \textbf{Reaction 21}$$

Also in the experiments of Grabke, [62] the analysis of deposits has shown that the outer layers of the protective oxide scales contain sulfates such as $CaSO_4$, Na_2SO_4, K_2SO_4, $PbSO_4$, and $ZnSO_4$ while the inner scales contain metal chlorides such as $CaCl_2$, KCl, $PbCl_2$ and $ZnCl_2$. The formation of sulfates in the deposit is due to the sulfation of the alkali chlorides and is assumed to happen at the outer surface of the deposits. [68] Metal chlorides in the deposits react with gaseous SO_2 and or SO_3 forming condensed alkali sulfates (reaction 22). [69] These reactions release gaseous chlorine that diffuses towards the metal/oxide interface creating a sequence of reactions similar to that of active oxidation.

$$2(K,Na)Cl_{(s)} + SO_{2(g)} + \frac{1}{2}O_2 \rightarrow (K,Na)_2SO_{4(s)} + Cl_{2(g)} \qquad \textbf{Reaction 22}$$

However, Grabke [62] analyzed ash deposits exposed at different SO_2 partial pressures atmospheres, showing that the interactions of SO_2 and deposits might led to the formation of pyrosulfates (reaction 23) which melt at metal temperature range. If the melt reaches the deposit/oxide interface, it will destroy the oxide scale forming a complex sulfate (reaction 24) increasing the corrosion rate. Otherwise the conversion of chlorides into sulfates (reaction 22) can also take place mainly near the surface of the deposit, so most of the chlorine will go to the atmosphere, leaving less chlorine to diffuse again into de bulk to produce active oxidation, which will decrease corrosion rates. Furthermore Grabke [62] added the effect of HCl to the gas which reacts with the mixed sulfate of the deposit (reaction 25). This reaction generates chlorides that lead to chlorine formation within the deposit not at deposit/scale interface so most of it diffuses to the atmosphere. The equilibrium of reaction 25 also generates SO_2 which may diffuse to the scale/metal interface and form FeS or shift the reaction to the left side and sulfation of chlorides takes place leaving less chloride for active oxidation. Therefore the active oxidation is suppressed by the presence of SO_2 in the gas and the formed sulfates in the deposits, under these conditions corrosion rates could decrease as long as melt sulfates don’t reach the deposit/scale interface. If they do it would be corrosion by molten ash-salts.

$$Na_2SO_4 + SO_2 + \frac{1}{2}O_2 \rightarrow Na_2S_2O_{7(s)} \qquad \textbf{Reaction 23}$$

$$Na_2\,S_2O_{7(l)} + Fe_2O_3 \rightarrow 2Na_3Fe(SO_4)_{3(l)} \qquad \textbf{Reaction 24}$$

$$(K,Na)_2Ca_2(SO_4)_3 + 2HCl \rightarrow 2(K,Na)Cl + 2CaSO_4 + SO_2 + H_2O + \frac{1}{2}O_2 \qquad \textbf{Reaction 25}$$

I.3.1.3.2 Corrosion by molten ash-salts mixtures

Attack by molten ash-salt mixtures in WtE incinerators is essentially a form of hot corrosion. [70] Hot corrosion is the accelerated oxidation of metal surfaces exposed in a high-temperature gaseous environment and coated by a thin fused salt film. [53] Hot corrosion is classified into type I and type II. [71,72] The type I refers to temperatures above the melting point of the condensed salt, in type II a molten salt is formed below the melting point of the pure salt. In the latter case, the melting point is lowered due to dissolution of formed corrosion products. Several studies have suggested a fluxing mechanism in which protective oxide dissolves in the fused salt and precipitates as non-protective particles within the salt or at the salt/gas interface. [73]

Formation of salt mixtures is generally believed to be the main reason for low temperature metal corrosion, in the temperature range of 250°C to 400 °C. Some salt mixtures either chloride-chloride or chlorine-sulfate, have lower melting temperatures (eutectic solutions) than the pure compound. For example, KCl and NaCl have a melting point of 774°C and 801°C respectively but may form low-temperature eutectics in solution with several other substances such as $ZnCl_2$ lowering their melting point to 230°C and 262°C respectively (Table 4). Field exposures and laboratory tests [74,75] have tried to explain the effect of the compounds of the ash on the corrosion rates, [74,76–79] the mechanism of deposition of chlorides, [68] kinetics of HCl emission from chlorides and solubility of oxides in fused salts [72]. Some of them identified fused zinc and lead chlorides as a major concern, [74,79,80] since these are known to have low melting points and form low melting eutectic mixtures with other salts (Table 4). Otsuka [74] determined that the relative amount of fused salts in non-fused ash constituents at 550°C increased with increasing the chlorine content of the ashes. The author also identified a correlation between the corrosion rate and the relative amount of fused salt in the deposit at 550°C.

In Table I.4 a non-exhaustive list of compounds and eutectic mixtures that may cause molten salt corrosion are listed. Certainly, more complex mixtures, not found in binary or ternary phase diagrams, may be present.[81,82] Both chloride and sulphate melts may form on superheater tubes during waste incineration, although the molten chlorides are more frequently encountered due to their lower melting points. Also the concentration of the compounds of the salt mixtures can vary in some degrees the melting point of the eutectic as shown in Table I.5. Deposits also present oxides and silicates, Lindberg [82] measured and calculated liquidus temperatures of synthetic ash with oxides and silicates that showed higher values than that of sulfates. Therefore, oxides and silicate may contribute to increase the ash fusion temperature of the salt mixtures.

Once the melting point is reached, the liquid phase on the metal surface accelerates the corrosion rate due to the following reasons:

a) Chemical reactions are faster in the liquid phase than in the solid phase

b) A liquid phase provides an electrolyte, i.e. a pathway for ionic charge transfer, for the electrochemical attack.

c) The liquid phase provokes the dissolution of the protective oxide scales.[83]

Corrosion can also take place through mass transfer due to thermal gradient in the melt. This mode of corrosion involves dissolution of an alloying element at hot spots and deposition of that element at cooler spots. This can result in severe fouling and plugging in circulating system. [84]

Table I.4. Melting points of compounds and salt mixtures found in WtE boilers. [79,81,83,85]

Single compounds	Melting point (°C)	Salt Mixtures	Melting point (°C)
$ZnCl_2$	283	KCl - $ZnCl_2$	230
$PbCl_2$	489	$NaCl$ - $ZnCl_2$	262
KCl	775	KCl - $FeCl_2$	355
$NaCl$	801	$NaCl$- $FeCl_2$	370
$ZnSO_4$	730	K_2SO_4 - $ZnSO_4$ - Na_2SO_4	388
$PbSO_4$	1170	KCl - $PbCl_2$	412
Na_2SO_4	884	$NaCl$ - $PbCl_2$	415
K_2SO_4	1076	$NaCl$ - $CrCl_2$	437
$FeCl_2$	673	KCl - $CrCl_2$	462
$CrCl_2$	821	KCl - $NiCl_2$	508
$CrCl_3$	947	$NaCl$ - $NiCl_2$	560
$NiCl_2$	1001	KCl – $NaCl$	657
Quaternary salt mixtures		**Melting point (°C)**	
$(NaCl)_2$–$CaCl_2$–Na_2SO_4–$CaSO_4$		485°C	
$(KCl)_2$–$CaCl_2$–K_2SO_4–$CaSO_4$		580°C	
$(NaCl)_2$–$(KCl)_2$–Na_2SO_4–K_2SO_4		515°C	
KCl–K_2SO_4–$ZnCl_2$–$ZnSO_4$		265°C	
$NaCl$–Na_2SO_4–$ZnCl_2$–$ZnSO_4$		255°C	

Table I.5.Composition and melting points of common eutectics found in WtE boilers. [37]

Salt Mixtures	Melting point (°C)	Composition (wt%)
KCl - $ZnCl_2$	250	48:52
KCl - $ZnCl_2$	262	82:18
KCl - $ZnCl_2$	262	84:16
$NaCl$ - $PbCl_2$	410	31:69
$NaCl$ - $PbCl_2$	415	17:83

Recently Otsuka [73] revealed important findings from the evaluation of carbon steel with deposits taken from boilers of waste incinerators. In this study, corrosion initiated at temperatures when the deposits started to melt, became severe when fused salts constituents increased and become limited when most of the deposits became fused and solidified, since this might hamper the gas transport from flue gas to metal substrate.

In summary, according to experimental findings the most important variables in the high-temperature corrosion process are: $T_{Flue\ gas}$, as it governs the chemistry of elements and promotes the condensation of corrosive species on the surface of the materials, T_{Metal}, as it promotes the metallic chlorine sublimation and the ash fusion on the metal surface. O_2 and H_2O in the gas as oxidizing agents promotes oxide scale formation in the alloy, which increases the alloy corrosion resistance. HCl in the gas provides Cl_2 to active oxidation and produces chlorides in the deposits which decrease the ash fusion temperature, increasing the corrosion rates. SO_2 in the gas has an ambiguous effect, as it can contribute to sulfation of chlorides to avoid active oxidation but simultaneously this reaction releases Cl_2 that promotes metal chlorides formation. In the deposits heavy metal (Pb, Zn) and alkaline (Na, K) chlorides present the lowest melting temperature in the ash composition, followed by heavy metal (Pb, Zn) and alkaline sulfates. Finally there are the oxides, which present the highest melting temperature and contribute to stabilize solidus temperature in salt mixtures.

I.3.2 Effect of the alloys composition

The real importance of materials selection for waste incineration plants and the alloying elements in the different alloy systems is the ability of forming a stable, adherent, uniform and protective oxide layer at high-temperatures. Although most metals and alloys form oxide layer in contact with air, the characteristics in oxides can be different. For engineering purposes these characteristics are significant since they determine the component life-time. [36]

I.3.2.1 Oxidation of metals

Most metallic materials react spontaneously with the surrounding environment forming different corrosion products depending on the specific environment. Oxidation of a metal surface is considered to begin with the adsorption of oxygen molecules from the atmosphere, followed by nucleation and thereafter the formation of a thin oxide layer. [86] Once a thin film is formed, oxidation continues by the diffusion of reactants through the solid film. A defect-rich or even porous oxide scale will be a less efficient diffusion barrier compared to a lattice with low defect concentrations. During exposure of metals and alloys suitable for use at high-temperatures, the diffusion of reactants across the oxide scale is usually the rate-determining step, the oxidation rate decreases as the oxide thickens. [36] Nevertheless in presence of molten salts, the reaction at metal/environment interface can participate to the overall kinetics control.

For engineering metals and alloys oxidation is a spontaneous reaction with a negative change in the Gibbs free energy, ΔG. The Ellingham diagrams can be used to determine which element in a multi-component alloy is most likely to react, or even react at all, with the surrounding environment. Figure I.17 shows the Ellingham diagram for stainless steel that indicates the variation of free energy for the main alloying elements in at different temperatures. [87] The chromia scale is the most stable of all oxide layers.

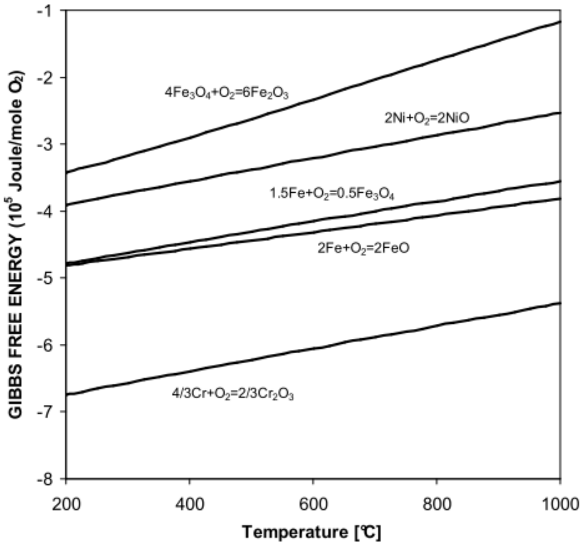

Figure I.17. Ellingham diagram for the main alloying elements in stainless steel. [87]

In the complex atmospheres of waste-to-energy plants, only elements with a high oxygen affinity will be oxidized. The same behavior is also expected underneath deposits where a low oxygen partial pressure is established. The oxidation characteristics of the main elements in alloys are described as follows:

I.3.2.1.1 Iron

Iron is the base material in most alloys, and low-alloyed ferritic steels are frequently used as superheater materials. Under oxidizing atmospheres, iron exhibits multilayer scale formation: above 570 ºC the scale consists of; FeO (wüstite), Fe_3O_4 (magnetite) and Fe_2O_3 (hematite). FeO layer is the closest to the substrate and the thickest while Fe_2O_3 has the highest content of oxygen and is in the outermost layer with high oxygen pressure. At 1000 ºC the relative thickness of the oxides are found at a ratio of 95:4:1 for $FeO:Fe_3O_4:Fe_2O_3$. [88] A vacancy-rich crystal structure explains the fast diffusion rate, and the reason for the relative thickness of FeO compared to the other oxides. Below 570 ºC only the semi-protective oxides Fe_3O_4 and Fe_2O_3 are stable. In atmospheres containing sulfur, chlorine and low O_2 partial pressures, iron based alloys are sensitive to form volatile chlorides at the metal/oxide interface. These compounds limit the oxide scale adherence and promote multiscale corrosion products. However sulfates might limit the formation of volatile chlorides.[69] The solubility curve of Fe_3O_4 in molten salts at 727°C in alkali chloride and 550°C in alkali chloride/sulfate mixture exhibit a minimum at pO^{2-} about -15 and -7 respectively and solubility of Fe_3O_4 will be slower in basic molten salts (low pO^{2-}). [89]

I.3.2.1.2 Nickel

Nickel forms only one oxide, the cubic phase NiO. In steels, nickel is added as alloying element to maintain the austenitic (FCC) structure. Ni is also an element comparatively stable against reaction with chlorine. Nevertheless, in presence of sulfur, NiS can be formed at low pO_2 as well as $NiSO_4$ at higher pO_2. Solubility of NiO in molten salts at 727°C in alkali chloride and 550°C in alkali chloride/sulfate mixture decreases with decreasing pO_2. Thus NiO will be more resistant to molten salts in basic molten salts. [89] But, the enhanced high-temperature corrosion resistance in Ni-base alloys is produced by the presence of chromium. Higher nickel contents increases the Cr-activity and/or decrease the Fe-activity, delaying the growth of iron-rich oxides. [90]

I.3.2.1.3 Chromium

Chromium is the most important and common alloying element for high-temperature applications as it forms the stable oxide Cr_2O_3 with the hexagonal corundum structure. Diffusion through Cr_2O_3 is very slow and thus it is considered as a protective oxide. Cr will also be less reactive to Cl and sulfur than iron or nickel. However, large additions of Cr under high Cl-contents atmospheres might contribute to form chromium chlorides ($CrCl_2$). [36,37,62]

When chromium is added as alloying element to Fe-base alloys, the formation of FeO is suppressed, instead a more protective Fe_3O_4 is formed and at higher chromium concentrations a mixed spinel, $Fe(Fe,Cr)_2O_4$, is formed. This transformation in oxide structures reduces the diffusion rate across the scale and thus the oxidation rate. A further increase in chromium content will further enhance the corrosion resistance. Steels with Cr-content above 12% are defined as stainless steels. However at high-temperatures higher Cr-contents (18%-20) are needed.[91] Cr-content of 30% is considered an optimum concentration for engineering alloys to ensure good micro structural stability, workability, ductility, and weldability.[92]

Studies of the solubility of Cr_2O_3 in chlorine molten salts [89] have shown that dissolution of Cr_2O_3 tend to be larger in basic conditions. Cr_2O_3 is dissolved as hexavalent chromium ion (CrO_4^{2-}). Furthermore, authors claim that Cr_2O_3 oxide scale is still stable in molten sulfate salts (like gas turbine) considering that pO_2 is high enough to be near to the minimum of the solubility curve (V-shape curve) of Cr_2O_3.

I.3.2.1.4 Aluminum

Aluminum forms α-Al_2O_3 which is the most stable oxide from Al-oxidation. It has the hexagonal corundum structure with excellent protective properties. However, during the transient oxidation of aluminum other less protective crystal structures such as θ-Al_2O_3, γ-Al_2O_3 and δ- Al_2O_3 may also form at low temperature ($T<1000°C$). [93,94] Alumina forming alloys may be preoxidised in controlled atmospheres to ensure the α-Al_2O_3 formation.

Phongphiphat et al.[95] showed that aluminide-coated nickel-based alloy 59 and aluminide-coated stainless steel 310 reach higher corrosion resistance in WtE environments than Ni-based alloys (Inconel 625, alloy 59) or iron based alloy (alloy 556, stainless steel type 310). Coating on nickel based alloy consisted of Ni/Al-intermetallic phases and corrosion products were θ-Al_2O_3, α-Al_2O_3, NiO, $NiCr_2O_4$, Cr_2O_3, MoO_2 and MoO_3. On the other hand coating on stainless steel consisted of Fe/Al- intermetallic phases and corrosion products were θ-Al_2O_3, α-Al_2O_3, Fe_2O_3, FeO(OH), NiO, Cr_2O_3 and CrO_2. The aluminized stainless steel did not perform as well as the aluminized Ni-based alloy, but it had greater resistance to hot corrosion, than uncoated Ni-based alloys (alloy 59 and alloy 625). However, chloridation resistance was not particularly high, due to higher Fe-content in the coated stainless steel.

I.3.2.1.5 Silicon

Low concentrations of silicon are often used in high-temperature steels as its high oxygen affinity leads to the formation of a silicon oxide sub-layer beneath the chromia scale. Different crystal structures are possible depending on the specific conditions. The protective vitreous silica (SiO_2) is frequently found.[96,97] SiO_2 oxide may have a relatively low solubility in chloride-sulfate molten salt according to Ishistuka [92] results particularly at estimated waste environment basicity ($5<pO^{2-}<10$). In addition silica layers are known to be protective in presence of molten sulfates.[98] However, this oxide is poorly adherent during thermal cycling conditions. [99,100] Silicon content should be kept below 2-3 % to avoid embrittlement of the material but coating could be promoted.

I.3.2.1.6 Molybdenum

Mo is less reactive against Cl and form Mo oxides (MoO_2, MoO_3) at corrosion interface according to Kawahara et al.[49] experiments In this study, the addition of Mo-content of approximately 5 wt.% or more is effective especially in severe corrosive environment. The evidence of beneficial effect of Mo is the outstanding performance and extensive use of 9Mo containing alloy 625 for WtE applications. Addition of Mo above 9 wt.% will decrease corrosion resistance by acidic dissolution of Cr_2O_3.[89] However, large additions of Mo which is a ferrite stabilizer, accelerates the formation of intermetallic compounds that reduce the structural stability of the material. Therefore, to optimize the Mo-content regards the Ni, Cr, and Fe concentrations is required.

I.3.2.2 High-temperature resistant alloys

In waste incineration plants, the corrosion resistance determines the component life-time. [36] The corrosion behavior of iron, chromium and nickel as base metals shows differences. These differences are due the different reactivity of the metals in the following process: a) the formation of chlorides and oxides, b) differences in vapor pressures and c) differences in the thermodynamic equilibria between volatile chlorides and solid oxides. [37] Different materials are commonly used for superheater tubes: low-alloyed ferritic steels, ferritic-martensitic-austenitic stainless steels, and nickel-base alloys. Also numerous studies have showed the materials performance under different conditions.

Low-alloyed ferritic steels have the body centered cubic (BCC) structure and are ferromagnetic. They have poor oxidation resistance and creep rupture strength limit its use at 500 ºC. However, their low cost makes them an interesting alternative at lower temperatures (steam temperatures 400°C-450°C in WtE applications). Ferritic-martensitic steels exhibit higher creep rupture strength than the low-alloyed ferritic alloys. [36] These materials are normally alloyed with 9-12%Cr, which is beneficial for the high-temperature corrosion resistance, but not enough, since alloys with less than 15% Cr are generally very susceptible to hot corrosion attack. [84] In general ferritic stainless steels with Cr-content of 18-30 wt.% have shown good resistance to high-temperature corrosion. [101] The considerably faster chromium diffusion rate in the alloy when compared to austenitic steels promotes the formation of a protective chromium oxide.

Austenitic stainless steels have the face centered cubic (FCC) structure. Ni is added to stabilize the austenitic structure, which makes the alloys more expensive than the ferritic steels. The austenitic stainless steels are non-magnetic, have higher thermal expansion and lower thermal conductivity than the ferritic ones. Ni-base alloys also have the face centered cubic (FCC) structure and are frequently used in high-temperature applications due to the combination of excellent mechanical properties and good corrosion resistance. These alloys often outperform other candidate alloys, but are very expensive due to the high nickel content. [36]

On high alloyed steels, low corrosion rates are usually correlated to a scale dominated by the protective oxides Cr_2O_3, Fe_3O_4, Al_2O_3 and SiO_2, while nickel and the other iron oxides as well as mixed spinel type oxides usually indicate accelerated corrosion rates.[88] Over the years numerous studies have evaluated different materials in corrosion environments for waste incineration applications. Rapp [102] and Ishitsuka [92] measured the solubility of several oxides in molten chlorides which showed that a protective Cr_2O_3 scale easily dissolves in molten chlorides at the melting point of eutectic composition, the addition of molybdenum and/or silicon improved the corrosion resistance of alloys.

Kawahara [103] performed field corrosion tests on single tube materials and two welded overlay materials during 3000 hours, in three typical Japanese waste incineration plants. The test results indicated that austenitic alloys containing higher concentrations of [Cr + Ni + Mo] show excellent corrosion resistant properties. Later Kawahara [104] studied the formation of scale structures and the effect of corrosion-resistant alloying elements, which showed that the severity of corrosion environments is influenced by the penetration extent of corrosive matters through deposits while scales and the protective effect of oxide films derived from alloying elements prevents the corrosion progression as shown in Figure I.18. The ability of oxides to prevent the penetration of corrosive deposits was found to be in the following order: $Fe_2O_3 \gg Fe_3O_4 > Cr_2O_3 > Al_2O_3 > SiO_2$. [105] Nevertheless, the stability of chlorides was in the following order: $Cr > Fe > Ni \approx Mo$ at temperatures of 500°C. [95] However the author also showed that thermal fluctuation characteristic of this kind of environment sometimes causes the breaking and peeling of the oxide scales increasing corrosion rates.

Mannan [89] evaluated the corrosion resistance of materials under simulated WtE environments at different temperatures which showed, that alloy 622 (60Ni-21Cr-14Mo-3W-2Fe wt.%) has better corrosion resistance than 625 (61Ni-22Cr-9Mo-3Nb-3Fe wt.%) at 550°C and 650°C. However, at 500°C the contrary occurs, which is consistent with the results of Kawahara and Kaihara,[49] who reported beneficial effects of high Mo-contents at higher temperatures. In the same study alloy 625 performed better than 825 (42Ni-20Cr-3Cu-1Ti-29Fe wt.%), this might be associated to higher Fe-content in alloy 825. In this study the presence of higher Fe-content in the alloys was found to be detrimental and Ni, Cr and Mo were beneficial for corrosion resistance. However at 550°C increasing Cr content from 22wt% to 30wt% in alloy 625-type alloy did not improve the corrosion resistance. The cumulative Mo content (wt% Mo + 0.5 wt% W) was found beneficial at 550°C. Therefore, performance of alloys is rather sensitive to test temperature and test environment, different alloys might perform better under different conditions. Lay [106] discusses the feasibility of using 625 overlay cladding in WtE boilers, as corrosion rates, in most cases have been found to be less than 5 mpy (mils per year). However, in some aggressive boilers, alloy 625 overlay tubes have been less than adequate in performance. This may be due to boilers burning waste containing more chlorine and/or heavy metals, combined with higher operating temperatures, higher flue gas velocities and soot-blower erosion, among other factors. It can be concluded that the behavior of materials varies depending on the conditions of exposure. Even using high performance alloys in WtE applications, process conditions must be controlled.

In summary, higher ratios of Fe/Ni (wt.%) are detrimental to the alloy resistance in WtE atmospheres due to the high sensitivity of iron in chlorinated atmospheres. The alloying elements such as Cr, Al, Si contribute to materials resistance, as the ability of oxides to prevent the penetration of corrosive deposits was found in the following order: $Fe_2O_3 >> Fe_3O_4 > Cr_2O_3 > Al_2O_3 > SiO_2$. [105] Mo also was found to increase resistance but at high concentration > 5% and higher temperatures T > 550°C. Al-coatings showed to be a good alternative to increase the alloys resistance.

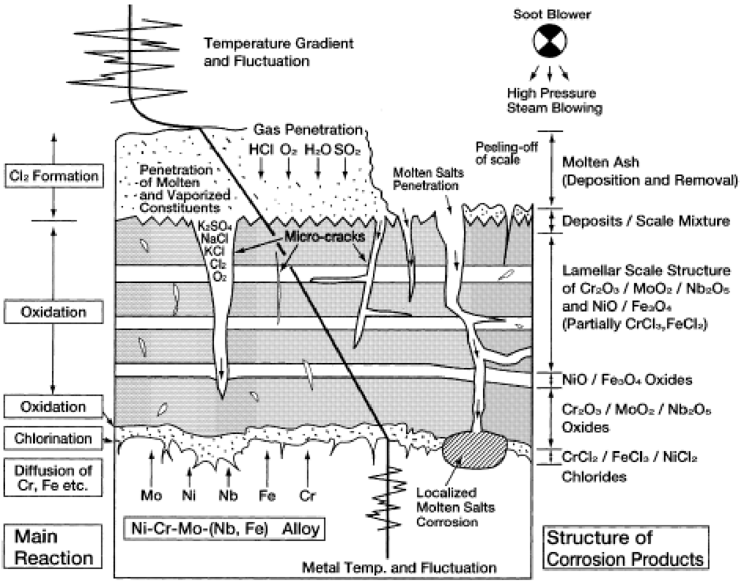

Figure I.18. Scale structure and corrosion mechanism for Ni-Cr-Mo-Nb-Fe alloy. [103]

I.3.3 Kinetics modeling of high-temperature corrosion

Over the years few models have been proposed by different authors to predict high-temperature corrosion rates. However, given the number of environmental factors and materials to be considered, it is difficult to establish a single law that associates a corrosion rate to all of these factors.

Waldman [107] defined a parabolic rate law from measurements made with electrochemical sensors (Linear Polarisation Resistance - LPR - measurement) mounted on cooled probes located on-site in the industry. These devices measured corrosion rates of carbon steel as a function of the variation of flue gas temperatures at constant metal temperature as well as the variation of metal temperatures at constant flue gas temperature. Figure I.19a shows the variation of the metal temperature as a function of flue gas temperature on-site. Figure I.19b shows that metal thickness loss rate increases with the flue gas temperature.

Figure I.20 shows the parabolic growth kinetics obtained from measurements taken during 2200 hours. Metal thickness loss increases with time whereas the thickness of the iron chloride layer and iron oxide layer become stable with time. The model is based on the combination of two kinetics laws by equation (12) where $\boldsymbol{k}$ is the rate constant, $\boldsymbol{k_0}$ is the rate pre-exponential factor and $\Delta \boldsymbol{G_1}$ and $\Delta \boldsymbol{G_2}$ are the activation energies. The validity domain is shown in Table I.6. The model is valid only for carbon steel and the effect of other factors as atmosphere characteristics is not considered.

$$\boldsymbol{k} = \boldsymbol{k_0} \exp\left(-\Delta G_1 \left(\frac{1}{RT_{Metal}} - \frac{1}{RT^0_{Metal}}\right)\right) \exp\left(-\Delta G_2 \left(\frac{1}{RT_{Metal}} - \frac{1}{RT^0_{Metal}}\right)\right) \qquad \textbf{Equation 12}$$

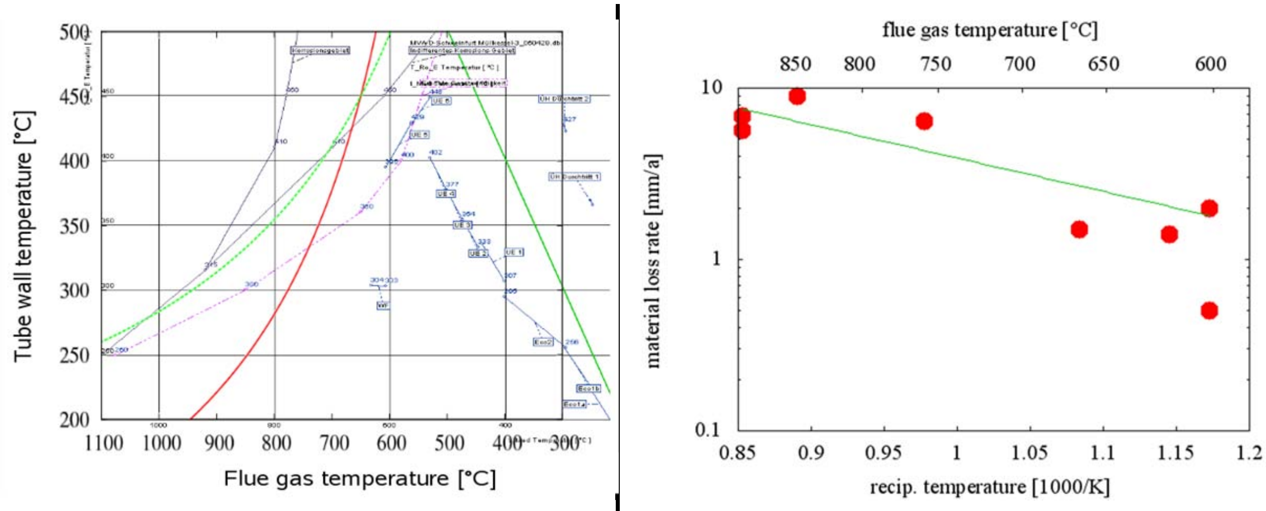

a)

b)

Figure I.19. a) Metal tube temperature as a function of flue gas temperature. b) Metal thickness loss rate as a function of flue gas temperature. [107]

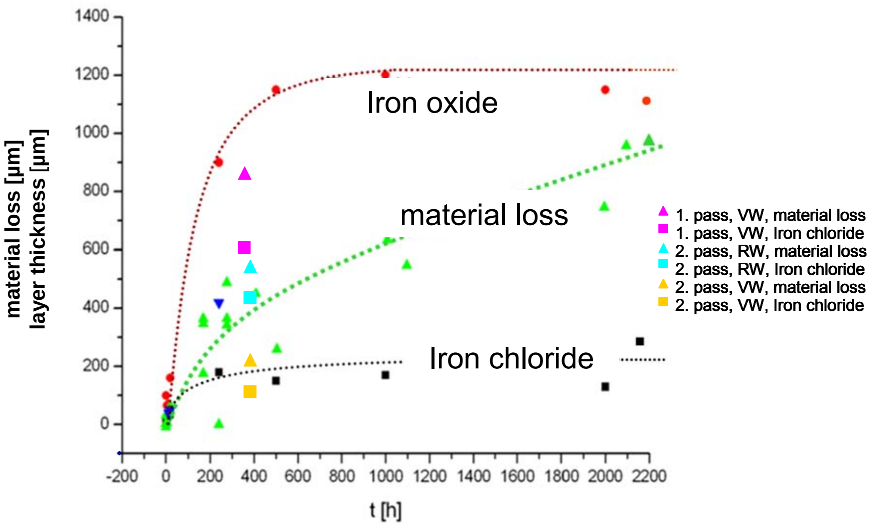

Figure I.20. Kinetics of iron oxide and iron chloride layers and metal thickness loss [107]

Lebel [51] proposed a parametric model by equations (13) and (14) based on thermal gradient experiments that takes into account a single metal temperature in a wide range of flue gas temperatures (°C), different compositions of HCl (ppm) and SO_2 (ppm) in the gas, and the Cl-content in the deposits. The domain of validity of the model is shown in Table I.6.

$$\log \boldsymbol{R_{Corr}} = -\mathbf{0,73} + \mathbf{0.0026} \times \boldsymbol{T_{Flue\ gas}} \times \mathbf{0.0156} \times [\boldsymbol{Cl}]_{\boldsymbol{Deposits}} \qquad \textbf{Equation 13}$$

$$\log \boldsymbol{R_{Corr}} = \mathbf{0.58} + \mathbf{0.0001}[\boldsymbol{HCl}]_{\boldsymbol{Gas}} \times \mathbf{0.001}[\boldsymbol{SO_2}]_{\boldsymbol{Gas}} + \mathbf{0.007}[\boldsymbol{Cl}]_{\boldsymbol{Deposits}} \qquad \textbf{Equation 14}$$

The model was built based on laboratory experiments and set parameters very similar to Veolia WtE boiler operational conditions. However the model considers neither the *vol%*O_2 nor *vol%*H_2O in the gas, nor the gas velocity. The effect of the variables is limited to carbon steel. Figure I.21 shows a diagram of the variation of corrosion rate at $T_{Flue\ gas} < 650°C$ and $T_{Metal} = 450°C$ as a function of $HCl_{(ppm)}$ and $SO_{2(ppm)}$ contents in the gas at constant wt.%Cl in deposits obtained from equation (13).

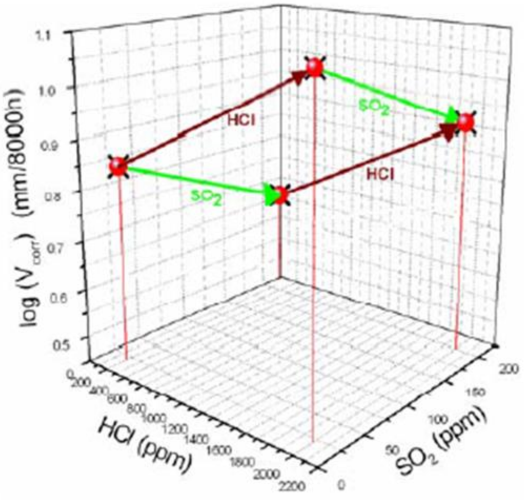

Figure I.21. Corrosion rates of carbon steel as a function of HCl and SO_2 contents in the gas phase at $T_{Flue\ gas} < 650°C$ and $T_{Metal} = 450°C$. [51]

Kawahara [103,108] proposed a model which assumes that high-temperature corrosion follows a linear rate law or a parabolic rate law as follows.

$$\boldsymbol{\Delta W = k_{p-l} \times t} \qquad \textbf{Equation 15}$$

$$\boldsymbol{(\Delta W)^2 = k_{p-p} \times t} \qquad \textbf{Equation 16}$$

Where ΔW is the corrosion loss (mm), k_{p-l} the linear corrosion rate constant, k_{p-p} the parabolic corrosion rate constant and t the time (h). k_{p-l} and k_{p-p} are assumed to be functions of five variables: gas temperature (T_{Gas}), metal temperature (T_{Metal}), $[HCl]_{gas}$ the HCl concentration in the flue gas given in ppm, $[Cl]_{ash}$ is Cl content of the ash deposits on the tube surface given in wt.% and the sum of Cr, Ni and Mo contents of alloys $[Cr + Ni + Mo]$ is given in wt.%, which were considered important variables for high-temperature corrosion according to field tests. To derive the least square value of these constants, nonlinear regression was performed. A total of 185 field test data were used for modelling. Samples from several alloys were exposed at three WtE boilers for 700, 3000, ad 6000 hours. Equations (17) and (18) were obtained and derived from regression analysis on the validity domain shown in Table I.6

$$\boldsymbol{k_{p-l} = 10^{-44.15} \times T_{Gas}^{10.2} \times T_{Metal}^{4.0} \times [HCl]^{0.6} \times [Cl]^{0.4} \times [Cr + Ni + Mo]^{-0.4}} \quad \textbf{Equation 17}$$

$$\boldsymbol{k_{p-p} = 10^{-86.9} \times T_{Gas}^{21.5} \times T_{Metal}^{7.5} \times [HCl]^{1.3} \times [Cl]^{0.6} \times [Cr + Ni + Mo]^{-0.8}} \quad \textbf{Equation 18}$$

According to the model both corrosion constants increase with T_{Gas}, T_{Metal}, $[HCl]_{Gas}$, $[Cl]_{Ash}$ and decrease with [Cr+Ni+Mo]. The coefficient of (T_{Gas}) is about 3 times (T_{Metal}) which means that the effect of flue gas temperature is larger than the effect of metal temperature on the corrosion rates. The corrosion lifetime estimations between both equations are largely different from each other. For field tests results, the corrosion rates were fit with the parabolic law. However for severe corrosive environments the linear law provided a better fit. Furthermore, the same methodology was applied for tests performed in a pilot plant. In this case the linear law in equation (19) was a better fit.

$$\boldsymbol{k_{p-l} = 10^{-33.8} \times T_{Gas}^{5.7} \times T_{Metal}^{4.9} \times [HCl]^{0.6} \times [Cl]^{0.4} \times [Cr + Ni + Mo]^{-0.4}} \quad \textbf{Equation 19}$$

The effect of the variables is also similar for the field test except for T_{Gas} and T_{Metal}. It can be noticed in Table I.6 that T_{Gas} and T_{Metal} are quite close and T_{Gas} remains below condensation temperature of alkali chlorine. From this model it can be concluded that a linear law fits better in most cases. However, even when this model is the most complete, it does not consider O_2, H_2O (vol.%) and SO_2 (ppm) in the gas, the gas velocity, the presence of molten phases and the Fe-content in alloys. Moreover the influence of alloying elements is not independently evaluated. Also, the variables $[HCl]_{Gas}$ and $[Cl]_{Ash}$ were evaluated without considering presence of molten phases and no sulfur in the deposits. In addition, it is admitted, in some conditions that $[Cl]_{Ash}$ is more damaging than $[HCl]_{Gas}$ in presence of molten phases and these models show the contrary effect. This might be due to low test temperatures considered in this model. Under these conditions, molten salts corrosion probably does not control the corrosion kinetics in comparison to the gas phase attack.

Finally, Ots [109] suggested a model to determinate the intensity of wear on boiler tubes. The wear is considered a high-temperature corrosion process of boiler tubes in which the periodic destruction of protective oxide film on the tube surface during the cleaning is the accelerating factor. The depth of wear of boiler tubes also depends upon the type of metal, chemical composition of the ash deposit covering the metal surface, metal temperature and the period between the cleaning cycles. Equation (20) is the basic formula for calculating the depth of wear of the boiler heat transfer surfaces under conditions of periodic cleaning from ash deposit. The validity domain is shown in Table I.6.

Figure I.22 shows the wear of boiler tube heat transfer surface under the influence of a cleaning force. The vertical axis indicates the depth of wear of a tube ($\Delta \boldsymbol{s}$), and the horizontal axis is the cleaning force **(P)** that may remove the ash deposit from the surface. Figure I.22 expresses the depth of wear at a given time and at constant metal temperature. If the period between the cleaning cycles is τ_0 , then time $\boldsymbol{\tau} = \sum_{i=0}^{m} \boldsymbol{\tau_{0i}}$, where $\boldsymbol{m}$ is the number of cleaning cycles with period $\boldsymbol{\tau_0}$.

In equation (21), $\boldsymbol{\xi}$ expresses the degree of destruction of the oxide film which is equal to the ratio of the depth of wear caused by the action of the cleaning force ($\Delta \boldsymbol{s} - \Delta \boldsymbol{s}'$) to the maximum possible depth of wear ($\Delta \boldsymbol{s}'' - \Delta \boldsymbol{s}'$). If the cleaning force is small, the oxide film on the tube is not destroyed, $\boldsymbol{\xi} = \mathbf{0}$, but when the oxide film is totally destroyed, $\boldsymbol{\xi} = \mathbf{1}$. The accelerating effect of the cleaning force on the wear intensity of the metal is expressed by the relation $\boldsymbol{\xi}(\boldsymbol{B}\,\boldsymbol{m}^{\mathbf{1}-\boldsymbol{n}} - \mathbf{1})$. Then $\boldsymbol{n}$ depends on the composition of fuel ash and on type of steel. With the increase of $\boldsymbol{n}$**,** the depth of wear approaches the value of $\Delta \boldsymbol{s}'$. Hence, the higher the exponent $\boldsymbol{n}$ is, less sensitive the metal is to the periodic destruction of the oxide film.

In equation 20, $\Delta \boldsymbol{s}$ is the depth of wear, $\boldsymbol{\xi}$ is given by equation (21), the term ($\boldsymbol{B}\,\boldsymbol{m}^{\mathbf{1}-\boldsymbol{n}} - \mathbf{1}$) is given by equation 21, $\Delta \boldsymbol{s}'$ is given by equation (23) and $\Delta \boldsymbol{s}''$ is given by equation 24. In equations (23) and (24), $\boldsymbol{A}$ is the temperature dependent coefficient given by equation (25) (Arrhenius law), ρ_m density of metal, n exponent of oxidation, $m = \frac{\tau}{\tau_0}$ number of cleaning cycles during the time τ. The value of B depends on composition of the deposit, period between the cleaning cycles, temperature and type of metal. In equation (25), k_0 is the pre-exponential factor, E activation energy, R universal gas constant, and T absolute temperature of metal.

$$\Delta \boldsymbol{s} = [\mathbf{1} - \xi(\boldsymbol{B}\,\boldsymbol{m}^{\mathbf{1}-\boldsymbol{n}} - \mathbf{1})]\,\boldsymbol{\Delta s}' \qquad \textbf{Equation 20}$$

$$\xi = \frac{(\Delta s - \Delta s')}{(\Delta s'' - \Delta s')} \qquad \textbf{Equation 21}$$

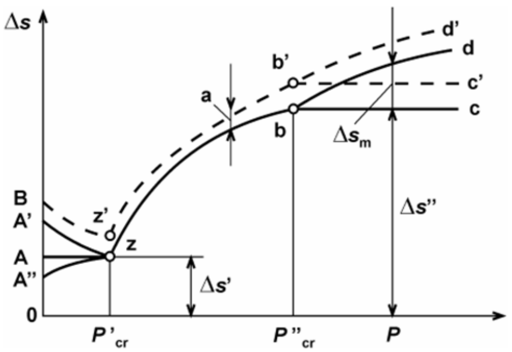

a)

$$\boldsymbol{v} = \frac{\Delta s''}{\Delta s'} - \mathbf{1} = \boldsymbol{B}\boldsymbol{m}^{\mathbf{1}-\boldsymbol{n}} - \mathbf{1} \qquad \textbf{Equation 22}$$

$$\Delta \boldsymbol{s}' = \boldsymbol{A}\boldsymbol{\rho}_{\boldsymbol{m}}^{-\mathbf{1}}(\boldsymbol{m}\boldsymbol{\tau}_{\mathbf{0}})^{\boldsymbol{n}} \qquad \textbf{Equation 23}$$

$$\Delta \boldsymbol{s}'' = \boldsymbol{B}\boldsymbol{A}\boldsymbol{\rho}_{\boldsymbol{m}}^{-\mathbf{1}}\boldsymbol{m}\boldsymbol{\tau}^{\boldsymbol{n}} \qquad \textbf{Equation 24}$$

$$\boldsymbol{A} = \boldsymbol{k}_{\mathbf{0}} \exp\left(-\frac{\boldsymbol{E}}{\boldsymbol{RT}}\right) \qquad \textbf{Equation 25}$$

b)

Figure I.22. Ots model development [109] a) Depth of wear depending on cleaning force b) Equations of the model.

This model allows evaluating the corrosion-erosion mechanism present in the walls of the tubes after deposits cleaning. The model takes into account the metal temperature and composition of the alloys, ash composition, the type of cleaning, and the time between cleaning cycles. The domain of validity depends on the operational conditions of the plant and seems to be a good approach of scaling kinetics of the oxide layer. However this model needs data that might be difficult to obtain to evaluate certain parameters like coefficient $\boldsymbol{n}$. Moreover the model must be validated using a larger population of field data to assess its accuracy.

Baker [110] uses the same approach of that for metal dusting (Section I.2.6) [29,30] for high-temperature corrosion in a simulated waste incineration environment. The author shows two equations (26) and (27) obtained by multiple linear regression. Corrosion rates are explained as a function of the sum of the element concentrations (wt.%) in the alloys.

$$\boldsymbol{R_{Corr}}(\frac{\boldsymbol{mm}}{\boldsymbol{y}}) = \boldsymbol{Ni} + \boldsymbol{2}\ (\boldsymbol{Cr} + \boldsymbol{Mo} + \boldsymbol{W})(\boldsymbol{wt}\%) \qquad \textbf{Equation 26}$$

$$\boldsymbol{R_{Corr}}(\frac{\boldsymbol{mm}}{\boldsymbol{y}}) = \boldsymbol{Cr} + \boldsymbol{2}\ (\boldsymbol{Mo}) + \boldsymbol{W}\ (\boldsymbol{wt}\%) \qquad \textbf{Equation 27}$$

In the models the corrosion rates decrease with the increase of Cr and Ni. However these equations are valid only for assessing the behavior of materials under a specific atmosphere, as shown in Table II.6. Furthermore, the accuracy (R^2) of the linear regressions is not shown (Figure I.23a, I.23b) and there is very few data per number of variables.

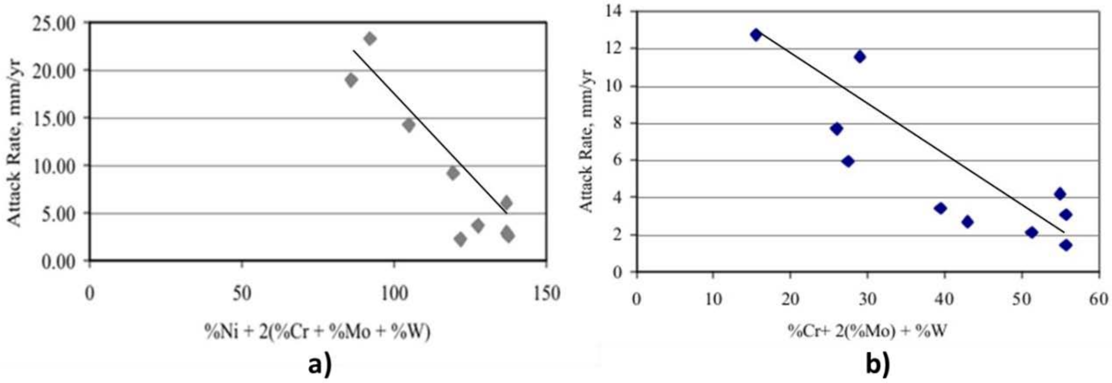

Figure I.23. Corrosion rate as a function of the alloy composition, alloys exposed for 336h in N_2-10% O_2-10% CO_2-20% H_2O-1500ppm HCl-300ppm SO_2. a) 650°C b) 550°C [110]

Table I.6. Summary of kinetics models for high-temperature corrosion

Author	Material	Magnitude	Equation	Validity domain
Waldman [107]	Carbon Steel	Thickness of: • Material loss • Iron chloride • Iron oxide	11	T_{Metal} (°C)= 600 - 900 $T_{Flue\text{-}Gas}$ (°C) = 300 - 1100 Operational conditions
Lebel [51]	Carbon Steel	• Thickness loss	12 and 13	T_{Metal} (°C)= 400 $T_{Flue\text{-}Gas}$ (°C)= 450 - 850 HCl(g) (ppm) = 200 - 2000 SO_2(g) (ppm) = 20 - 200 $Cl_{deposits}$ (wt%) = 0 - 40
Kawahara [103,108]	Several Alloys	• Thickness loss	16, 17, 18	Field Tests T_{Metal} (°C)= 450 - 550 $T_{Flue\text{-}Gas}$ (°C)= 583 - 675 HCl(g) (ppm) = 568 - 1420 $Cl_{deposits}$ (wt%) = 0.3 – 10.5 Pilot Plant Tests T_{Metal} (°C)= 429 - 500 $T_{Flue\text{-}Gas}$ (°C)= 488 - 621 HCl(g) (ppm) = 690 $Cl_{deposits}$ (wt%) = 1.2 – 11.1
Ots [109]	• 12Cr1MoV • Cr18Ni12Ti	• Depth wear	19	T_{Metal} (°C)= 415 – 525 Brown coal ash Na_2O = 0.4, K_2O = 0.6 Cl = 0 (wt%) Oil shale ash Na_2O = 0.2, K_2O = 6.0 Cl = 0.5 (wt%)
Baker [110]	803, 890, 825, FM272, C276, 622, C22, 686, C2000, 625, 690, 600	• Thickness loss	25 and 26	T_{Metal} (°C)= 550, 650 HCl(g) (ppm) = 1500 SO_2(g) (ppm) = 300 $10O_2$ - $10CO_2$ - $20H_2O$ (vol%)

I.4 Life assessment modeling

An important method of preventing corrosion failures on power plants is the prediction of the corrosion rate and corrosion allowance of materials used in the plant constructions. [111] Furthermore, once in service, any operational change implicates variations in the material performance that should be also predicted in order to assure the reliability of the industrial facilities.

The lifetime prediction of components can be made either by extrapolation of well-known kinetics laws or by the application of statistical distributions. However, many corrosion profiles do not fit any of the commonly used statistical models, particularly when a combination of corrosion processes operates at the same time, giving multimodal distributions. Under such circumstances the probabilities must be calculated graphically or some other stochastic approaches should be taken.

In the industrial field, the reliability is the study of the operational system, which can be represented by an equipment, device or component capable of being in or out of service at a given time. There are different contributions from the mathematics field to reliability. Two approaches are possible: static and dynamic. The first focuses on the system properties at a given time t, for example, the study of the structural functions, Bayesian networks and failures trees. The second visualizes the system properties in a timeline.[112]

The data obtained from laboratory or field experiments may follow a kinetics law that allows the extrapolation in time (dynamic), but when the data does not fit to any of the statistical models, the evolution of these systems over time is random and is modeled as a stochastic process. This type of study has two parts: a statistical part to determine a stochastic model that fits better to the data and a probabilistic part that comes from a stochastic model, which aims to analyze the random behavior of the system and make the estimations. [113]

Several statistical approaches have been applied for modeling non-conventional corrosion kinetics. Nicholls et al. [114,115] proposed a statistical approach for modeling corrosion profiles when the corrosion surface is non-uniform. The authors suggested an extreme value model to successfully predict corrosion rates when the corrosion process exhibits a rough or pitted surface texture. John et al.[116] developed an information system used to manage corrosion of metals and alloys by high-temperature gases found in many different oil refining, petrochemical, power generation, and chemical processes. The database currently represents about 7.9 million hours of exposure time for about 5,500 tests with 89 commercial alloys for a temperature range of 200 –1,200 °C. The software manages corrosion data from well-defined exposures and determines corrosion product stabilities. Use of these data allows prediction of stable corrosion products and hence identification of the possible dominant corrosion mechanisms and lifetime predictions are made according to the mechanism: oxidation, sulfidation, sulfidation/oxidation, and carburization. Examples of accuracy obtained using the system is shown in Figure I.24a. However the lifetime prediction procedure is not shown. Figure I.24b illustrates an example of a corrosion map also given by the software that shows the depth of penetration of carburization for different materials as a function of the temperature.

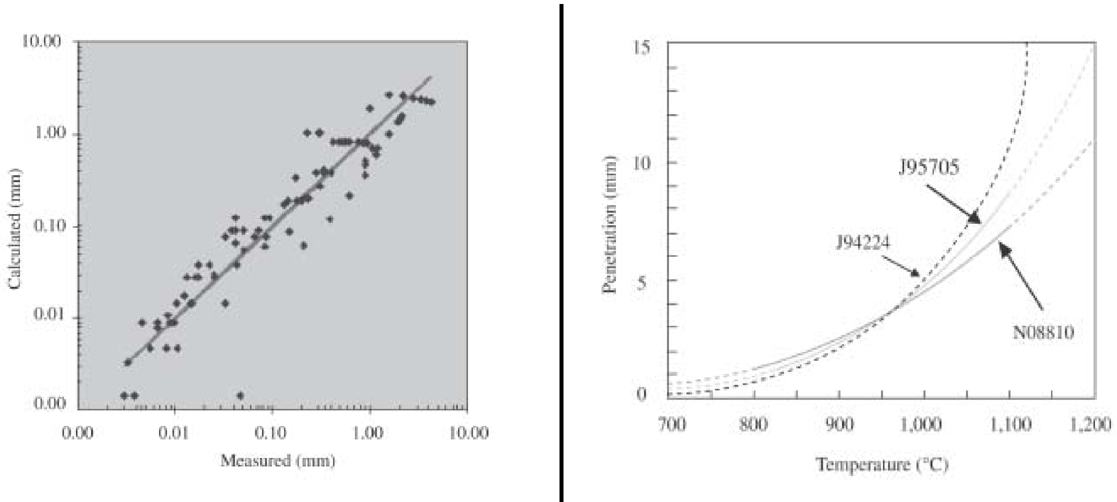

a)

b)

Figure I.24. a) Example of prediction accuracy of the software b) Example corrosion map by the system calculations “Carburization of several alloys exposed to solid carbon and 2 × 10 -4 atm H_2S”[116]

Makkonen [117] provided a system based on image analysis (Optical microscopy and SEM (Scanning Electron Microscopy)) of samples cut from superheaters during shutdowns. The results of the image analyses, allows determining the degree and type of corrosion. The corrosion rate of a superheater material can be more reliable when is detected directly from a commercial boiler. However this is a challenging tasks, because in order to have reliable measurements, the samples must be located in a special, temperature-controlled probe and exposed to the corrosive environment for a desired time. Also the analysis of samples taken from superheaters after exposure to corrosive must be reliably analyzed, if the corrosion chemistry can be appropriately determined, then an estimate of the material lifetime can be given.

In modeling procedures, a limitation lies when relations between inputs and corrosion rates are poorly known, in this case conventional models depending on corrosion theories will fail. Makkonen [118] proposed a predictive model based on a neural network which is capable of learning from errors and improving its performance as the amount of data increases. Neural networks are an effective prediction method when the relations that affect the result are uncertain. The use of neural networks is based on teaching the network with existing data, after sufficient prediction accuracy has been achieved; the network is used by feeding new input data to achieve a solution to the problem. The decision chain behind the answer does not have to be known, and a result can be derived with little data. However, in order to create a reliable device for prediction, a large amount of data is required for the learning process.

On the other side, in the materials selection field, other studies have developed important methodologies. Shanian and Savadogo [119] proposed a material selection model based on the concept of multiple attribute decision making, a new approach for the use of the ELECTRE (Elimination and Choice Expressing the Reality) model. By producing a material selection decision matrix and criteria sensitivity analysis, ELECTRE has been applied to obtain a more precise material selection for a particular application, including logical ranking of considered materials. A list of all possible choices from the best to the worst suitable materials can be obtained taking into account all the material selection criteria, including the cost of production. There is a good agreement between the results of the method and available data in Cambridge Engineering Selector (CES) databases. Rao [120] also proposed a decision making methodology for material selection. It is a logical procedure based on an improved compromise ranking method known as VIKOR which consider the material selection attributes and their relative importance for the application considered.

All these studies proposed different mechanisms to predict materials behavior for materials selection criteria or decision making tools. All of them have in common the use of large databases and the necessity to establish hierarchization methods to deal with large amounts of data and determine the most important variables in the processes. For ranking compositional data sets other approaches has been used. Jimenez-Come [121] developed an automatic system to study pitting corrosion behavior in stainless steel, based on support vector machines (SVMs) and k-nearest neighbor. The influence of the principal environmental factors involved in pitting corrosion was analyzed. Different feature selection techniques are applied such as Principal Component Analysis (PCA), Linear Discriminant Analysis (LDA) and Fisher criterion (FDR) to select the principal variables at the pre-processing stage. The model becomes an effective strategy for modelling pitting corrosion and it may be considered as useful tool in the design of structures.

Gandia [122] studied the corrosion of carbon steel in water through voltammetric techniques. The study has been performed in aqueous solutions varying several parameters. Principal component analysis (PCA) was performed with the cyclic voltammetric data. Values of corrosion potential and corrosion current obtained with traditional methods are compared to the conclusions arisen by the PCA. These results show the ability of PCA for the evaluation and diagnosis of corrosion processes.

Saikaew [123] presented a corrosion severity ranking methodology and a predictive model for corrosion growth based on environmental and corrosion growth data for six operational air force bases in the United States. The method of Principal Component Analysis (PCA) is used to analyze compositional data sets of atmospheric conditions for defining corrosion severity ranking by locations (air force bases). This technique is basically used to reduce the number of variables involved in a process without losing much information.

Benstock and Cegla [124] recently proposed a modeling approach by using Extreme value analysis (EVA) as a tool for partial coverage inspection (PCI), it allows an inspector to build a statistical model of the smallest thicknesses across a component. The extreme value models are based on the selection of the smallest thicknesses from the inspection data. The method selects a sample of thickness minima for a large number of correlated exponential and Gaussian surfaces and the method is tested using real inspection data collected from an ultrasonic thickness C-scan of a rough surface.

In the lifetime prediction modeling for high-temperature corrosion and metal dusting, in which there are numerous parameters to be considered, the statistical approaches explained above might be useful for ranking the most important variables involved in both processes for further statistical fitting.

I.5 Summary

In this chapter, we have discussed in some details the metal dusting and high-temperature corrosion processes and the corrosion mechanisms for different alloy systems submitted to different exposure conditions. The various factors affecting both processes have also been detailed. We have then proceeded to analyze the different approaches used for modeling both processes kinetics in several studies. It can be concluded that both mechanisms of high-temperature corrosion are controlled by numerous variables from which only the most important should be considered for modeling the corrosion kinetics. Likewise for creating reliable predictive models for both mechanisms, a large amount of experimental data is required to establish clear correlations between variables, and therefore further statistical analysis is also required to prioritize the variables according to their relative importance on the corrosion rates. In the following chapter, we will give details on the experimental approach used for evaluating mechanisms, the database construction procedure and the statistical tools used to analyze the collected data.

Chapter 2. Experimental set-up, statistical methods

Contents

II Chapter 2. Experimental set-up, statistical methods

This chapter describes the experimental set-up utilized in the SCAPAC project to evaluate metal dusting corrosion and high-temperature corrosion under deposits.[125,126] This is followed by the procedure of construction of two databases which were conceived for each corrosion mechanism to enter the experimental results found in literature, in order to have sufficient amount of data for modeling. Finally, a description of the statistical techniques is given to analyze all the information contained in the databases and create the statistical models.

II.1 Metal dusting

II.1.1 Experimental set-up

Different material compositions were evaluated during A. Fabas's thesis [125] within the ANR SCAPAC project. The corresponding results were used as input for this present PhD work. Two different test conditions were investigated: atmospheric pressure tests and high pressure tests. The alloy chemical composition and test conditions applied to each group of alloy are presented in Table II.1 and Table II.2. The alloys were chosen in view of the industrial interest to know the kinetics of metal dusting degradation in alloys susceptible to be installed in service. [127]

Table II.1. Alloy compositions tested at low pressure conditions

Test Conditions									
CO	H_2	CO_2	CH_4	H_2O	Temperature °C	Pressure (bar)	Gas Rate (mm/s)	a_C	pO_2 (bar)
(vol%)									
47.25	47.25	-	-	5.5	570	1	0.02	33	2.1×10^{-27}

Alloy Composition													
(wt%)	Fe	Ni	Cr	Mo	Co	Cu	Al	Si	W	Nb	Ti	Mn	C
Khantal	71.5	0.2	21.8				5.9	0.3				0.1	
800HT	45.0	32.0	21.0				0.4	0.1			0.4	0.9	0.1
CROFER	75.3	0.04	23.3				0.1			0.2		0.7	
AC66	38.8	31.4	27.9					0.3		0.8		0.6	
HR 120	33.0	37.0	25.0	1.0	3.0	0.5	0.1	0.6	0.5			0.7	0.1
H230	3.0	57.0	22.0	2.0	5.0		0.3	0.4	14.0	0.5	0.1		0.1
IN 601	14.0	58.9	23.4			0.7	1.4	0.3	0.8	0.2		0.3	
IN 600	7.9	73.7	16.2				0.1	0.3			0.2	0.3	
IN 602	14.0	58.9	23.4			0.7	1.4	0.3	0.8	0.2		0.3	
IN 690	9.9	58.5	29.8		0.2		0.3			0.3	0.3	0.4	

Atmospheric pressure tests were carried out at atmospheric pressure and low gas rate in a CO-H_2-H_2O composition indicated below on a bench in the ICA Laboratory (Ecole des Mines Albi, France). A gas mixture 50CO-50H_2 (vol%) at 60°C was enriched with water steam by bubbling, before being introduced into the horizontal furnace as shown in Figure II.1. The bubbler temperature was set at 35 ° C, which allows to humidify the gas mixture to 5.5 $H_2O_{(g)}$ (vol%), until the water steam pressure saturation.[127]

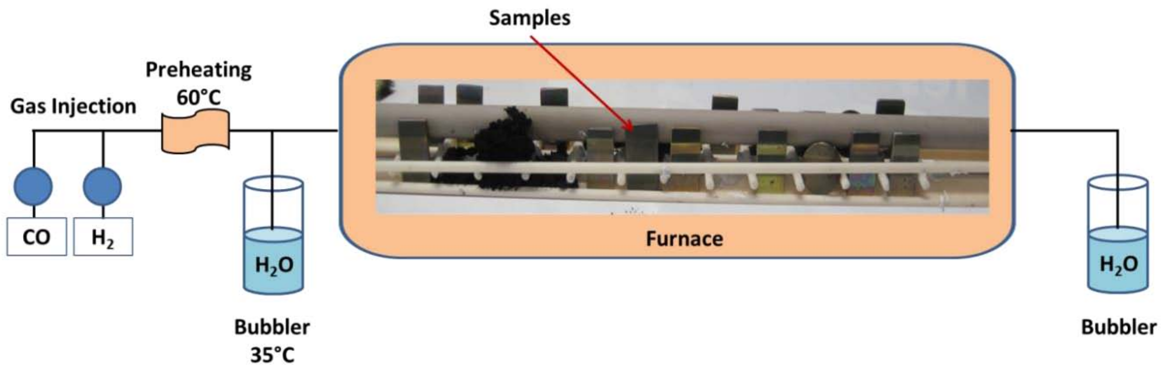

Figure II.1. Test set up at atmospheric pressure

High pressure tests were performed in a vertical furnace at Air Liquid Research Center (CRCD – France) under the supervision of Sebastien Doublet, as shown in Figure II.2. The gas mixture was obtained by first creating a mixture of H_2, CO, CO_2 and CH_4 using pure pressurized gases and mass flow controllers on each line for the injection of the dry gas composition. The water was introduced in the preheated gas via a calibrated High Pressure Liquid Chromatography (HPLC) pump. The gas composition was homogenized through a ceramic foam placed at the furnace inlet. The total pressure of the system was controlled downstream by a backpressure regulator placed in the outlet dry gas line. The amount of water was controlled by weighting the condensed water at the furnace outlet. The carbon activity a_C was calculated from the synthesis reaction (reaction 1) by equation (1) and the partial pressure of oxygen pO_2 was calculated from the steam water decomposition (reaction 4) by equation (4).

Table II.2. Alloy compositions tested at high pressure conditions

Test Conditions									
CO	H_2	CO_2	CH_4	H_2O	Temperature °C	Pressure (bar)	Gas Rate (mm/s)	a_C	pO_2 (bar)
(vol%)									
12.8	49.1	3.1	1.6	33.4	570	21	2.8	32	7.1×10^{-26}

Alloy Composition													
(wt%)	Fe	Ni	Cr	Mo	Co	Cu	Al	Si	W	Nb	Ti	Mn	C
800HT	45.0	32.0	21.0				0.4	0.1			0.4	0.9	0.1
HR 120	33.0	37.0	25.0	1.0	3.0	0.5	0.1	0.6	0.5			0.7	0.1
IN 625	4.6	59.4	22.5	8.9			0.3	0.2		3.7	0.3		
IN 617	3.0	49.2	22.0	9.0	12.5	0.5	1.2	1.0			0.6	1.0	0.1

The samples were cut in a commercial rod to obtain disc specimens with a diameter and a thickness of approximately 14 mm and 1.6 mm respectively. A hole was drilled at the center of each sample. These samples were held by alumina to the arrangement for exposure. The samples were chamfered to limit the effect of the samples and were mechanically ground to a P600 grit finish. Finally they were ultrasonically cleaned in acetone and in ethanol, and finally dried before the experiment. [127]

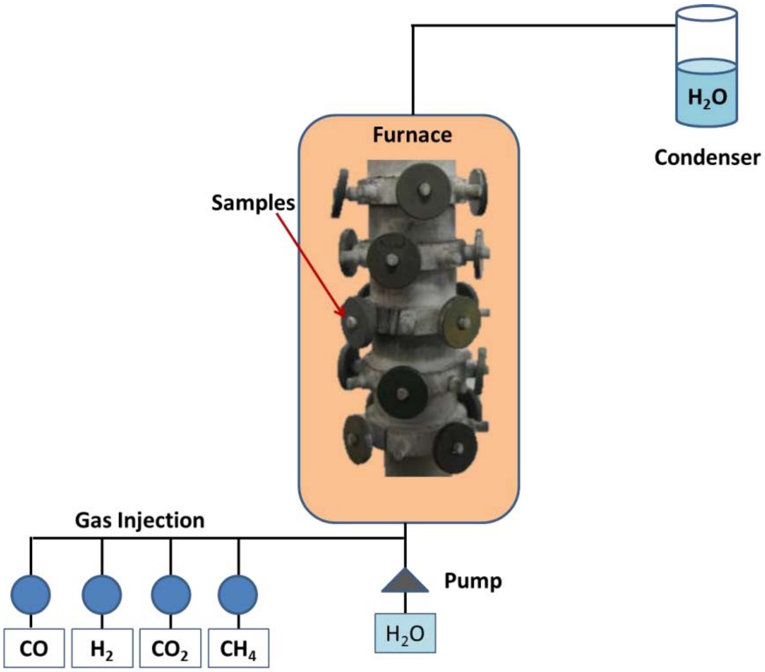

Figure II.2. Tests set up at high pressures

During exposure, the samples were removed every 500h. They were cleaned ultrasonically in ethanol, dried and weighted on a Sartorius CPA225DOCE balance with a precision of 0.01 mg in order to measure the mass loss after each period of exposure. The incubation times were determined by extrapolating backwards to zero size of the pit diameter growth. [127]

II.1.2 Database construction: Metal Dusting

In order to achieve the main objective of this study, the amount of tests, materials and conditions described above was insufficient. To compensate this lack of data, a large database was built from corrosion tests found in literature. In this database, all the information concerning to corrosion results obtained by several authors in laboratory tests at different conditions was entered. Table II.3 shows the different published research that were examined and added to the metal dusting database.

After reviewing the articles, all the information available concerning the corrosion tests were organized in different groups of variables. The input variables were defined as a set of values that will provide an output variable. In the present study the input variables are the conditions established by the experimenter in order to obtain a corrosion rate as the output variable.

An arbitrary input is called an independent variable, while an arbitrary output is called a dependent variable. [128] Therefore, in this case, the independent variables are the experimental conditions that will explain the corrosion rates as a dependent variables.

Table II.3. Published research added to metal dusting database

Ref. n°	Title of the published research
AF_ME01	A. Fabas , PhD Thesis, Toulouse 2015 - Metal Dusting tests ANR SCAPAC Project. [125]
SC_MP01	Nickel-base material solutions to metal dusting problems. [29]
SC_MP02	Utilization of alloy 693 in metal dusting environments. [30]
SC_MP03	Development of materials resistant to metal dusting degradation. [129]
SC_MP04	Relationship between coking and metal dusting. [10]
SC_MP05	Effects of grain size, cold working, and surface finish on the metal dusting resistance of steels. [18]
SC_MP06	Metal dusting behavior of several nickel- and cobalt-base alloys in CO–H_2–H_2O atmosphere. [130]
SC_MP07	Effect of copper on metal dusting of austenitic stainless steels. [22]
SC_MP08	Metal dusting corrosion of austenitic 304 stainless steel. [131]
SC_MP09	Kinetics and mechanisms of nickel metal dusting I. Kinetics and morphology. [8]
SC_MP10	Metal dusting behavior of Cr-Ni steels and Ni-base alloys in a simulated syngas mixture. [132]
SC_MP11	Metal dusting of nickel-base alloys. [13]
SC_MP12	Protective behavior of newly developed coatings against metal dusting. [133]
SC_MP13	Metal dusting resistant alumina forming coatings for syngas production. [134]
SC_MP14	Influence of hafnium additions and preoxidation treatment on the metal dusting of ni–al alloys. [135]
SC_MP15	Contributions of carbon permeation and graphite nucleation to the austenite dusting reaction: A study of model Fe–Ni–Cu alloys. [136]
SC_MP16	Metal dusting of alumina-forming creep-resistant austenitic stainless steels. [137]
SC_MP17	Metal Dusting of type 316 stainless steel in high pressure environments between 450 °C and 650°C. [27]

II.1.2.1 Input variables

In metal dusting, independent variables are clustered into two groups: the conditions of the test atmosphere which include the gas composition, pressure and temperature set for the experiments (Table II.4) and the materials composition which includes the elementary chemical composition of the materials used for the experiments as shown in Table II.5.

Table II.4. Atmosphere conditions included in the database

Ref. N°	T_{Metal} (°C)	1/T (K^{-1})	P_{Int} (bar)	V_{gas} ($m.s^{-1}$)	CH_4	H_2O	CO_2	CO	H_2	a_C	pO_2 (bar)
					(vol%)						
					pCH_4	pH_2O	pCO_2	pCO	pH_2		
					(bar)						
1											

Table II.5. Chemical composition of the materials included in the database

Ref. N°	Material	Chemical Composition (wt%)													Surface polish Grit N°
		Fe	Ni	Cr	Mo	Co	Cu	Al	Si	W	Nb	Ti	Mn	C	
1	Alloy 1														

II.1.2.2 Output variables

The output variables are all measurable magnitudes resulting from the corrosion tests. These variables will be exploited to calculate the corrosion rates which will be used as dependent variables. Table II.6 gathers the variables concerning the different periods of time measured during the test, these variables are described as follows:

Isothermal Y/N: indicates whether the test was conducted under isothermal conditions or thermal cycling condition.

Cycle N°: the number of periods in which the test remains under constant high-temperature regime.

Cycle Time (h): the duration at high-temperature regime in one cycle.

Total Time (h): the duration at high-temperature regime in a full test.

Incubation Time (h): the initial period in which the sample remains unchanged without damage.

Frequency (F) (1/h): the number of cycles per unit time. The cycle time is the duration of time of one cycle, so the frequency is the reciprocal of the cycle time: $\left(F = \frac{1}{cycle\ time\ (h)}\right)$

Table II.6. Kinetics information of the tests included in the database

Ref. N°	Isothermal Y/N	Cycle N°	Cycle Time (h)	Total Time (h)	Incubation Time (h)	Frequency (1/h)
1						

The authors differ in the parameters measured during metal dusting tests to represent the material degradation. Some of them measure the mass gain and/or mass loss of the specimen during the test and others measure the depth, the diameter and/or the area occupied by pits grown during the test, as shown in Table II.7.

Table II.7. Measured variables from each test entered in the database

Ref. N°	Mass Loss	Mass Gain	Pit Depth	Pit Diameter	Pit Density
	mg/cm^2		µm		N°/cm^2

Either way, mass or pits, both are preceded by an incubation period in which the specimen remains apparently unchanged. In the case of the mass loss, three kind of mass loss rates can be calculated as a function of the time period considered. Metal dusting kinetics shown in Figure II.3 illustrates the different corrosion rates calculated, based on the selected time period, resulting in the corrosion rates shown in

Table II.8. We define the Mass Loss rate (MLr) as the material loss during the full test, equation (28). The Instantaneous Mass Loss rate (IMLr) is the material loss during one cycle of the test, equation (29) and the Mass Loss Rate after incubation (AIMLr) characterizes the material loss during the period following the incubation time elapsed before the initial damage, equation (30).

$$MLr\ \left({}^{mg}/_{cm^2h}\right) = \frac{m_x}{t_x} \qquad \textbf{Equation 28}$$

$$IMLr\ \left({}^{mg}/_{cm^2h}\right) = \frac{m_x - m_{x-1}}{t_x - t_{x-1}} \qquad \textbf{Equation 29}$$

$$AIMLr\ \left({}^{mg}/_{cm^2h}\right) = \frac{m_x}{t_x - t_{Inc}} \qquad \textbf{Equation 30}$$

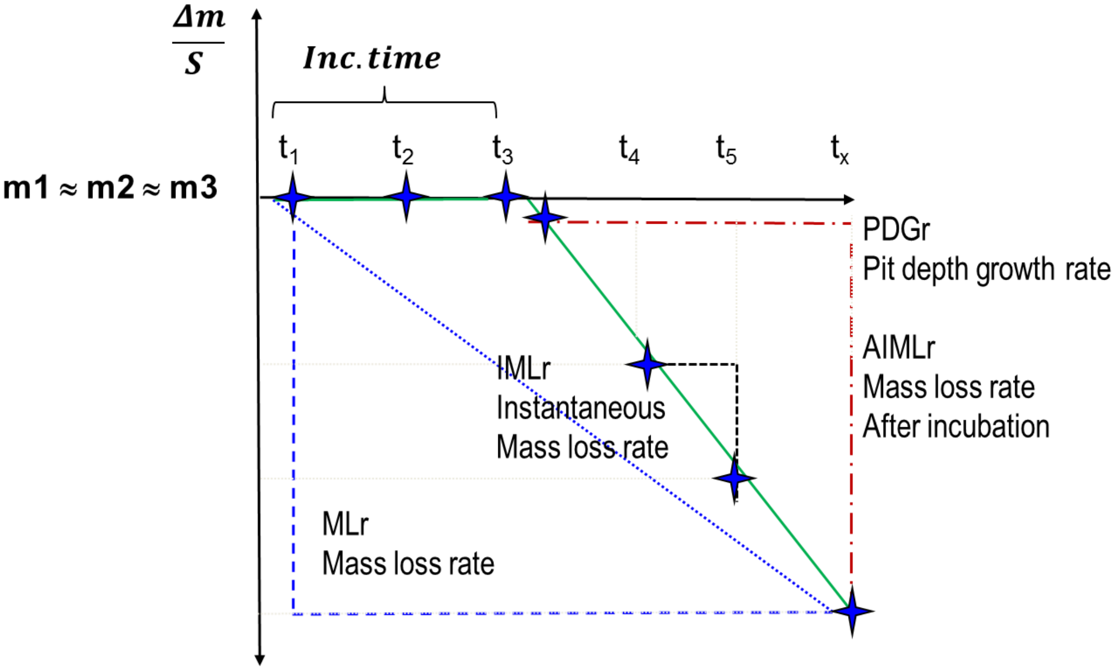

Figure II.3. Mass loss rates calculated from a metal dusting test.

Pits' growing begins after the incubation period. Thus the depth growth rate, diameter growth rate and density growth rate of pits will be equivalent to the regime of mass loss rate calculated after the incubation period.

Table II.8. Measured variables converted into corrosion rates

Ref. N°	Mass Loss Rate	Instantaneous Mass Loss Rate	AfterIncubation Mass Loss Rate	Mass Gain Rate	Pit Depth Rate	Pit Diameter Rate	Pit Density Rate
	mg/cm²·h				µm/h		N°/cm²·h
1							

After entering the data of the corrosion tests from SCAPAC project and literature, corrosion rates were calculated for every parameter, every test and every cycle of the test. Due to corrosion rates were represented by different output parameters, subsequent quantification of output parameters was performed.

After quantification, the most adequate dependent variables were selected for modeling procedures, based on the amount of data and the utility of the variable for lifetime prediction purposes.

The diagram in Figure II.4 shows the quantification of parameters. It can be concluded that Mass Loss rate (MLr) is the most suitable variable for predictive modeling, followed by Pits Depth Growth rate (PDGr). Indeed, MLr is the most frequent indicator in the data population which allows obtaining robust models in a wide range of conditions, as well as enable domain filtering if necessary without affecting the amount of data needed to construct the model. MLr can be converted into thickness loss but with high inaccuracy. It should be noticed that when the incubation time is not negligible regards the total duration of the experiment, MLr will increase with time even if AIMLr is constant, which constitute a significant source of error. PDGr can be more representative of the material thickness loss, which is the most useful parameter in equipment design procedures. Mass Loss rate after the incubation period (AIMLr) and incubation time (IT) were also analyzed in order to identify the difference between both regimens and because they present better correlation with the corrosion variables.

After selecting the dependent variable to be treated, several statistical methods were applied to analyze the data distribution and to select the independent variables that explain better the corrosion rates. This procedure is described in section II.3.

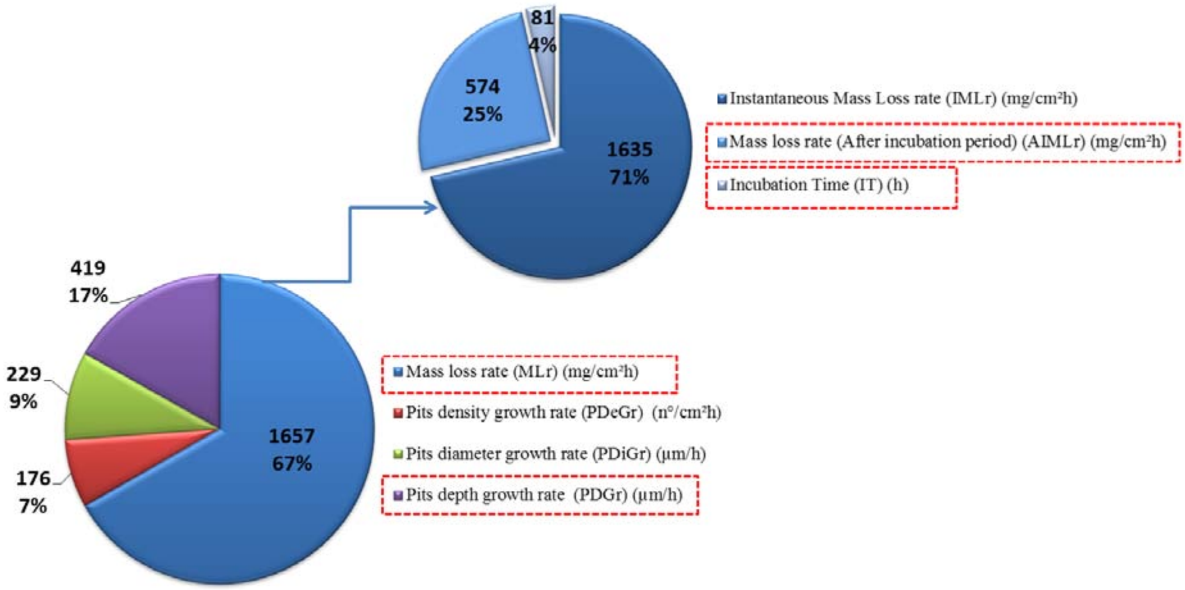

Figure II.4. Quantification of dependent variables that express corrosion rates

II.2 High-temperature corrosion

II.2.1 Experimental set-up

For this study different material compositions were evaluated during E. Schaal PhD thesis within ANR SCAPAC project. [126] These results were used as input for this present PhD work. Several test conditions were investigated: isothermal tests in pure air (crucible tests) and isothermal tests in complex atmospheres (pilot plant tests). Commercial alloys were chosen in view of the industrial interest to know the kinetics of high-temperature corrosion under deposit on alloys susceptible to be installed in service. Also model alloys were synthesized in the laboratory in order to evaluate the effect of the main alloying elements on the corrosion behavior. The model alloys were synthesized by fusion of the pure elements, using a high frequency induction furnace. The alloy chemical composition and the ash chemical composition used in the experimental protocol are presented in Table II.9 and Table II.10, respectively. Test matrix is presented in Table II.11.

Table II.9. Alloy chemical compositions tested in corrosion tests

Material	Fe	Ni	Cr	Mo	Co	Cu	Al	Si	W
	(wt%)								
Commercial Alloys									
16Mo3	97.3	0.3	0.3	0.4		0.3		0.4	
IN 625	5.0	61.0	21.5	9.0			0.1	0.2	
HR 120	27.5	37.0	25.0	2.5	3.0	0.2	0.1	0.6	2.5
Synthesized Alloys									
IN 625 Model	4.0	61.5	22.0	9.0					
IN 625 Fe-	0	66.5	22.0	9.0					
IN 625 Fe+	8.0	57.5	22.0	9.0					
IN 625 Cr-	4.0	67.5	16.0	9.0					
IN 625 Cr+	4.0	58.5	25.0	9.0					
IN 625 Mo-	4.0	66.5	22.0	0.0					
IN 625 Mo+	4.0	54.5	22.0	16.0					

The synthetic ashes were prepared with NaCl (99%, SDS), KCl (99.5%, Roth), Na_2SO_4 (98 %, VWR), K_2SO_4 (99 %, Acros Organics) and $CaSO_4$ (97 %, Sigma Aldrich) salts. Their composition is given in Table 10. The compounds were ground to obtain a maximum grain size of 250 µm and mixed together in a shaker (Turbula T2FN) during 24 h. [138]

Table II.10. Ash chemical compositions used in corrosion tests (compounds converted into elements)

Compound (wt%)	**$ZnCl_2$**	**NaCl**	**KCl**	**Ca_2SO_4**	**Na_2SO_4**	**K_2SO_4**	**SiO_2**	**Al_2O_3**	**Fe_2O_3**
Elemental (wt%)	**S**	**Cl**	**Na**	**K**	**Zn**	**Ca**	**Si**	**Al**	**Fe**
Ash 1		20	20	50	5	5			
	13.8	21.5	9.6	12.8		14.7			
Ash 2		5	5.0	80	5	5			
	20.9	5.4	3.6	4.9		23.5			
Ash 3	10	5	5	70	5	5.			
	18.5	10.6	3.60	4.88	4.8	20.6			
Ash 4		20	20	20	5	5	17	8	5
	6.8	21.5	9.55	12.78		5.9	7.93	4.2	3.5
Ash 5	10	5	5	40	5	5.	17	8	5
	11.5	10.6	3.60	4.88	4.8	11.8	7.93	4.2	3.5

For isothermal tests in laboratory air (crucible tests), samples were immersed into an alumina crucible with ashes as describe in Figure II.5 according to ISO/DIS 17248 standard. [139] The corrosive ash was flattened by applying a uniform pressure with a jig (about 0.04 MPa, i.e. 40 g/cm^2) in order to keep reproducibility of the test. However, the air atmosphere was still able to reach the metal/oxide interface.

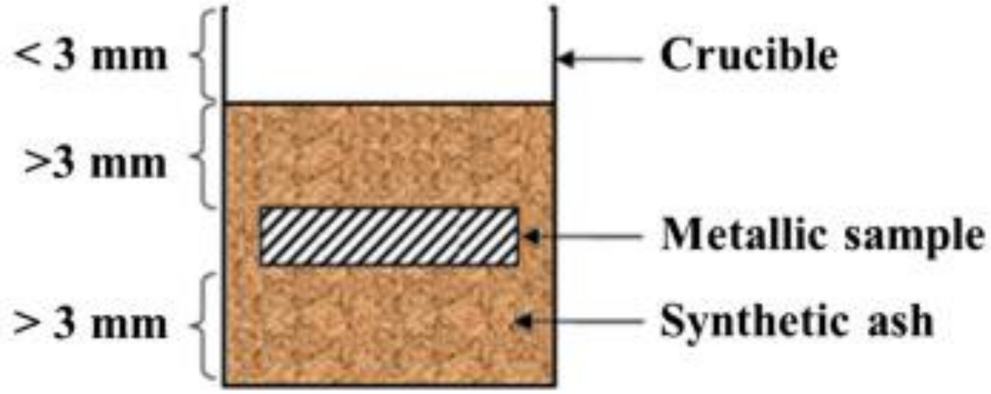

Figure II.5. Scheme of crucible for corrosion tests in pure air [138]

The corrosion tests were performed, at IJL Nancy, in a muffle furnace (Nabertherm LT15/12/P330, N11/H) in laboratory air (no gas flow) at isothermal temperatures (between 450°C and 650°C). The humidity in the atmosphere corresponded to air humidity in Nancy during test periods. The test's temperatures have been chosen around the solidus temperature (appearance of melting phases) of the synthetic ashes. [138]

Table II.11. Test matrix of isothermal corrosion tests in laboratory air and complex atmosphere

Laboratory air (20% O_2 – 79% N_2 – 1% other gas) (vol%)$_{Air}$			
Material	**Temperature (°C)**	**Ash N°**	**Time (h)**
16Mo3, IN 625	450-500-550-600-650	1,2,3	100 – 500 - 1000
HR120	450-600-650	1	500
IN 625 Pattern IN 625 Fe-, IN 625 Fe+ IN 625 Cr-, IN 625 Cr+ IN 625 Mo-, IN 625 Mo+	450-600-650	1	500
Complex Atmosphere (8% O_2 – 18%H_2O – 1100 ppm HCl – 110 ppm SO_2) (vol%)$_{Gas}$			
16Mo3, IN 625 IN 625 Pattern IN 625 Fe-, IN 625 Fe+ IN 625 Cr-, IN 625 Cr+ IN 625 Mo-, IN 625 Mo+	600	1,4,5	500
HR 120	600	1,4,5	500

For isothermal tests in complex atmosphere, samples were conducted in a pilot developed in a previous study. [51] This pilot was originally intended to reproduce the heat exchangers temperature gradient. For our study, the pilot has been adapted to accommodate standard crucible tests.

The complex atmosphere tests have been performed by Veolia Environment (project partner) under the supervision of Jean-Michel Brossard. The sample preparation and ash preparation were performed according to the protocol described above. Figure II.6 shows the installation of the pilot for the crucible tests. HCl was introduced through the injection of a solution of hydrochloric acid and SO_2 by gas in bottle. Moisture content in gas phase was controlled adjusting the concentration and flowrate of hydrochloric acid solution. The operation of the pilot does not allow introducing the heated samples. Therefore the samples were set up at room temperature prior to raise the temperature inside the pilot. The rate of temperature increase was set to 8°C/min up to the test temperature.

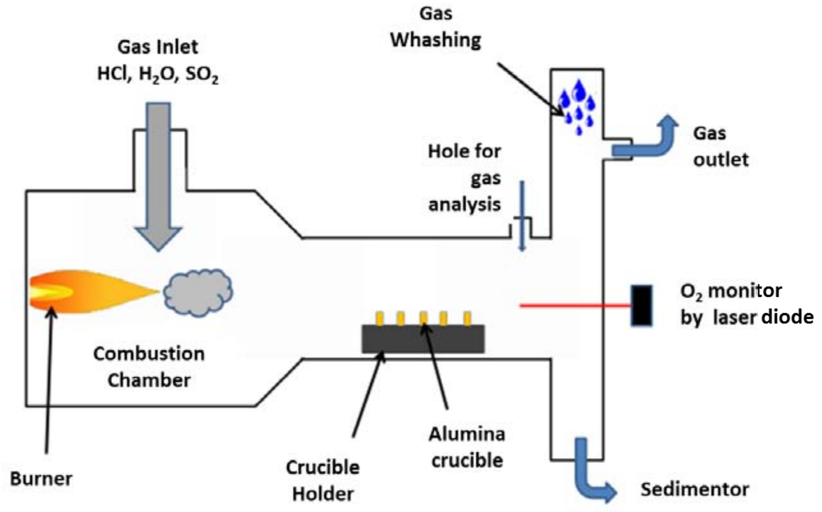

Figure II.6. Scheme of the pilot for corrosion tests at complex atmosphere. [51]

After the exposure, the specimens used to measure thickness loss were cold mounted in epoxy. Then, the samples were cut off in the middle (in order to obtain two half cylinders) with a manual cut-off machine in dry condition (without water) and the surface was ground with 400, 800, 1200 and 2400 grit SiC papers in dry condition too. These metallographic preparations under dry conditions were used to avoid dissolution of corrosion products and Cl-containing compounds. The metallographic cross-sections were characterized using scanning electron microscopy (SEM) LEO 435 VP coupled with energy dispersive X-ray spectrometry (EDS) IMIX system from PGT. The SEM images were in backscattered electron mode, in order to get phase contrast. The average thickness loss was calculated by subtracting the average of 20 residual thickness of the sample to the initial thickness measured before the test (also an average of 20 measurements). [138] Additionally, corrosion product scales were removed from other specimen used to evaluate the weight loss by chemical washing following ISO/DIS 17248 standard. [139]

II.2.2 Database construction

In order to achieve the main objective of this study, the same way as metal dusting, the amount of tests, materials and conditions fixed for high-temperature corrosion in the SCAPAC project was also insufficient. To compensate this lack of data, a large database was built from corrosion tests found in literature. All the information concerning corrosion results obtained by several authors in laboratory tests at different conditions was entered in the database. Table II.12 shows the published research that were examined and added to the high-temperature corrosion database.

The same way as metal dusting, after reviewing the articles, all the information available concerning the corrosion tests were organized in different groups of variables. As explained in section II.1.2, in the present study, the input variables are the conditions set up in laboratory tests in order to obtain a corrosion rate as the output variable.

Table II.12. Published research added to the high-temperature corrosion database

Ref. n°	Title of the published research
ES_CE01	E. Schaal's thesis, 2015. High-temperature corrosion tests - ANR SCAPAC project.[126]
SC_CP01	Laboratory corrosion tests for simulating fireside wastage of superheater materials in waste incinerators.[75]
SC_CP02	Fireside Corrosion of Boiler Materials – Effect of Co-Firing Biomass with Coal.[140]
SC_CP03	Chloridation and oxidation of iron, chromium, nickel and their alloys in chloridizing and, oxidizing atmospheres at 400°C-700°C.[40]
SC_CP04	The Effects of chloride, and sulfur dioxide in the oxidation of steels below deposits.[62]
SC_CP05	Influence of gas phase composition on the Hot Corrosion of steels and nickel-based alloys beneath a (Ca-Na-K)-sulfate mixture containing $PbSO_4$ and $ZnSO_4$.[64]
SC_CP06	Performance of commercial alloys in simulated waste incineration environments.[110]
SC_CP07	High-temperature corrosion of iron-base and nickel-base heat resistant alloys in a simulated waste incineration environment.[141]
SC_CP08	High-temperature corrosion in a 65 MW waste to energy plant.[142]
SC_CP09	Stability of protective films in waste incineration environment solubility measurement of oxides in molten chlorides.[92]
SC_CP10	Corrosion prevention of waterwall tube by field metal spraying in municipal waste incineration plants.[143]
SC_CP11	Effect of chlorine on waterwall fireside corrosion.[144]
SC_CP12	Application of new corrosion resistant superheater tubing for 500 °C, 100 Kgf/cm^2g high efficiency WTE plant.[145]
SC_CP13	Recent trends in corrosion resistant tube materials and improvements of corrosion environments in WtE plants.[49]
SC_CP14	Evaluation of new corrosion resistant superheater tubing in high efficiency waste-to-energy plants.[103]
SC_CP15	Performance of commercial and developmental corrosion resistant alloys in simulated waste incineration environments.[89]
SC_CP16	Fireside corrosion of alloys for combustion power plants.[146]
SC_CP17	Experience of superheater tubes in municipal waste incineration plant.[147]
SC_CP18	Corrosion of experimental superheater alloys in waste fuel combustion.[148]
SC_CP19	A corrosion mechanism for the fireside wastage of superheater materials in waste incinerators.[74]
SC_CP20	Corrosion of superheater materials in a waste-to-energy plant.[78]
SC_CP21	Chemistry and melting characteristics of fireside deposits taken from boiler tubes in waste incinerators.[73]
SC_CP22	High-temperature corrosion mechanisms and effect of alloying elements for materials used in waste incinerations environments.[104]
ES_CP01	Formation of Si diffusion layer on stainless steels and their high-temperature corrosion resistance in molten salt.[149]
ES_CP02	Sulfur recirculation for increased electricity production on Waste-to-Energy plants.[150]
ES_CP03	High-temperature corrosion behavior of the superheater materials.[151]
ES_CP04	Investigation into high-temperature corrosion in a large-scale municipal waste to energy plant.[95]
ES_CP05	Corrosion behavior of various model alloys with NaCl-KCl coatings.[152]
ES_CP06	Alloy 625 - Impressive Past/Significant presence/awesome future.[153]
ES_CP07	Type II Hot Corrosion: Kinetics Studies of CMSX-4.[154]
ES_CP08	Etude des phénomènes de corrosion à haute température en environnement type UVED.[51]

II.2.2.1 Input variables

In high-temperature corrosion, independent variables are clustered into three groups: the test atmosphere which includes the gas composition, pressure and temperatures set by the experimenter in the tests (Table II.13), the materials composition which includes the elemental chemical composition of the materials used by the experimenter in the tests (Table II.14) and the ash chemical composition used by the experimenter in the tests (Table II.15).

Table II.13. Atmosphere conditions included in the database

Ref. N°	$T_{\text{Flue Gas}}$ (°C)	T_{Metal} (°C)	P_{Int} (bar)	V_{gas} ($m.s^{-1}$)	O_2	H_2O	CO_2	CO	N_2	H_2	HCl	SO_2
					(vol%)						ppm	

Table II.14. Chemical composition of materials included in the database

Ref. N°	Material	Chemical Composition (wt%)													Coating Y/N
		Fe	Ni	Cr	Mo	Co	Cu	Al	Si	W	Nb	Ti	Mn	C	
1	Alloy 1														

In the case of the third group, the ash chemical composition was found in literature in wt% of compounds present in the ash and in wt% of elements present in the ash. In order to standardize the quantities and to adequately process the data, the compositions expressed as compounds were converted to their elemental form, for subsequent statistical treatment, as shown in Table II.16.

Table II.15. Ash chemical composition included in the database (as compounds)

Ref. N°	Solid Fuel	Ash Name	T_{Solidus} (°C)	Oxides	SO_3	SiO_2	Al_2O_3	P_2O_5	Fe_2O_3	CaO
				Sulfates	$CaSO_4$	Na_2SO_4	K_2SO_4	$PbSO_4$	$ZnSO_4$	
				Chlorides	$PbCl_2$	$ZnCl_2$	NaCl	KCl	$(wt\%)_{Ash}$	

Table II.16. Ash chemical composition included in the database (in elemental form)

Ref. N°	Solid Fuel	Ash Name	T_{Solidus} (°C)	S	Cl	Na	K	Pb	Zn	P	Si	Al	Ca	Fe
				$(wt\%)_{Ash}$										

II.2.2.2 Output variables

The output variables are all measurable parameters resulting from the corrosion tests. These variables will be exploited to calculate the corrosion rates which will be used as dependent variables. Table II.17 gathers the variables measured at the end of each test, the total time of the test and its corresponding equivalent rate obtained by dividing the measured magnitude by the total time of the test. Unlike metal dusting testing for high-temperature corrosion, neither incubation periods, nor frequency are determined.

Table II.17. Measured variables converted into corrosion rates

Ref. N°	Thickness Loss (Max)	Thickness Loss (Mean)	Mass Loss	Mass Gain	Total Time	Thickness Loss Rate (Max)	Thickness Loss Rate (Mean)	Mass Loss Rate	Mass Gain Rate
	mm		mg/cm^2		hours	mm/y		$mg/cm^2 \cdot h$	
1									

After entering the data of the corrosion tests, corrosion rates were calculated for every parameter, and every test. As corrosion rates were represented by different output parameters, subsequent quantification of output parameters was performed (Figure II.7). After quantification, the most adequate dependent variable was selected for modeling procedures, based on the amount of data and the utility of the variable for lifetime prediction purposes.

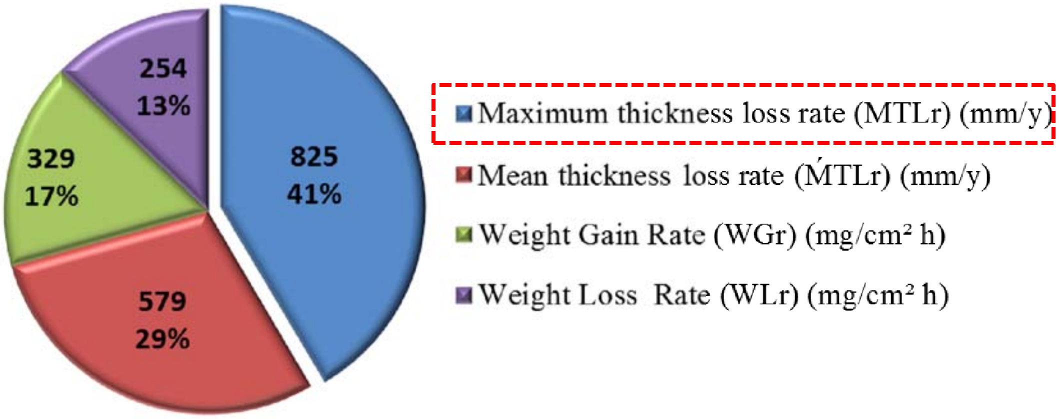

Figure II.7. Data population for each output parameter present in the database

The diagram in Figure II.7 shows the quantification of data and we can clearly see that Maximum Thickness Loss rate (MTLr) is the most suitable variable for predictive modeling for two reasons. First, it is the largest in data population which allows obtaining robust models in a wide range of conditions as well as enable domain filtering if necessary without affecting the amount of data needed to construct the model. Second, the calculation of the MTLr is the most useful magnitude in equipment design procedures, which will allow a better adjustment of the models to real conditions.

After selecting the dependent variable to be treated, several statistical methods were applied to describe the data distribution and to select the independent variables that explain better the corrosion rates.

II.3 Statistical Methods

As explained above, an input variable is an independent variable, while an output variable is a dependent variable, whose behavior can be modeled by independent variables. [128] In statistics, the dependent variable is the event studied and expected to change whenever the independent variables are altered. In mathematical modelling, the dependent variable is studied to see if and how much it varies as the independent variables vary.

The most common symbol for the input variable is $\boldsymbol{x}$, and for the output one is $\boldsymbol{y}$; the function itself is commonly written $\boldsymbol{y} = \boldsymbol{f}(\boldsymbol{x})$. It is possible to have multiple independent variables and/or multiple dependent variables.[128] In metal dusting the output variable (corrosion rate) can be explained by approximately 23 independent variables. In high-temperature corrosion the output variable can be explained by approximately 34 independent variables. However, it becomes necessary to know the data distribution of each variable and the levels of correlation they have with the corrosion rate, and with each other, in order to choose the variables that explain better the corrosion rates.

II.3.1 Descriptive Statistics

Before using advanced statistical analysis methods like, for example, multiple regressions, the first step is to describe the data in order to identify trends, locate anomalies (outliers) or simply have available essential information such as the minimum, maximum or mean of a data sample. Descriptive statistics techniques are an attempt to use numbers to visualize data. In this study, box plots and correlation tests have been applied to attaint this objective.

II.3.1.1 Box Plots

The box plot is a standardized way of displaying the distribution of data based on five number summary: minimum, first quartile, median, third quartile, and maximum. In the box plot of Figure II.8, the central rectangle spans the first quartile to the third quartile (the interquartile range or IQR). A segment inside the rectangle shows the median and the "whiskers" above and below the box show the locations of the minimum and maximum. [155]

Box plots are useful describe a distribution and to identify the outliers of a data set. Outliers are either 3×IQR or more above the third quartile or 3×IQR or more below the first quartile. Suspected outliers are slightly more central versions of outliers: either 1.5×IQR or more above the third quartile or 1.5×IQR or more below the first quartile.

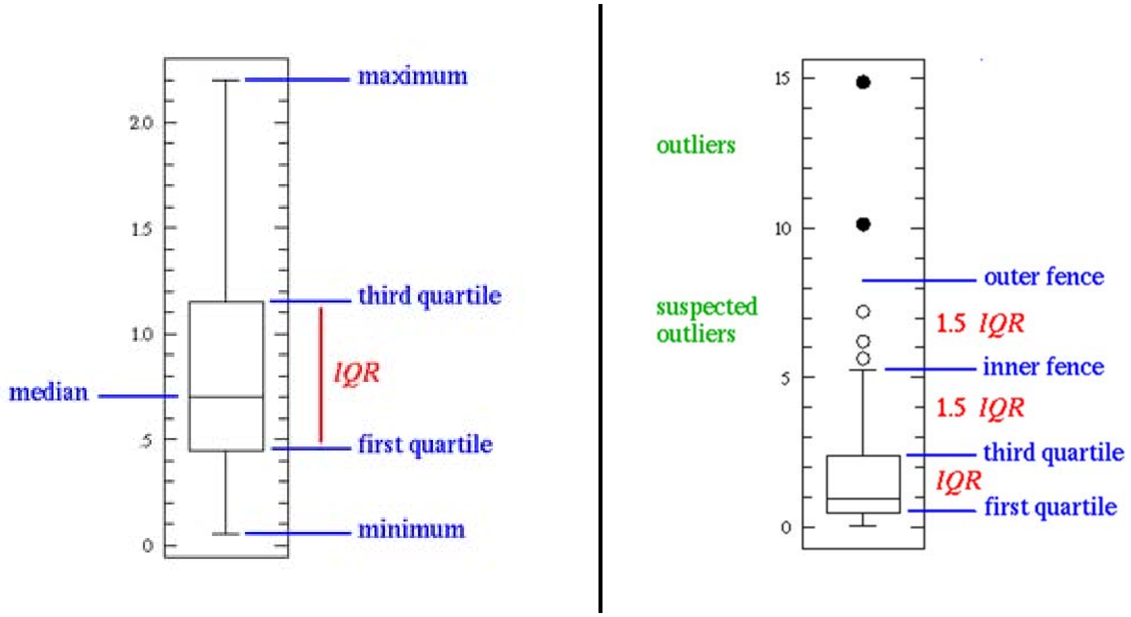

Figure II.8. Scheme of box plot analysis. [155]

The outliers are not necessarily "bad" data-points. They should not be automatically removed from the dataset. Before removing outliers, they should be analyzed to understand why they are isolated from the main dataset. They may be the key to the phenomenon under study, the result of human errors or can be produced for anomalous conditions that do not correspond to the interest of the study. This technique was applied to every variable of the metal dusting database and high-temperature corrosion database.

Once the outliers were identified for each variable, it became necessary to determine whether or not it affects the correlation between corrosion rates and each independent variable.

II.3.1.2 Correlations Tests

Correlation is a bivariate analysis that measures the strengths of association between two variables. In statistics, the value of the correlation coefficient varies between +1 and -1. When the value of the correlation coefficient lays around 1 or -1, then it is said to be a perfect degree of association between the two variables. As the correlation coefficient value goes towards 0, the relationship between the two variables will be weaker. Usually, in statistics, there are three types of correlations: Pearson correlation, Kendall rank correlation and Spearman correlation.

In order to determine the level of association between each independent variable and the corrosion rate (Figure II.9a), as well as the effect of the outliers found in the corrosion rates (Figure II.9b), the technique of correlation test by Pearson was applied. Pearson correlation is the most common coefficient and indicates the strength of a linear association between two variables.

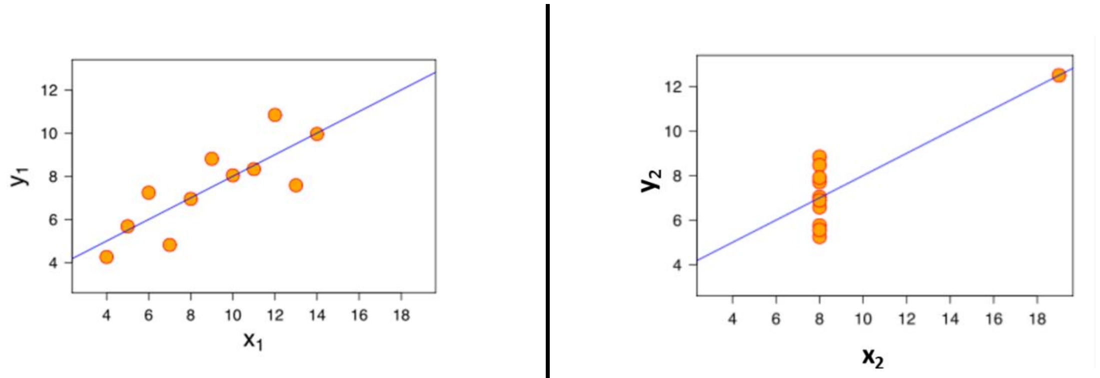

a)

b)

Figure II.9. Sets of data with the same Pearson correlation r = 0.816. a) Normal distribution b) Outlier effect

If we have a series of n measurements of X and Y written as x_i and y_i where $i = 1, 2, \ldots, n$, then the Pearson sample correlation coefficient can be used to estimate the population correlation r between X and Y. The sample correlation coefficient is written (31): [156]

$$r_{xy} = \frac{\sum_{i=1}^{n}(x_i - X)(y_i - Y)}{(n-1)S_x S_y} = \frac{\sum_{i=1}^{n}(x_i - X)(y_i - Y)}{\sqrt{\sum_{i=1}^{n}(x_i - X)^2 \sum_{i=1}^{n}(x_i - X)^2}} \qquad \textbf{Equation 31}$$

where $\boldsymbol{\mathcal{X}}$ and $\boldsymbol{\mathcal{Y}}$ are the sample means of $\boldsymbol{X}$ and $\boldsymbol{Y}$, and S_x and S_y are the sample standard deviations of $\boldsymbol{X}$ and $\boldsymbol{Y}$. For the case of a linear model with a single independent variable, the coefficient of determination (R^2) is the square of $\boldsymbol{r}$, Pearson's product-moment coefficient. [156] In the statistical analysis the p-values that are computed for each correlation coefficient allow testing the null hypothesis. The null hypothesis usually refers to a general statement that there is no relationship between two measured groups. Rejecting the null hypothesis allows to conclude that there is a relationship between two groups. [157]

In statistics, statistical significance (or a statistically significant result) is obtained when a p-value is less than the significance level. Before the test is performed, a threshold value denoted as α is chosen, for the significance level of the test, traditionally 0.05 (5%). [157] If the p-value is smaller than the significance level (α), it suggests that the null hypothesis must be rejected with error probability lower than α. Thus there is a relationship between the two measured groups with statistical significance.

Table II.18 shows an output of the correlation test between Y and X_n variables, correlations statistically significant are indicated in bold which p-values are lower than the significance level ($\alpha = 0.05$). The variable X_2 shows a low correlation with a p-value higher than the significance level ($\alpha = 0.05$), therefore this correlation is not statistically significant. In Figure II.10 is shown a two-tailed test, the rejection region for a significance level of $\alpha=0.05$ is partitioned to both ends of the sampling distribution and makes up 5% of the area under the curve (white areas). [157]

Table II.18. Correlation test computed results

Variables	Y	p-values:
X_1	**-0.221**	**< 0.0001**
X_2	-0.016	0.558
X_3	**0.162**	**< 0.0001**

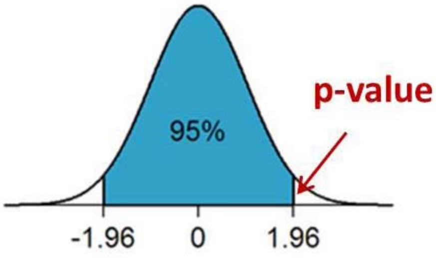

Figure II.10. Rejection region for a significance level of α=0.05 in a two-tailed test.

At the moment of the analysis, we should be cautious with the following aspects: [157]

- Correlations cannot be used to infer a causal relationship between the variables; consequently, establishing a correlation between two variables is not a sufficient condition to establish a causal relationship.
- The Pearson correlation coefficient indicates the strength of a linear relationship between variables, but its value generally does not completely characterize their relationship. The correlation coefficient, as a summary statistic, cannot replace visual examination of the data.

Figure II.9 shows two data distributions with the same correlation coefficient. In Figure II.9a the distribution is linear but in Figure II.9b the distribution is not really linear, it is an artefact because the distribution is discontinuous. The effect of the outlier disturbs the reliability of the coefficient.

This means that the correlation test gives an idea of the linear relationship between variables but it is the experimenter whom has the ability to interpret the results and decide the handling of data according to their experience in the physical phenomenon.

II.3.2 Multiple Linear Regression (MLR)

The lifetime prediction of components every day becomes more essential, to design new equipment as to improve maintenance strategies in service that enable cost reduction and resources optimization. Multiple regression is a tool that allows to develop an equation that can be used to predict materials lifetime, determining corrosion rates.

Multiple regression is a technique used to predict scores on a single outcome variable Y on the basis of scores on several predictor variables, X_i. The X_i may be called independent variables, predictor variables, or just predictors, and Y may be referred to as the dependent variable, the predicted variable, or the outcome measure. [158] In this study Multiple Linear Regression (MLR) was chosen to predict corrosion rates for several reasons described as follows:

- Our goal is lifetime prediction, hence a linear regression can be used to fit a predictive model to an observed data set of Y and X values. After developing such a model, if an additional value of X is then given without its accompanying value of Y, the fitted model can be used to make a prediction of the value of Y.
- Given a variable y and a number of variables $x_1, x_2, \dots x_p$ that may be related to y; a linear regression analysis can be applied to quantify the strength of the relationship between y and the $x_{1,2,3}$, to assess, which x_p may have no relationship with y at all, and to identify which subsets of the x_p contain redundant information about y.
- Additionally, linear regression was the first type of regression analysis to be studied rigorously, and has been applied extensively in practical applications. Models which depend linearly on their parameters are easier to fit than models which are non-linearly related to their parameters also the statistical properties of the resulting estimators are easier to determine.

Multiple Linear Regression (MLR) attempts to model the relationship between two or more explanatory variables and a response variable by fitting a linear equation to observed data. Every value of the independent variable $\boldsymbol{x}$ is associated with a value of the dependent variable $\boldsymbol{y}$. For more than two predictors, the estimated regression equation yields a hyperplane for $\boldsymbol{p}$ explanatory variables $x_1, x_2, \dots, x_p$ is defined by equation (32): [158]

$$\boldsymbol{\mu_y = \beta_0 + \beta_1 x_1 + \beta_2 x_2 + \dots + \beta_p x_p} \qquad \textbf{Equation 32}$$

Equation 32 describes how the mean response μ_y changes with the explanatory variables. The observed values for μ_y vary around their means μ_y and are assumed to have the same variance σ. The fitted values $b_0, b_1, \dots, b_p$ estimate the parameters $\beta_0, \beta_1, \beta_2, \dots, \beta_p$ of the population regression line. The letter b is used to represent a sample estimate of a β coefficient. Thus b_0 is the sample estimate of β_0, b_1 is the sample estimate of β_1, and so on. The fitted values are denoted by the equation (33) and the residuals by the equation (34), is the difference between the observed and fitted values. The sum of the residuals is equal to zero.

$$\boldsymbol{\hat{Y}_i = b_0 + b_1 x_{i1} + b_2 x_{i2} + \dots + b_p x_{ip}} \qquad \textbf{Equation 33}$$

$$\boldsymbol{e_i = y_i - \hat{y}_i} \qquad \textbf{Equation 34}$$

Since the observed values for y vary about their means μ_y, the multiple regression model includes a term for this variation named "the residual". The residual term is denoted ε and represents the deviations of the observed values y from their means μ_y, which are normally distributed with mean 0 and variance σ. Formally, the model for multiple linear regression, given n observations, is given by equation (35)

$$\boldsymbol{y_i = \beta_0 + \beta_1 x_{i1} + \beta_2 x_{i2} + \ldots + \beta_p x_{ip} + \varepsilon_i} \qquad \boldsymbol{i}=1,2,\ldots,n \qquad \textbf{Equation 35}$$

In the least-squares model, the best-fitting line for the observed data is calculated by minimizing the sum of the squares of the vertical deviations from each data point to the line (if a point lies on the fitted line exactly, then its vertical deviation is 0), as shown in Figure II.10a. Due to the deviations are first squared, then summed, the coefficient is denoted as sum of squared errors (SSE), thus are no cancellations between positive and negative values. [158] MSE is the mean-squared error also known as the variance of the errors given by equation (36) and the estimate of the standard error of each prediction RMSE is given by equation (37)

$$\boldsymbol{MSE = \frac{SSE}{n-p-1}} \qquad \textbf{Equation 36}$$

$$\textbf{RMSE} = \sqrt{\boldsymbol{MSE}} \qquad \textbf{Equation 37}$$

R^2, is the determination coefficient for the model that represents the proportion of variation in $\boldsymbol{y_i}$ explained by the multiple linear regression model with predictors $x_{i1}, x_{i2}, \ldots, x_{ip}$. The coefficient value is is between 0 and 1. When R^2 is closest to 1, the model will offer a better fit of the data and more accuracy in its predictions. The coefficient is given by equation (38). Where, SSTO (total sum of squares errors) is calculated as the sum of squares of the vertical deviations from each data point to the horizontal line that pass through the mean of all the predicted values. Figure II.11 shows an example of the interpretation of the coefficients, in the example 82% of the variance in the model is explained by the model while 18% is explained by other variables not considered in the group of predictors.

$$\boldsymbol{R^2 = 1 - \frac{SSE}{SSTO}} \qquad \textbf{Equation 38}$$

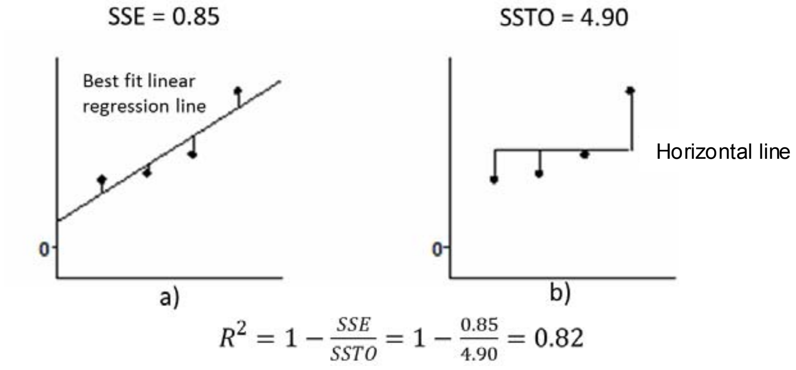

Figure II.11. Calculated distances of the deviations by least-squares model.

Adjusted R^2, is the adjusted determination coefficient for the model. The adjusted R^2 can be negative if the R^2 is near to zero. The coefficient has no practical interpretation. It is useful for model building purposes, when comparing two models used to predict the same response variable, the model with the higher value of Adjusted R^2 is generally preferred. The coefficient is given by equation (39).

$$\boldsymbol{Abjusted\ R^2 = 1 - \frac{(n-1)}{(n-p)}\left(1 - R^2\right)} \qquad \textbf{Equation 39}$$

II.3.2.1 Size data

MLR analysis needs at least 3 variables of metric scale. A rule for the sample size is that regression analysis requires at least 20 cases per independent variable in the examination. In the simplest case of having just two independent variables, it requires $n > 40$ cases. [159]

II.3.2.2 Assumptions of the MLR [158]

MLR analysis also makes several key assumptions in order to create a precise model. The following are the major assumptions:

II.3.2.2.1 Linear relationship

MLR analyzes the linear relationship between the independent and dependent variables to be linear. It is also important to check for outliers since MLR is sensitive to outlier effects. For the models presented in this study the linearity assumption was tested with correlations tests explained in section II.3.1.2.

It is known that high-temperature corrosion processes are thermally activated following and Arrhenius law which is not linear. However, the linear relationship was chosen in first place in order to evaluate the relative contribution of the main parameters. Although the possibility that nonlinear regression would give better results, is not excluded.

II.3.2.2.2 Multivariate normality

MLR analysis requires all variables to be normally distributed. For the models presented in this study, this assumption was checked with a histogram and a fitted normal curve.

II.3.2.2.3 No auto-correlation

In MLR, autocorrelation occurs when the residuals are not independent from each other. For the models presented in this study, this assumption was checked with the Durbin-Watson test (DW). As a rule of values of $1.5 < DW < 2.5$ show that there is no auto-correlation in the MLR data.

II.3.2.2.4 Homoscedasticity

Homoscedasticity means that the variance of errors is the same along the regression line. For the models presented in this study, this assumption was checked with the scatter plot of standardized residuals.

II.3.2.2.5 Lack of multicollinearity

MLR assumes that there is little or no multicollinearity in the data. Multicollinearity occurs when the independent variables are not independent from each other. In the case of multicollinearity, the predictor β will be non-identifiable, not reliable; the null hypothesis will be not rejected. For the models presented in this study, this assumption was checked with the correlation matrix resulting from the correlation test, the tolerance coefficient (T). With $T < 0.2$ there might be multicollinearity in the data and with $T < 0.01$ there is certainly multicollinearity.

In order to avoid multicollinearity between variables in the MLR, the method of Principal Component Analysis has been performed which will be explained in section II.3.3.[160]

II.3.2.3 Multiple linear regression calculations

For each multiple linear regression, a number of parameters were obtained and analyzed to verify the validity of the model. These are described as follows:

1. The regression equation (40) of the model was obtained to make it easier to read or re-use the model.

$$y = \beta_0 + \beta_1 x_1 + \beta_2 x_2 + \beta_3 x_3 + \beta_4 x_4 \quad \textbf{Equation 40}$$

2. Table II.19 displays the validity domain of the model and the data set used for validation. This means the maximum and minimum values of the variables included in the model.

Table II.19.Validity domain of the model.

	Model		**Validation**	
Variable	**Minimum**	**Maximum**	**Minimum**	**Maximum**
Y				
X_1				
X_2				
X_3				
X_4				

3. Table II.20 displays the goodness of fit statistics. It shows the statistics relating to the fitting of the regression model. Satisfactory models have a value R^2 and Adjusted R^2 greater than or equal to 0.6. RMSE will determine the mean error of the predictions of the model (± value) and Durbin Watson coefficient (no auto correlation assumption).

Table II.20. Goodness of fit statistics of the model.

R^2	**> 0.6**
Adjusted R^2	**> 0.6**
MSE	
RMSE	
DW	**1.5 >-<2.5**

4. Table II.21 displays the predictor's coefficients of the equation, the corresponding standard errors, the Student's t (**T**) and the corresponding p-values (Pr > |t|). Parameters with p-values smaller than the significance level ($\alpha=0.05$) suggest that the null hypothesis is rejected with a small probability of error (lower than α), thus the coefficient is significant. Parameters with p-values larger than the significance level ($\alpha=0.05$) suggest that the null hypothesis is rejected with a high probability of error, if the null hypothesis is not rejected the coefficient is not significant, thus it could be removed from the model. However the variable could remain if the experimenter considers that provides important information to the phenomenon.

Table II.21. Statistic of model predictors.

Source	Value (β_i)	Standard error	T	Pr > |t|
Intercept	1.2	6.4	-1.1	**< 0.0001**
X_1	0.3	0.0	2.3	**< 0.0001**
X_2	0.0	0.2	0.2	**0.500**
X_3	-0.3	0.1	-1.6	**< 0.0001**
X_4	0.3	0.2	1.3	**0.001**

5. Table II.22 shows the analysis of variance which is used to evaluate the explanatory power of the explanatory variables. Degrees of freedom (DF) of the model, sum of squares and mean squares of the fitted part of the model and the residuals, the significance F-test and the p-value of the F-test (Pr > F).

   The F-test rejects the null hypothesis that the value of R is zero, thus enables us to decide whether there is a significant linear relationship between the dependent variable and the set of independent variables taken together. In this study $F > 14$ and $|Pr > F| < 0.05$ indicates that there is a significant linear relationship. Therefore it can be concluded that the hyperplane defined by the regression equation provides a good fit to the data population. This criterion was also used to compare two models with similar characteristics, higher value of F better the model is.

Table II.22. Analysis of variance:

Source	DF	Sum of squares	Mean squares	F	Pr > F
Model	4	630.1	157.5	**>14**	**< 0.0001**
Error	65	3479.7	53.5		
Corrected Total	69	4109.7			

6. The chart of standardized coefficients (also called beta coefficients) shown in Figure II.12 is used to compare the relative weights of the variables. The higher the absolute value of a coefficient, the more important the weight of the corresponding variable in the model.

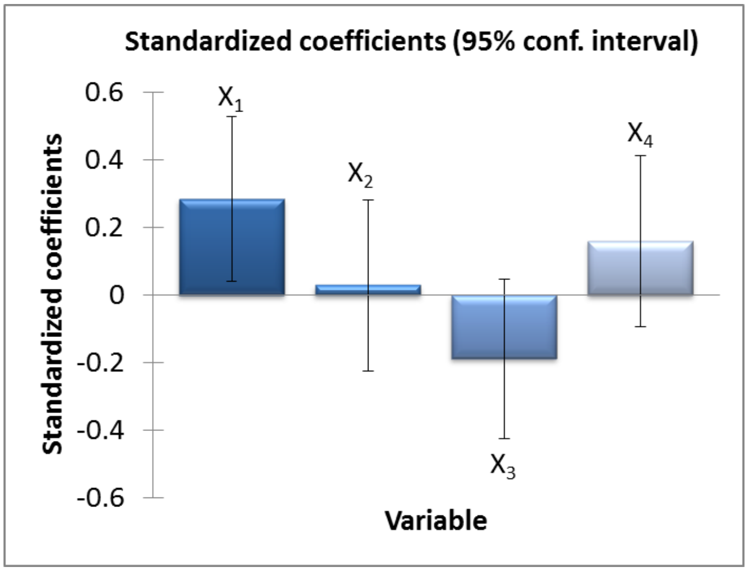

Figure II.12. Chart of standardized coefficients

7. The precision chart in Figure II.13 shows, the distance between the predictions and the experimental observations. For an ideal model, the points would all be on the bisector. Blue points represent those data points used to construct the model and the red ones represent the data points used to validate the model which are not included in the first group.

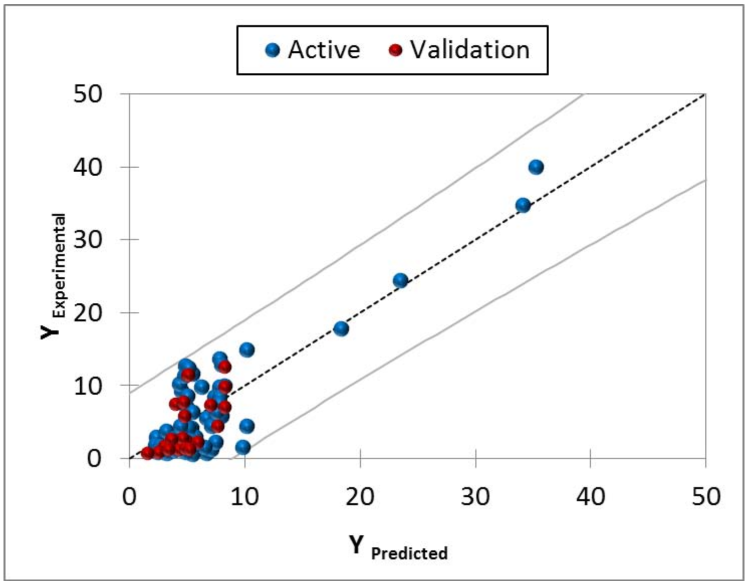

Figure II.13. Precision chart comparative between predictions and the observations

II.3.3 Principal Component Analysis

II.3.3.1 Variables selection

As it was explained in section II.3, in metal dusting the corrosion rates are explained in theory by approximately 23 independent variables and in the case of high-temperature corrosion the corrosion rates are explained by approximately 34 independent variables. Before performing multiple linear regressions it became necessary to know which variables explain better the corrosion rates and which of them are correlated with each other in order to avoid multicollinearity.

Lack of multicollinearity is one of the assumptions to be met to create a valid model by MLR. To achieve this aim, the method of Principal Component Analysis was applied to the raw data.

In statistics, variance measures how far a set of numbers is spread out. A small variance indicates that the data points tend to be very close to the mean (expected value) and hence to each other, while a high variance indicates that the data points are very spread out around the mean and from each other. An equivalent measure is the square root of the variance, called the standard deviation. [161]

Principal component analysis (PCA) is a statistical procedure that uses an orthogonal transformation to convert a set of observations of possibly correlated variables into a set of values of linearly uncorrelated variables called principal components (new coordinate system). The number of principal components is less than or equal to the number of original variables. The first principal component has the largest possible variance (as much of the variability in the data as possible), and each succeeding component in turn has the highest variance possible under the constraint that it is orthogonal to the preceding components. The principal components are orthogonal because they are the eigenvectors of the covariance matrix, which is symmetric. [162]

PCA is mostly used as a tool in exploratory data analysis and for making predictive models. It is a way of identifying patterns in data, and expressing the data in such a way as to highlight their similarities and differences. Once these patterns in the data are found, the data can be compressed, by reducing the number of dimensions, without losing information. This technique allowed reducing the number of variables for the model, based on the following criteria:

1. Highest cumulative variability in the first two factors (F1, F2) in order to visualize most of the information in the 2 axes (% in the top of the diagram), as shown in example of Figure II.14.

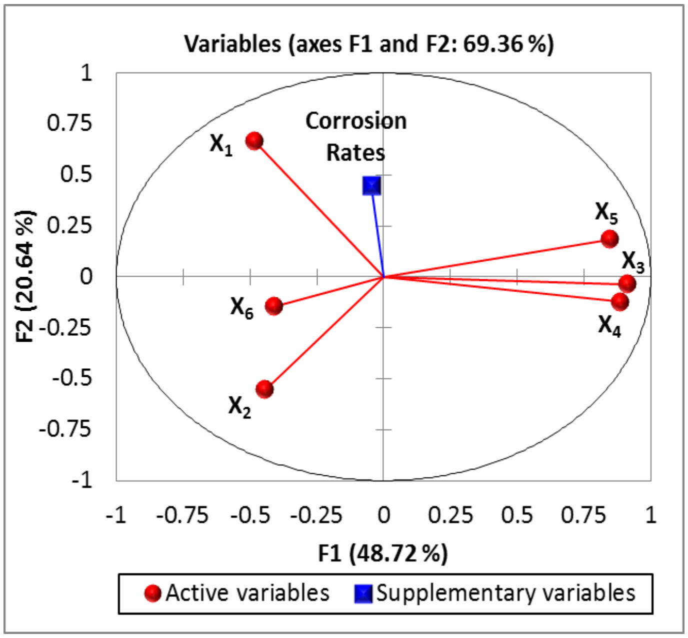

Figure II.14. 2D diagram obtained during the PCA analysis

2. Highest correlations between the corrosion rates and all the explanatory variables. In the diagram corrosion rate is indicated in blue as a supplementary variable not included in the linear combination of the independent variables in red. The corrosion rate can be represented by any dependent variable chosen according to the case of study. Table II.23 shows the correlation matrix set up with the regression coefficients between vectors in the diagram. Higher correlations are indicated in red.

Table II.23. An example of a correlation matrix obtained during the PCA analysis

Variables	**X_1**	**X_2**	**X_3**	**X_4**	**X_5**	**X_6**	**Corrosion Rate**
X_1	**1**	0.2	-0.3	-0.4	-0.1	0.3	0.3
X_2	0.2	**1**	-0.2	-0.3	-0.2	0.3	-0.2
X_3	-0.3	-0.2	**1**	**0.8**	**0.9**	-0.2	-0.1
X_4	-0.4	-0.3	**0.8**	**1**	**0.7**	-0.2	-0.1
X_5	-0.1	-0.2	**0.9**	**0.7**	**1**	-0.2	0.1
X_6	0.3	0.3	-0.2	-0.2	-0.2	**1**	-0.1
Corrosion Rate	0.3	-0.2	-0.1	-0.1	0.1	-0.1	**1**

When the correlation coefficient is ≥ 0.7, there is multicollinearity between variables. Due to the high collinearity between X_3, X_4 and X_5, only one of them can be included in the model. Typically the most correlated variable with the corrosion rate will be chosen. However in the case of being imperative to include all of them in the model for their relevance to the physical phenomenon, a fusion of variables into one can be made in order to avoid collinearity in the model.

3. Lowest correlations among the variables, in order to avoid multicollinearity by MLR that is repeating variables in the model with the same information contained.

4. The correlations are represented by the angles between vectors (∠). Those which are orthogonal are not correlated at all, those which are very close between them ($\angle < 90°$) are positively correlated and those who are on opposite sides ($\angle > 90°$) are negatively correlated.

5. Priority is given to the well-represented variables on the axes in order to increase the reliability of the correlations and physical trends. The representation on the axes is indicated by the radius of the vector, the closer it is to the circle perimeter the better it is.

In this study the PCA's were carried out by groups of variables depending on the type of information. As shown in Table II.24, for-high-temperature corrosion, PCA_1 was applied on alloy composition, PCA_2 was applied on conditions related to the test environment such as metal temperature and gaseous phase characteristics, and PCA_3 was applied on ash chemical composition in elemental form. A group of PCA's was performed according to each scenario. In the case of metal dusting as shown in Table II.25, PCA_1 was applied on alloy composition; PCA_2 was applied on conditions related to the test environment such as metal temperature and gaseous phase characteristics. A group of PCA's was performed according to each dependent variable to evaluate.

Table II.24. PCA's performed for high-temperature corrosion

PCA Analysis	Active Variables	Supplementary Variable
PCA_1: Environment (Gas composition + Tests Conditions)	T_{Gaz}, T_{Metal},^{c} O_2, H_2O, CO_2,^{d} HCl, SO_2 ^{e}	$MTLr^a$
PCA_2: Alloys nominal composition	Fe, Ni, Cr, Mo, Co, Cu, Al, Si, W, Nb, Ti, Mn, C ^{b}	$MTLr^a$
PCA_3: Ash chemical composition	$T_{Solidus}$, Cl, Ca, Na, K, Pb, Zn, Si, Al, P, Fe ^{f}	$MTLr^a$

[a] Maximum thickness loss rate (MTLr) (mm/y), [b] (wt% Alloy), [c] (°C), [d] (vol% Gas), [e] (ppm Gas), [f] (wt% Ash)

Table II.25. PCA's performed for metal dusting

PCA Analysis	Active Variables	Supplementary Variable
PCA_1: Environment (Gas composition + Tests Conditions)	$1/T_{Metal}$ ^{e}, $p_{Internal}$, pCO, pH_2O,pCO_2, pO_2^{f}, a_C ^{g}	MLr^a PDGr ^{b} IT ^{c}
PCA_2: Alloys nominal composition	Fe, Ni, Cr, Mo, Co, Cu, Al, Si, W, Nb, Ti, Mn, C ^{d}	MLr^a PDGr ^{b} IT ^{c}

[a] Mass Loss Rate (MLr) (mg/cm^{2}h), [b] Pit depth growth rate (PDGr) (µm/h), [c] Incubation times (IT) (h), [d] (wt% Alloy), [e] (1/K), [f] gas partial pressures (bar), [g] carbon activity.

Once performed the PCA's, the variables to be included in the models were chosen, according to the principles of correlation and multicollinearity between dependent and independent variables. About 30 multiple regression simulations were executed for each scenario in order to generate the model with the best fit of R^2 and the relative weight of the variables in correspondence with the experimental findings in the metal dusting and high-temperature corrosion domains.

II.4 Summary

This chapter gathers the experimental protocols of the studies used as reference in the framework of modeling in the SCAPAC project. The process of construction of the databases has been explained, as well as the inputs and outputs considered in statistical analysis. The statistical approaches applied for modeling were also described. These techniques do not admit missing values in their analyses. Therefore, there is a group of variables that play an important role in the corrosion mechanisms, which were not considered in the statistical treatment, due to lack of information. Since the addition of null values instead of missing data can add significant error sources to the statistical analysis, missing values on the modeling parameters impedes their incorporation in statistical treatment.

In the case of metal dusting, few studies in the reviewed literature report explicit values of parameters such as, gas velocity, surface finish and grain size. Likewise, in high-temperature corrosion, the gas velocity and the ash melting temperatures are generally not reported in most of the studies that were included in the database. An artifice created to estimate the ash melting temperatures will be explained further below.

Chapter 3. Modeling of metal dusting corrosion rate

Contents

III Chapter 3. Modeling of metal dusting corrosion rate

In this chapter, we begin with a discussion of the experimental results about metal dusting kinetics obtained from A. Fabas's thesis [125] and Air Liquide research laboratory in the SCAPAC project. This is followed by the statistical treatment of the data contained in the database that come from experimental tests of the SCAPAC project and literature results. Lastly, the variable selection procedure and lifetime modeling results are presented.

III.1 Experimental results

Metal dusting kinetics was measured by mass loss and pit depth growth. Figure III.1 and Figure III.2 show the mass loss kinetics of the different alloys evaluated under isothermal conditions at 1bar and 21bar respectively, both tests were performed at the same temperature (570°C) and different gas compositions resulting in the same a_C (32). The gas compositions are indicated in the Section II.1.1 (Table II.1 and Table II.2)

Figure III.1 shows the mass loss kinetics at 1bar (47%CO-47%H_2-5.5%H_2O-pO_2 = $2.1\text{x}10^{-27}$-a_C = 32 – T=570°C). We can observe that both incubation times and mass loss rates vary depending on the type of alloy. The mass loss rates can be considered as a constant after the incubation time. As all samples were tested in the same conditions, in terms of reproducibility, it is observed that HR120 presents the same mass loss rates for different samples. However, this behavior may change, in the case of alloys Khantal and 800HT, because different samples of the same material showed mass loss rates significantly different. This could be attributed to the different location of the samples in the sample holder with respect to gas exposure during the test. Also these differences could be due to the fact that mass loss measurements suffer from a lack of reproducibility.

Under the same conditions these differences are attributed to the effect of the alloying elements on the alloy resistance. The higher mass loss rate corresponds to Crofer, the only Fe-based alloy that was evaluated, followed by Fe/Ni based high-temperature alloys (HR120, 800HT) and Khantal (FeCrAl) with similar behavior. In the last place, Ni-based alloys and one of the 800HT sample were the most resistant to the atmosphere conditions. This result corresponds with expectations because even when Crofer has a high chromium content, the protective capacity of chromium lies in its ability to form a protective oxide layer.[163] Previous experiments at Argonne National Laboratory have shown that high Fe-contents in the alloy lead to the formation of Cr, Fe spinels when Cr is present, which are not as protective against metal dusting as chromia layers.[164]

Figure III.2 shows the mass loss kinetics at 21bar (1.6%CH_4-13%CO-3.1%CO_2-49%H_2-33%H_2O - pO_2 = $7.1\text{x}10^{-26}$ - a_C = 33 –T=570°C). The mass loss rates are significantly higher than that at 1bar and the incubation periods are shorter than that at 1 bar, except for Inconel 625, which shows a very good resistance, remaining in the incubation period after 14000 hours. As all samples were tested in the same conditions, the reproducibility of the experiments can be discussed. Different samples of the same material showed similar mass loss rates, which indicate better reproducibility of results in high pressure tests than under atmospheric pressure. Regard to material performance, the alloys presented a similar ranking than that at 1bar: Fe/Ni based high-temperature alloys (HR120, 800HT) are less resistant than Ni-based alloys.

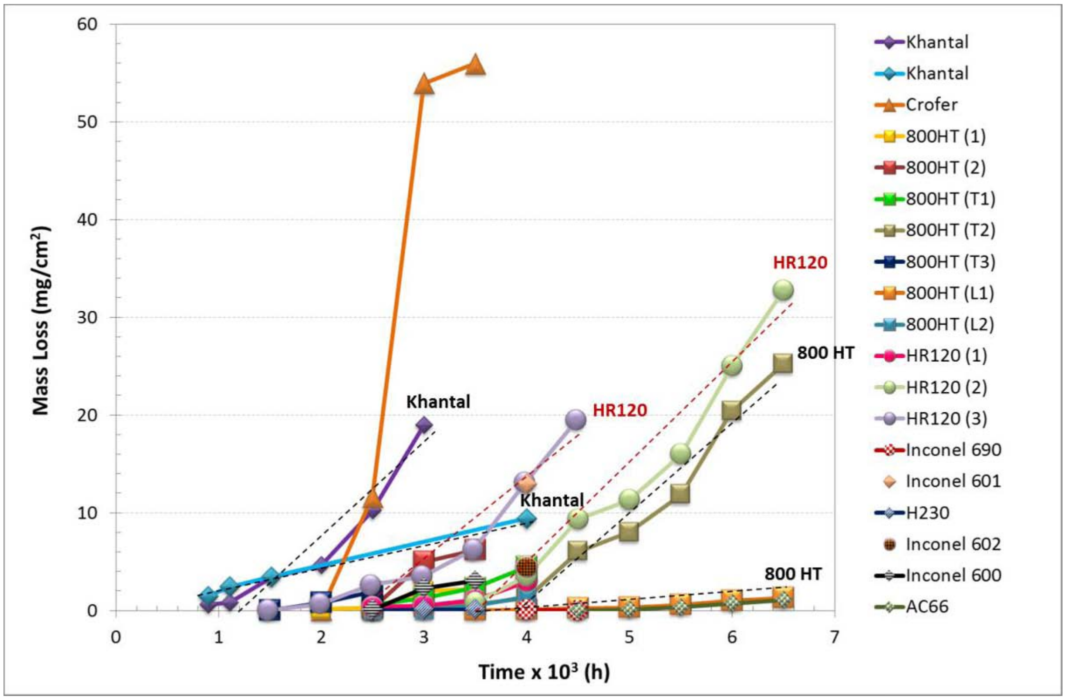

Figure III.1. Mass loss kinetics of alloys tested at atmospheric pressure conditions (1bar)

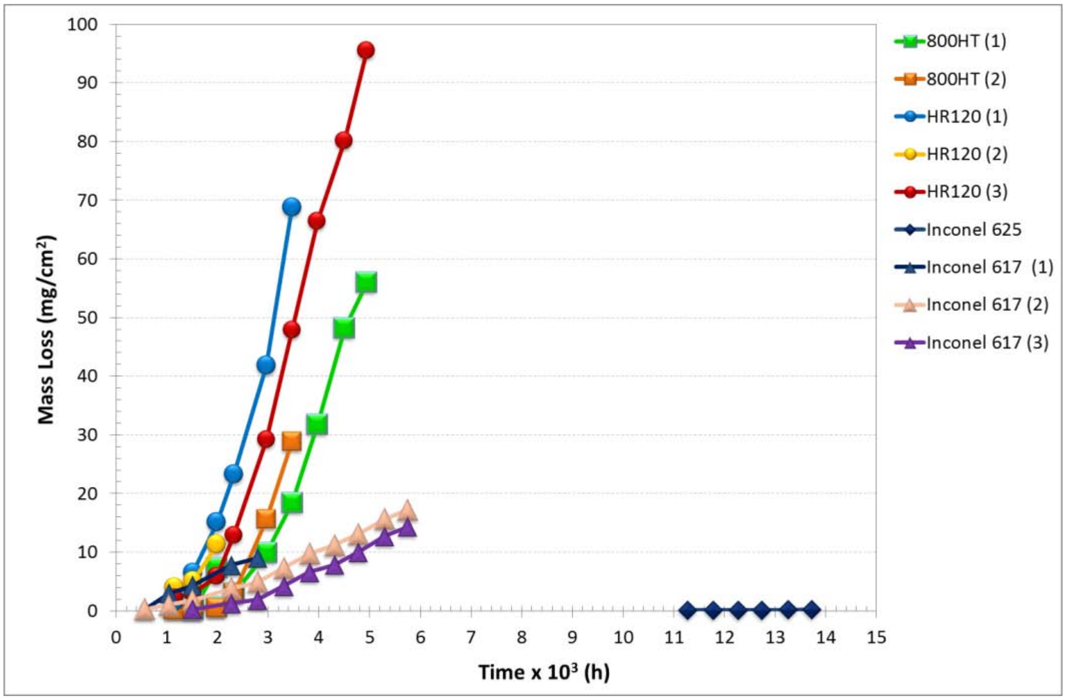

Figure III.2. Mass loss kinetics of alloys tested under high pressure conditions (21bar)

Correlation tests were performed by using the corrosion kinetics. Figure III.3 shows the linear correlation coefficients (r) between the mass loss rates (MLr) and the alloying elements that presented more than four different compositions. As can be seen from the chart, alloys with higher Ni/Fe ratio show increased metal dusting resistances. However, the protective effect of chromium in both conditions is not obvious. The effect of Al and Si cannot be seen, it might be biased by the influence of the major elements at 1bar and their low variability at 21 bars. Therefore, the coefficients are not reliable and it is difficult to compare them with experimental findings. The dominant effect of the Fe/Ni ratio is consistent with the major role of the matrix.

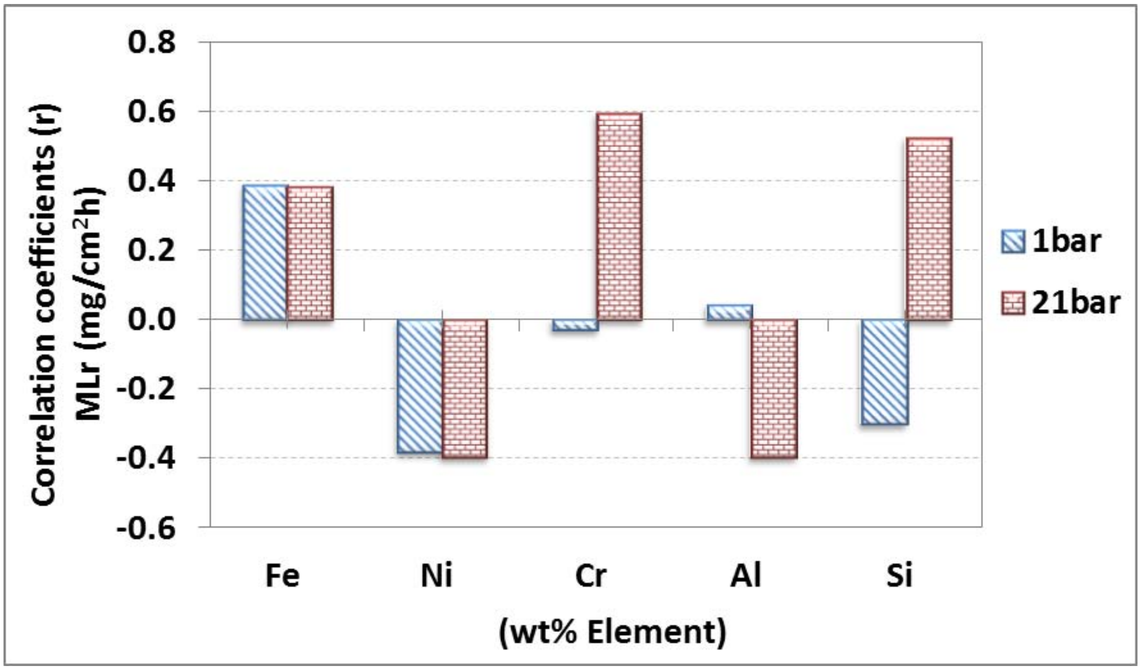

Figure III.3. Correlation coefficients (r) for MLr as a function of the alloying elements (1bar - 21bar)

In Figure III.4a, the diagram shows no correlation (r = 0.02) between MLr and Cr-content at 1bar. This is because there are Fe-based alloys and Ni-alloys in the same analysis. Between two Ni-based alloys (600, 690) increasing the Cr-content decreases MLr. However, the peak of MLr which corresponds to Crofer (Fe-based alloy) alters the expected tendency of the analysis. Even when the Cr-content in Crofer is high enough, the Fe-matrix does not have the same protective properties as the Ni-matrix. The same effect is observed between HR120 (Fe/Ni-based alloy) and 617 (Ni-based alloy). The protective effect of chromium is overlapped by the matrix effect. Therefore, the Cr-effect should be evaluated only among alloys with the same matrix.

At 21 bars, Figure III.4b, shows a high correlation (r = 0.6) between MLr and Cr. However, there are only four alloys and the variability of the Cr-content is not continuous, as the alloy HR120 acts as an outlier. Therefore, there is not enough data for the correlation analysis to be valid.

These correlations are consistent with numerous studies that have shown that the Ni/Fe ratio is a key parameter for metal dusting resistance. Fe-based and Ni-based alloys show different mechanism of reactions.[6–8,13–15,24,129] Changing composition within the austenite phase modifies the rate of graphite deposition.[15,165] Therefore, to study the effect of alloying elements on the corrosion rate in further treatment, it becomes pertinent to classify the alloys by type of matrix: ferritic, austenitic Fe/Ni-based and austenitic Ni-based, in order to avoid a biased effect of the major elements on corrosion rates.

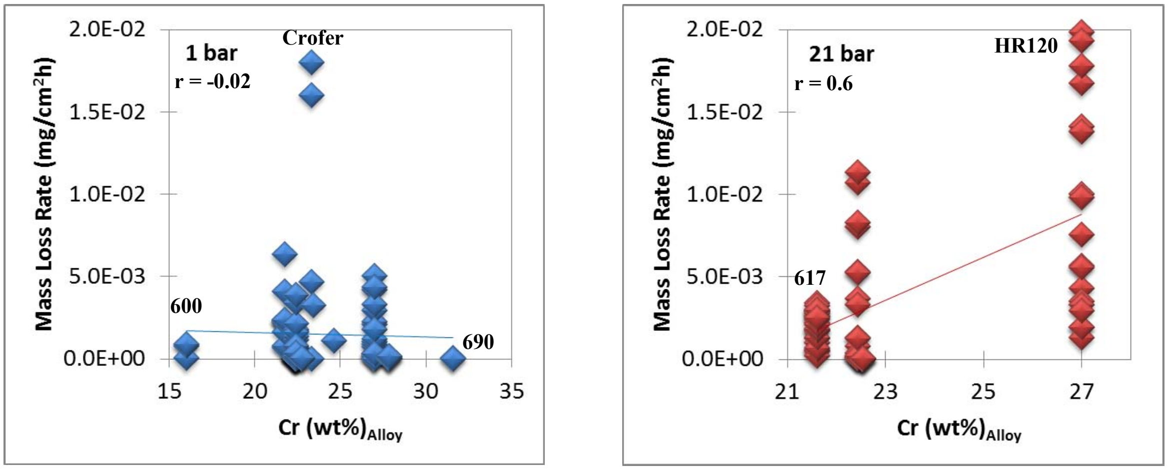

a) b)

Figure III.4. Correlation tests for mass loss rates as function of Cr-contents a) 1bar b) 21 bar

Figure III.5 shows the cross section of the pit characterized in 800HT at a) 1bar and b) 21bar by Fabas.[125] Pits characterization consisted of tracking the pit diameter and the pit depth evolution during the tests of those pits located away from the sample edges. [127] At atmospheric pressure, pits presented a flattened and irregular morphology. This leads to large standard deviations in measurements, and hence, a not reproducible pit depth quantification. In contrast, at high pressures pits presented a circular geometry in surface and spherical cap morphology in depth, and hence, pit depth growth measurement was reproducible. It was found that the pit depth is about the fifth (1/5) of the pit diameter.

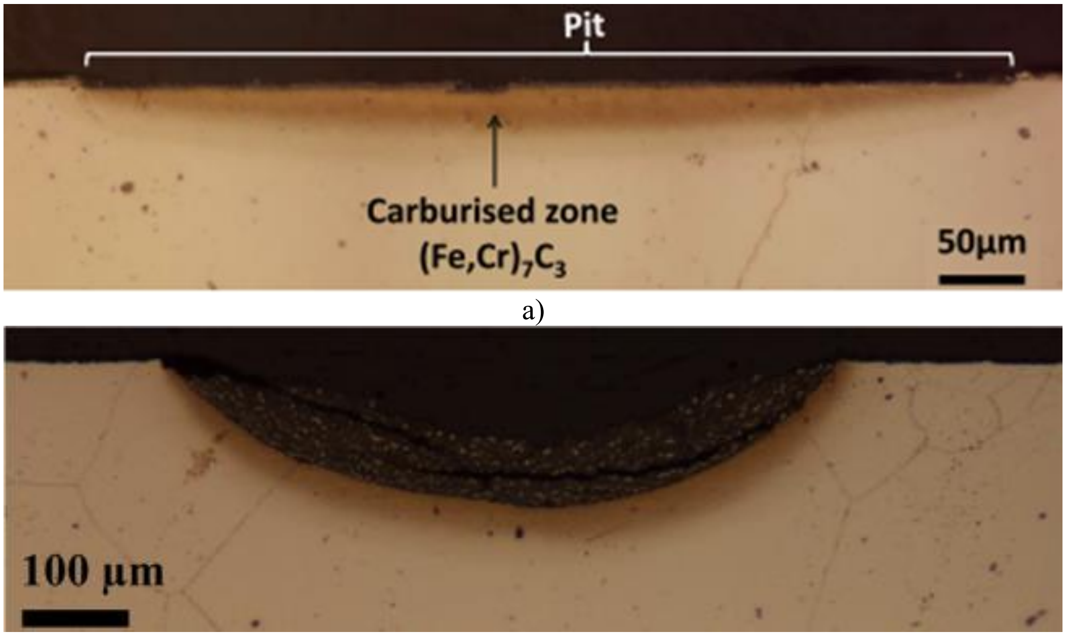

a)

b)

Figure III.5. Cross section of etched 800HT a) after 4000 h of exposure at 1 bar. b) after 1987 h of exposure at 21 bar. [127]

Figure III.6 shows the pit depth measurements made in the alloy 800HT tested at 21bars. It can be observed that different pits can show different incubation periods but the pit depth growth rate remains constant after the incubation period. Pits nucleation zones might depend on the stability of the protective oxide layer in determined areas on the alloy surface. Hence, the incubation periods will end once in the zones this stability is interrupted. The processes of heating and cooling at every cycle of the tests can affect the stability of the protective layers, creating local defects in the oxide layers. As soon as these local defects are created they can act as nucleation zones for nucleation and growing of pits. Once the pits begin to grow, the ability of regeneration of the oxide layers is limited, which produce continuous growth at constant rate.

Regarding the material performance, Figure III.7 shows the pit depth growth of HR120 and 800HT from different samples. Both alloys present similar incubation times, this might be because both alloys have Fe/Ni-based austenitic matrix. Both alloys also presented a similar behavior in the pit depth growing regime, even when HR120 has higher contents of Ni, Cr, Mo and other elements, which confirms that once the pits nucleate the protective capacity of the alloy is limited.

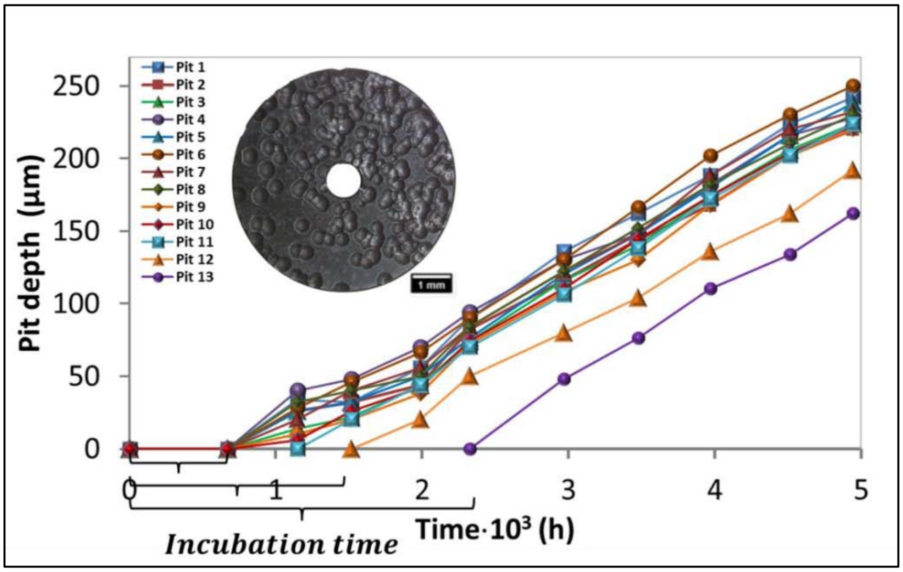

Figure III.6. Pit depth measurements on the alloy 800HT at 21 bars.[125]

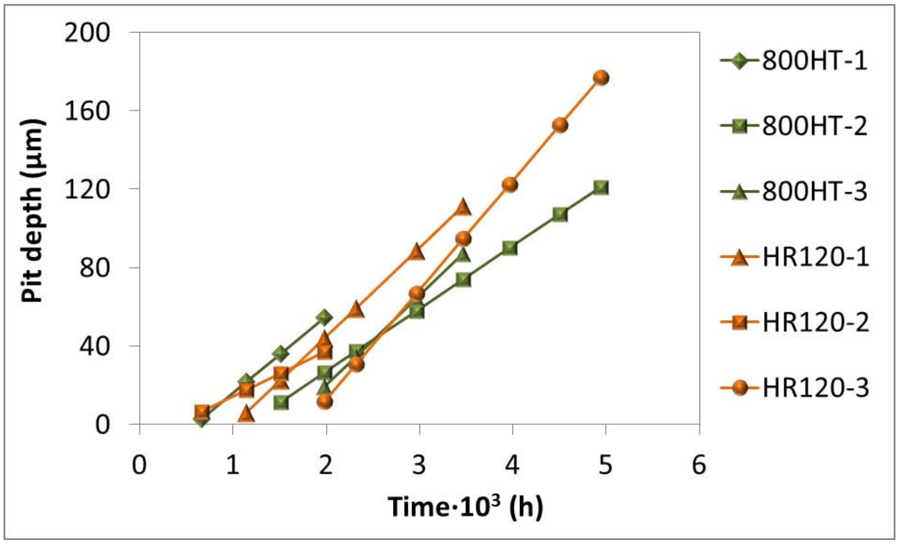

Figure III.7. Pit depth growth as a function of time on the 800HT and HR120 at 21 bars.[125]

After analyzing the kinetics of experimental results from the SCAPAC project, these were included in the database to be integrated with literature data for further statistical treatment.

III.2 Raw database

Around 130 metallic materials were added to the database, including pure metals, binary alloys, coatings, ternary model alloys and commercial alloys. Figure II.8 shows a 3D diagram with the different materials added to the database located in the diagram as a function of their main elements.

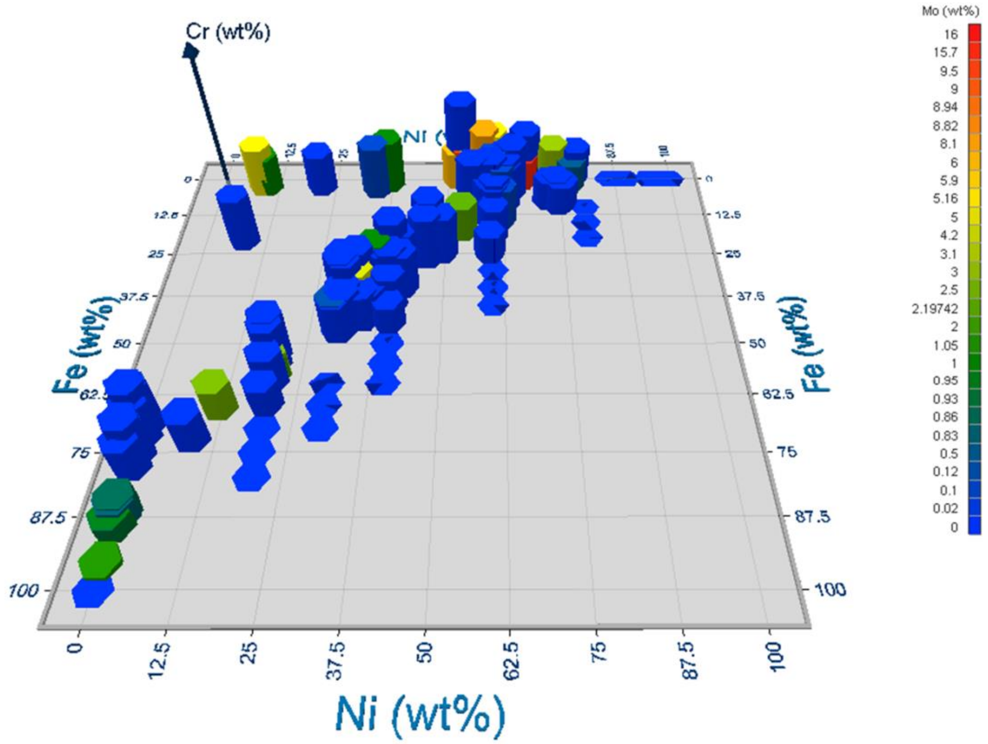

Figure III.8. 3D diagram with the composition of the different materials added to the database.

Figure III.9 is showing the box plot applied to the chemical composition of the materials included in the database. The box plot identifies the variance of the data distribution and its outliers. In the case of the main elements, the composition range of Fe is wider than that of Ni. In both sets of data pure Fe and pure Ni are outliers in the data distribution (a,b). In order to avoid a source of errors or disturbance in the calculations generated by uncommon alloy systems, pure metals were eliminated of the materials domain, only commercial and model alloys were selected for statistical analysis. The outliers on the other elements are atypical cases in the materials population that will be analyzed later (blue circles), according to their effect on the dependent variables to be modeled. In the box plot, the outliers are described as follows:

a. Fe-outliers
b. Ni-outliers
c. Cr-outliers belong to Cr-rich coatings.
d. Co-outlier belongs to Co-based alloys, which are uncommon among the materials of the database.
e. Cu-outlier belongs to the Monel alloy.
f. Al-outliers belong to a NiAl model alloys.

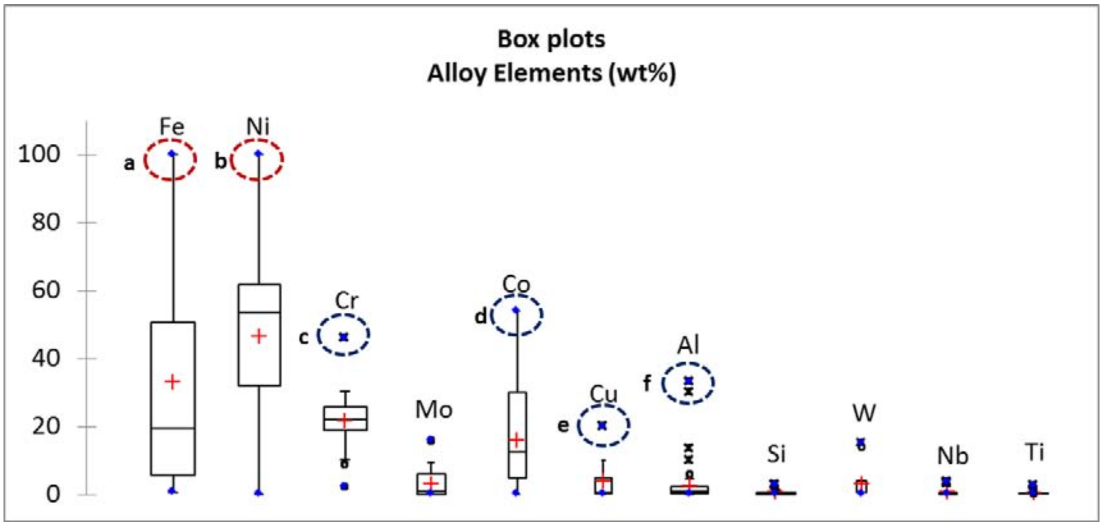

Figure III.9. Box plot applied to the chemical composition of the materials added to the database.

III.3 Statistical modeling

In the SCAPAC project, 14 materials and two different atmosphere conditions were evaluated. To achieve the objective of this study of creating a lifetime prediction model for materials in a wide range of conditions, approximately 400 data with sufficient variability of conditions would be required. In our case the amount of data was insufficient. In order to create a model by linear regression that estimates the relative weight of the variables involved on the corrosion rates, the experimental results obtained in this study were unified with the literature results included in a metal dusting database which construction was explained in the section II.1.2 of this document.

After quantifying the different dependent variables to be modeled in section II.1.2.2, four dependent variables were chosen for modeling (Table III.1) to create a multiple linear regression equations. Mass Loss rate (MLr), Pit depth growth rate (PDGr), Mass Loss rate after the incubation period (AIMLr) and Incubation times (IT) are the dependent variables ($\boldsymbol{Y_i}$), which are explained by two groups of independent variables ($\boldsymbol{X_i}$) : atmosphere conditions and alloy composition, as indicated in Table III.1. Figure III.10 shows the structure of the model equation, which is composed of the most important variables from both groups, for the corrosion process. The variables of the equation were chosen according to statistical results and the analysis of experimental findings.

Table III.1. Dependent variables to be modeled and explanatory variables by group.

$\boldsymbol{Y_i}$	*Group*	$\boldsymbol{X_i}$
MLr (mg/cm² h)[a]	Atmosphere conditions	Frequency (1/h), 1/$T_{Metal(K)}$, a_C $p_{Internal}$, pCO, pH_2O, pH_2,pCO_2, pO_2 (bar)
AIMLr (mg/cm² h)[b]		
IT (h)[c]	Alloy composition	Fe, Ni, Cr, Mo, Co, Cu, Al, Si, W, Nb, Ti (wt%)
PDGr (µm/h)[d]		

[a] Mass Loss rate (MLr), [b] Mass Loss rate after the incubation period (AIMLr), [c] Incubation times (IT) [d] Pit depth growth rate (PDGr).

$$\overbrace{Y_i}^{\substack{\text{Output variable}\\ \textbf{Corrosion Rate}}} = \underbrace{\beta_0}_{\text{Intercept}} + \underbrace{\underbrace{\beta_1 X_1 + \beta_2 X_2}_{\text{Atmosphere}} + \dots + \underbrace{\beta_p X_p + \beta_p X_p}_{\text{Alloys}}}_{\text{Input variables}} + \underbrace{\varepsilon_i}_{\text{Residuals}}$$

Figure III.10. Structure of the multiple linear regression equation for metal dusting kinetics models.

III.3.1 Data filtering and variables selection

III.3.1.1 Mass Loss rate (MLr)

To model the mass loss rate (MLr) as the dependent variable, the mass loss rates measured from 13 different studies were analyzed by statistical methods. Figure III.11 shows the mass loss measured as a function of time on 110 materials submitted to different atmosphere conditions in 192 laboratory tests[13,18,22,29,127,129,130,132–137]. Approximately 1389 mass loss rates were calculated which are explained by two groups of variables (Table III.1): atmosphere conditions and alloy composition.

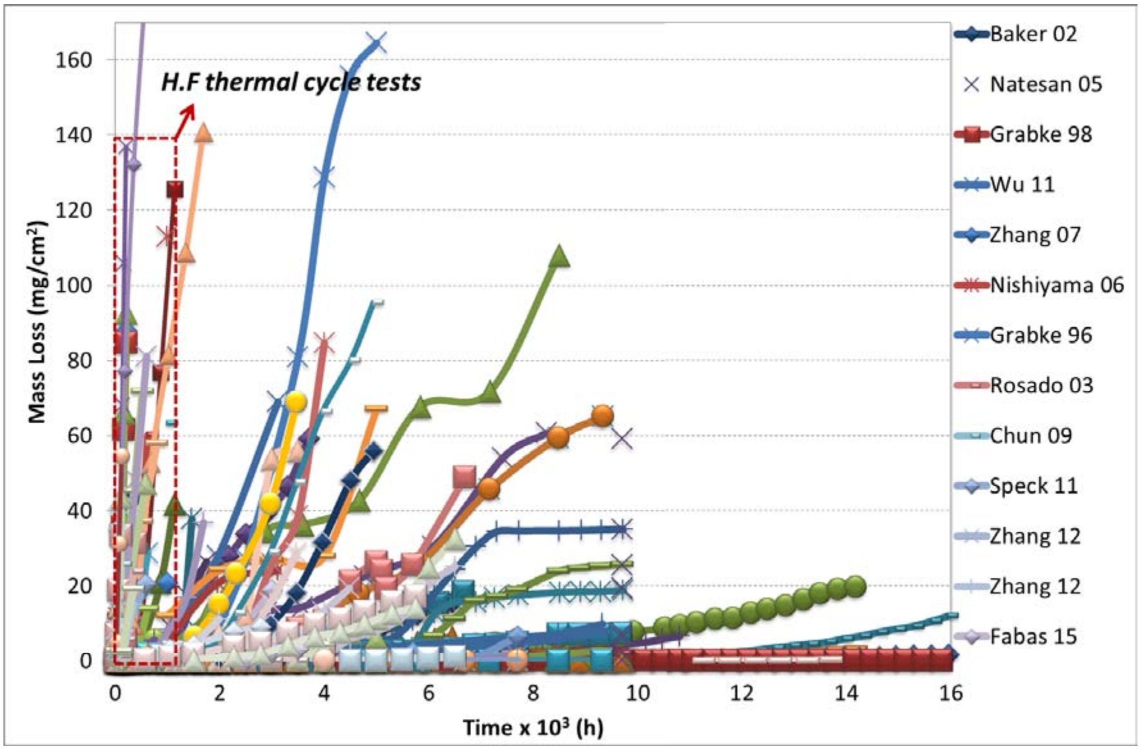

Figure III.11. Mass loss as a function of time measured from 192 laboratory tests in 13 studies.[13,18,22,29,127,129,130,132–137]

Data filtering can refer to a wide range of strategies or solutions for refining data sets. This means that the data sets are refined depending on what a user (or set of users) needs, without including other data that can be repetitive, irrelevant or even sensitive. In order to find patterns and correlations between the independent variables that explain the mass loss rates (MLr), a first exploratory analysis was performed using Principal Component Analysis (PCA) and Correlations Tests (CT) in the original data set.

III.3.1.1.1 Principal Component Analysis and Correlation Tests

III.3.1.1.1.1 Atmosphere conditions

Figure III.12 shows the PCA_1 applied on the group of independent variables corresponding to the atmosphere conditions of the test. In the analysis, the mass loss rate (MLr) was set as a supplementary variable in order to determine the linear correlation coefficients (r) between corrosion rates and independent variables in the initial data set. Correlations in bold indicate that p-values associated with regression coefficients are inferior to 0.05, which means that correlations are statistically significant. PCA_1 correlation matrix is given in Appendix I.A

The PCA_1 score plot shows that 77% of the variance is explained by principal components analysis F1 and F2 applied to atmosphere conditions and may be interpreted in the following manner:

1.1 We can clearly see that the principal component axis F1 and F2 are attributed to the partial pressures of the test and those related with carbon activity of the atmosphere, respectively. Partial pressures of different gases were considered as one family in axis F1, they are highly correlated among them because they all depend on the internal pressure of the system, as the data distribution presents three different pressure levels (Figure III.13.a). This hampers to see the relation between the composition of the different gases and their effect on the corrosion rate. Therefore the correlations between corrosion rates and partial pressures are not consistent.

1.2 The second family considered in axis F2 is a_C, 1/T and pO_2, this result corresponds with expectations since it is well known that a_C is inversely proportional to the temperature and the oxygen partial pressure in the gas. Regarding to their correlations with the corrosion rate (MLr) which is in axis F4 not shown in the diagram, it can be seen that the temperature shows the higher effect on MLr. The correlations with pO_2 and a_C are low and not statistically significant. Furthermore, they are not consistent with theoretical findings.

1.3 The frequency is also found in axis F1, even when it is not related to any variable of the atmosphere. Its effect on the corrosion rate is the highest of all. This is consistent with the fact that cyclic tests are more aggressive than isothermal tests.

Conclusion: in order to emphasize in the effect of atmosphere variables on the corrosion rates a filtering procedure was performed through correlation test analysis. The results will be shown below.

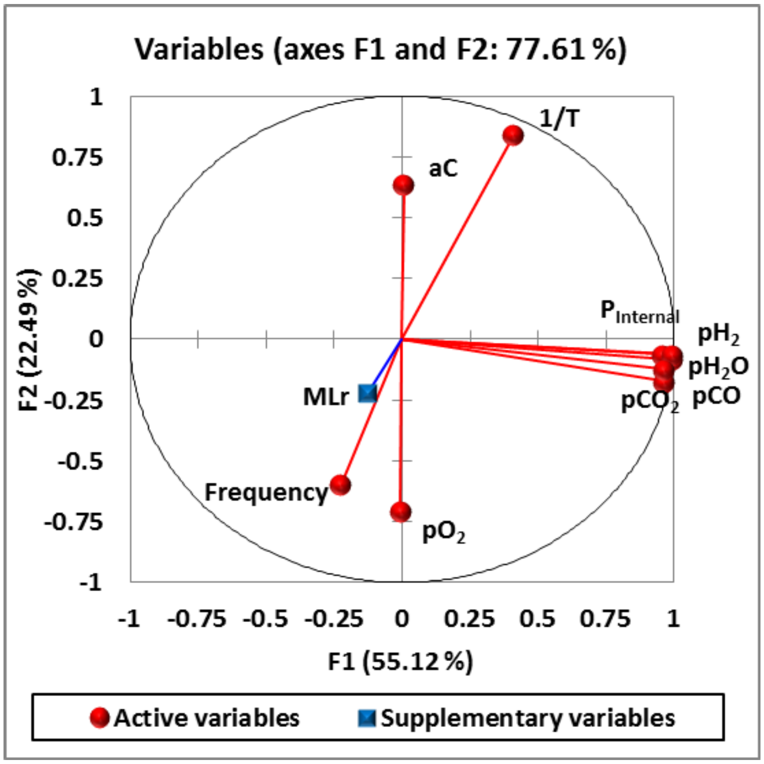

Correlations (r)

Variables	MLr (mg/cm^2h)
Frequency (1/h)	**0.29**
1/T (K^{-1})	**-0.22**
$P_{Internal}$ (bar)	**-0.10**
pH_2O (bar)	**-0.09**
pCO (bar)	**-0.07**
pH_2 (bar)	**-0.10**
pCO_2(bar)	**-0.12**
a_C	-0.02
pO_2 (bar)	**0.16**

Values in bold are different from 0 with a significance level α = 0.05

Figure III.12. PCA$_1$ applied to the group of variables: atmosphere conditions.

Correlation tests were applied in order to establish the criteria for filtering treatment. This statistical method allowed us to visualize the linear correlation coefficients (r) obtained in the PCA$_1$ and to identify the outlier's location and analyze its effect in the corrosion behavior. After filtering, the new correlation coefficients (r) regarding corrosion rates are shown further below in the PCA$_2$. In the following diagrams, red data indicate positive correlations and blue data indicate negative correlations. The test correlation matrix of the initial data distribution is indicated in Appendix I.A and the test correlation matrix of the filtered data distribution is indicated in Appendix I.B.

The correlation tests shown in Figure III.13 were applied to the partial pressures of the system which is the family of variables found in the first component F1 in PCA$_1$. In the diagram *III.13a* we can see that the variable P$_{Internal}$ shows low variability with only 3 values, and a discontinuous distribution. Most results belong to tests performed under atmospheric pressure (1bar). Tests performed at high pressures act as outliers in the P$_{Internal}$ data distribution as well as in the pCO, pH$_2$, pH$_2$O, pCO$_2$ data distributions. Moreover, these results do not correspond with the experimental findings of the SCAPAC project, which showed that materials under high pressures develop higher corrosion rates. This result is due to the high variability of materials and gas compositions present on the data at atmospheric pressure, which makes difficult to compare all the gas compositions at 1bar with the few existing data at 15bar to 25bar in the database.

In order to avoid disturbances in the adjustment by linear regression, the few data at high pressures were eliminated from the main domain; as a result the model is now limited to assess the variables under atmospheric pressure (1bar). Figure III.14 shows the new data distribution regarding the system partial pressures after the filtering process. We can clearly see that the elimination of outliers at high pressures reveals a continuous variability for pCO, pH$_2$ and pH$_2$O, whereas, pCO$_2$ shows a low variability. Due to the lack of data in pCO_2, this variable is unsuitable to be included in the model. Correlation between pCO and corrosion rates became slightly positive and inversely proportional to pH_2 as it might be expected, because most metal dusting tests are performed under CO-H_2 mixtures with low amounts of H_2O, and hence, this creates correlations between both gas compositions.

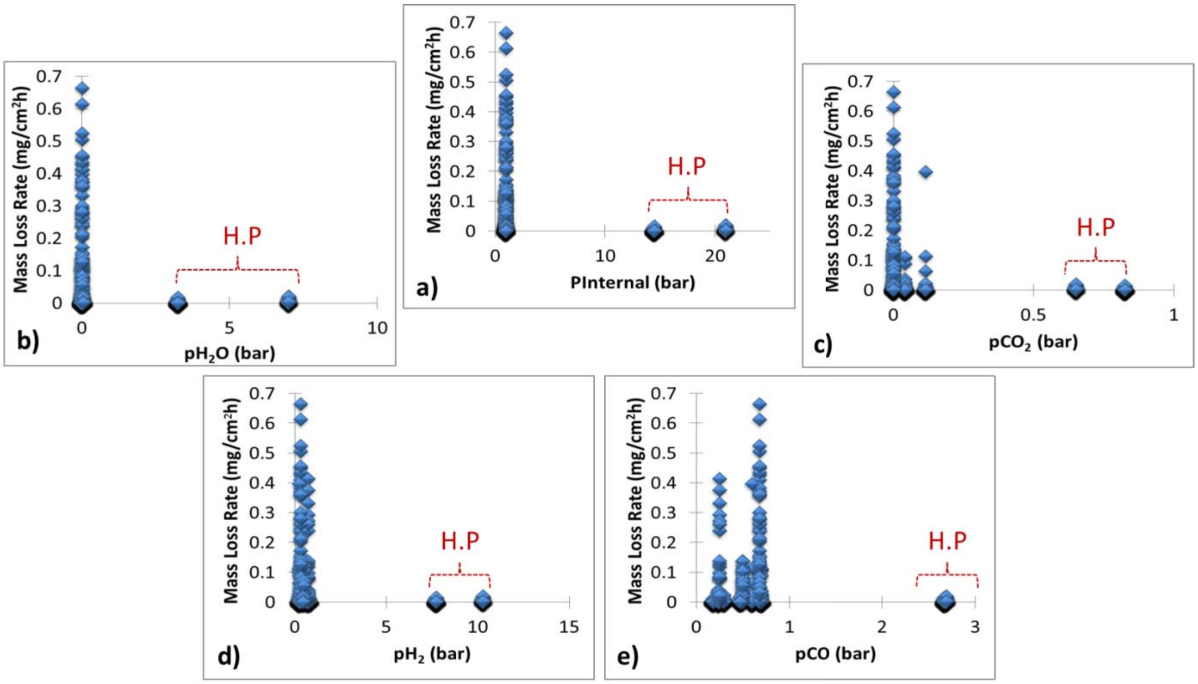

Figure III.13. Correlation tests applied to gas pressures variables: $P_{Internal}$, pCO, pH_2, pH_2O,and pCO_2. CT_1 and PCA_1 correlation matrix is given in Appendix I.A

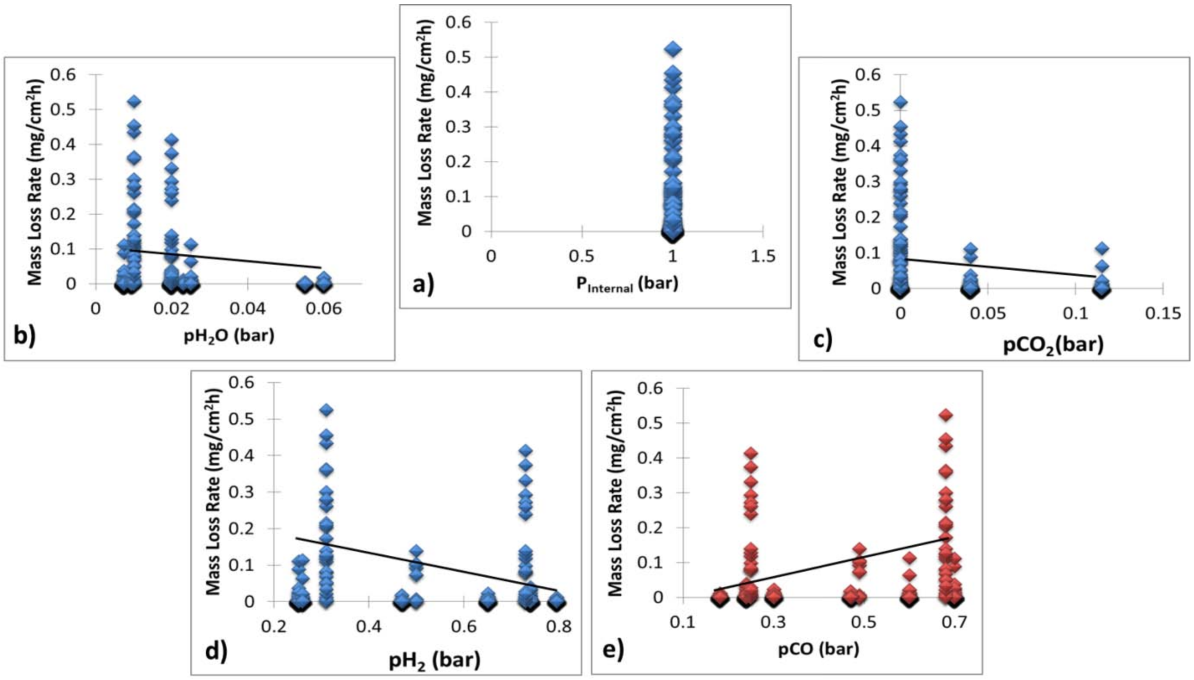

Figure III.14. Correlation tests applied to gas pressures variables: $P_{Internal}$, pCO, pH_2, pH_2O, pCO_2 after filtering procedure. CT_2 and PCA_2 correlation matrix is given in Appendix I.B

The same filtering procedure was applied to the a_C whereby data distributions in 1/T and pO_2 were also affected for being closely related. Figure III.15a shows the correlation tests applied to corrosion rates as a function of $1/T(K^{-1})$, this data distribution corresponds with the findings of Chun et al. [10,24] who showed that corrosion rates follow three regimes as a function of the temperature (in a bell shape).

In the diagram *III.15a* corrosion rates are very small at low temperatures (400°C). This point corresponds with the highest carbon activity found in diagram *III.15b* (a_C = 9904), but also with the lowest kinetics of reaction and solid state diffusion which follows the Arrhenius law. Next, there is a lack of data between 400°C and 570°C, then corrosion rates increase up to a maximum around 680°C, above this temperature corrosion rates start to decrease. After 700°C there is no data, but it is well known by experimental finding that above 720°C the a_C is <1 and metal dusting rates become very low. [10,24] The data at low temperature (400°C) and high carbon activity (a_C = 9904) represent outliers in the data distributions, which generates untrue linear regressions. The diagram *III.15c* shows that the a_C outlier has no visible effect in the pO_2 distribution. The diagram *III.15d* shows that thermodynamic correlation between a_C and 1/T (K^{-1}) is also biased by the outlier in a_C. In order to avoid disturbances in the adjustments by linear regression for the variables a_C and 1/T, the few data belonging to the a_C-outlier which is the same to the 1/T-outlier were eliminated from the main domain, limiting the model to the temperature range between 570°C and 700°C and the a_C-range between 6 and 104.

Figure III.16a, Figure III.16b and Figure III.16c show the new data distribution after the filtering process regarding 1/T, a_C and pO_2, respectively. The new correlation coefficients regarding the corrosion rates are indicated in PCA_3 (Figure III.18).The elimination of outliers exposes a continuous variability for 1/T and a_C. The diagram *III.16d* shows the expected thermodynamic correlation between a_C and temperature. In the case of the temperature, corrosion rates increase to a maximum value that is shifted to 650°C. Above this temperature corrosion rates start to decline. In the case of a_C, corrosion rates vary also nonlinearly with a_C which explains its low linear regression coefficient, even after removing the a_C-outlier (Figure III.16b). In the case of pO_2, corrosion rates might be expected to be retarded with increasing oxygen partial pressure. The diagram *III.16c* shows lower corrosion rates at higher pO_2. However there is insufficient data at high pO_2 to confirm this trend. In fact, the correlation coefficient shows no linear relation between corrosion rates and pO_2.

A correlation tests was also applied to corrosion rates as a function of the thermal cycle frequency, as shown in Figure III.17a. It is well known that high frequency tests might produce more damage than low frequency and isothermal tests, due to the numerous heating/cooling cycles over short periods of time and their associated thermal stresses. This can be verified in the Figure III.11 where high frequency thermal cycle tests develop higher corrosion rates without incubation times. The correlation test shows that thermal cycle tests at high frequency act as outliers in the data distribution. This means that given the case where the same materials are evaluated under similar conditions at different thermal cycling conditions, serious variations in the corrosion rates can be generated. Therefore both types of test should not be analyzed together. In order to avoid disturbances in the adjustments by linear regression caused by two types of tests, the high frequency cyclic tests (1 hour cycle and 45 min cycle) were eliminated from the main domain. As a result the model is limited to assess the variables for low frequency thermal cycle tests, and isothermal tests (Figure III.17b).

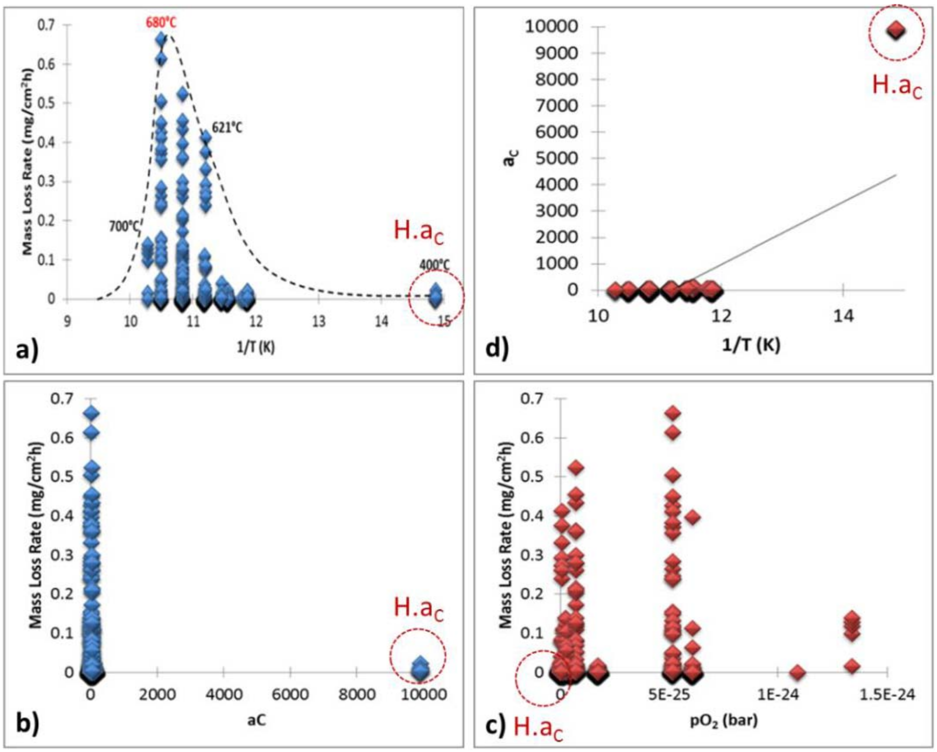

Figure III.15. Correlation tests applied to 1/T (K), a_C and pO_2 (bar). CT_1 and PCA_1 correlation matrix is given in Appendix I.A

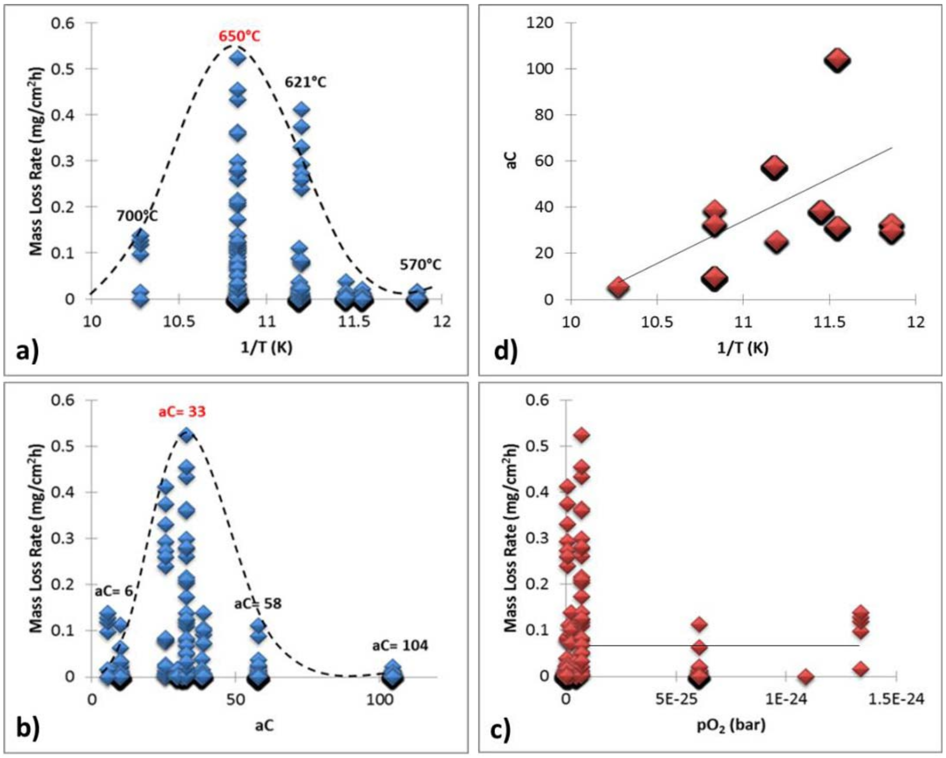

Figure III.16. Correlation tests applied to 1/T (K), a_C and pO_2 (bar) after filtering. CT_2 and PCA_2 correlation matrix is given in Appendix I.B

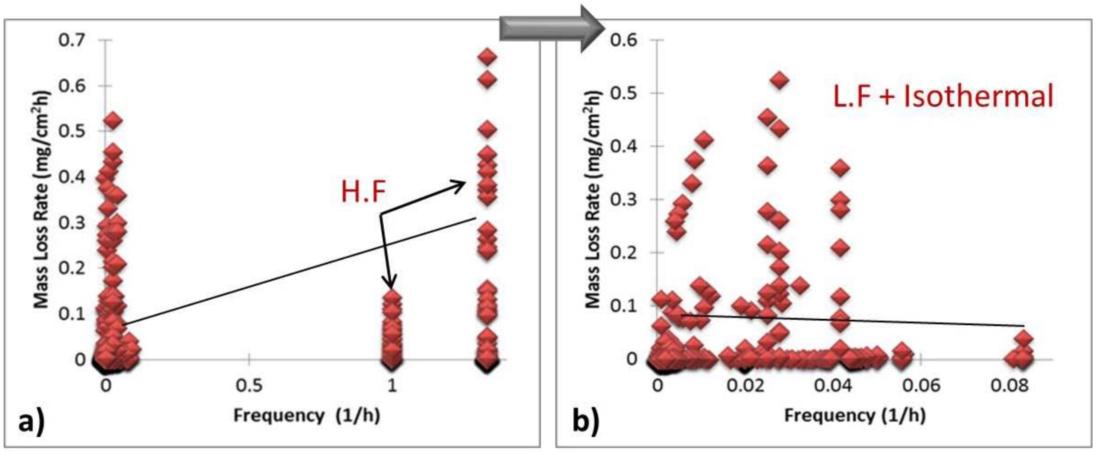

Figure III.17. Correlation tests applied to test Frequency (1/h). a) Before filtering (Appendix I.A) b) After filtering (Appendix I.B) High frequency tests (H.F) Low frequency tests (H.F)

After filtering, the exclusion of high pressures, high carbon activities and high frequency thermal cycle tests from the main domain, allowed us to reveal new correlations among the atmosphere conditions and their effect on the corrosion rate through PCA_2. Figure III.18 shows the score plot for PCA_2 applied to atmosphere conditions at atmospheric pressure. The correlation matrix is given in Appendix I.B. The PCA_2 score plot shows 64% of the variance explained by principal components analysis F1 and F2 and may be interpreted in the following manner:

2.1 The principal component axis F1 is attributed to the temperature (1/T), and to the partial pressures of CO_2, and reducing gases such as pH_2, pCO. However, (1/T) is not correlated with any of the gas partial pressures, even when they are in the same principal component F1. The oxidant gas pH_2O is found in F3 not seen in the diagram; it is not correlated with the pH_2, pCO and pCO_2. None of the partial pressures of the gases keeps statistically significant correlations with the corrosion rate (p-values > 0.05).

2.2 The correlation between pCO and corrosion rates became slightly positive, but they are still not statistically significant. Experimental findings of Grabke et al. [25] showed that carbon deposition increases with pCO and pH_2 and decreases with pH_2O. However the relation between carbon deposition and metal wastage rate might not be proportional in some systems, which might explain why the correlation coefficients between corrosion rates and the gas partial pressures are low.

2.3 The second family considered in axis F2 is a_C and pO_2, which corresponds with expectations since it is well known that a_C is inversely proportional to the oxygen partial pressure in the gas. However both variables shows no effect on the corrosion rate

2.4 The frequency is shifted to the axis F4, the influence on corrosion rates decreases but it is still positive, due to the damaging effect of thermal cycling in the protective layers of the material. However, since the modeling domain was limited to low frequency thermal cycle tests and isothermal tests; this variable is no longer considered.

When we analyze correlations between independent variables (see Appendix I.C), we can clearly see that pCO is inversely proportional to pH_2 (diametrically opposed) ($r = -0.99$). This is because most experiments are performed in H_2-CO mixtures with low amount of H_2O and CO_2 or even CH_4, and most of the time without Argon dilution, and hence, pH_2 and pCO are often-times inversely proportional.

Due to the high collinearity between pCO and pH_2, these variables cannot be used independently in the model. However, this result is consistent with the observation by Muller-Lorenz et al. [23] which showed that for iron base alloys, at temperatures higher than 540°C the cementite decomposition becomes faster than some other processes with a lower activation energy. Through experiments at 650°C with different partial pressures this process is dependent on pCO and pH_2 and independent on pH_2O. The maximum rate was observed at $CO/H_2 = 1{:}1$ which indicates that the metal wastage rate in the high-temperature range is proportional to the product pCO x pH_2. Chun et al.[10] performed the same experiment in pure iron at 550°C and found that the corrosion rate goes through a maximum, which also occurs at the $CO/H_2 = 1{:}1$ composition. If we consider that our temperature range goes from 570°C to 700°C, after applying the same approach of the previous authors [10,23] to our data distribution, the correlations between corrosion rates and pCO (Figure III.19a) and pH_2 (Figure III.19b) became pCO x pH_2 (Figure III.19c). The new variable pCO x pH_2 showed higher correlation than the individual variables as well as it became statistically significant (p-values < 0.05).

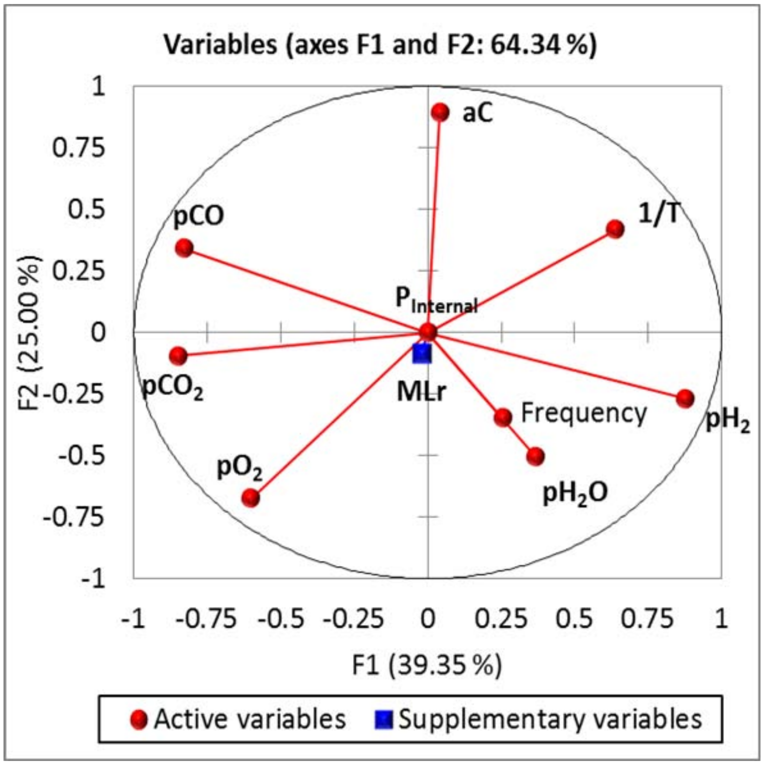

Correlations (r)

Variables	**MLr (mg/cm^2h)**
Frequency (1/h)	**0.17**
1/T (K^{-1})	**-0.19**
pH_2O (bar)	-0.07
pCO (bar)	0.05
pH_2 (bar)	-0.02
pCO_2(bar)	-0.14
a_C	**-0.09**
pO_2 (bar)	**0.03**
$pCOxpH_2$	**0.20**

Values in bold are different from 0 with a significance level α = 0.05

Figure III.18. PCA_2 applied to the group of variables: atmosphere conditions (after filtering)

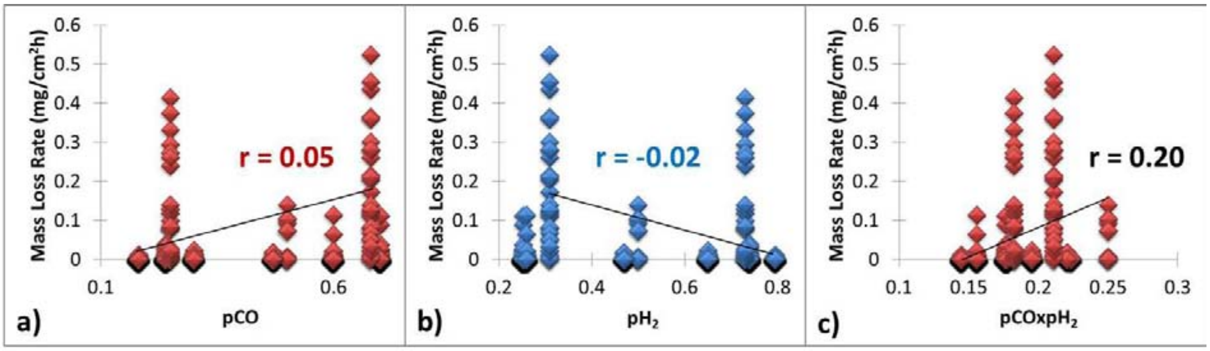

Figure III.19. Correlation tests: conversion of the variables pCO and pH_2 into (pCO x pH_2)

Conclusion: according to statistical results concerning the atmosphere conditions, the parameters that should be taken into account for modeling are: 1/T and (pCO x pH_2). However, this could vary according to the alloy domain and the adjustment to be needed, which will be discussed below.

III.3.1.1.1.2 Alloy composition

Figure III.20 shows a 3D diagram of the initial materials domain as a function of the main elements (Fe-Ni-Cr-Mo). The initial domain was composed of Fe-based alloys (ferritic matrix), austenitic stainless steels, Fe/Ni-based high-temperature alloys, Co-based alloys and Ni-based alloys. The amount of data available per group of materials is indicated within the parentheses.

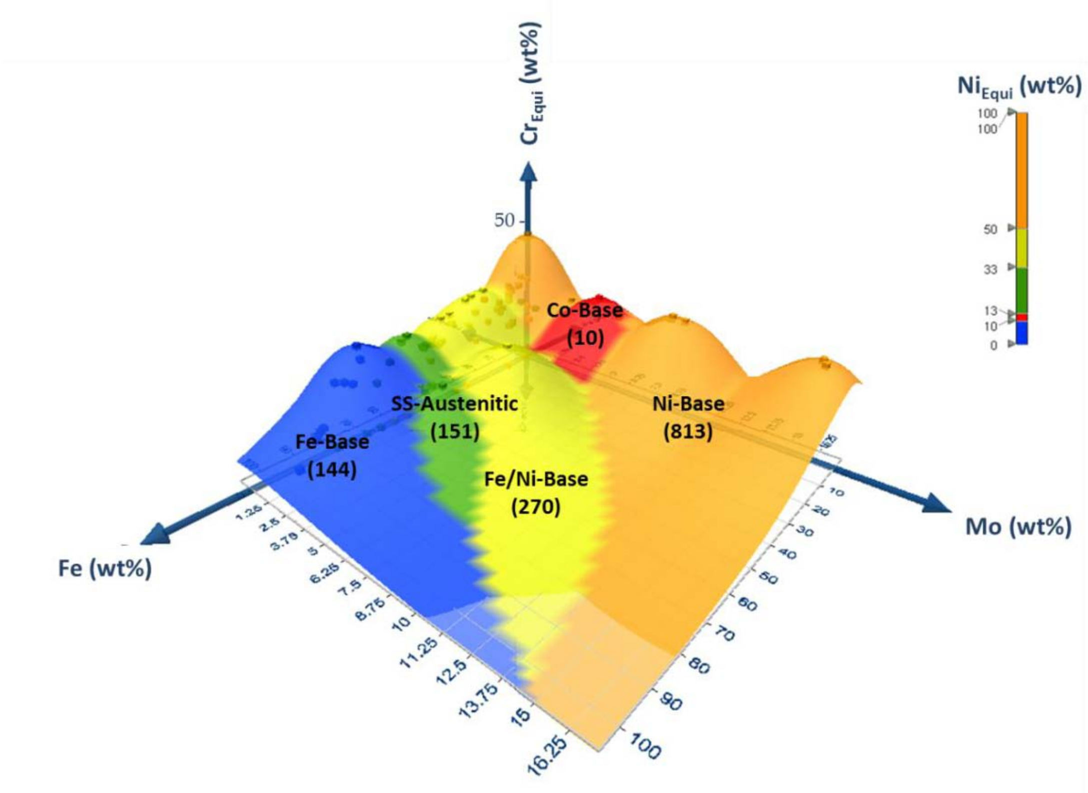

Figure III.20. Initial composition domain of the alloys as a function of the main elements Fe-Ni-Cr-Mo

Figure III.21 shows the PCA_3 applied on the group of independent variables corresponding to the materials chemical composition. In the analysis, the mass loss rate (MLr) was set as a supplementary variable in order to determine the linear correlation coefficients (r) between corrosion rates and independent variables in the initial data set. The data distributions are shown on the correlations tests in the Figure III.22 and the test correlation matrix is indicated in Appendix I.C. The PCA_3 score plot applied to materials chemical composition shows 38% of the variance explained by principal components analysis F1 and F2 and may be interpreted as follows:

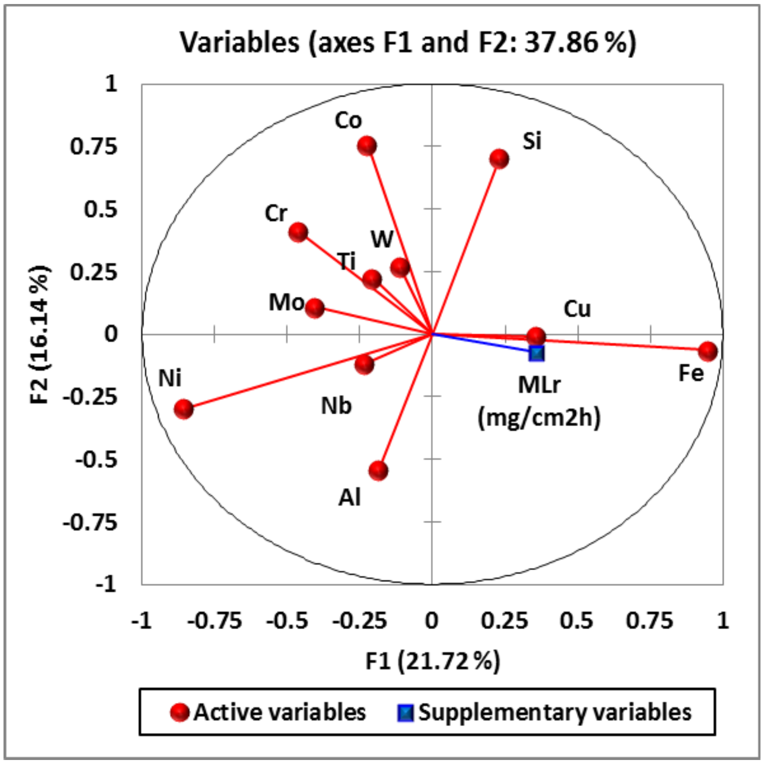

Correlations (r)

Variables (wt%)	MLr (mg/cm^{2}h)
Fe	**0.29**
Ni	**-0.24**
Cr	**-0.34**
Mo	**-0.08**
Co	**-0.06**
Cu	**0.37**
Al	**-0.06**
Si	0.01
W	-0.02
Nb	-0.04
Ti	**-0.11**

Values in bold are different from 0 with a significance level α = 0.05

Figure III.21. PCA_3 applied to the group of variables: materials chemical composition

3.1 The principal component axis F1 is attributed to Fe and Ni, as the major elements of the alloys they are inversely correlated. The principal component axis F2 is attributed to Co, Al, Si, as a group of alloying elements and the principal component axis F3 which is not seem in the diagram is attributed to Cr and Mo as another group of alloying elements.

3.2 The corrosion rate MLr is also found in F1 along with Fe and Ni. These elements exert an opposite influence on the corrosion rate, which correspond with experimental findings which showed that high Ni/Fe ratio increases metal dusting resistance. [6–8,13–15,24,129] Cr presented the highest correlation, even when there is a high variability between Fe-based and Ni-based alloys that show different corrosion mechanisms. This is expected, due to the ability of Cr to form protective layers that increase corrosion resistance.

3.3 Si, W and Nb may improve corrosion resistance in metal dusting conditions, because they are strong carbide formers. However, these elements showed low correlations that were also statistically not significant (p-value>0.05). Due to the lack of alloys with varying concentrations of these elements in the database, their effect is not clearly detected by the statistical method. All correlations correspond to the expected effects except for the Cu whose effect in reducing the corrosion rate has been shown by several studies. [20,22,166,167] However, its effect has been biased, by high frequency thermal cycle tests [20,22] and by the negative effect of this element when is found in high concentrations and precipitates. [22]

Conclusion: although the correlations and patterns correspond with what might be expected according to corrosion literature, only 38% of the variance was represented on axis F1 and F2 in the analysis. This can be attributed to the high variability of the data, caused by the combined treatment of Fe-based and Ni-based alloys as well as the atypical atmosphere conditions mentioned in PCA_1. In order to obtain better results, a filtering procedure was performed through correlation test analysis that will be showed in the next section.

Figure III.22 shows the correlation tests (CT_3) for corrosion rates as a function of the alloying elements in the initial materials domain. These analyses were applied to visualize the linear correlation coefficients (r) obtained in the PCA_3. This was done to identify the outlier's location and analyze their effects on corrosion behavior. The test correlation matrix of the initial data distribution that corresponds to PCA_3 and CT_3 is indicated in Appendix I.C.

The previous filtering was carried out as a function of the atmosphere conditions, but this process also affected the alloy composition domain. The correlation test diagrams also show the data that were removed (red dashed marks), as follows:

1. After removing high pressure tests, some Fe/Ni high-temperature alloys [127,129] were eliminated of the alloy domain.
2. After removing high activity/low temperature tests, some Fe-based alloys [133] were eliminated of the alloy domain.
3. After removing the high frequency tests (cyclic), NiAl binary alloys, [135] Co-based alloys [130], model Cu-austenitic stainless steel, [22] alumina-forming austenitic stainless steel [137] were eliminated of the alloy domain. Also Monel [29] was eliminated for being an outlier in Cu-correlation test.

After filtering, the final data distributions obtained through correlation tests (CT_4) are shown in the Figure III.23 in which, red data indicate positive correlations and blue data indicate negative correlations. The final domain was also evaluated by PCA_4 (shown in the Figure III.24) in order to analyze correlations of the final distribution and verify the effect of filtering procedures on the variance of the analysis. The test correlation matrix of the initial data distribution that corresponds to PCA_4 and CT_4 is indicated in Appendix I.C.

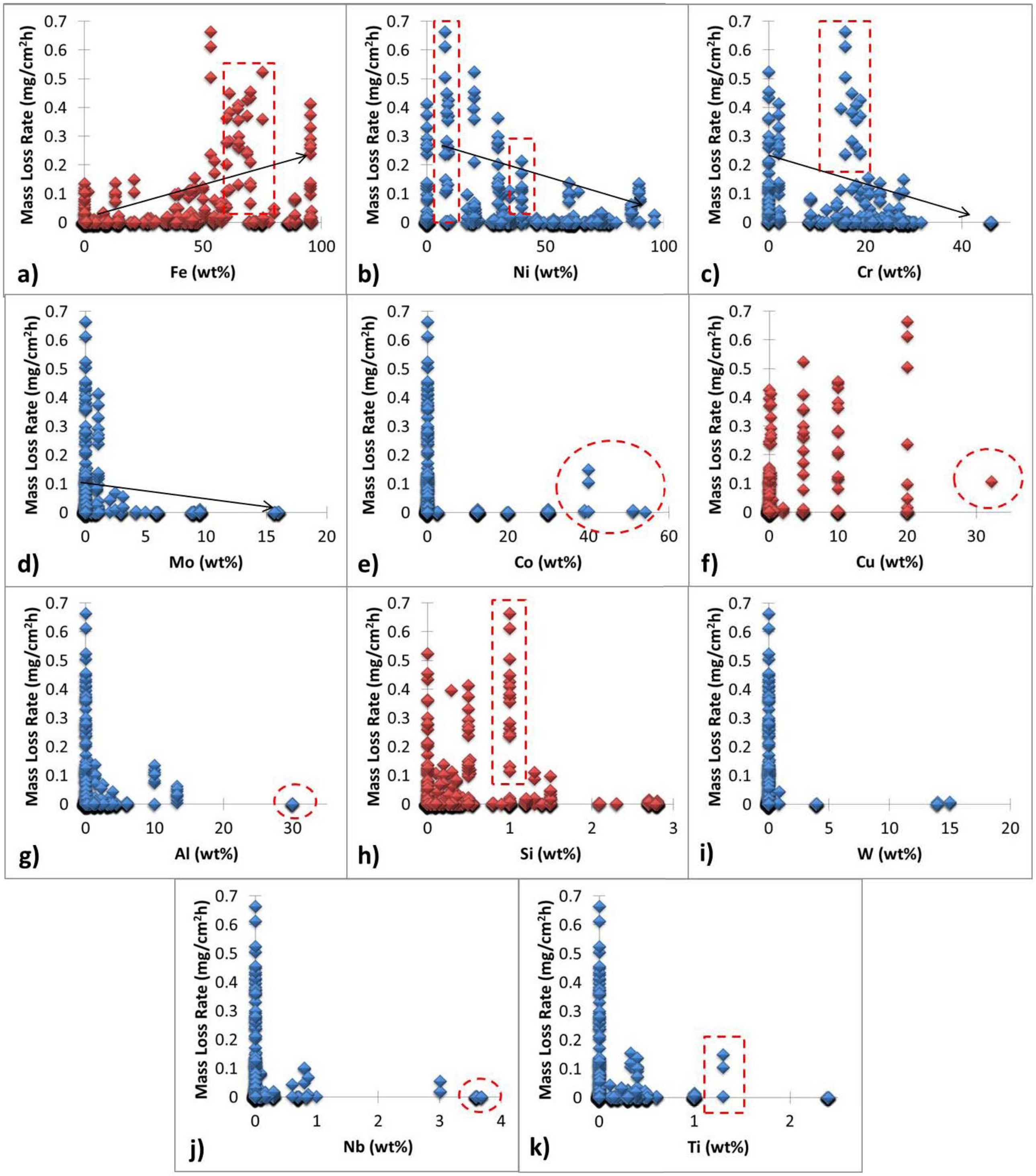

Figure III.22. Correlation test (CT_3) applied to the initial material's chemical composition. CT_3 and PCA_3 correlation matrix is given in Appendix I.C

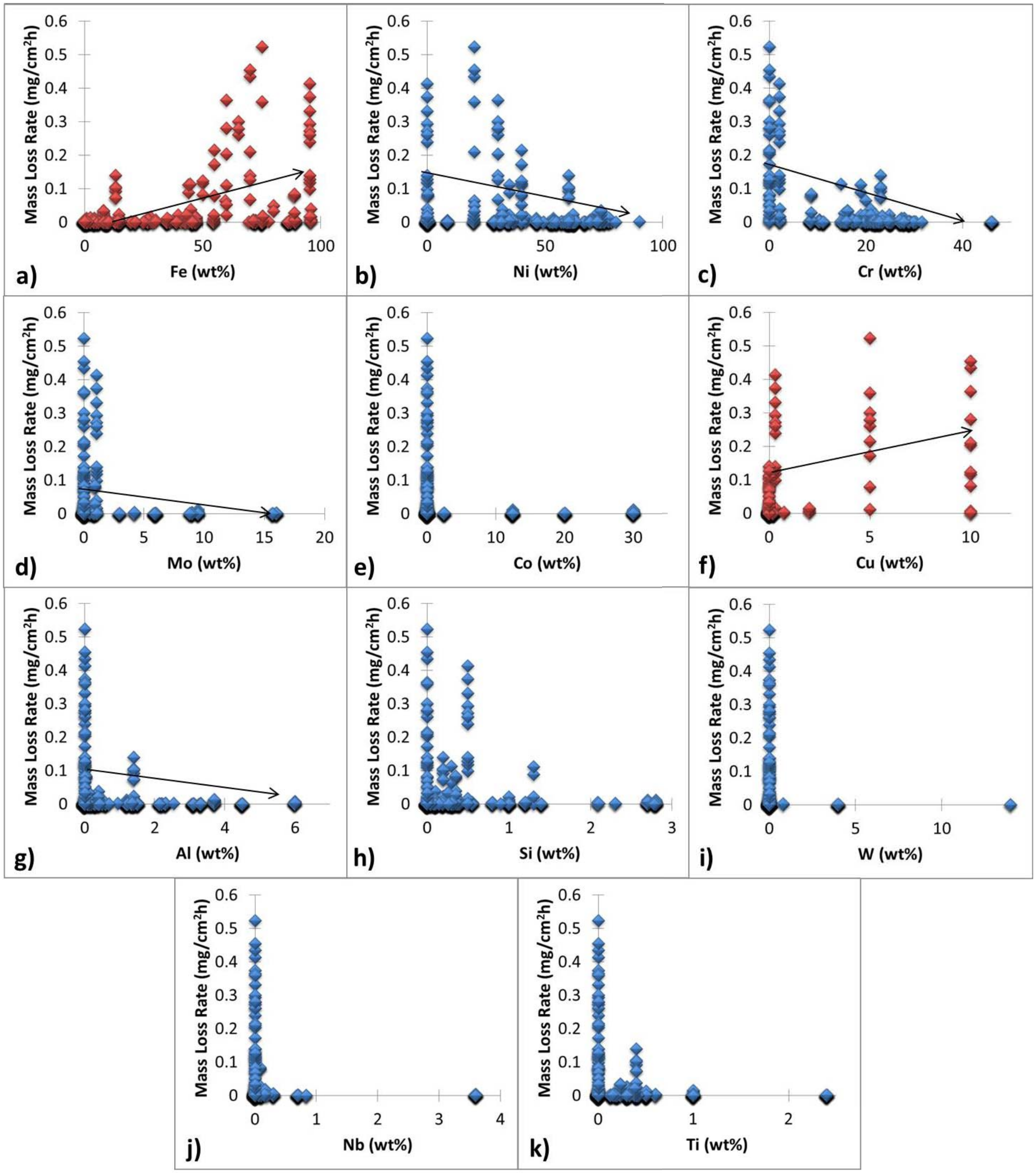

Figure III.23. Correlation test (CT_4) applied to the final material's chemical composition after the filtering process. CT_4 and PCA_4 correlation matrix is given in Appendix I.D

The final domain was also evaluated by PCA_4, as shown in the Figure III.24. The test correlation matrix of the filtered data distribution that corresponds to PCA_4 and CT_4 is indicated in Appendix I.D. The PCA_4 score plot applied to materials chemical composition after the filtering procedure shows 38 % of the variance explained by principal components analysis F1 and F2 and may be interpreted as follows:

4.1 The principal component axis F1 is attributed to Fe, Ni and Cr, as the major elements of the alloys, Fe is highly correlated with Ni (diametrically opposed) (r = -0.93) and Cr (r = -0.60) that correspond with the variation of the alloys chemical composition along the domain.

4.2 Fe and Ni continue keeping an opposite correlation with the corrosion rates that correspond with experimental findings, which showed that high Ni/Fe ratio increases metal dusting resistance [6–8,13–15,24,129]. The correlation between Cr-contents and corrosion rates increased after filtering, even when there is still a high variability along the domain, since Fe-based and Ni-based alloys show different corrosion mechanisms.

4.3 The principal component axis F2 is attributed to Co, Al, Si, as a group of alloying elements and the principal component axis F3 not seen in the diagram is attributed to Mo. F4 not seen in the diagram is attributed Cu, Ti, W, and Nb as another group of alloying elements.

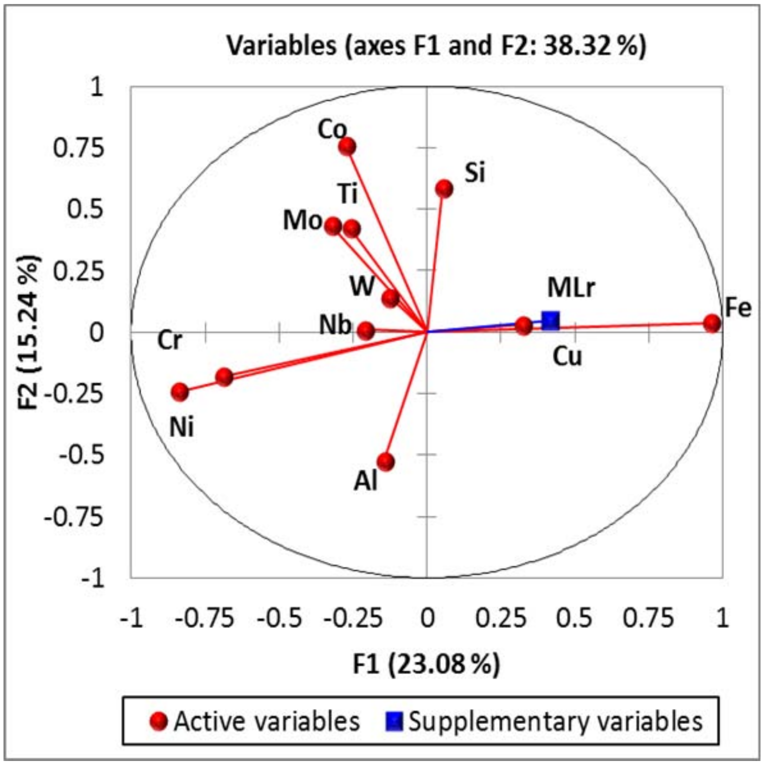

Correlations (r)

Variables (wt%)	MLr (mg/cm^2h)
Fe	**0.30**
Ni	**-0.21**
Cr	**-0.46**
Mo	**-0.06**
Co	-0.06
Cu	**0.55**
Al	**-0.13**
Si	-0.06
W	-0.03
Nb	-0.04
Ti	**-0.10**

Values in bold are different from 0 with a significance level α = 0.05

Figure III.24. PCA_4 applied to the group of variables: materials chemical composition (after filtering)

4.4 Regarding the effect of the minor elements on the corrosion rate (Mo, Co, Al, Cu, Si, W, Nb, Ti), only the correlation of the Al regarding the corrosion rate, increases and becomes significant. The rest of the elements keep their negative low correlation on the corrosion rate but also a low significance (p-value>0.05). Cu keeps having a positive correlation with the corrosion rate, which is contrary to literature review.[20,22] This is because the studies about the Cu-effect included in the database were performed at aggressive atmospheres compared to others conditions, which may bias the effect of Cu. Also, the lack of data on some distributions does not allow the correlations to be analyzed adequately.

Conclusion: although the correlations and patterns are in agreement with the admitted effects of the alloying elements, the quantity of information represented in the first two component (F1, F2) is still low (38%). This result is due to the high variability in the data, caused by the combined treatment of all the alloy families. In order to obtain better results, a classification of alloys was conducted, as shown in the Figure 25 for further correlation analysis. The results are presented in the next section.

III.3.1.1.1.3 Alloy classification and correlation tests

From PCA_4, it was concluded that the high variability of the data, could be caused by the combined treatment of Fe-based and Ni-based alloys. This result is consistent with experimental findings that have demonstrated different reaction mechanisms as a function of the alloy matrix. Due to the high variability still present in PCA_4 after the filtering process, a classification of alloy systems was conducted in the final materials domain, in order to obtain better results in modeling. The classification was performed as a function of $Ni_{Eq.}$ and $Cr_{Eq.}$ (wt.%) calculated by the Schaffler equations (41) and (42). [101]

$$\boldsymbol{Ni_{Eq} = Ni + 30C + 0.5Mn\ (wt.}\%) \quad \textbf{Equation 41}$$

$$\boldsymbol{Cr_{Eq} = Cr + Mo + 1.5Si + 0.5Nb\ (wt.}\%) \quad \textbf{Equation 42}$$

Figure III.25 shows a 3D diagram of the final materials domain as a function of the main elements (Fe-Ni-Cr-Mo). The final domain was composed of Fe-based alloys (ferritic matrix), austenitic SS, Fe/Ni-based high-temperature alloys and Ni-based alloys with in parentheses the amount of data available per group of materials to model MLr as dependent variable. Since the austenitic-SS group presented a small amount of data and a low variability in its conditions, it was combined with Fe/Ni HT alloys domain. The main domain was classified into three alloy systems to be analyzed and modeled: Fe-based alloys (ferritic matrix), austenitic SS + Fe/Ni-based high-temperature alloys and Ni-based alloys.

After filtering and classification, the alloy domain consists of three groups of alloys: ferritic alloys (Fe-based), austenitic stainless steels and high-temperature steels (Fe/Ni-based) and Ni-based alloys. Each group was analyzed by correlation tests to evaluate corrosion rates as a function of both groups of the independent variables, i.e. atmosphere conditions and alloy composition.

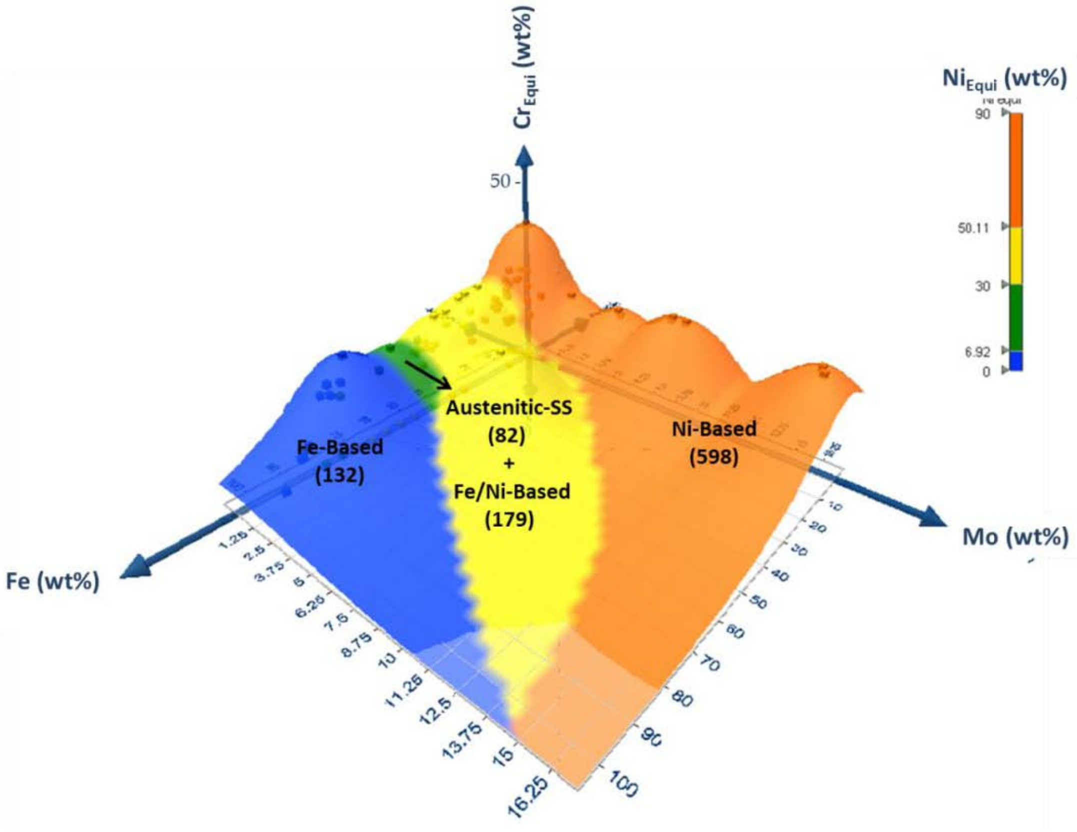

Figure III.25. Distribution of the alloy's composition as a function of Fe-Ni$_{Eq}$-Cr$_{Eq}$-Mo, final materials domain classified into three groups of alloy systems.

The bar chart in the Figure III.26 shows the correlation coefficients (r) obtained from correlations tests CT$_5$, CT$_6$ and CT$_7$ applied to corrosion rates as a function of the atmosphere conditions for Fe-based alloys, austenitic stainless steels + Fe/Ni-based alloys and Ni-based alloys, respectively. The correlation matrix is given in Appendix I.E, I.F and I.G. Correlation coefficients were improved after alloy classification.

1. *Effect of 1/T:* Corrosion rates increase with temperature in Fe-based alloys and Fe/Ni-based alloys, this result corresponds with findings by Grabke et al [12,23] who showed that metal dusting rates of several Fe-based and Fe/Ni-based alloys increase with temperature up to 600° C. However Ni-based alloys showed no correlation with temperature which is also consistent with findings by Chun et al.[10] who showed that the corrosion rate of Ni at a given gas phase composition is nearly independent of temperature in the 600-1050°C range. The main difference between Fe and Ni mechanisms is the formation of carbides M$_3$C, as Ni does not form a carbide [7]. Nevertheless, Ni does undergo metal dusting corrosion. Chun et al.[10] exposed that in absence of carbides, the activation energy for the rate-limiting step in corrosion is negligible and the most likely rate-limiting step is the diffusion of Fe or Ni through graphite. Young et al.[6] also expose that the lack of reliable information on the temperature effect prevents dissection of the mechanism using activation energy values. Therefore, according to the statistical correlation and experimental findings from the authors, [7,10,12,23] we may infer that the temperature affects strongly the kinetics of attack in presence of Fe$_3$C as in the case of Fe-based and Fe/Ni base alloys. In these systems the cementite decomposition becomes faster than some other

process with lower activation energy at higher temperatures. For Ni-based alloys, which do not show carbide layer formation, metal dusting mechanism becomes less dependent of the temperature.

2. *The effect of pH_2O:* H_2O is an oxidizing gas that could promote oxide layers formation and then decrease the corrosion rate. [168] However, Fe-based materials show no effect of pH_2O. Its inhibitory effect increases on Fe/Ni alloys, which might be related to higher Cr-contents in this group of alloys that is more susceptible to form protective oxide scales.

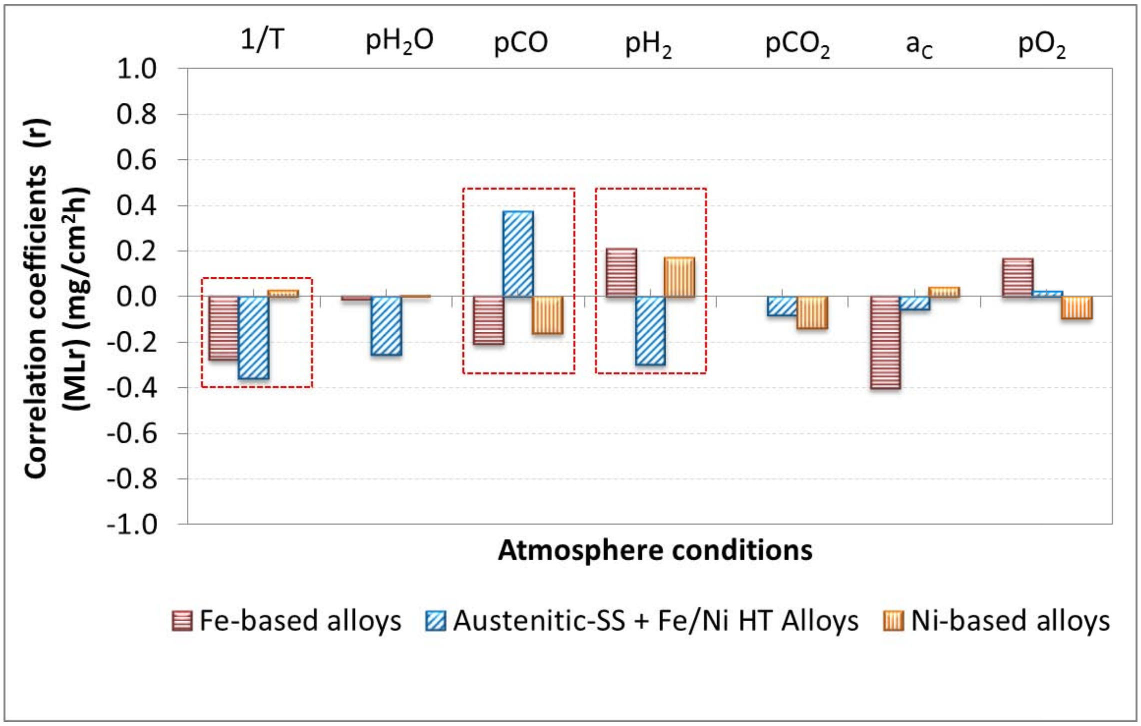

Figure III.26 : Variation of the correlation coefficients (r) for each family of alloys regarding the atmosphere conditions

3. *The effect of pCO and pH_2* changes from one alloy domain to another, but they are inversely proportional on the three groups of alloys, due to the gas composition at atmospheric pressure which is determined based on 100 vol.%. This confirms the high correlation between both gas concentrations and the need to convert the variable into pCO x pH_2 to avoid collinearity in linear regressions. The assumption of this variable would imply that metal wastage rate in the high-temperature range can be proportional to the product pCO x pH_2 as indicated by Muller-Lorenz et al. [23] and Chun et al. [10]

4. *The effect of pCO_2* is even more limited to conclude about this variable, due to a low variability in the data distribution.

5. *The effect of a_C and pO_2* changes from one alloy domain to another. They are slightly inversely proportional on the three groups of alloys. Both effects on the metal wastage rates are low, except for a_C on Fe-based alloys which is high and negative. This result is expected because in Fe-based alloys, at the studied temperature range [570°C – 700°C], the cementite decomposition becomes faster with increasing temperature and a_C decreases when temperature increases.

As a conclusion of the analysis, according to statistical correlations concerning the atmosphere conditions on each alloy system, the parameters that should be taken into account for modeling are: 1/T and the product (pCO x pH_2).

The bar chart in Figure III.27 shows the correlation coefficients (r) obtained from correlations tests CT_8, CT_9 and CT_{10} applied to corrosion rates as a function the alloy elements for Fe-based alloys, austenitic stainless steels + Fe/Ni-based alloys and Ni-based alloys. The correlation matrix is given in Appendix I.H, I.I and I.J, respectively. Correlation coefficients were improved after alloy classification.

1. *Effect of Fe*: metal dusting rates tend to increase for alloys with higher Fe-contents, in every alloy domain. This result corresponds with numerous experimental findings. Higher Fe-contents favor higher diffusivity of carbon and Fe_3C formation [6,7,9,15,17,25]. It can be also noticed that the individual effect of Fe on Ni-based alloys is negligible, since studies have shown that for Ni-based alloys there is no carbide Fe_3C formation in metal dusting reactions and hence it does not depend of the Fe-content.[7,12,13,17]

2. *Effect of Ni*: metal dusting rates tend to decrease in alloys with higher Ni-contents for Fe-based and Fe/Ni-based alloys. This result corresponds with experimental findings which showed that higher Ni/Fe ratios increase metal dusting resistance [13,17,24,25,131]. Ni-based alloys show an unexpected positive correlation, which might be due a high variability of environments, since approximately 598 rates, 72 Ni-base alloys were evaluated under a wide range of atmosphere conditions. Some conditions are more aggressive than others, resulting in higher rates even for the most resistant alloys. The effect of the Ni-content might be overlapped. Also, higher concentrations of Ni may imply lower concentrations of Cr, and hence less stability in protectives oxides layers.

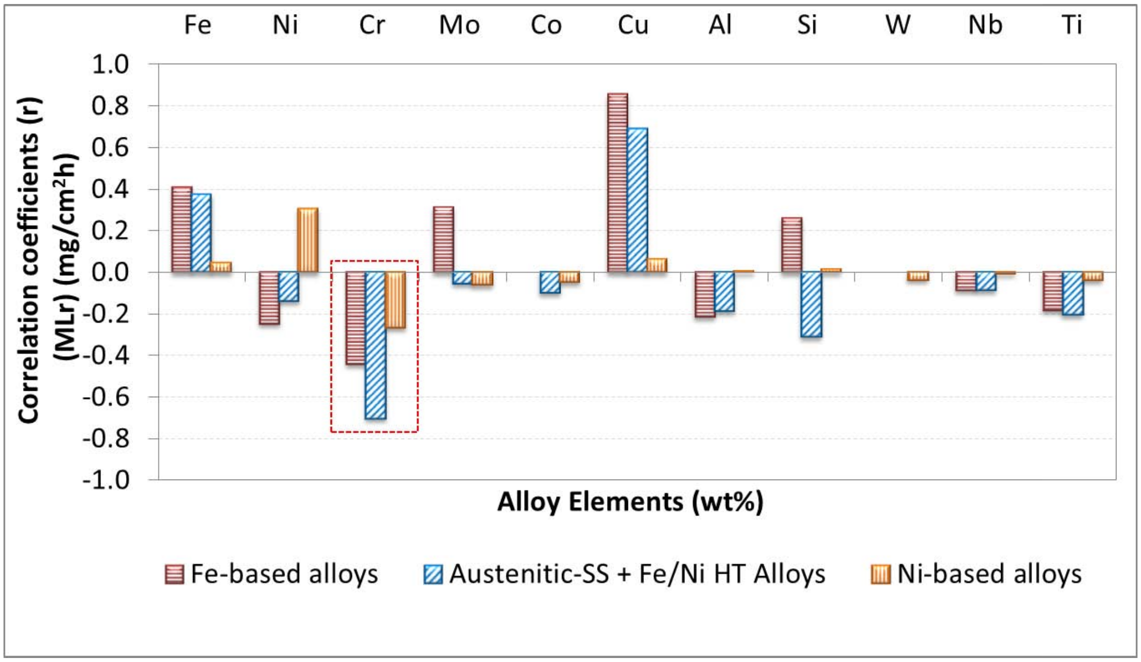

Figure III.27 : Variation of the correlation coefficients (r) for each family of alloys regarding the contents of the alloying elements

3. *Effect of Cr:* the suppressive effect of chromium stands out, in every alloy domain. This statistical result corresponds with experimental findings of numerous studies. Scales of Cr-oxide is expected to provide effective diffusion barriers to carbon and no significant catalytic effect for carbon deposition from the gas. [6] For the temperature range of metal dusting, a chromia-rich layer is an efficient protection [9,12,17,18]. The resistance to metal dusting increases with increasing Cr-contents [17]. In fact, Schuler et al. [169] and Schillmoller [170] presented a qualitative criterion for resistance to carburization and metal dusting based on chromium equivalent equations.

4. *Effect of Mo and Co:* these elements seem to decrease the corrosion rate but the effect is low on Fe/Ni-base alloys and Ni-based alloys. Mo is expected to provide surface and internal carbides with diffused carbon.[6,9] In Fe-based alloys, Co and Mo present a misleading correlation coefficient, which is influenced by high corrosion rates obtained under high-temperature conditions. Therefore these elements should be not considered for modeling in this domain.

5. *Effect of Cu:* it does not correspond with the expected. Studies suggest that alloys with an adequate Cu-content do not react with CO in the gas mixture even without an oxide scale barrier [20–22,136]. However in Fe-based group, the Cu-content is low (up to 0.3%) thereby the misleading correlation value is influenced by other factors. In Fe/Ni based group the materials with high Cu-content (5-10%) belong to the study of Zhang et al. [136] where Fe-Ni-Cu alloys showed high corrosion rates at 650°C (temperature peak in our domain). Furthermore, in this study the author also concluded that in low nickel content alloys the solubility for copper is reduced. Austenite-copper phase boundaries are thought to act as favorable graphite nucleation sites, thereby promoting the dusting reactions[136].

6. *Effect of Al and Si:* these elements show negative correlations which correspond with a suppressive effect on corrosion rates, but the correlations are low. Al and Si are expected to provide stable protective oxides Al_2O_3 and SiO_2 [6,94,99,100,134,137] but these protective oxide scales are difficult to form at low temperatures due to low diffusion rates in the matrix and to small contents of Al and Si. Moreover, when SiO_2 layers are formed, these are thin and brittle, susceptible to be damaged. In Fe-based alloys, Si presented a misleading correlation value which is influenced by high corrosion rates obtained under high-temperature conditions (as in the case of Mo).

7. *Effect of W, Nb and Ti:* these elements also showed in general a suppressive effect on corrosion rates, however the correlations are low. W, Nb and Ti are expected to provide surface and internal carbides with diffused carbon. [9,16,17,171] These carbides are more stable than Cr-carbides. Therefore the Cr remains available to form protective chromia scales.

Conclusion: according to statistical correlations concerning the alloying elements, after studying in detail the correlations for each alloy system, the principal element that should be taken into account in first order for modeling is the Cr-content in the alloy, due to its strong influence in the corrosion rates in every alloy system.

Once performed the data filtering and the variable selection, through the interpretation of the Principal Component Analysis and Correlation Tests, the variables selected from the atmosphere conditions group to be considered for modeling are 1/T and (pCO x pH_2). However in some cases pH_2O will be added to improve the linear regression fit. From the group of alloy elements, the variable to be considered for modeling is the Cr. However, in the case of the most complex alloy systems (Fe/Ni-based and Ni-based)

Mo and Al will be added in order to improve the linear regression fit. Fe or Ni will not be used due to their high correlation with Cr.

III.3.2 Modeling: Multiple Linear Regression

Approximately 30 multiple regressions simulations were performed for each scenario in order to reach the best possible fit that showed the best statistical indicators.

Figure III.28 shows a schematic of the scenarios to be modeled that will be explained further below. On the first level, there are three models obtained for each alloy system as a function of the mass loss rate (MLr) (1,2,3). However for Ni-based alloys the result was not satisfactory, therefore the analysis of a second level of data was performed, which was justified by the importance of the incubation time in the experimental data. This second set of tests was dissected into two variables to be modeled: the incubation time (IT) and the mass loss rate after incubation time (AIMLr). Models 4a (IT) and 4b (AIMLr) were obtained for Fe/Ni based and Ni-based alloys of which only the model of incubation times was satisfactory. Model 4b does not show satisfactory results; as a result the analysis of a third level of data was performed, which refers to those tests which were analyzed in terms of the pits depth growth kinetics (PDGr). The PDGr starts after the incubation time, so this variable is considered equivalent to the AIMLr regime. It was shown in A. Fabas's thesis that this variable is more representative of the material degradation kinetics as well as more representative of the material thickness affected by metal dusting corrosion, and therefore more useful for design purposes. Finally, model 5 for pit growth kinetics (PDGr) was obtained on Fe/Ni based and Ni-based alloys with satisfactory results. This overall modeling strategy is summarized in the Figure III.28.

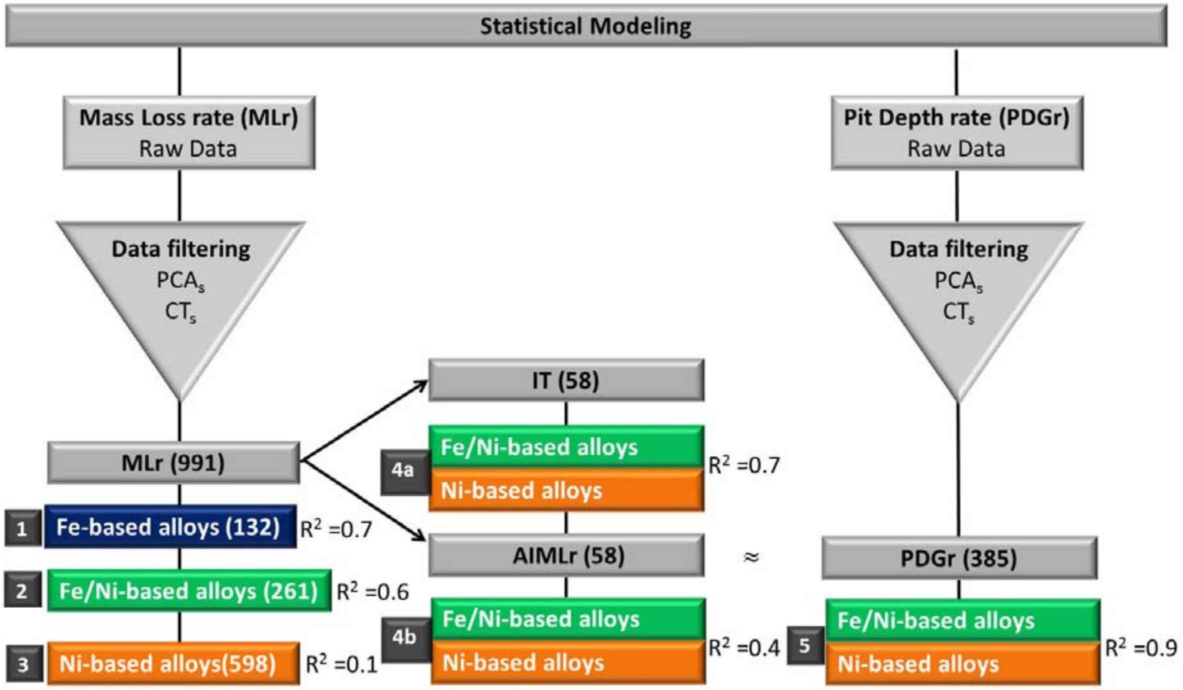

Figure III.28. Schema of the different scenarios considered for modeling metal dusting kinetics

III.3.2.1 Mass Loss rate (MLr)

III.3.2.1.1 Model 1: Fe-based alloys

A model was generated from the Fe-based alloys data set (131 data). Approximately 75% of the original data set was randomly selected to create the equation of the model (43). In order to validate the model, the remaining 25% of the data set was used to verify the predictive ability of the model. The validation data set was within the model validity domain but not included in the data set used to determine the predictors of the model. Table III.2 shows the model validity domain and the goodness of fit statistics, Figure III.29 shows the relative weights of the variables in the model and Figure III.30 shows the accuracy chart of the model.

$$MLr = 2.2 \times 10^{-1} - 6.5 \times 10^{-2} \times \frac{1}{T} - 1.7 \times pH_2O + 3.3 \times pCOxpH_2 - 3.3 \times 10^{-3} \times [Cr]$$

Equation 43

Where, MLr is given in $\frac{mg}{cm^2h}$, temperature (T) in *Kelvin*, pH_2O, pCO, pH_2 in *bar* and $[Cr]$ in *wt%*

Table III.2. Statistics of model 1. a) Validity domain b) Goodness of fit statistics

Variable	Minimum	Maximum
MLr (mg/cm^2h)	0.0	0.139
1/T (K^{-1})	10.3	11.9
T (°C)	570	700
$P_{Internal}$ (bar)	1.0	
pH_2O (bar)	0.01	0.06
pH_2 (bar)	0.25	0.74
pCO (bar)	0.24	0.70
$pCOxpH_2$ (bar^2)	0.18	0.22
a_C	5.7	57.9
pO_2 (bar)	1.2×10^{-27}	1.3×10^{-24}
Cr (wt%)	2.1	28.0

a)

Goodness of fit statistics:	
R²	0.74
Adjusted R²	0.73
DW	0.85
MSE	0.00
RMSE	0.01
Analysis of variance:	
F	64.9
Pr > F	< 0.0001

b)

Table III.2a shows the highest and lowest variable limits between which the model is valid. This model can be applied on ferritic alloys within the following composition ranges given in wt.%: $[0-8]$ Ni and $[2.2-28]$ Cr, at temperatures in the $[570-700]$°C range, under atmospheric pressure, in a gas composition within the following concentration ranges given in vol.%: $[25-74]$ H_2, $[24-70]$ CO, $[1-6]$ H_2O or the partial pressures product $(pCO\ x\ pH_2)$ between 0.18 and 0.22 bar^2.

Table III.2b shows the goodness of fit statistics of the model. As the coefficient of determination R^2 is the proportion of variability in a data set that is accounted for by a statistical model. The $R^2 = 0.74$ means that 74% of the variation of the mass loss rates was explained by the model. The DW = 0.85 shows that the residuals are dependent from each other. The coefficient values F = 65 and $|Pr > F| < 0.0001$ means that there is a significant linear relationship between the MLr and the set of independent variables taken together in the model (Figure 29), thus the model is satisfactory from a statistic point of view.

Figure III.29 shows the relative weight of the independent variables: $\frac{1}{T}, pH_2O, pCO\ x\ pH_2$ and $[Cr]$ on the MLr. Corrosion rates increase with temperature in the 570° C -700°C range which corresponds with experimental findings. [7,10,12,23] The variables pH_2O and wt% Cr has a negative effect on corrosion rates. The variable pH_2O was added to the model to obtain a better fit, its negative effect corresponds with experimental findings by Hoffman et al. who showed that Fe-based alloys suffered little damaged in high water vapor containing syngas environments in the 538-566°C range. [168] According to the model, higher Cr-contents decrease corrosion rates, due to the ability of forming a more protective chromium rich oxide film, which is also favored in presence of the oxidizing gas H_2O. [9,12,17,18] Also, high water vapor concentrations prevent high carbon deposit to diffuse in the material bulk as stated by Grabke et al.[25] Corrosion rates increase with $(pCO\ x\ pH_2)$ rather than with the other variables. This result is consistent with the observation by Muller-Lorenz et al. [23] which showed that at temperatures higher than 540°C the cementite decomposition becomes faster and proportional to the product $pCO\ x\ pH_2$.

The model explains 74% of the variation of the corrosion rates by the set of independent variables considered in the equation. However, there is a remaining 26% of information not yet explained by the model that can be attributed to variables not considered for modeling, such as: grain size, surface finish and gas velocity. These variables were not included in the model due to the lack of data reported in literature and thus in the database.

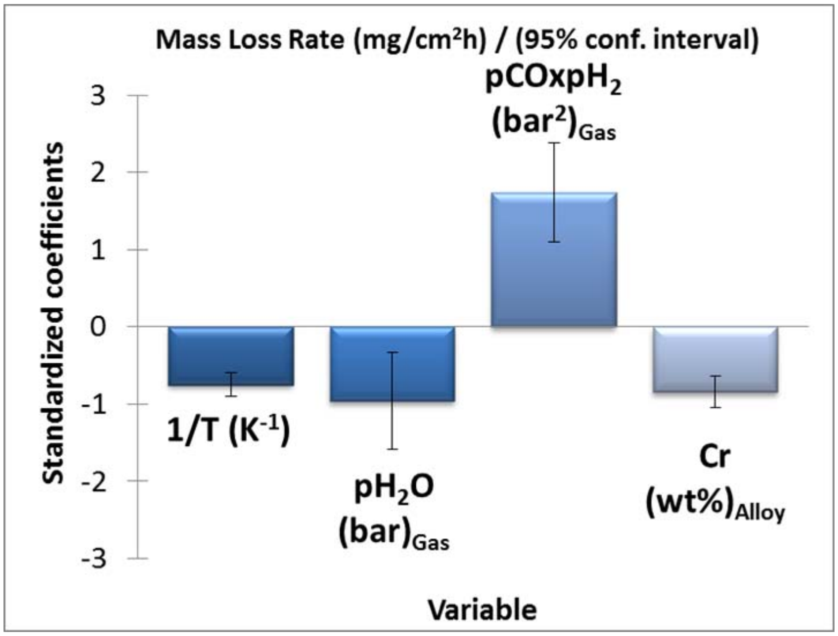

Figure III.29. Standardized coefficients chart: relative weight of the independent variables on model 1 for the metal dusting kinetics of Fe-based alloys

Figure III.30 shows the accuracy chart of the model that represents the residuals between experimental values and predicted values. Blue data are within the data population utilized to calculate the predictors of the model while red data correspond to the validation of the model, in a separate data population. The coefficient RMSE = 0.01 indicates the standard deviation of the predictions of the model, leading to equation 44.

In the model, each input condition produces a predicted rate, and the experimental rates (MLr) are the average corrosion rates calculated from the beginning to the end of the experiment. Therefore, when corrosion kinetics shows an incubation time followed by a mass loss regime, the average mass loss rates increase with time, and thus is not constant. This produces a range of results for the same test condition, as shown in the diagram. This experimental feature adds a source of error to the model, which is related to the dependent variable. Due to the lack of standardization of the metal dusting tests, mass loss measurements in general present several sources of error, such as: different measurement methods used by the authors as well as different sample shapes. Furthermore, sometimes mass change shows fluctuations and/or a nonlinear evolution.

The model does not predict well the low corrosion rates, instead it predicts negative rates (Figure III.30). This feature is due to the low mass loss rates present in the data distribution, which typically belongs to the incubation times with negligible mass change or even mass gain due to oxidation, but they are included in the linear regression. However, Fe-based alloys show short incubation times or no incubation time at all, therefore the model would be predicting corrosion rates mostly in the mass loss regime, which might explain the good agreement obtained.

$$\boldsymbol{MLr_{Experimental} = MLr_{Predicted} \pm 0.01\ \frac{mg}{cm^2h}} \qquad \textbf{Equation 44}$$

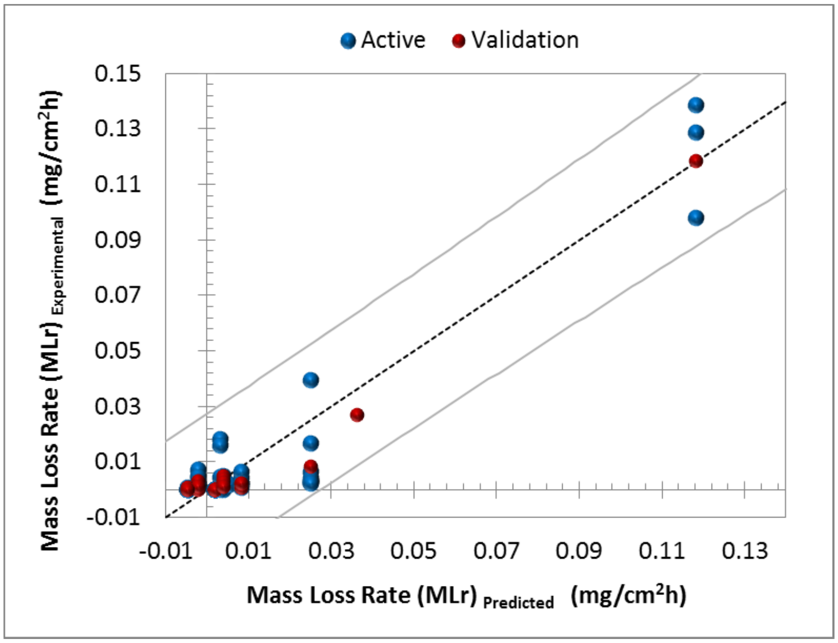

Figure III.30. Accuracy chart: the residuals between experimental values and predicted values by model 1 for the metal dusting kinetics of Fe-based alloys

III.3.2.1.2 Model 2: Fe/Ni-based alloys

The same procedure was applied for modeling the Fe/Ni-based alloys data set (261 data). Approximately 50% of the original data set was randomly selected to create the model. Equation (45) shows the equation of the model. In order to validate the model, the remaining 50% of the data set was used to verify the predictive ability of the model. The validation data set was within the model validity domain but not included in the data set used to determine the predictors of the model. Table III.3 shows the model validity domain and the goodness of fit statistics, Figure III.31 shows the relative weights of the variables in the model and Figure III.32 shows the accuracy chart of the model.

$$\boldsymbol{MLr = 2.9 \times 10^{-1} - 1.8 \times 10^{-2} \times \frac{1}{T} + 3.9 \times 10^{-1} \times pCOxpH_2 - 5.7 \times 10^{-3} \times [Cr]}$$

$$\boldsymbol{-5.3 \times 10^{-3} \times [Mo] - 2.4 \times 10^{-3} \times [Al]} \qquad \textbf{Equation 45}$$

Where, MLr is given in $\frac{mg}{cm^2h}$, temperature (T) in *Kelvin*, pCO, pH_2 in *bar* and $[Cr]$, $[Mo]$, $[Al]$ in *wt.%*

Table III.3. Statistics of model 2. a) Validity domain b) Goodness of fit statistics

Variable	Minimum	Maximum
MLr (mg/cm^2h)	0.00	0.46
1/T (K^{-1})	10.8	11.9
T (°C)	570	650
$P_{Internal}$ (bar)	1.0	
pH_2O (bar)	0.01	0.06
pH_2 (bar)	0.25	0.80
pCO (bar)	0.18	0.70
$pCOxpH_2$ (bar^2)	0.14	0.22
a_C	10	104
pO_2 (bar)	$1.9x10^{-28}$	$6.6x10^{-25}$
Cr (wt%)	0.00	30.3
Mo (wt%)	0.00	4.2
Al (wt%)	0.00	1.5

a)

Goodness of fit statistics:	
R²	0.60
Adjusted R²	0.55
DW	1.70
MSE	0.00
RMSE	0.05
Analysis of variance:	
F	49.41
Pr > F	< 0.0001

b)

Table III.3a shows the highest and lowest variable limits between which the model is valid. This model can be applied on austenitic alloys within the following composition ranges given in wt.%: $[9 - 49]$ Ni, $[0 - 30.3]$ Cr, $[0 - 4.2]$ Mo and $[0 - 1.5]$ Al, at temperatures in the $[570 - 650]$°C range under atmospheric pressure conditions, in a gas concentration within the following ranges given in vol.%: $[25 - 80]$ H_2, $[18 - 70]$ CO, $[1 - 6]$ H_2O or the partial pressures product $(pCO\ x\ pH_2)$ between 0.18 and 0.70 bar^2.

Table III.3b shows the goodness of fit statistics of the model. The $R^2 = 0.6$ means that 60% of the variation of mass loss rates was explained by the model. The DW = 1.7 shows that the residuals are independent from each other. The F = 49 and $|Pr > F| < 0.0001$ means that there is a significant linear relationship between the MLr and the set of independent variables taken together in the model (Figure III.31), all this indicators show that the model is satisfactory from the statistical point of view.

Figure III.31 shows the relative weight of the independent variables: $\frac{1}{T}, (pCO\ x\ pH_2), [Cr], [Mo], [Al]$ on the MLr. Corrosion rates increase with temperature and $(pCO\ x\ pH_2)$, in the temperature range 570°C - 650°C which corresponds with experimental findings.[7,10,23,12] However, for Fe/Ni-based alloys the effect of $(pCO\ x\ pH_2)$ seems to be lower than that of Fe-based alloys. Corrosion rates decrease significantly with $[Cr]$ and then with $[Mo]$ and $[Al]$ with a minor influence. The suppressive effect of Cr stands out in the model as a parameter of 1st order, this means that increasing the Cr-content decreases corrosion rates due to the formation of protective chromium rich oxide films that provide diffusion barriers to carbon, and no significant catalytic effect for carbon deposition from the gas. [9,12,17,18,23]

The slight suppressive effect of Mo comes from the ability to form surface and internal carbides with diffused carbon, [6,9] and hence more chromium will enable protective oxide formation that increases the corrosion resistance.

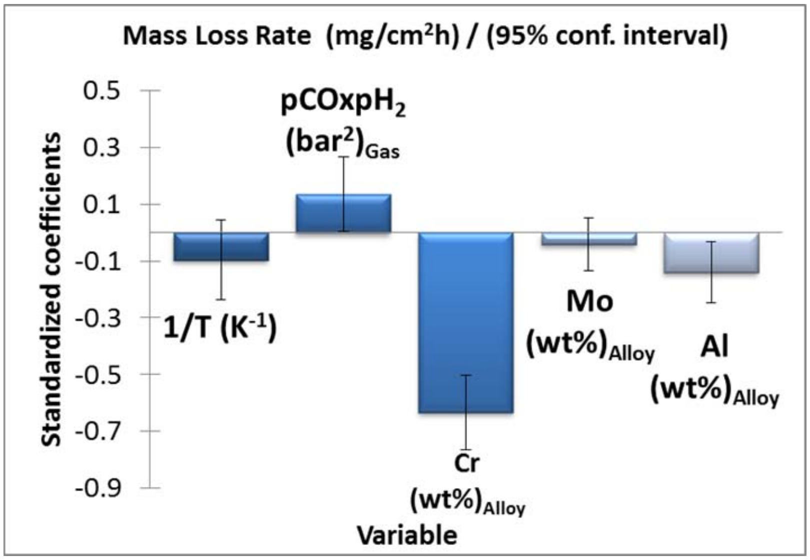

Figure III.31. Standardized coefficients chart: relative weight of the independent variables on model 2 for the metal dusting kinetics Fe/Ni-based alloys

The suppressive effect of aluminum is higher than Mo but significantly lower than Cr. Generally, the addition of Al and Cr to steel increases the corrosion resistance. Protective alumina scales can be formed on austenitic SS with 2.5 to 4 wt% Al and 12 to 15 wt% Cr. The third element effect states that Cr decreases the amount of Al required to establish alumina layer on the surface, so the combined effect of Cr and Al will favor the oxide layer formation. [172] The continuous alumina film provides protection against metal dusting corrosion since carbon does not migrate through the oxide film.[134] Besides, at higher Ni-contents (Fe/Ni based high performance alloys), Al and Cr permit stabilization of a strong austenitic matrix microstructure, which is more resistant to carbon diffusion.[173–175] However, alumina scale grows much slower than chromia, with a parabolic rate constant of one or two orders of magnitude, this very slow growth can prevent the formation of a continuous scale. Also, in the model Al-upper limit is 1.5 wt% and thus Al-content in the alloy might be insufficient to form a protective alumina scale at the typical temperature range of metal dusting. If the Al-content is insufficient then internal oxidation of Al will occur below the chromia scale in the metal, and this can be detrimental to metal dusting resistance. [172]

Figure III.32 shows the accuracy chart of the model that represents the residuals between experimental rates and predicted rates. The coefficient RMSE = 0.05 indicates the standard deviation of the predictions of the model, leading to equation 46. The model explains 60% of the variation on the corrosion rates, the accuracy decreases compared to model 1. The model predicts well high corrosion rates, but it does not predict correctly extremely low rates. This is because Fe/Ni-based alloys present higher content of Cr, which favors protective oxide layers formation that may delay the metal dusting attack. Longer incubation times imply that different corrosion rates are reported in the experimental data for similar experimental conditions, depending on the total duration of the experiment. The existence of two kinetics regimes for the same test condition hampers the linear regression fitting.

$$\boldsymbol{MLr_{Experimental} = MLr_{Predicted} \pm 0.05\ \frac{mg}{cm^2h}} \qquad \textbf{Equation 46}$$

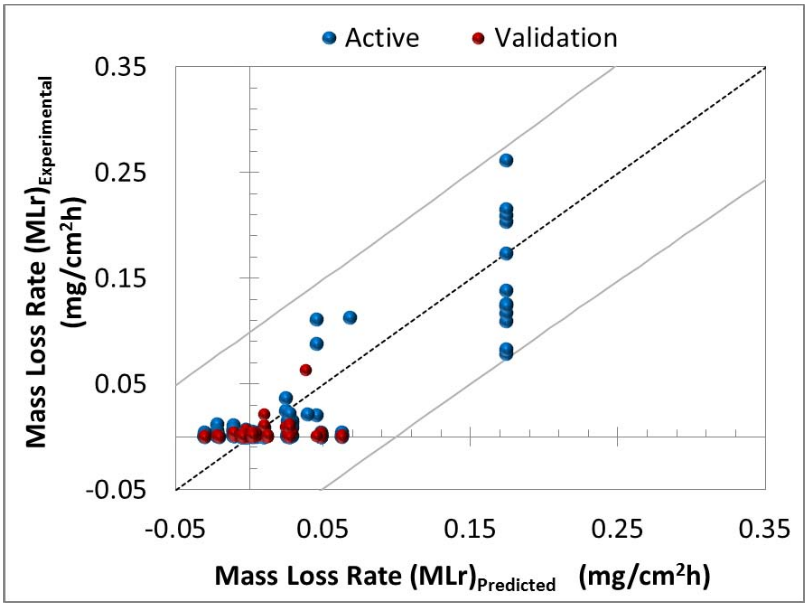

Figure III.32. Accuracy chart: residuals between experimental values and predicted values by model 2 for the metal dusting kinetics of Fe/Ni-based alloys

III.3.2.1.3 Model 3: Ni-based alloys

Following the same procedure, a model was generated for the Ni-based alloys data set (598 data). The model is described by Equation (47). Table III.4 shows the model validity domain and the goodness of fit statistics while the Figure III.33 and Figure III.34 shows the relative weights of the variables in the model and the accuracy chart of the model, respectively.

$$\boldsymbol{MLr} \ = \ -\mathbf{4.3} \times \mathbf{10^{-3}} + \mathbf{7.4} \times \mathbf{10^{-4}} \times \frac{\mathbf{1}}{\boldsymbol{T}} - \ \mathbf{2.5} \times \mathbf{10^{-2}} \times \boldsymbol{pH_2O} + \ \mathbf{1.4} \times \mathbf{10^{-2}} \times \boldsymbol{pCOxpH_2}$$

$$-\mathbf{1.9} \times \mathbf{10^{-4}} \times [\boldsymbol{Cr}] - \mathbf{1.7} \times \mathbf{10^{-4}} \times [\boldsymbol{Mo}] - \mathbf{1.1} \times \mathbf{10^{-4}} \times [\boldsymbol{Al}] \qquad \textbf{Equation 47}$$

Where, MLr is given in $\frac{mg}{cm^2h}$, temperature (T) in *Kelvin*, pH_2O, pCO, pH_2 in *bar* and $[Cr], [Mo]$ and $[Al]$ in *wt%.*

Table III.4. Statistics of model 3. a) Validity domain b) Goodness of fit statistics

Variable	Minimum	Maximum
MLr (mg/cm^2h)	0.0	0.03
1/T (K^{-1})	10.8	11.9
T (°C)	570	650
$P_{Internal}$ (bar)	1.0	
pH_2O (bar)	0.01	0.06
pH_2 (bar)	0.25	0.80
pCO (bar)	0.18	0.70
$pCOxpH_2$ (bar^2)	0.14	0.22
a_C	5.7	57.9
pO_2 (bar)	$1.2x10^{-27}$	$1.3x10^{-24}$
Cr (wt%)	0	46
Mo (wt%)	0	16
Al (wt%)	0	4

a)

Goodness of fit statistics:	
R^2	0.20
Adjusted R^2	0.11
DW	0.6
MSE	0.000
RMSE	0.003
Analysis of variance:	
F	12
Pr > F	< 0.0001

b)

Table III.4a shows the highest and lowest limits of the variables between which the model is valid. The model can be applied on Ni-based alloys $[\%Ni > 50]$ at alloy compositions given in wt..% in the following range: $[0 - 46]$ Cr, $[0 - 16]$ Mo, $\left[0 - 4\right]$ Al, at the temperatures in the $[570 - 650]$°C range under atmospheric pressure, in gas concentrations within the following ranges given in vol.%: $[25 - 80]$ H_2, $[18 - 70]$ CO, $[1 - 6]$ H_2O or the partial pressures product $(pCO\ x\ pH_2)$ between 0.18 and 0.70 bar^2.

Table III.4b shows the goodness of fit statistics of the model. The $R^2 = 0.2$ means that only 20% of the variation of the mass loss rates was explained by the model. The DW = 0.85 shows that the residuals are dependent from each other. The F = 12 and $|Pr > F| < 0.0001$ means that there is not a significant linear relationship between MLr and the set of independent variables (Figure III.33) taken together in the model. The breach of all the assumptions of the linear regression indicates that the model does not work effectively. Therefore, no validation was performed. However important information can be elucidated from this model for further analysis, in order to apply other approaches for the kinetics modeling of metal dusting.

Figure III.33 shows the relative weight of the independent variables: $\frac{1}{T}, pH_2O, (pCO\ x\ pH_2), [Cr], [Mo]$ and $[Al]$ on the MLr. All the variables are consistent with those reported in literature and the previous models for Fe-based alloys and Fe/Ni-based alloys, except for the temperature that shows a contrary effect. However, the model only explains 20% of the variation of the corrosion rates on Ni-based alloys. There is still 80% of the variation not explained. This might be due to the following sources:

- Metal dusting kinetics on Ni-based alloys is not linear, which suggests using other modeling approaches instead linear regression. This would imply the individual analysis of the corrosion rate as a function of the independent variables using nonlinear regressions or nonlinear correlations to be fitted in another linear regression.

- Metal dusting kinetics on Ni-based alloys is controlled by other variables not considered in the model, which suggests including in the database more data regarding to relevant parameters, such as: grain size and surface finish of the materials, and gas velocity. However, this is a difficult task, since there is a few data in literature that reports the variation of these parameters. Therefore more experiments would be needed in a wide range of conditions of these parameters.

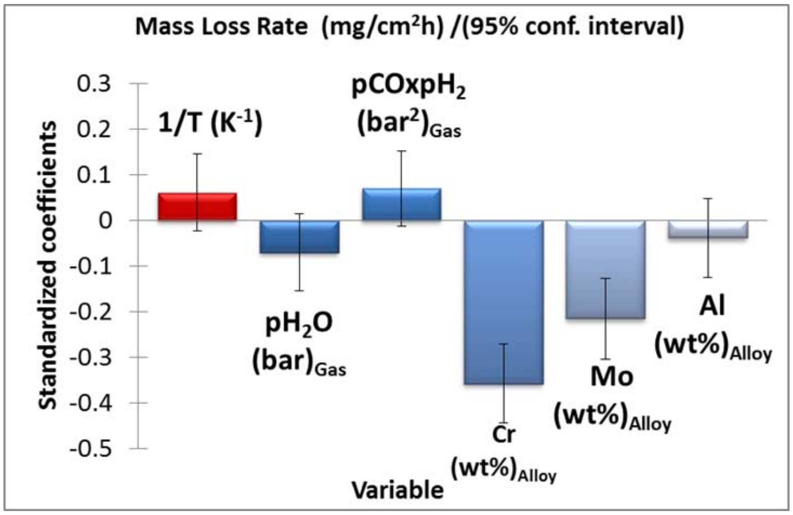

Figure III.33. Standardized coefficients chart: relative weight of the independent variables for the model 3 for the metal dusting kinetics of Ni-based alloys

- The linear model does not adapt well to both kinetics regimes: incubation period and after incubation period. Figure III.34 shows the accuracy chart of the model that represents the residuals between experimental rates and predicted rates. The model does not predict well the highest mass loss rates typically developed after the incubation periods which is the opposite of the observed in the previous models for Fe-based alloys and Fe/ Ni-based alloys. This suggests that most data belong to low corrosion rates developed during the incubation periods which also should be longer for Ni-based alloys. The predictors of the model were calculated based on the setting of most data i.e (incubation rates). Since, the existence of two kinetics regimes is highlighted for Ni-based alloys, the need to separate both parameters as dependent variables (incubation times (IT) and mass loss rates after the incubation period (AIMLr)) is proposed in the next section.

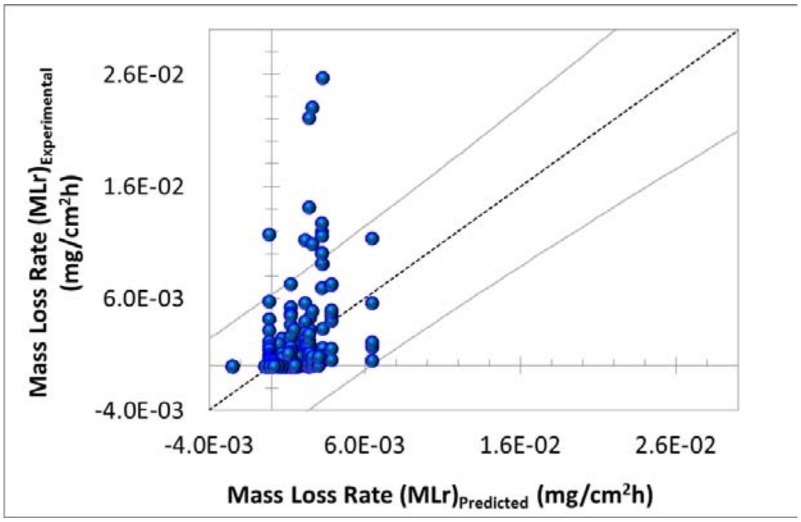

Figure III.34. Accuracy chart with the residuals between experimental values and predicted values by model 3 for the metal dusting kinetics of Ni-based alloys

III.3.2.2 Mass Loss rate after the incubation period (AIMLr)

As explained above, given that the linear model does not adapt well to both kinetics regimes: incubation period and after incubation period, a new modeling approach needs to be developed. This feature leaded to model the incubation times and the mass loss rates developed after the incubation times in a separate way. The extraction of those tests showing both regimes from the original data set was performed. Figure III.35 shows 81 tests from 6 different studies that showed incubation periods clearly defined.[13,22,127,129,130,132,133,137] The kinetics curves were dissected in two parts: the incubation times (IT) and the mass loss region after the incubation times. Mass loss rates (AIMLr) were calculated through the slope of the straight line after incubation for each test.

The histogram in Figure III.36 shows the incubation times developed by each alloy systems under study. We can clearly see that Fe-based alloys exhibit short or no incubation periods (average 400h). Fe/Ni-based alloys have longer incubation periods than Fe-based (average 1600h), and Ni-based alloys have longest incubation periods (average 3000h).

Both data distributions for IT (81 data) and AIMLr (571 data) were treated the same way as the original data set for MLr. As performed in the original data set, high pressures, high activities and cyclic tests were removed from the domain and PCA_S and correlation tests were applied.

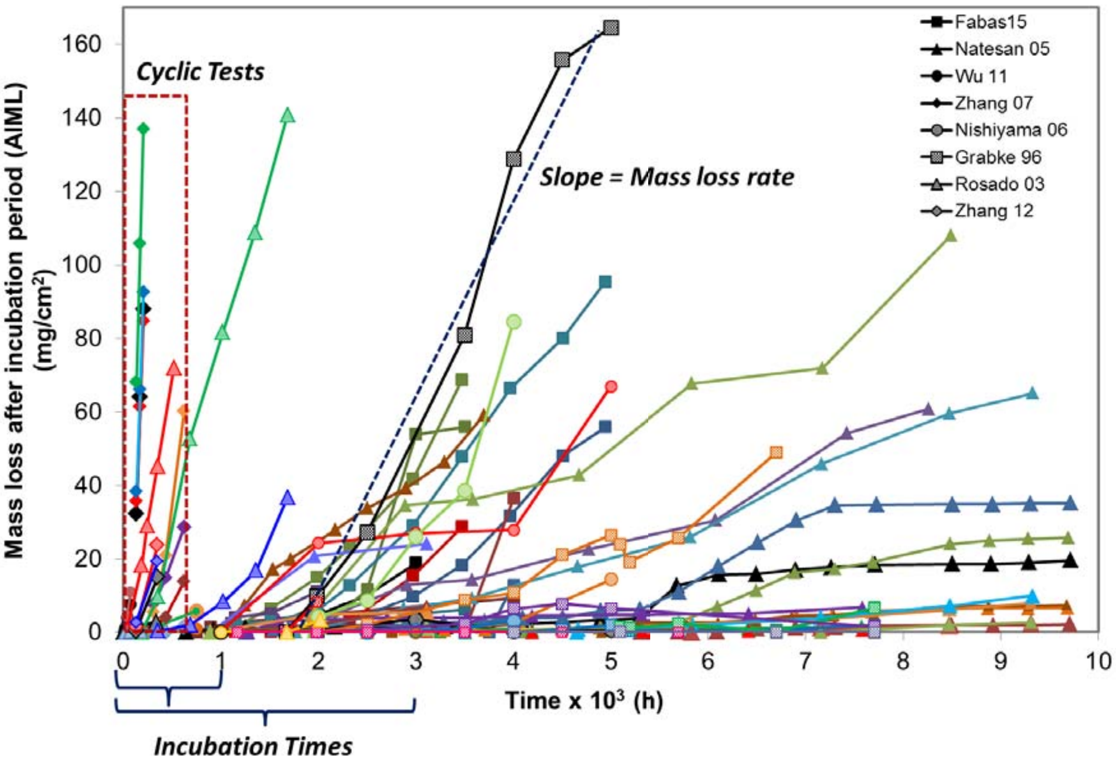

Figure III.35. Metals dusting tests showing incubation times and mass loss rates after the incubation times [13,22,127,129,130,132,133,137].

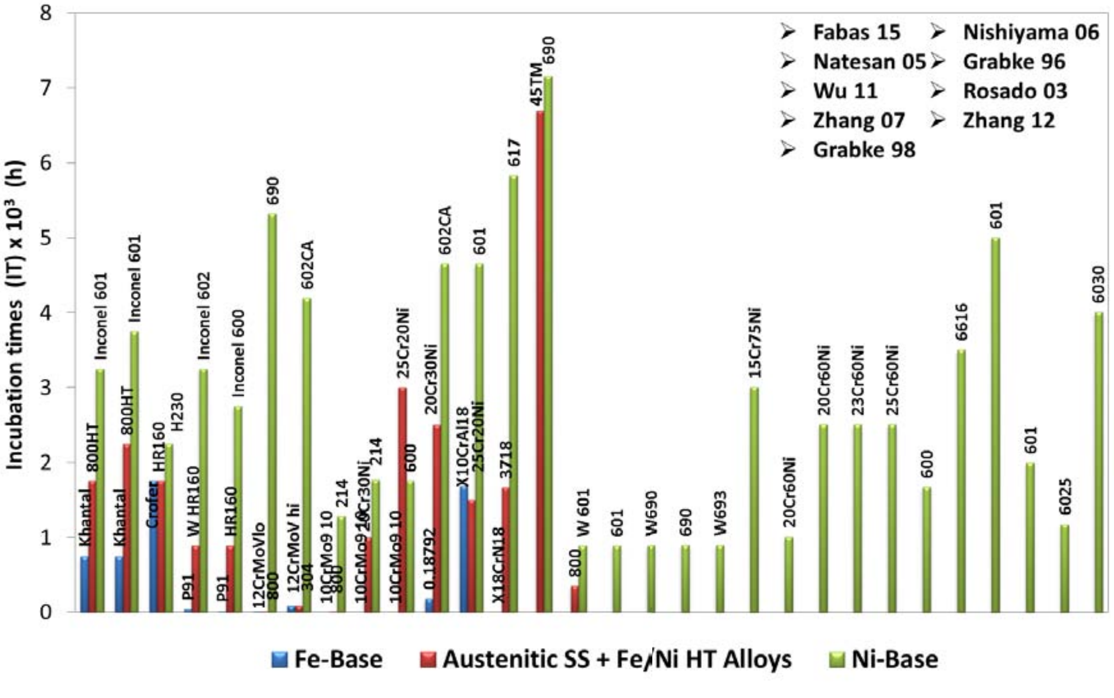

Figure III.36. Incubation times determined from metal dusting tests from Figure III.35

The results of PCA_5, PCA_6 and correlation tests ($CT_{5,6}$) are shown in Appendix II. From PCA_5, both parameters (IT and AIMLr) presented low correlations with respect to the atmosphere conditions, except for IT that showed high correlation with the frequency of thermal cycling. This is expected because high frequencies of thermal cycling produce more damaged in the oxide layers, initially formed on the materials surface. PCA_6 showed that IT is more related to alloy composition than AIMLr, which shows very low correlation with respect to the alloy composition.

Regarding the correlation between independent variables, similar results were obtained to those of mass loss rates (MLr). The independents variables selected to explain IT and AIMLr were: $\frac{1}{T}, pCO\ x\ pH_2$ from the atmosphere conditions and $[Ni], [Cr], [Mo]$ and $[Al]$ from the alloy composition domain. These variables showed the best correlations with IT and AIMLr and were not correlated between them.

The separation of each alloy system for this AIMLr domain was not possible due to the lack of data. Therefore Fe/Ni based alloys and Ni/based, which have an austenitic matrix and exhibited the longest incubation periods, were unified in a single domain in order to have sufficient amount of data for modeling. Fe-based alloys were removed from the domain, and the remaining data set consisted of: IT (55 data) and AIMLr (55 data).

III.3.2.2.1 Model 4 for a) Incubation times (IT) and b) Mass Loss rate after the incubation period (AIMLr)

A model was generated for the two kinetics regimes of corrosion kinetics, which are described by two different dependent variables: incubation times (IT) (55 data) and the corresponding mass loss rate after the incubation period (AIMLr) (55 data). In both cases approximately 75% of the data set was randomly selected to create the model and the remaining 25% of the data set was used to verify the predictive ability of the model. The validation data set was within the model validity domain but not included in the data set used to determine the predictors of the model.

Table III.5a shows the highest and lowest limits for the variables between which the model is valid. Both equations show the same validity domain. These models can be applied on Fe/Ni-based alloys and Ni-based alloys with compositions in the following range given in wt.%: $[10-78]$ Ni, $[0-28]$ Cr, $[0-16]$ Mo, with $[0-4]$ Al, at temperatures in the 570°C – 700°C range, under atmospheric pressure, in a gas concentrations within the following ranges given in vol.%: $[25-80]$ H_2, $[18-70]$ CO, $[1-6]$ H_2O or the partial pressures product ($pCO\ x\ pH_2$) between 0.14 and 0.24 bar^2.

Table III.5b shows the goodness of fit statistics of the model 4a and 4b, the coefficient of determination R^2 varies depending on the dependent variable.

For model 4a (IT), the $R^2 = 0.7$ means that 70% of the variation of IT was explained by the model. The DW = 1.5 shows that the residuals are independent from each other. The F = 16 and $|\Pr > F| < 0.0001$ means that there is a significant linear relationship between the IT and the set of independent variables taken together in the model (Figure III.37a), as a consequence the model is satisfactory. The coefficient F is close to the acceptability limit, which is caused by the large number of variables used to model a small amount of data. However, the variability in the test conditions is significant and the p-value of the model rejects the null hypothesis. Therefore, the predictors are different from zero.

For model 4b (AIMLr), the $R^2 = 0.3$ means that only 30% of the variation on AIMLr was explained by the model. The DW = 0.85 shows that the residuals are dependent from each other. The F = 2.5 and $|Pr > F| > 0.045$ means that there is not a significant linear relationship between the AIMLr and the set of independent variables taken together (Figure III.37b), all these indicators show that the model does not work effectively.

Table III.5. Statistics of model 4. a) Validity domain b) Goodness of fit statistics

Variable	Minimum	Maximum
MLr (mg/cm^{2}h)	0.0	1.14
IT (h)	228	5320
1/T (K^{-1})	10.8	11.9
T (°C)	570	700
$P_{Internal}$ (bar)	1.0	
pH_2O (bar)	0.01	0.06
pH_2 (bar)	0.25	0.80
pCO (bar)	0.18	0.70
$pCOxpH_2$ (bar^2)	0.14	0.24
a_C	5.7	57.9
pO_2 (bar)	1.2×10^{-27}	1.3×10^{-24}
Ni (wt%)	10	78
Cr (wt%)	12	28
Mo (wt%)	0	16
Al (wt%)	0	4

a)

Goodness of fit statistics:		
	Model 4a	**Model 4b**
R²	0.73	0.31
Adjusted R²	0.68	0.30
DW	1.5	1.10
MSE	689944.4	0.04
RMSE	830.6	0.20
Analysis of variance:		
F	16	2.55
Pr > F	< 0.0001	0.04

b)

Equation (48) and (49) explain both kinetics behaviors. Table III.5 shows the models validity domain and the goodness of fit statistics. Figure III.37 shows the relative weights of the variables on the models and Figure III.38 shows the accuracy chart for both models.

Model 4a

$$IT = -8046.5 + 698.2 \times \frac{1}{T} - 11836.1 \times pCOxpH_2 + 31.2 \times [Ni] + 130.5 \times [Cr]$$
$$+191.8 \times [Al] + 116.8 \times [Mo] \qquad \textbf{Equation 48}$$

Model 4b

$$MLr = 9.5 \times 10^{-1} - 5.4 \times 10^{-2} \times \frac{1}{T} + 9.8 \times 10^{-1} \times pCOxpH_2 - 2.5 \times 10^{-3} \times [Ni]$$
$$-1.7 \times 10^{-2} \times [Cr] - 1.2 \times 10^{-2} \times [Al] - 1.3 \times 10^{-2} \times [Mo] \quad \textbf{Equation 49}$$

Where, IT is given in hours (h), $AIMLr$ is given in $\frac{mg}{cm^2h}$, temperature (T) in *Kelvin*, pH_2O, pCO, pH_2 in *bar* and $[Cr], [Mo]$ and $[Al]$ in *wt%.*

Figure III.37a and Figure III.37b show the relative weight of the independent variables: $\frac{1}{T}, (pCO\ x\ pH_2), Ni,\ Cr, Mo, Al$ on the IT and the $AIMLr$, respectively.

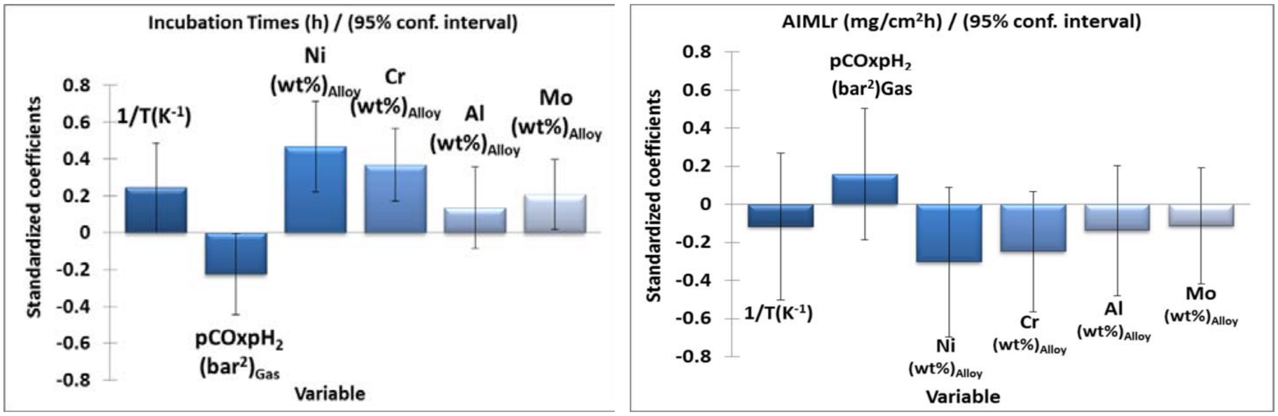

a) **b)**

Figure III.37. Standardized coefficients chart: relative weight of the independent variables for Fe/Ni-based alloys + Ni based alloys on a) model 4a b) model 4b

Model 4a explains 70% of the variation of the incubation times (IT). It is clearly defined that alloy composition plays an important role on the delay of the incubation periods, through its protective ability. Incubation times decrease with temperature and $(pCO\ x\ pH_2)$ in the 570°C -700°C range. Longer incubation times might be translated into lower corrosion rates in time, which corresponds with experimental findings from the authors. [7,10,12,23]

According to the model, in the 1st order of relative significance, there are Ni and Cr. Incubation times increase mostly with increasing the Ni-content in the alloys, which corresponds with experimental findings in the SCAPAC project and from other authors who showed that incubation times are longer for Ni-based alloys. [16,29,30,125] Higher Cr-contents increase incubation times due to the formation of protective Cr-rich oxide films that provide diffusion barriers to carbon and no significant catalytic effect for carbon deposition from the gas. [9,12,17,18,23]

In the 2nd order, there are Al and Mo. Al-oxide layers or Al-rich oxide scales can also increase the incubation times and hence the corrosion resistance. Protective alumina surfaces can be formed on austenitic stainless steel with only 2.5 to 4 wt.% Al and 12 to 15 wt.% Cr (Cr aids in stablishing the alumina surface). Although they are ferritic stainless steel stabilizers, these relative low levels permit stabilization of a strong austenitic matrix microstructure with Ni levels of 12 to 35 wt.%Ni (depending on Al/Cr content). [173–175] However, in the model the effect of Al is twice lower than that of Cr. This could be due to the difficulty of the alumina to form a continuous and protective scale at such low Al-content and such low temperatures, which may hamper the Al-migration to the alloy surface. Mo also delays metal dusting appearance due to the ability to form surface and internal carbides with diffused carbon, which prevents Cr-carbide formation. [6,9]

On the other hand, since the alloy composition also determines the expansion coefficient of the materials, this may affect the duration of the incubation times from the point of view of the oxide layer resistance. The oxide scale may be damaged by thermal cycling tests because thermal stresses are proportional to the thermal expansion mismatch between the substrate and the oxide scale. In this sense, other approaches may be proposed.

The model 4b for AIMLr is improved compared to model 3 for Ni-based alloys for MLr. The AIMLr in model 4b also undergo the estimated effect with respect to the same variables, which is opposite to that of the incubation times. Incubation time decreases with temperature and (pCO x pH$_2$) and increases at higher contents of Ni, Cr, Al, Mo while mass loss rates after the incubation time increase with temperature and (pCO x pH$_2$) and decrease at higher contents of Ni, Cr, Al, Mo. The results obtained are logic and correspond with experimental findings. However, the statistical accountability of the model (30%) is too low to be conclusive. The remaining 70% of the variation of the data might be explained by other variables not considered in the statistical analysis, due to the lack of information. Therefore, these findings need to be confirmed in a larger set of experimental data, especially related to the kinetics of the mass loss after the incubation time. As mentioned above, mass loss measurements may be submitted to high percentages of error. For example, experimental findings by Fabas [125] have shown a preferential attack at the edges of the samples. Other parameters may be more accurate to model metal dusting reaction progress, such as pit depth growth kinetics might be used, as it is described in the next section.

Figure III.38a shows the accuracy chart of the model 4a. The coefficient RMSE = 830 means the standard deviation of the predictions of the model, leading to equation 50. This value indicates the good ability of the model to predict the short and long incubation times along the domain. Figure III.38b shows the accuracy chart of the model 4b. The coefficient RMSE = 0.2 leads to equation 50, which is high and also indicates the deficiencies of the model.

$$\boldsymbol{IT_{Experimental} = IT_{Predicted} \pm 830\ h} \qquad \textbf{Equation 50}$$

$$\boldsymbol{AIMLr_{Experimental} = AIMLr_{Predicted} \pm 0.20\ \frac{mg}{cm^2 h}} \qquad \textbf{Equation 51}$$

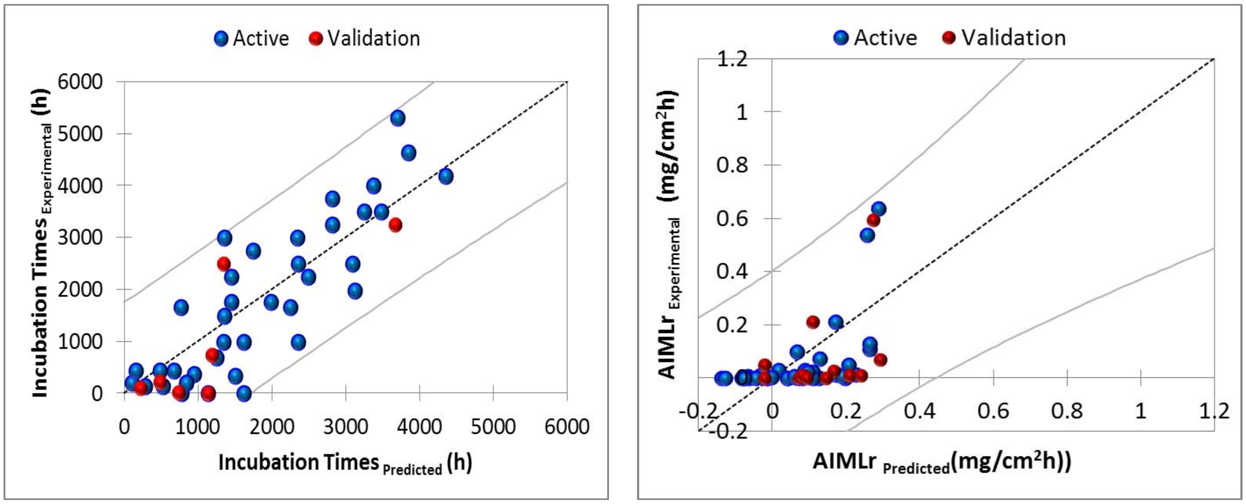

a) b)

Figure III.38. Accuracy chart with the residuals between experimental values and predicted values a) model 4a (IT) b) model 4b (AIMLr) for Fe/Ni-based alloys + Ni based alloys

III.3.2.3 Pit depth growth rate (PDGr)

Given that mass loss kinetics for Fe/Ni-based alloys and Ni based alloys, is not always representative of the material resistance to metal dusting, even when incubation times are considered; similar procedures were applied for modeling the pit depth growth rate (PDGr), which is the second parameter more numerous in the database. This also follows up the experimental findings of Fabas [125] who showed that pit depth growth kinetics is more reliable and provides more information than mass loss kinetics. Figure III.39 shows 385 pit depth growths measured as a function of time for 41 commercial alloys evaluated in 67 metal dusting tests from 6 different studies. [27,29,30,127,129,132]

As the previous procedure for MLr, Figure III.40 shows the three alloy systems present in the main domain for PDGr. The 41 commercial alloys evaluated were classified into three systems: Fe-based alloys, Fe/Ni based alloys and Ni/based alloys. For Fe-based alloys there was only a Fe-Cr-Al alloy (alloy 956) that was removed from the main domain, in order to equalize the domain to that evaluated in model 4 for IT and AIMLr. Fe/Ni based alloys and Ni/based alloys were grouped in the same domain to analyze PDGr, as shown in the Figure III.40.

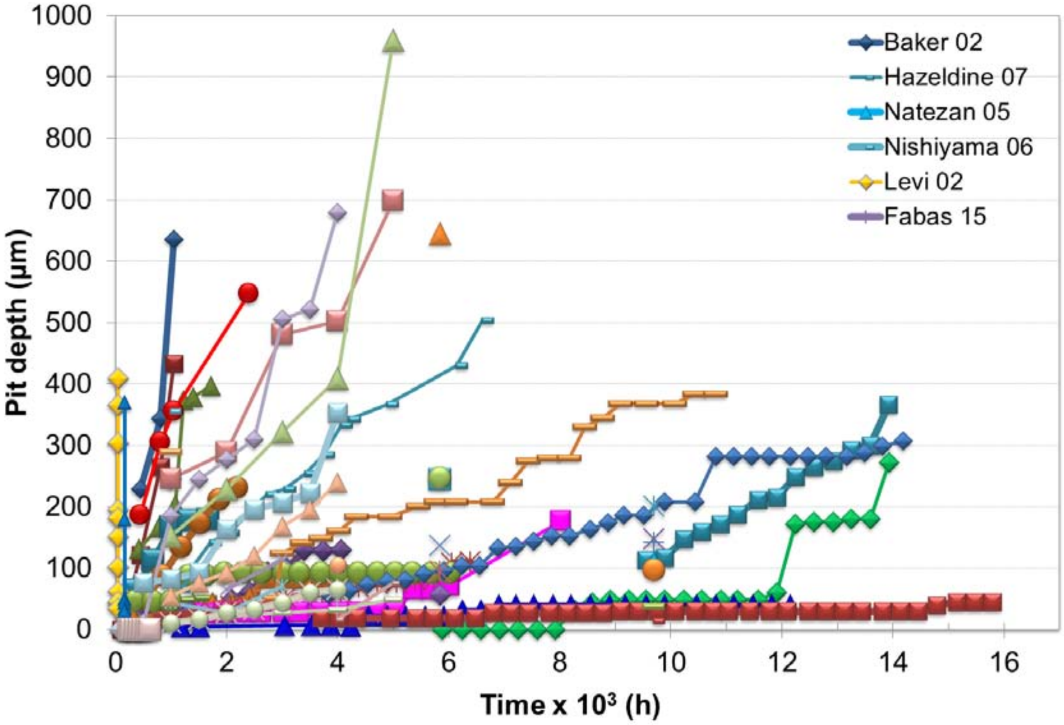

Figure III.39. Pit depth as a function of time [27,29,30,127,129,132]

The data distribution for $PDGr$ (360 data) was treated the same way as the original data set for MLr except that no high pressures were removed, because there was enough pressure data to be included in the modeling process. Likewise, there were neither high activities nor high frequency thermal cycling tests acting as outliers to be removed from the domain. PCA$_{7,8}$ and correlation tests CT$_{7,8}$ were also performed (shown in Appendix III.A). The independents variables selected to explain $PDGr$ were: $\frac{1}{T}, P_{internal}$, $(pCO\ x\ pH_2)$ from the atmosphere conditions and $[Ni], [Cr], [Mo]$ and $[Al]$ from the alloy composition. These variables showed the best correlations with $PDGr$ and were not correlated with one another.

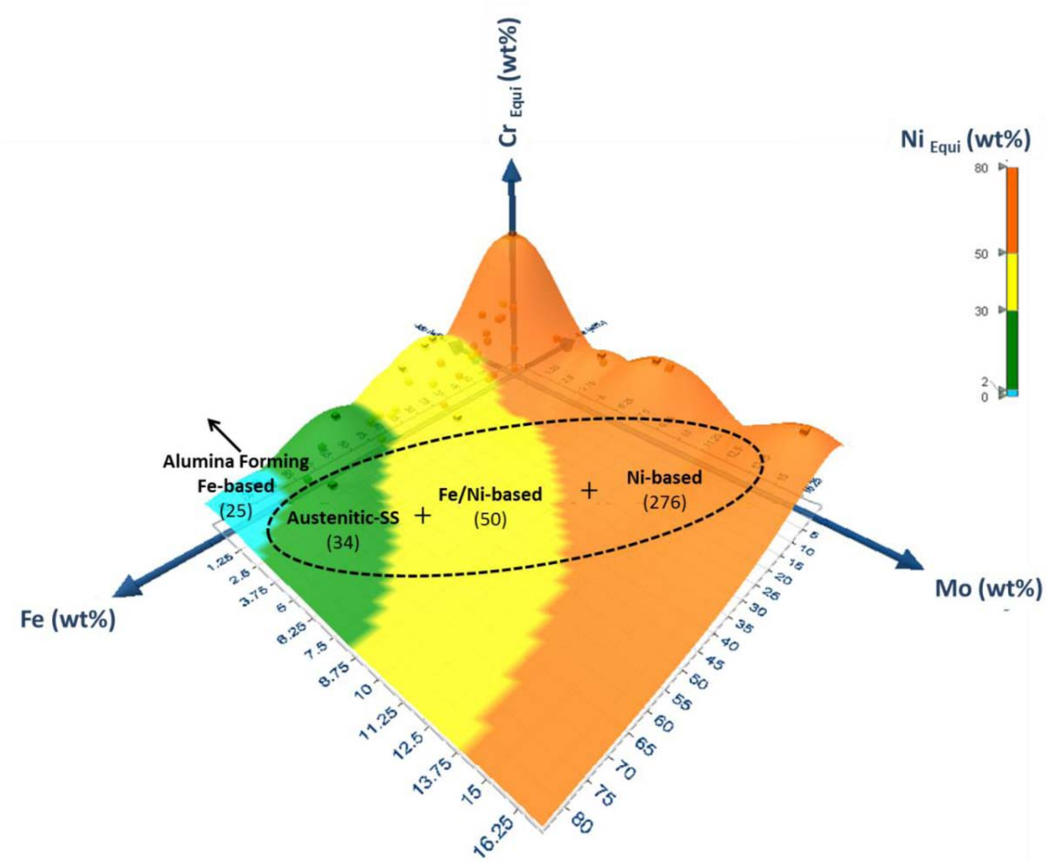

Figure III.40. Distribution of the alloy composition as a function of Fe-$\mathrm{Ni_{Eq}}$-$\mathrm{Cr_{Eq}}$-Mo: PDGr materials domain and its classification into three groups of alloy systems. [27,29,30,127,129,132]

III.3.2.3.1 Model 5: Pit depth growth rate (PDGr)

A model was generated from the PDGr data set (360 data). Approximately 50% of the data set was randomly selected to create the model. The model is described by equation (52). In order to validate the model, the remaining 50% of the data set was used to verify the predictive ability of the equation. The validation data set was within the model validity domain but not included in the data set used to determine the predictors of the equation. Table III.6 shows the model validity domain and the goodness of fit statistics. Figure III.41 shows the relative weights of the variables in the model and Figure III.42 shows the accuracy chart of the model.

$$\boldsymbol{PDGr = 2.2 - 2 \times 10^{-1} \times \frac{1}{T} + 8.6 \times 10^{-2} \times P_{Internal} + 6.4 \times 10^{-1} \times pCOxpH_2}$$

$$\boldsymbol{-3.9 \times 10^{-3} \times [Ni] - 2.6 \times 10^{-3} \times [Cr] - 2.5 \times 10^{-3} \times [Al] - 4.1 \times 10^{-3} \times [Mo]} \quad \textbf{Equation 52}$$

Where, $PDGr$ is given in $\frac{\mu m}{h}$, temperature (T) in *Kelvin*, $P_{Internal}, pCO, pH_2$ in *bar* and $[Ni], [Cr], [Mo]$ and $[Al]$ in *wt%.*

Table III.6a shows the highest and lowest variable limits between which the model is valid. This model can be applied on austenitic stainless steels, Fe/Ni based alloys and Ni-based alloys at the following compositions ranges given in wt.%: $[12 - 78]$ Ni, $[14 - 46]$ Cr, $[0 - 3.7]$ Al, $[0 - 16]$ Mo, at temperature in the $[450\ -\ 650]$°C range, at total pressures (1-30 bar), in a gas partial pressures within the following ranges (bar): $[0.2 - 9.4]$ H_2, $[0.01 - 0.08]$CO, $[1x10^{-15} - 44]$ H_2O or the partial pressures product $(pCO\ x\ pH_2)$ between 0.01 and 21 bar^2.

Table III.6b shows the goodness of fit statistics of the model. The $R^2 = 0.98$ means that 98% of the variation of the mass loss rates was explained by the model. The DW = 0.7 shows that the residuals are dependent from each other. The indicators F = 1009.5 and $|Pr\ >\ F| < 0.0001$ means that there is a significant linear relationship between the MLr and the set of independent variables (Figure 41) taken together in the model, the model is satisfactory from the statistical point of view.

Table III.6. Statistics of model 6. a) Validity domain b) Goodness of fit statistics

Variable	Minimum	Maximum
MLr (mg/cm^2h)	$2x10^{-3}$	6.3
1/T (K^{-1})	10.8	13.8
T (°C)	450	650
$P_{Internal}$ (bar)	1	30
pH_2O (bar)	$1x10^{-15}$	44.2
pH_2 (bar)	0.20	9.40
pCO (bar)	0.01	0.08
pCO x pH_2 (bar^2)	0.02	5.72
a_C	10	7600
pO_2 (bar)	$1.2x10^{-34}$	$6.1x10^{-25}$
Ni (wt%)	12	78
Cr (wt%)	14	46
Al (wt%)	0	3.7
Mo (wt%)	0	16

a)

Goodness of fit statistics:	
R²	0.98
Adjusted R²	0.97
DW	0.70
MSE	0.01
RMSE	0.09
Analysis of variance:	
F	1009.5
Pr > F	< 0.0001

b)

Figure III.41 shows the relative weight of the independent variables: $\frac{1}{T}, P_{Internal}, (pCO\ x\ pH_2), [Ni], [Cr], [Mo]$ and $[Al]$ on the $PDGr$. Pit growth rates increase with the atmosphere conditions in the 1st order of relative significance: the temperature and $(pCO\ x\ pH_2)$ in the temperature range 450°C-650°C which corresponds with experimental findings from the authors. [7,10,12,23] In this case we can clearly see the high dependence on $P_{Internal}$, which also corresponds with the few studies performed at high pressures. [27] The accelerating effect of $P_{Internal}$ and $(pCO\ x\ pH_2)$ stands out in the model, and the effect of alloy elements in pits growth is very low.

The increase of PDGr with $P_{Internal}$ of the system as well as $(pCO\ x\ pH_2)$, is consistent with the results of experimental tests by Fabas in SCAPAC project, [125] who found that PDGr in 800HT alloy at 21bar and $(pCO\ x\ pH_2 = 27)$ is 2 to 5 times higher than PDGr at 1 bar. At atmospheric pressures the pit nucleation may depend on the sample geometry, Cr depletion zones and local defects on the oxide layer, at high pressures all these areas are susceptible to be activated faster and at the same time. The effect of the sample geometry can be eliminated when the experiments only deal with pits formed far away from corners and edges. Higher pressure implies a faster kinetics of attack. Figure III.39 shows constant pit depth growth kinetics in most tests. Fabas [125] showed elliptical pits at high pressures, growing at constant rate.

Pit depth rates slightly decrease in alloys with higher Ni-contents followed by Cr, Mo and Al (negligible influence even when there is a high content). The effect of these elements has already been explained before. Cr protects the alloy by chromium rich oxide films [9,12,17,18,23] that provide diffusion barriers to carbon diffusion. Mo promotes internal carbides formation with diffused carbon [6,9] and the Al form protective alumina scales against carbon diffusion. However, the protective effect of these elements seems to become negligible in front of the pressures increase, which is not the case observed in the previous models at atmospheric pressure. In metal dusting environments pO_2 is already low at the alloy surface, so in the bottom of a pit where the atmosphere renewal is difficult, less O_2 might be available to oxide forming. This is also consistent with Fabas [125] microstructural analyses in which no protective scale are observed at the bottom of the pits, instead a severe attack by graphitization is found.

It can be concluded that once the pit nucleates and begins to grow, the effect of alloying elements promoters of protective layers formation is very restricted. Therefore, environment conditions determine the aggressiveness of the metal dusting corrosion once the protective scales have disappeared. Only the strongest and most stable austenitic matrix can slow the process slightly.

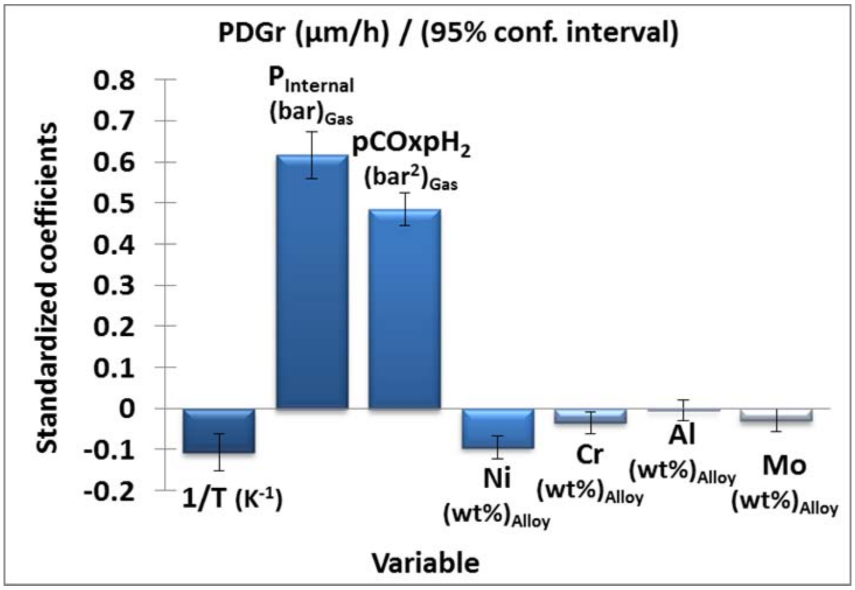

Figure III.41. Standardized coefficients chart: relative weight of the independent variables on model 5 for Fe/Ni-based alloys + Ni based alloys

Figure III.42a and Figure III.42b show the accuracy chart of the model that represents the residuals between experimental values and predicted values for PDGr. The coefficient RMSE = 0.09 means the standard deviation of the predictions of the model, leading to equation 53. The model shows satisfactory results for predicting both low rates at atmospheric pressure and high rates at high pressures. However, PDGr at high pressures in the database belong to austenitic stainless steels with low resistance to metal dusting environments. More experiments at high pressures are required for Ni-based alloys to balance the regression line respect to $P_{Internal}$.

$$\boldsymbol{PDGr_{Experimental} = PDGr_{Predicted} \pm 0.09\ \frac{\mu m}{h}} \qquad \textbf{Equation 53}$$

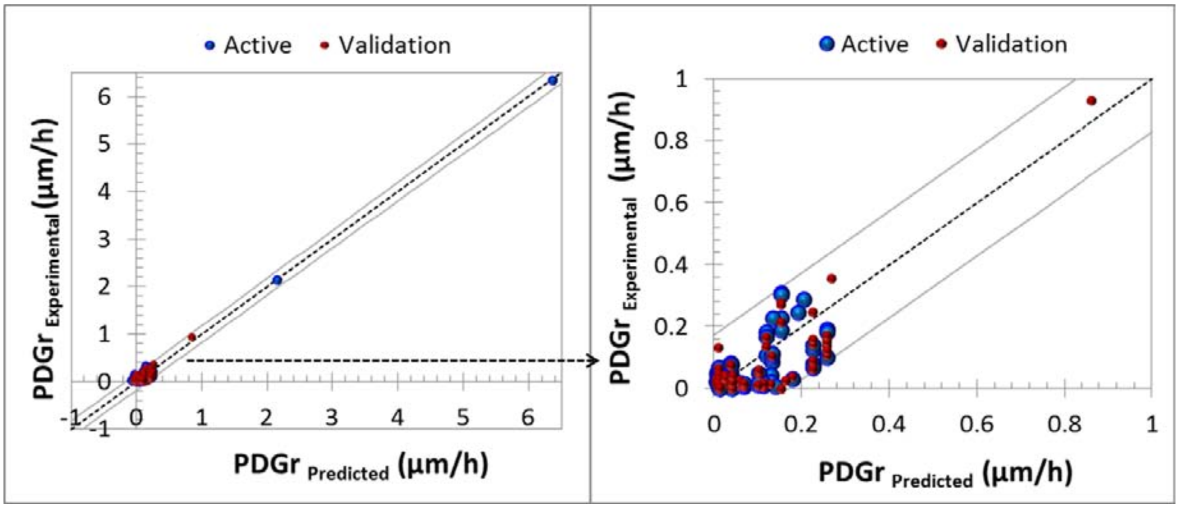

a) b)

Figure III.42. Accuracy chart with the residuals between experimental values and predicted values for model 5 a) Normal scale b) magnified mode for Fe/Ni-based alloys + Ni based alloys

III.4 Conclusions

A statistical method was successfully implemented in this study to determine the most significant variables for modeling of metal dusting kinetics in a wide range of conditions. The effect of the temperature 1/T, $(pCO\ x\ pH_2)$ and the alloying elements, such as Ni, Cr, Al, and Mo played an important role in metal dusting kinetics, for all the dependent variables used to quantify the phenomenon. However, mass loss rates in high performance alloys were difficult to model by multiple linear regressions due to the following possible causes: a) error sources caused by the variability of the experimental procedures b) metal dusting kinetics on Ni-based alloys may not be linear, which suggests using other modeling approaches instead linear regression c) metal dusting kinetics on Ni-based alloys is controlled by other variables that were not considered in the model because of the lack of data reported in literature, such as: grain size and surface finish of the materials, and gas velocity.

The linear models determined in this study, indicate that the alloy composition plays an important role in the delay of the metal dusting attack i.e. on the incubation periods. The protective capacity of the alloys can extend the incubation period previous to the attack. However, once the attack begins and pits nucleate, the alloying elements such as Cr or Mo may be concentrated in carbides or internal oxides, leaving the matrix of pure Fe and/or Ni. Therefore, the environment conditions determine the aggressiveness of the metal dusting corrosion after incubation (pit morphology and pits growth rate). More experiments are required at high pressures to strengthen the model for Ni-based alloys in a wide range of pressures.

The goal here was to show the reliability and the efficiency of statistical methodologies applied on laboratory tests with promising potential at the industrial scale. These results were obtained with a large database of laboratory experiments and the models developed agree with the data previously obtained from literature. However, some models presented very low percentages of explanation, which suggest the need to keep adding more data to the database related to those variables that are poorly reported in literature and can be relevant to the corrosion mechanisms. More experiments at high gas velocities as well as grain size and surface finish need to be further reported in studies.

It was shown that the lack of data at high pressure limits representing the effect of high pressures in a wide range of gas compositions. Concerning the correlated effect of pCO and pH_2 and the application of $pCOxpH_2$ for modeling, this may be modified by using Ar dilution in metal dusting experiments in order to assess independently the effect of these two variables in the models.

Concerning the effect of thermal cycling, it was seen that there is an information gap between low frequency tests and high frequency tests. Since, a high correlation was found between the incubation time and the thermal cycling frequency, this appears to be an important experimental parameter to include in modelling. However, the influence of this parameter is not often recognized in experimental studies, which sometimes do not use a constant frequency and do not report this information on their published research. This remark is also emphasized for the gas velocity in experimental studies.

Chapter 4. Modeling of high-temperature corrosion rate

Contents

IV Chapter 4. Modeling of high-temperature corrosion rate

In this chapter, we begin with a discussion on the experimental results of high-temperature corrosion tests obtained in the ANR SCAPAC Project by E.Schaal. [126] This is followed by the results of the statistical analyses performed to create the lifetime predictive models for high-temperature corrosion. Finally, the statistical results obtained from the database have been discussed and compared with experimental findings from literature, in order to select the variables for modeling over the different scenarios proposed.

IV.1 Experimental results

High-temperature corrosion rate was measured by the maximum thickness loss (MTL) undergone during one cycle test. Figure IV.1 shows the residual thickness measured on alloy HR120 after a 500h corrosion test under isothermal conditions in flue gas (8 vol.% O_2 – 18 vol.% H_2O – 1100 ppm HCl – 110 ppm SO_2). The maximum thickness loss rate (MTLr) was calculated according to equation (52).

$$\boldsymbol{MTLr} = \frac{\boldsymbol{t_i - t_r}}{\boldsymbol{Test\ duration}} \qquad \textbf{Equation 54}$$

Where MTL is given in $\left(\frac{mm}{y}\right)$, initial thickness t_i and residual thickness t_r are given in mm and the duration of the tests given in years (A year = 8000h)

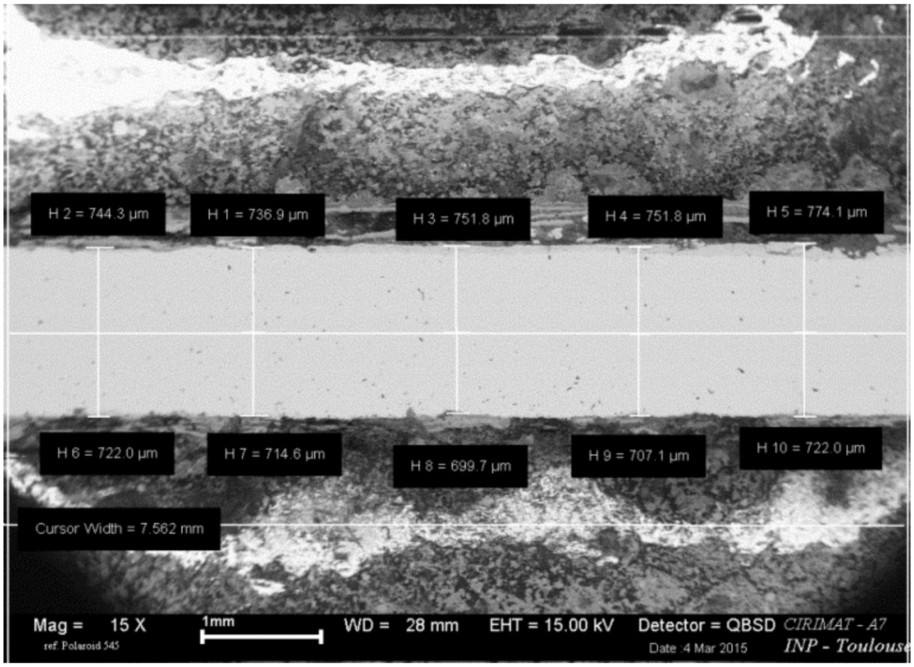

Figure IV.1. Thickness loss measured: HR120 T=600°C Ash n° 5 in flue gas.

Figure IV.2a shows the MTLr as a function of time of the different alloys evaluated, according to the test protocol given in Table II.11. Due to the high variability of materials and conditions, few comparisons must be made. In general, if we consider the 16Mo3 alloy as a reference in laboratory air, we can see that the corrosion rates increase with temperature. In most cases, the tests show reproducible results. Except for some particular cases (Figure IV.2b) that were performed at the same condition and show high standard deviations > 50% (a). Similarly, some tests performed at the same condition at different dwell times (Figure IV.2c) show that corrosion rates decrease with increasing time, showing standard deviations > 100%. This tendency is more pronounced at 550 °C (c). This fact indicates the importance of having reproducible results in corrosion tests to establish good comparisons, as well as to determine the kinetics law of the corrosion process in order to have more accurate predictions. This effect has been already reported for Kawahara [103,108] who analyzed the corrosion kinetics following linear and parabolic regimes, obtaining better results in linear regime.

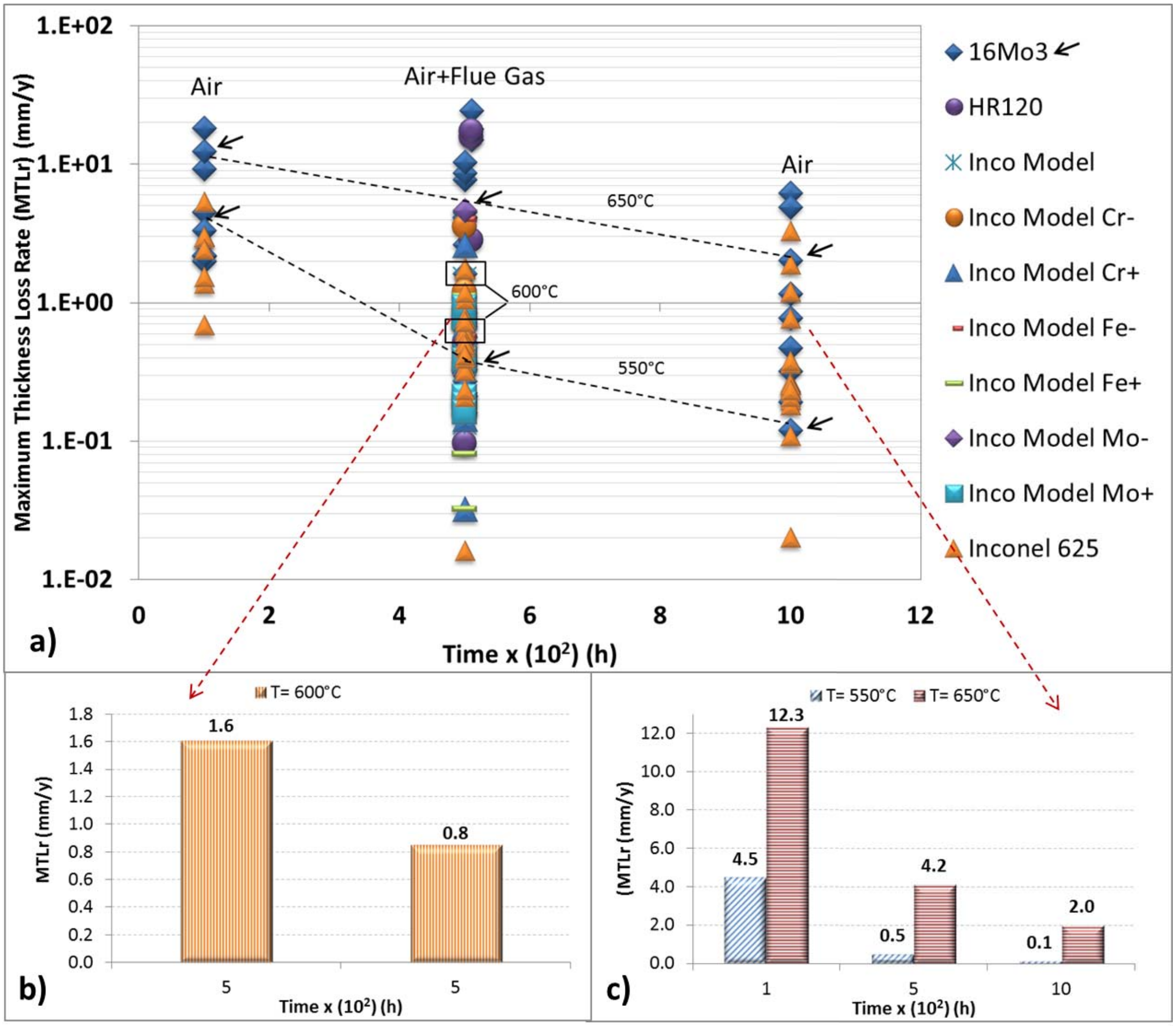

Figure IV.2. Maximum thickness loss rates (MTLr) undergone by the alloys during one cycle test at different conditions.[138]

From the experimental results obtained in the framework of the E. Schaal's thesis, correlation tests were performed as a function of the parameters that showed more than 4 values in the variability of conditions. Figure IV.3 shows the linear correlation coefficients (r) of the MTLr as a function of the temperature (°C), the main alloy elements (wt.%) and the ash elements (wt.%). The chart shows two scenarios: the tests performed in laboratory air at the temperature range (450-650 °C) and the tests performed in flue gas atmospheres at constant temperature (600°C). The first scenario shows that corrosion rates increase with temperature. Both scenarios show that alloys with higher Ni/Fe ratio show increased high-temperature resistances, as well as we can clearly see the suppressive effect of Cr, Mo, Si. This effect has been already reported in literature. [36,37,62,96,97,101] These correlations are higher in flue gas atmospheres. For the ash elements, the correlations were low and also inconsistent with experimental results, this can be attributed to insufficient ash compositions evaluated.

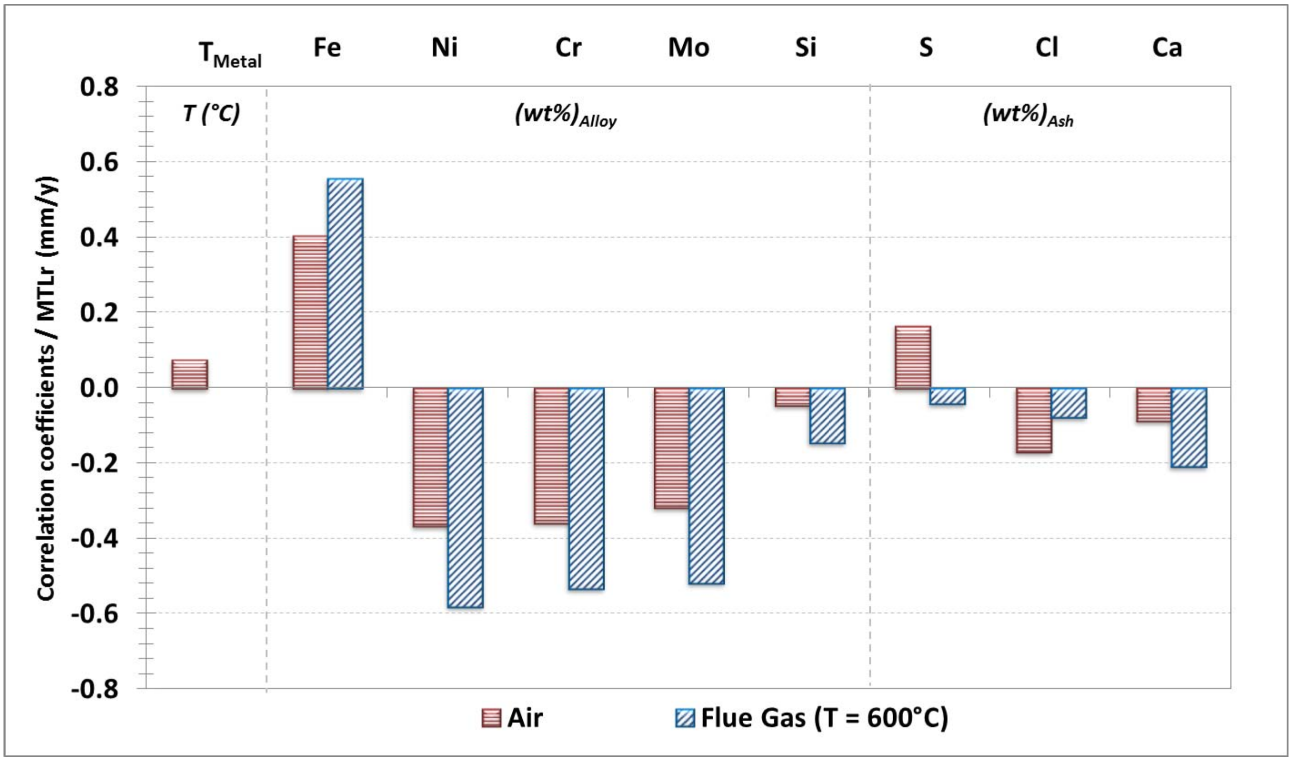

Figure IV.3. Correlation coefficients (r) obtained from correlation tests as function of the variables with a variability ≥ 4 for experimental results obtained in the E. Schaal's thesis.[126]

All the experimental results obtained in the E. Schaal's thesis [126] were included in the high-temperature database in the framework of the SCAPAC project. These results were unified with data from the literature, as described in section II.2.2, for further statistical treatment that will be described in the next section.

IV.2 Raw database

Approximately 118 metallic materials were added to the database, including pure metals, binary alloys, coatings, ternary model alloys and commercial alloys. Figure IV.4 shows a 3D diagram with the different materials added to the database located in the diagram as a function of their main elements Fe-Ni-Cr-Mo.

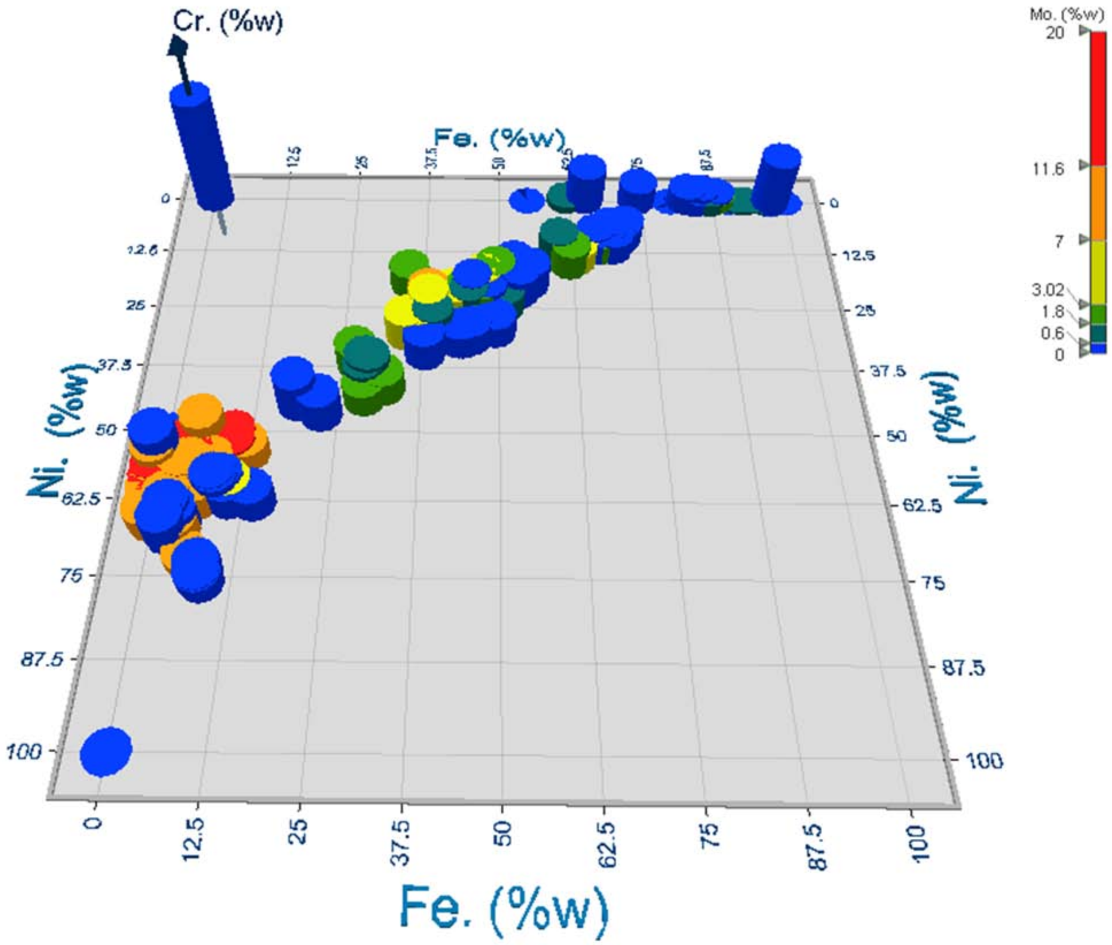

Figure IV.4. 3D diagram with the different materials added to the high-temperature corrosion database as a function of Fe-Ni-Cr-Mo

Figure IV.5 shows the box plot analysis applied to the chemical composition of the materials included in the database. The box plot identifies the variance of the data distribution and its outliers. In the case of the main elements, the Fe-composition range is wider than that of Ni. The variance of Cr is low and presents an outlier in the data distribution belonging to corrosion tests performed on pure Cr (100%). In all three data sets Fe, Ni and Cr as pure metals are abnormal cases in the data distribution (a,b,c). Al-outliers belong to FeAl and NiAl model alloys (d). All outliers are atypical cases in the materials population. In order to avoid source of errors or disturbance in the calculations generated by uncommon alloy systems, pure metals and binary alloys were excluded of the materials domain, only commercial alloys and ternary model alloys were selected for statistical analysis.

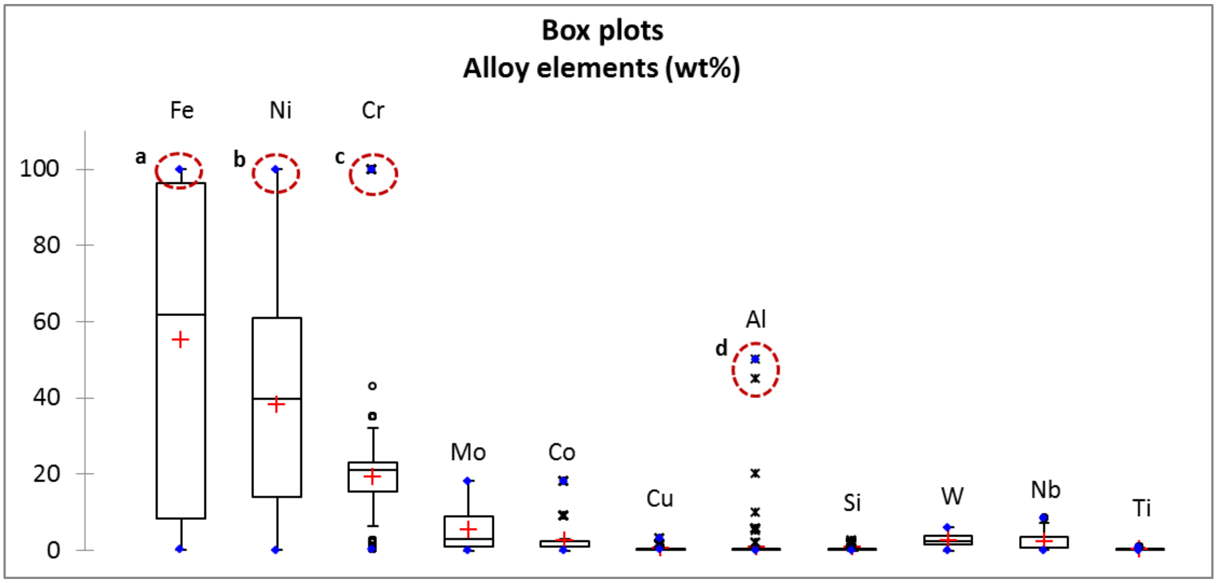

Figure IV.5. Box plot applied to the chemical composition of the materials added to the high-temperature corrosion database.

IV.3 Statistical modeling

The experimental results obtained in the E. Schaal's thesis [126] in the ANR SCAPAC project covered the analysis of 12 different materials, two atmosphere conditions and five different ash compositions at different temperatures. However, to achieve the objective of creating a lifetime prediction models in a wide range of conditions, the amount of data was insufficient. In order to create a model by linear regression that estimates the relative weight of the variables involved on the high-temperature corrosion process, the experimental results obtained in the framework of the project were unified with the literature results included in the high-temperature corrosion database. The database construction was explained in the section II.2.2 of this document.

After quantifying the different dependent variables to be modeled in section II.2.2.2, it was concluded that most corrosion rates results are expressed in maximum thickness loss rate (MTLr) (mm/y). As a consequence of this large population, this magnitude seemed most likely to be used as the dependent variable for modeling. This parameter allows us to analyze different scenarios and develop a model capable to be refined according to the environment of interest.

As shown in Table IV.1, MTLr is the dependent variable Y_i to be explained by three groups of variables (X_i), through a multiple linear regression equation whose structure is shown in Figure IV.6. In the schema MTLr is the output variable $(\boldsymbol{Y_i})$ explained by the most important variables to be chosen from each group of independent variables $(\boldsymbol{X_i})$: atmosphere conditions, alloy composition and ash composition.

Table IV.1. Dependent variable to be modeled by explanatory variables organized by group.

Y_i	Group	X_i
MTLr (mm/y) [(a)]	Atmosphere	$T_{\text{Flue gas}}$, T_{Metal},[(c)] O_2, H_2O, CO_2,[(d)] HCl, SO_2[(e)]
	Alloys	Fe, Ni, Cr, Mo, Co, Cu, Al, Si, W, Nb, Ti, Mn, C[(b)]
	Ash	S, Cl, Ca, Na, K, Pb, Zn, Si, Al, P, Fe[(f)]

[(a)] Maximum thickness loss rate (MTLr) (mm/y), [(b)] (wt%) alloy, [(c)] (°C), [(d)] (vol%) gas, [(e)] (ppm) gas, [(f)] (wt%) ash.

$$\overbrace{\boldsymbol{Y_i}}^{\substack{\text{Output variable}\\ \textbf{Corrosion Rate}}} = \underbrace{\boldsymbol{\beta_0}}_{\text{Intercept}} + \underbrace{\underbrace{\boldsymbol{\beta_1 X_1} + \boldsymbol{\beta_2 X_2}}_{\text{Atmosphere}} + \underbrace{\boldsymbol{\beta_2 X_2} + \boldsymbol{\beta_3 X_3}}_{\text{Alloys}} + \underbrace{\boldsymbol{\beta_4 X_4} + \boldsymbol{\beta_p X_p}}_{\text{Ash}}}_{\text{Input variables}} + \underbrace{\boldsymbol{\varepsilon_i}}_{\text{Residuals}}$$

Figure IV.6. Structure of the multiple linear regression equation for high-temperature corrosion models.

IV.3.1 Data filtering and variables selection

IV.3.1.1 Maximum thickness loss rate (MTLr)

For modeling MTLr as the dependent variable, all maximum thickness loss rates (MTLr) and the associated test set-ups in sixteen different studies, were analyzed by statistical methods. Figure IV.7shows approximately 867 MTLr calculated as a function of time on 72 materials submitted to different tests conditions from 400 laboratory and industrial tests [49,51,74,75,78,89,104,110,138,140–142,144,147,148,154]. Most data comes from short term tests performed up to 2000 h which are the most aggressive. Only 25% of the tests come from long-term tests performed up to 16000 h. The 51% of data come from laboratory tests and 49% come from industrial tests, which tend to have lower corrosion rates. Comparison patterns cannot be established due to the variability of conditions. This data set (867 MTLr) was successively explained by three groups of variables as indicated in Table IV.1.

In order to establish the criteria for filtering treatment and variable selection, a first exploratory analysis was performed using the statistical techniques: Principal Component Analysis (PCA) and correlation tests (CT_S).

Principal Component Analysis (PCA) was applied to find patterns and correlations between the independent variables that explain MTLr. The dependent variable MTLr was included in the analysis as supplementary variable in order to determine the intensity and direction of the linear correlation of MTLr as a function of each independent variable. As a result, the linear correlation coefficients (r) were obtained.

Correlation tests (CT_S) were applied to visualize the linear correlation coefficients (r) obtained in the PCA_s, to identify the outlier's location and to analyze its effect on the corrosion behavior, through correlation diagrams. In the diagrams, red data indicate positive correlations and blue data indicate negative correlations.

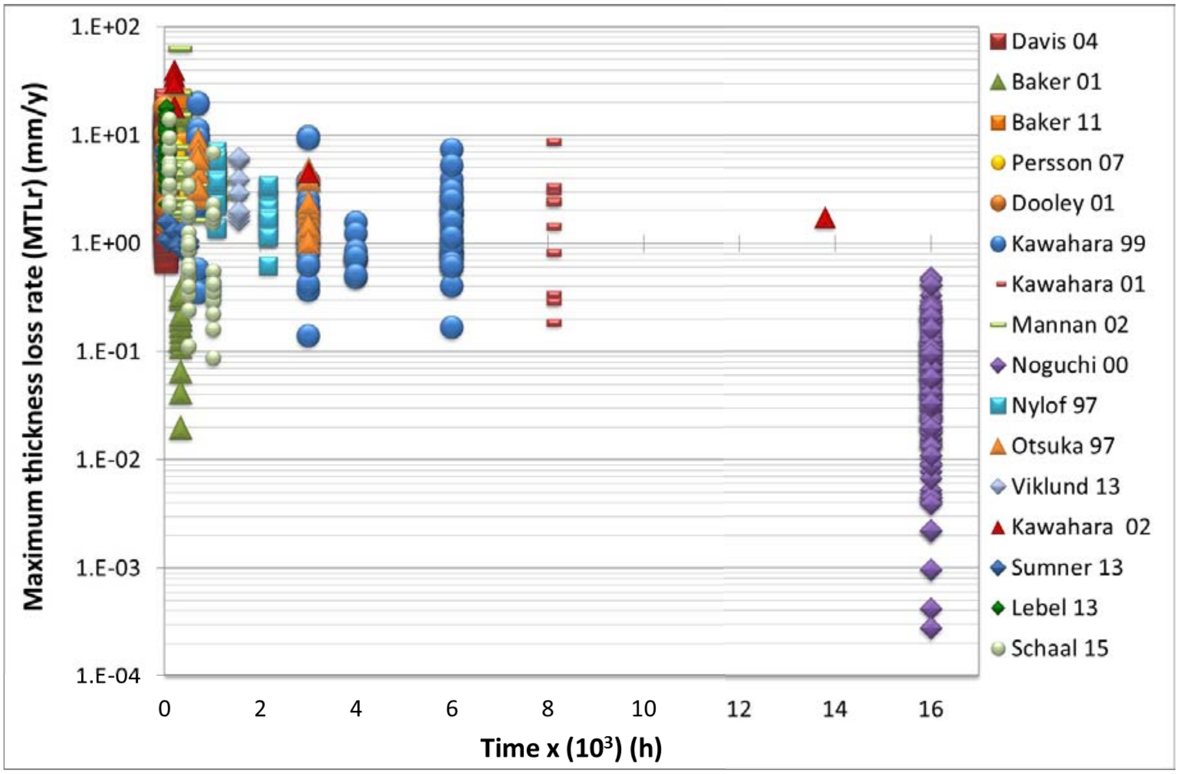

Figure IV.7. Maximum thickness loss rate (MTLr) as a function of time measured from 876laboratory and industrial tests from 15 studies. [49,51,74,75,78,89,104,110,138,140–142,144,147,148,154]

IV.3.1.1.1 Principal Component Analysis and Correlation Tests

The PCA_s and CT_s were performed by groups of variables depending on the type of information. As shown in Table IV.2. PCA_1/CT_1 were applied on conditions related to the test environment such as metal temperature and gaseous phase characteristics, PCA_2/CT_2 were applied on alloy composition, and PCA_3/CT_3 were applied on ash chemical composition in elemental form (compound compositions were converted to their elemental form to homogenize further treatment, as it was explained in section II.2.2).

Table IV.2. Principal Component Analysis (PCAs) by group of explanatory variables

PCA/CT Analysis	Active Variables	Supplementary Variable
PCA_1/CT_1: Environment (Gas composition + Tests Conditions)	T_{Metal},$^{(b)}$ O_2, H_2O, CO_2,$^{(c)}$ HCl, $SO_2$$^{(d)}$	MTLr$^{(a)}$
PCA_2/CT_2: Alloys nominal composition	Fe, Ni, Cr, Mo, Co, Cu, Al, Si, W, Nb, Ti, Mn, C$^{(e)}$	MTLr$^{(a)}$
PCA_3/CT_3: Ash chemical composition	S, Cl, Ca, Na, K, Pb, Zn, Si, Al, P, Fe$^{(f)}$	MTLr$^{(a)}$

$^{(a)}$ *Maximum thickness loss rate (MTLr) (mm/y),* $^{(b)}$ *(°C),* $^{(c)}$ *(vol%) gas,* $^{(d)}$ *(ppm) gas,* $^{(e)}$ *(wt%) alloy* $^{(f)}$ *(wt%) ash.*

Figure IV.8 shows PCA_1 for atmosphere conditions that include temperature and gas phase compositions applied on the original data set (867 test results) with 69% of cumulative variability. Correlation tests diagrams corresponding to interaction with the MTLr is shown in Figure IV.9. PCA_1/CT_1 correlation matrix is given in Appendix IV.A. Correlation coefficients (r) in bold indicates that the p-value associated with the regression coefficient is inferior to <0.05 (statistically significant). The PCA_1 score plot may be interpreted in the following manner:

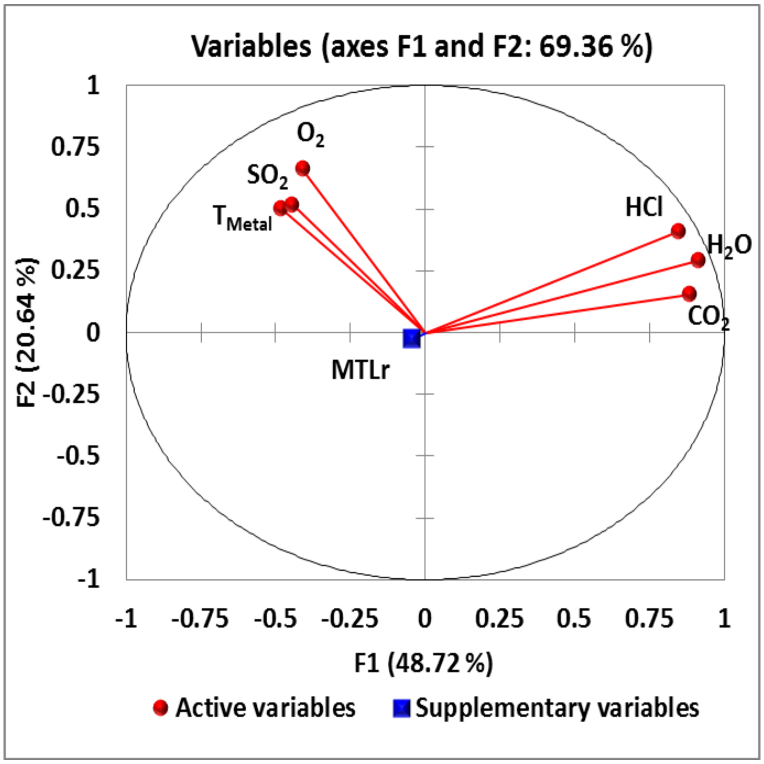

Correlations (r)

Variables	MTLr (mm/y)
T_{Metal} (°C)	**0.24**
O_2 (vol.%)	**-0.21**
H_2O (vol.%)	-0.03
CO_2 (vol.%)	**-0.09**
HCl (ppm)	**0.13**
SO_2 (ppm)	**-0.08**

Values in bold are different from 0 with a significance level α = 0.05

Figure IV.8. PCA_1 applied to the group of variables: atmosphere conditions

2.1 The principal axis F1 is attributed to T_{Metal}, SO_2 and O_2 and the axis F2 is attributed to H_2O, HCl, and CO_2, two families of not correlated variables, while MTLr as a supplementary variable is in the F3 axis (not shown in the diagram). As reported in literature, MTLr has the highest positive correlation with T_{Metal}, because the metal temperature not only influences the reaction rate, but also controls the melting of deposits and thus activates the corrosive reaction. [49,143] T_{Metal} does not show a significant correlation with the other variables. In the correlation test diagram (Figure IV.9a) corrosion rates are represented as a function of T_{Metal} for isothermal tests (red) and temperature gradient tests (yellow). In PCA_1 $T_{Flue\ gas}$ was not be included in order to avoid additional error sources when adding the null values ($T_{Flue\ gas} = 0$) on isothermal tests. T-gradient tests will be analyzed hereinafter.

2.2 From Figure IV.9b, we can clearly see that most data belong to corrosion tests performed under complex atmosphere rather than pure air, i.e. similar to the real conditions in service. However the presence of both scenarios produces two separate data populations which could create discontinuities in the data distribution with respect to gas composition variables. Therefore interpretations should be made with caution.

2.3 The negative correlations with $\%O_2$, $\%H_2O$, and $\%CO_2$ are consistent with studies in which the corrosion rate decreased with increasing the O_2, H_2O and CO_2 concentrations. [55,176] This is certainly related to the formation of protective oxide scales against the corrosiveness of ash, because these gases act as oxidizing agents to form protective layers. When protective oxide scales are dissolved by molten deposits, an oxidizing environment should supply the O_2 needed for rehealing the oxide layers in the presence of the oxide forming elements. [143] Statistically, O_2 does not show any correlation with any other variable and O_2-correlation respect to MTLr is the highest among the gases.

2.4 H_2O, CO_2 and HCl are positively correlated with each other. H_2O and HCl are linked by the Deacon reaction (26). [67] Higher concentrations of HCl produce more H_2O and Cl_2 and vice versa. Some studies have reported that increased levels of CO_2 and H_2O can be coupled with increased levels of corrosive gases such as HCl (and SO_2 for coal combustion systems). [177,178] Statistically, this means a high collinearity between them, thus, it is recommended to use just one of these variables for MLR. However, higher influence from CO_2 is observed in typical coal oxy-fuel combustion, rather than waste combustion[179]. H_2O holds a low correlation with MTLr. Therefore, in waste incineration environments it seems more significant to consider HCl as potential variable for modeling.

$$4HCl + O_2 \leftrightarrow 2H_2O + 2\,Cl_2 \qquad \textbf{Reaction 26}$$

2.5 HCl has a positive correlation with MTLr, because HCl is well known to initiate active oxidation at the metal/oxide scale interface, as reported in literature.[37] Nevertheless, the correlation with MTLr is low. This could be due to the effect of gaseous HCl is probably low compared to other parameters. Brossard, et al.[46] demonstrated in laboratory scale testing that the fireside corrosion rate in gaseous complex atmospheres (O_2, H_2O, HCl, and SO_2) is drastically higher in the presence of reactive ash. Lebel [51] also demonstrated that the effect of HCl is mainly visible at low temperatures under solid deposit while it is hampered at high-temperatures under molten salts deposit corrosion. Therefore, the effect of HCl must also be considered to explain the corrosion rate besides the ash composition, ash' melting temperature and metal temperature.

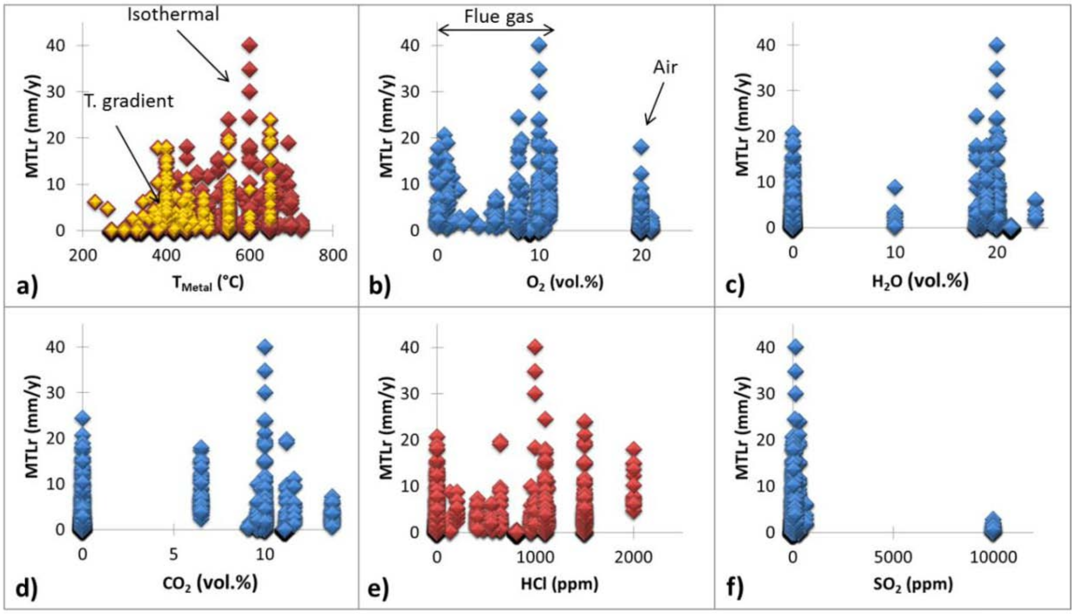

Figure IV.9. CT_1 applied to the group of variables: atmosphere conditions

2.6 SO_2 has a low correlation with MTLr, the Figure IV.9f shows that its effect is clearly influenced by an outlier corresponding to corrosion tests performed in SO_2 atmospheres that will be suppressed for further statistical treatment. [146] However its negative correlation is consistent with the results of Grabke et al. [62] who suggested that the mass loss of the alloys caused by HCl is reduced by the presence of SO_2 in the atmosphere. In the case of Fe-based alloys, FeS at the interface limits the formation of volatile FeClx. The equilibrium of reaction (27) that would cause mass loss is shifted by SO_2 to the left side. Moreover, sulfation of chlorides takes place according to reaction (28).[62] Nevertheless, sulfation generates Cl_2, which may participate actively in the corrosion process.

$$\mathbf{(K,Na)_2Ca_2(SO_4)_3 + 2\ HCl = 2\ (K, Na)Cl + 2\ CaSO_4 + SO_2 + H_2O + ½\ O_2} \qquad \textbf{Reaction 27}$$

$$\mathbf{2(K,Na)Cl + SO_2 + ½\ O_2 = (K, Na)_2SO_4 + Cl_2} \qquad \textbf{Reaction 28}$$

Conclusion: According to statistical results concerning the atmosphere conditions, the parameters that should be taken into account for modeling are T_{Metal}, O_2, and HCl because they present the highest linear correlation with the corrosion rate and they are not correlated with each other. However, depending on the scenario and the alloy domain, H_2O may be added to improve the adjustment of the linear regression.

Figure IV.10 shows the PCA_2 for alloys nominal composition applied on the original data set (867 test results) with 60 % of cumulative variability represented. Correlation tests diagrams corresponding to interaction with the MTLr is shown in Figure IV.11. PCA_2/CT_2 correlation matrix is given in Appendix IV.B. The analysis indicates the general correlation trends among the alloy elements, as well as the correlation between each element and the MTLr on the entire data population. Correlation coefficients (r) in bold indicates that the associated p-value with regression coefficient is inferior to <0.05 (statistically significant). The PCA_2 score plot may be interpreted in the following manner:

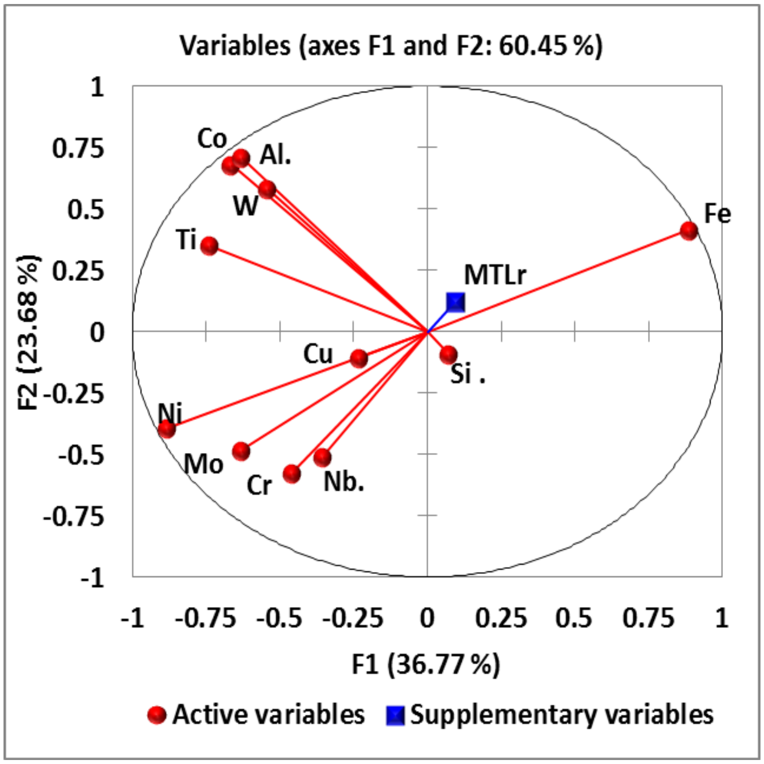

Correlations (r)

Variables (wt.%)	MLr (mg/cm^{2}h)
Fe	**0.22**
Ni	**-0.18**
Cr	**-0.25**
Mo	**-0.15**
Co	-0.04
Cu	0.09
Al	-0.03
Si	**-0.14**
W	0.00
Nb	**-0.12**
Ti	0.03

Values in bold are different from 0 with a significance level α = 0.05

Figure IV.10. PCA_2 applied to the group of variables: materials chemical composition

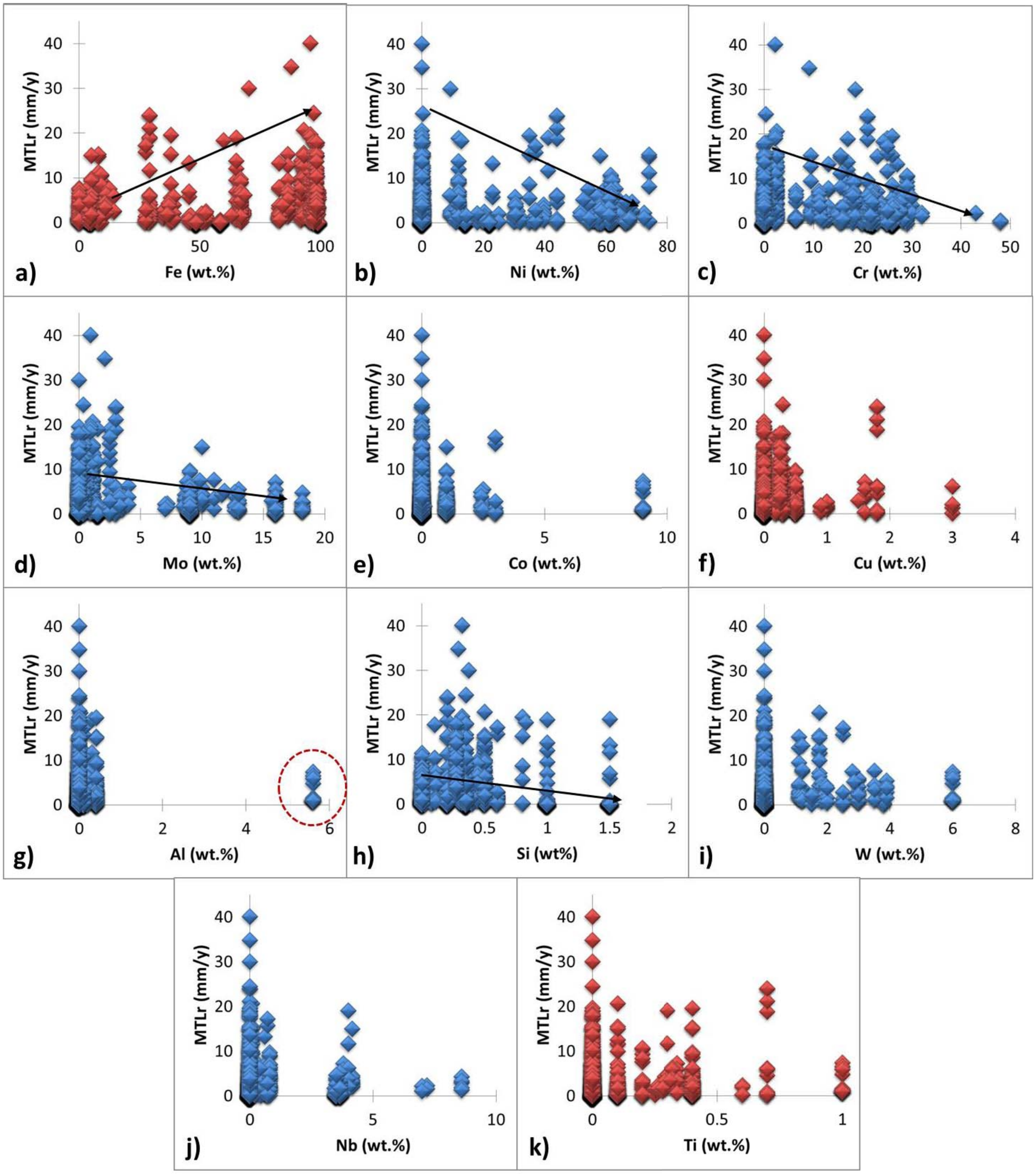

Figure IV.11. CT_2 applied to the group of variables: materials chemical composition

1.1 Most of the elements have a logical position regarding the effect on MTLr, even though they show low levels of correlation. Low correlations are explained by the large number of conditions and materials included in the data distribution, which generates high variability and low correlations ($r < 0.6$). However, from a statistical point of view, when there is high variability in the data set, the relative high correlations should be considered significant. Indeed, an environment containing oxygen, chlorine, sulfur, and other volatile species able to condensate and melt on the tube surface leads to very complex corrosion mechanisms. Therefore, it is also obvious that other variables control the corrosion process, besides the alloy composition.

1.2 In the PCA_2 the highest and significant correlations ($r > 0.2$) belong to the main elements of the alloys (Fe, Ni, Cr). Fe and Ni are highly correlated ($r= - 0.97$) which corresponds with the typical alloy chemical compositions along the domain. Since Fe-based alloys are less resistant to chloridizing environments than Ni-based alloy, the effect of the main elements is consistent with those reported in literature. [40,110,138,141] The high correlation also indicates collinearity, and hence, only one of them should be used for linear regression analysis.

1.3 Figure IV.8 also shows that the principal component axis F1 is attributed to Fe and Ni and the MTLr as a supplementary variable to the F3 axis (not shown in the diagram). Fe has a direct negative correlation with Ni, Cr, and Mo (diametrically opposed). Also, Ni, Cr, and Mo have positive correlation between them (nearby vectors). Therefore, in order to avoid collinearity among the variables in the MLR, only one of the following main elements must be used for modeling: Fe, Ni, Cr, or Mo. However, Fe, Ni, and Mo show lower correlations (< 0.2) with MTLr than Cr.

1.4 The corrosion resistance is improved by the combined effect of the main elements Ni, Cr, and Mo that corresponds with the negative effect on MTLr. However, Cr presents the highest correlation, this tendency is because it forms Cr_2O_3 as a major component of the protective oxide scale,[49] and thus, it is considered the most important resistant alloying element for high-temperature corrosion attacks.

1.5 The negative effect of Mo on MTLr is expected because the addition of Mo in a content of approximately 5% or more is effective to resist high-temperature corrosion. Mo is less reactive to chlorine than Fe and Ni.[49]

1.6 Al has a low negative correlation on the corrosion rate. However, this effect is influenced by an outlier corresponding to alloy CMSX-4 (diagram *IV.10.g*), a nickel-base superalloy that have demonstrated good combination of high-temperature strength, good phase stability oxidation and hot corrosion resistance.[180] Also, Kawahara et al. [143] have confirmed that the corrosion rate on Al-rich layers is relatively low, as it forms aluminum oxide (Al_2O_3) as a protective film that contributes to corrosion resistance depending on the conditions.

1.7 Si has a negative correlation with the corrosion rate. Si is supposed to improve the corrosion resistance, as silica layers are known to be protective in presence of molten sulfates.[98] However, this oxide is poorly adherent during thermal cycling conditions, [99,100] Moreover, Si reduces the microstructural stability, the tube manufacturing, and weldability of materials, adding Si only can be beneficial depending on the chosen application. [49,104]

1.8 Nb has a negative correlation with the corrosion rate, as it is known to be effective in improving the corrosion-resistance of alloy 625, which contains approximately 4% Nb[49]. It is also added to enhance other characteristics such as high-temperature strength and bending workability.[49,89,104]

1.9 The rest of the elements (Co, Cu, W, Ti) present low and no statistically significant correlations. Since PCA analysis includes several families of materials, the effect of the alloying elements depends on the major elements of the alloys, and hence, their effect can be overlapped by other elements.

Conclusion: PCA_2 and CT_2 showed consistent correlations with those values reported in literature. Low correlations were observed with minor alloying elements, because as the number of alloying elements in the materials increases, the behavior becomes more complex and the specific role of each element is difficult to differentiate.[40] Also, the content of these elements in the alloys of the database is not statistically representative to allow the identification of an influence.

The statistical analysis identified the chromium as the most viable element to be included in modeling because: a) Cr has the highest correlation with MTLr among the main elements of the alloys and b) Cr increases high-temperature corrosion resistance, as it has been reported in literature.[36,37,62] However, due to the variability of the data, caused by the combined treatment of Fe-based and Ni-based alloys, a classification of alloys should be conducted for further correlation analysis, in order to obtain better results.

Figure IV.12 shows PCA_3 for ash composition in elementary form, applied on the original data set (867 test results) with 63 % of the cumulative variability. Correlation tests diagrams corresponding to interaction with the MTLr is shown in Figure IV.13. PCA_3/CT_3 correlation matrix is given in Appendix IV.C. Correlations in bold indicate that the p-value associated with the regression coefficient is inferior to <0.05 (statistically significant). The PCA_3 score plot may be interpreted in the following manner:

3.1 Most of the variables are adequately represented by the F1 axis except for S and Ca, which are found on the F2 axis, while MTLr as a supplementary variable is poorly represented by the F4 axis (not shown in the diagram). Consequently, the correlations must be interpreted with caution as general trends of the variables' behavior regarding MTLr.

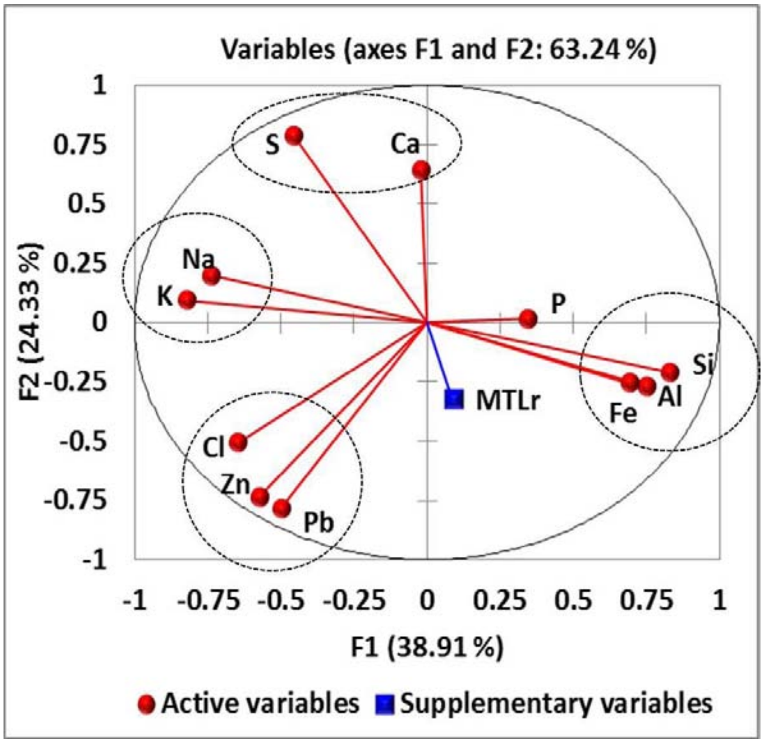

Correlations (r)

Variables (wt.%)	MTLr (mm/y)
S	**-0.31**
Cl	**0.18**
Na	**-0.16**
K	**-0.13**
Pb	**0.17**
Zn	**0.16**
Ca	**-0.07**
P	0.03
Si	**0.20**
Al	0.04
Fe	**0.10**

Values in bold are different from 0 with a significance level α = 0.05

Figure IV.12. PCA_3 applied to the group of variables: ash chemical composition

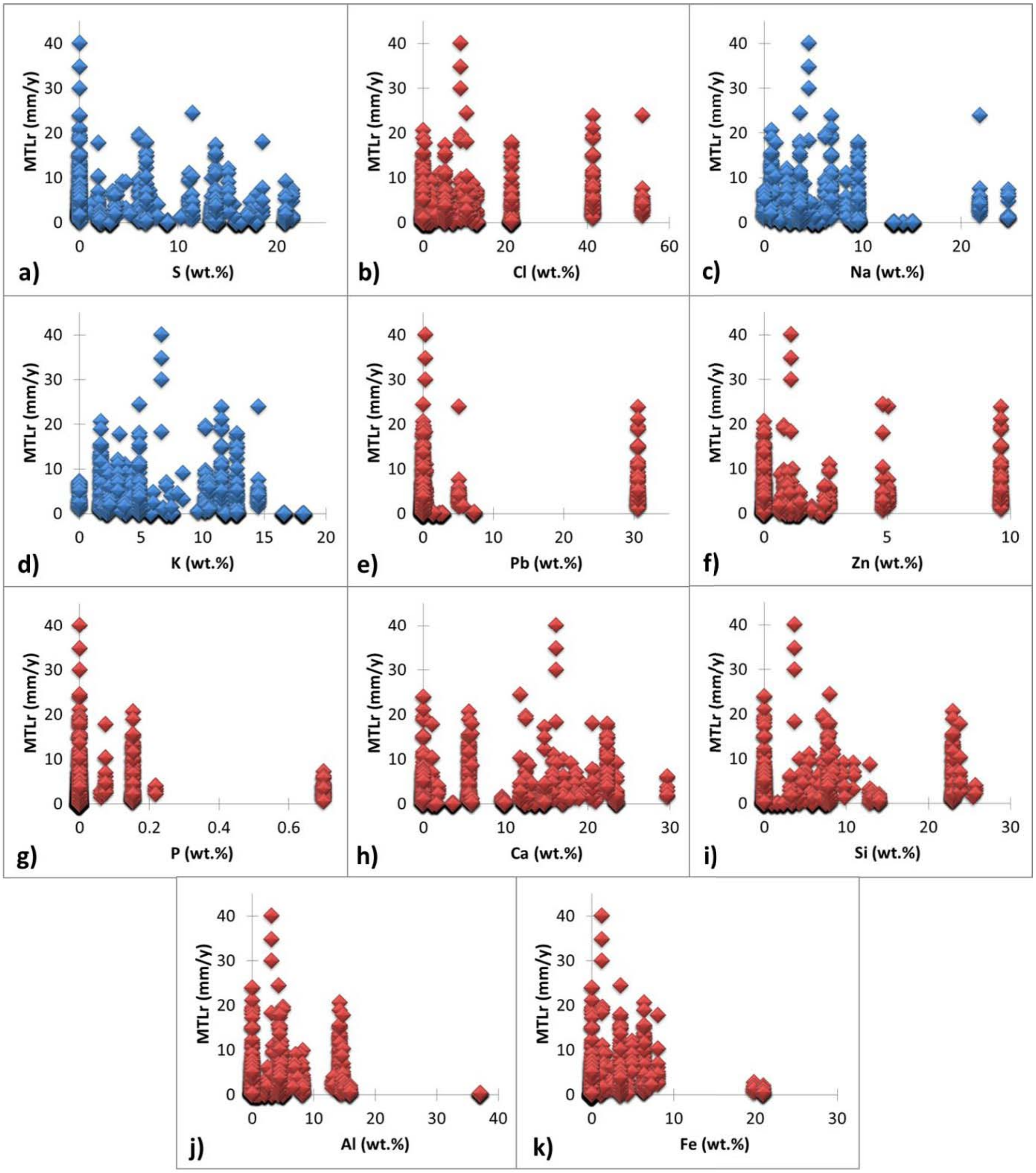

Figure IV.13. CT_3 applied to the group of variables: ash chemical composition

3.2 In the diagram, the arrangement of the elements shows their contrasting effect on the melting temperature of the ash and thus on the corrosion rate, and four groups can be distinguished. In the first group are the elements Al, Si, Fe, and P that are present as oxides in the ash (Al_2O_3, SiO_2, Fe_2O_3, and P_2O_5). Among these, Al, Si, and Fe each has a very low correlation with MTLr. This is expected, considering that they do not decrease the ash melting temperature. [181] During combustion, these elements form stable compounds, such as oxides, silica or alumina with high melting temperature. Thus Fe, Al, and Si are refractory oxides forming elements within the deposit compared to other deposit elements, as these compounds do not decrease ash melting temperature and limit the fraction of molten salts in the deposit. Therefore, deposits remain solid, avoiding an increase of the corrosion rate at high-temperatures. [140,182] The positive correlation of P is expected because it may forms P_2O_5, and other compounds with Ca, which reduce the ash melting temperatures and increase the corrosion rate. [183,184]

3.3 The second group of elements contains Cl and heavy metals Pb and Zn (forming chlorides $PbCl_2$ and $ZnCl_2$), which have the highest positive correlation with MTLr. This is expected because they reduce the ash melting temperature, thus increasing its corrosiveness [49,185]. Corrosion rates of alloys increase when the ash contains larger amounts of fused salts because the protective oxide scale formed on the surface of the alloys can be destroyed by the reaction with fused salts [75,186].

3.4 The same argument could be applied for the third group containing the alkali metals Na and K, which tend to decrease the ash melting temperature, thus increasing its corrosiveness[2]. Na and K are found between Cl and S, which is consistent with the fact that these elements form chlorides (NaCl, KCl) and sulfates (Na_2SO_4, K_2SO_4). Therefore, the low and negative correlation between Na, K and MTLr, is because they form compounds (chlorides or sulfates) with opposite effects on the corrosion rate. This also corresponds with earlier research, which showed that generally the relative amount of fused salts increases in ash with greater chlorine content, indicating that chlorinated compounds have generally lower melting temperatures than sulfates and oxides. [75,186]

3.5 The fourth group of elements contains S and Ca. The negative correlation of S on the corrosion rate confirms the findings of Kawahara et al. [143] who showed that when heavy metal sulfates were contained in the ash, they worked to suppress corrosion. Later, Baker [110] confirmed that sulfates are also present in waste incineration ash deposits, but they are typically much lower in concentration than chlorides and are not thought to play a primary role in the corrosion mechanism under the deposits. A particular reaction that is beneficial in reducing the corrosive effect of chlorine and chloride salts is the sulfation of volatilized alkali salts in the flue gases. This reaction transforms chlorides into sulfate salts and the chlorine released then reacts with water steam to form hydrochloric gas. Sulfate salts are less aggressive since sulfate corrosion occurs at higher temperature. [187] Ca mainly comes from the compound $CaSO_4$, which agrees with its high positive correlation with sulfur and its negative correlation with MTLr.

Conclusion: statistical results concerning the ash composition show high collinearity between melting elements and refractory oxides forming elements. These variables should be converted into two groups of variables in order to decrease collinearity. For modeling, it seems convenient to include Cl and S, because of their relevance in the corrosion process then Na, K, Pb, and Zn can be included as a single variable (Na+K+Pb+Zn) and Al, Si, Fe, and Ca as another single variable in the form of (Al+Si+Fe+Ca), the effect of both groups was also reported by Spiegel. [182] However, these two variables may also show collinearity in some scenarios, and hence, only one of them must be used. These particular scenarios will be analyzed further.

IV.3.1.1.2 Alloy classification and correlation tests

As was pointed out earlier in the PCA_1/CT_1 (Figure IV.8 and Figure IV.9), the hot corrosion mechanism is sensitive to alloy composition and different alloy systems might behave differently under a given environment. Therefore, for modeling over a wide range of conditions, it became necessary to classify the material's chemical composition domain in order to model the effect of the variables for a specific class of alloy. The classification was performed as a function of $Ni_{Eq.}$ and $Cr_{Eq.}$ (wt.%) calculated by the Schaffler equations (41) and (42) (Section III.3.1.1.1.3). [101]

Figure IV.14 shows the surface diagram of the composition domains as a function of the main elements (Fe-$Ni_{Eq.}$-$Cr_{Eq.}$-Mo). The initial domain consisted of four families of materials: Fe-based alloys (ferritic matrix), austenitic stainless steels, Fe/Ni-based high-temperature alloys and Ni-based alloys (in parentheses the amount of data available per family of materials to model MTLr as dependent variable). Since the austenitic stainless steels group presented a small amount of data and low variability in its conditions, it was combined with Fe/Ni based high-temperature alloys. The main domain was converted into three alloy systems to be analyzed and modeled: Fe-based alloys (ferritic matrix), austenitic SS + Fe/Ni-based high-temperature alloys and Ni-based alloys.

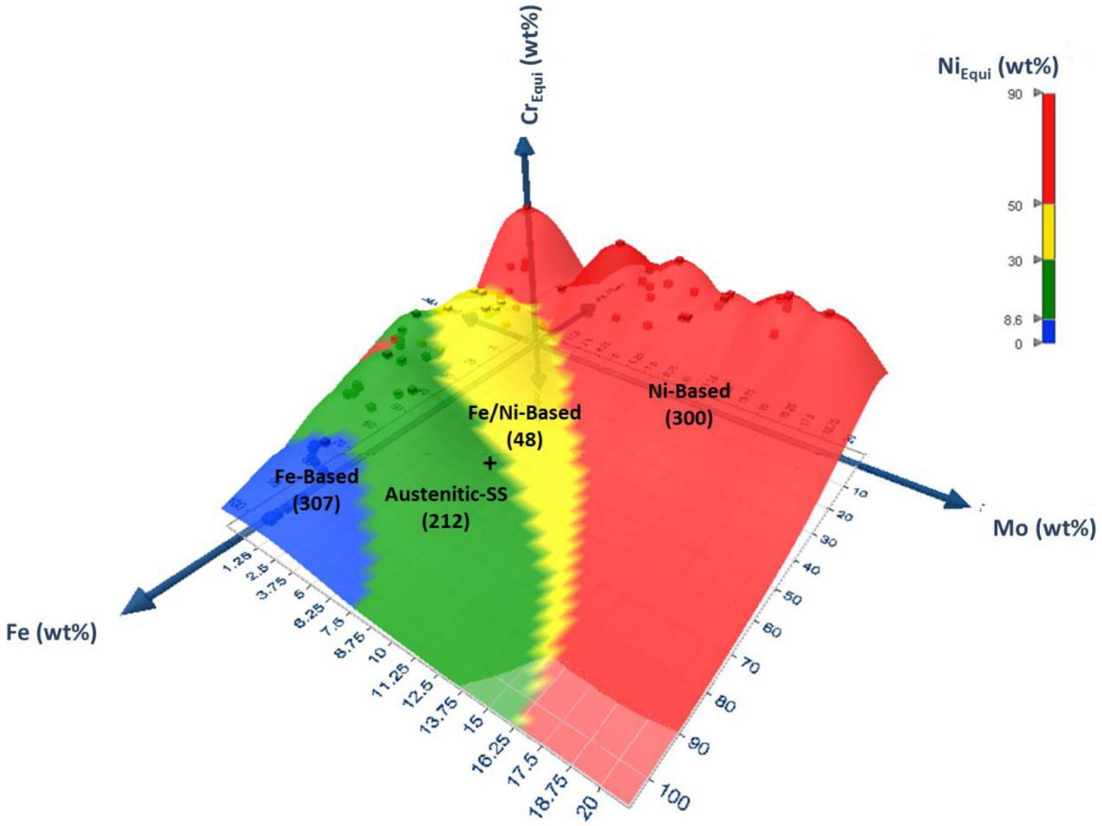

Figure IV.14 : 3D plot as a function of Fe-NiEq-CrEq-Mo: final materials domain classified into three groups of alloy systems.

It is well known that high-temperature corrosion mechanisms vary depending on the alloy family. [40] Upon completion of the alloy's classification, correlation tests regard each group of variables were performed for each alloy system, in order to determine the intensity and direction of the linear correlation of MTLr as a function of each independent variable. As a result, the correlation coefficients (r) obtained were represented in the bar chart shown in Figure IV.15, Figure IV.16 and Figure IV.17, respectively for each group of explanatory variable (environment, alloys, ash). Correlation matrix and statistics for correlations tests are given in Appendix IV.D.

Figure IV.15 shows that most correlations of MTLr with the atmosphere variables are consistent with experimental findings.[53] The correlations vary with the alloy family but also with the data variability which is different in every case, and hence, interpretations should be cautious. As a consistent trend, MTLr increases with T_{Metal} and HCl-content (ppm) in the gas. T_{Metal} increasing activates high-temperature corrosion mechanisms as active oxidation and molten ash corrosion on the metal surface, as well as HCl promotes active oxidation and provides Cl_2 for chlorides formation. MTLr decreases at higher contents of O_2-content (vol.%) in the gas, as it favors oxide formation. The other gases (H_2O, CO_2 and SO_2) hold low and negative correlations except for Ni-based alloys.

As mentioned above, data variability influences some correlations that should be examined separately. Contrary to experimental findings in literature regarding the effect of the gases [53,64,176] Ni-based alloys present high and positive correlations with oxidant gases (H_2O, CO_2 and SO_2). These effects are influenced by high corrosion rates from laboratory tests, performed at high-temperatures and high contents of HCl (1500 ppm). These results also produce positive correlations on H_2O, CO_2 and SO_2 as well as collinearity between them. Therefore, these gases should be omitted for Ni-based alloys.

Conclusion: for modeling purposes, it seems pertinent to include T_{Metal} and O_2 as constant variables in all domains. The other gases such as HCl, H_2O and SO_2 will be added depending on the scenario to improve fitting criteria.

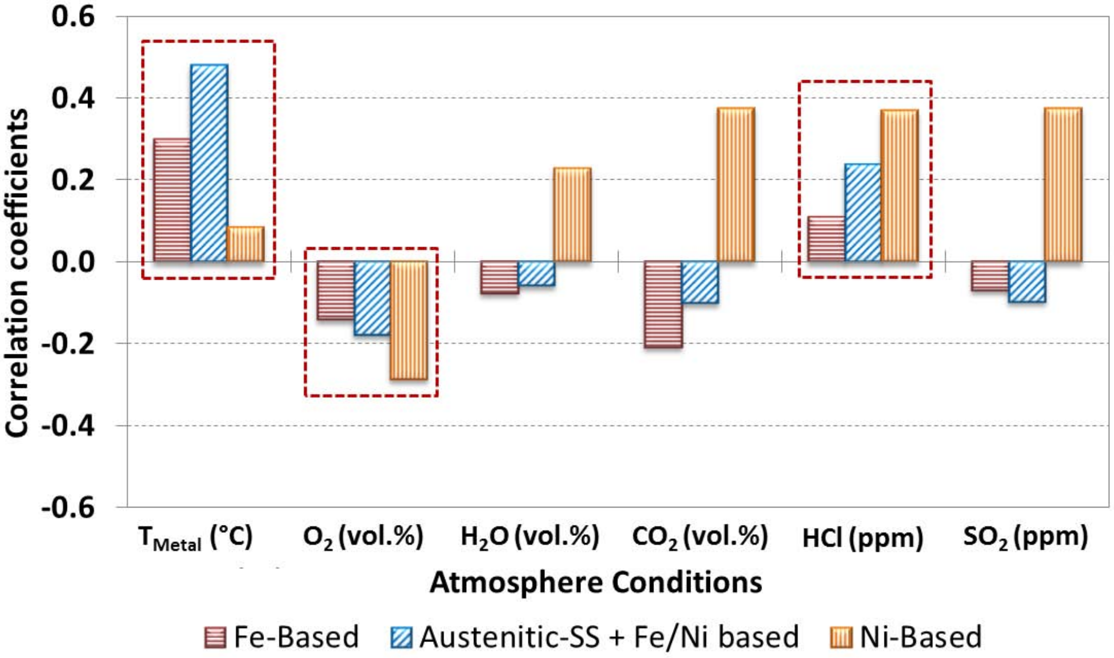

Figure IV.15. MTLr as a funtion of atmosphere conditions by family of alloys

Figure IV.16 shows incoherent correlations with respect to the main elements, such as Fe and Ni, protective elements like Mo, Cu and Al and refractory elements like W, Nb, Ti. In Fe-based alloys and Fe/Ni based alloys, the contents of Mo, Cu and Al are too low (wt.% <1) to be significant in the alloy protection. For Ni-based alloys Cu and Al contents become higher but their correlations are still too low to be conclusive. However, Mo highlights to be corrosion suppressor, as the Mo composition range increases up to 18% in this domain. Lastly, Si shows no effect on Fe-based alloys and Ni-based alloys, wherein Si-content is also low (wt.% < 0.5) to be significant, but Si stands out to be corrosion suppressor for Fe/Ni austenitic alloys, as its composition range increases up to 1.5% in this domain.

Conclusion: statistically, Cr content seems to be the most consistent in its beneficial role to improve corrosion resistance. Thus, as the Cr-content increases, corrosion rates decreases for every alloy system, due to its well-known protective ability. Therefore, Cr (wt.%) confirms to be the most suitable variable to be included in the models from the alloy composition domain. However, Si and Mo seem to be also relevant to be included in the fit evaluation for Fe/Ni austenitic alloys and Ni-based alloys, respectively.

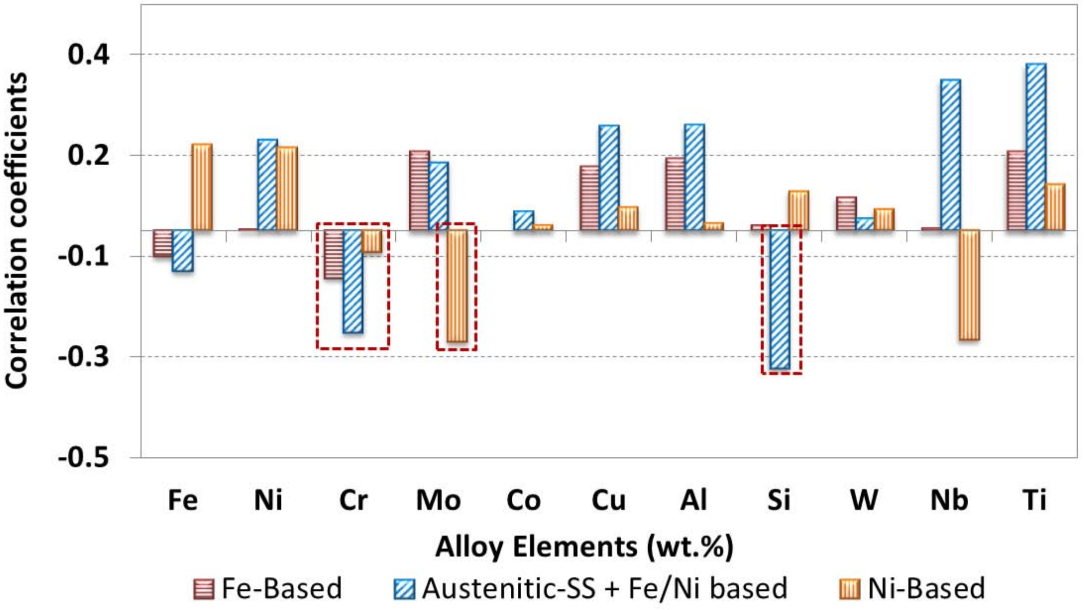

Figure IV.16. Correlation test : MTLr as a funtion of alloy elements by family of alloys

Figure IV.17 shows that correlations of MTLr with the main ash elements such as Cl and S are consistent with experimental findings. Cl promotes chlorides formation, which decreases the ash's melting point increasing corrosion rates. On the other hand, S promotes sulfates formation, which have higher melting points than chlorides, and hence, higher concentrations of sulfates in the ash rather than chlorides may decrease the corrosion rates.[53,75,186,187]

For the melting elements Na, Ka, Pb, Zn (alkaline and heavy metals) and the refractory oxide-forming elements Ca, Si, Al, Fe, the correlations vary with the alloy family and the data variability in every case. Data variability influences some correlations that should be examined separately. Melting elements such as Na, K, Pb and Zn are expected to show positive correlations with MTLr, since they decrease the ash's melting point, promoting the dissolution of the protective oxide layers. [53,68,185,188] Refractory oxide-forming elements are expected to show low or negative correlations since they keep constant the ash's melting point, avoiding ash melted zones. This is consistent with correlations observed on Fe/Ni-based alloys and Ni-based alloys but not for Fe-based alloys.

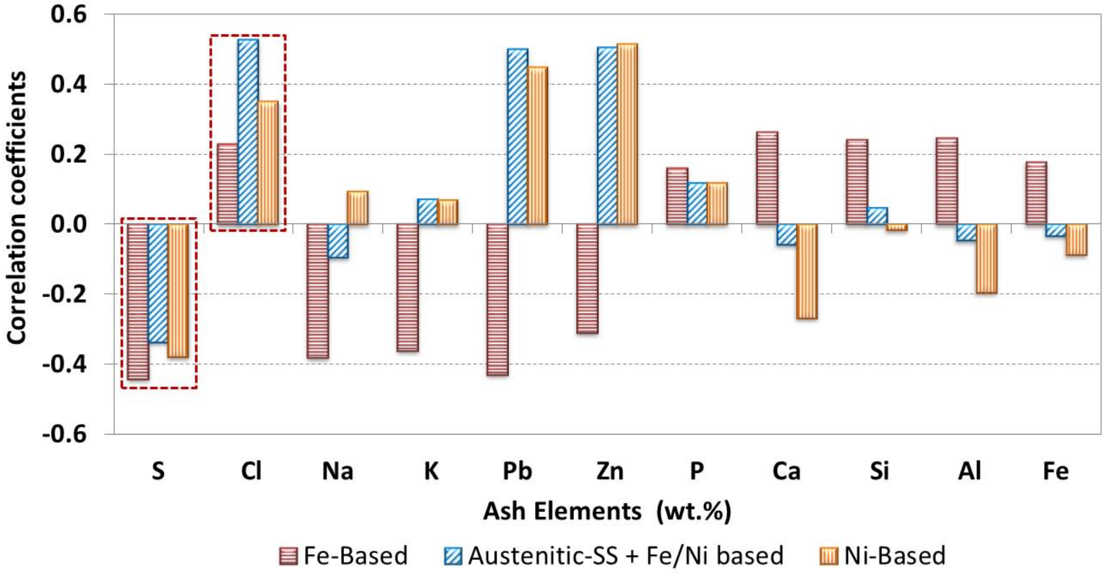

Figure IV.17. MTLr as a funtion of ash composition by family of alloys

In the case of Fe-based alloys, the expected relative effect of melting elements and refractory oxide-forming elements is inversed. This result comes from low corrosion rates developed during industrial tests (long term tests tend to be slower) that were performed at low temperatures (270°C), high contents of Na, Ka, Pb, Zn and low contents of Ca, Si, Al and Fe. This particular data set produces inverse correlations and highlights collinearity between both groups, as shown in the PCA_3. However, melting elements form harmful substances that favor molten salts mixtures that accelerates corrosion, and hence, its effect must be prioritized and monitored rather than refractory oxide-forming elements. Therefore, for modeling Fe-based alloys scenario, the effect of melting elements (Na, Ka, Pb, Zn) will be evaluated and refractory oxide-forming elements (Ca, Si, Al, Fe) will be omitted.

Numerous studies have pointed out that chlorine is the most detrimental element for the corrosion process, since it participates in active oxidation and promotes molten ash corrosion through chlorides formation with the melting elements (Na+K+Pb+Zn).[40,53] Therefore, further interaction between Cl and melting elements (Na+K+Zn+Pb) will be evaluated, in order to enhance the relative weight of chlorides forming elements in the model.

Conclusion: for modeling purposes, ash elements will be added to the models in order of priority: Cl and S as main elements, followed by the interaction factor between Cl and melting elements as a group (Na+K+Pb+Zn). The refractory oxide-forming elements (Ca+Si+Al+Fe) will be added to improve fitting criteria, but only in cases where no correlation exists with the melting elements (Na+K+Pb+Zn).

Another aspect to consider is the solidus temperature ($T_{Solidus}$) of every ash composition. The $T_{Solidus}$ is the locus of temperatures at which melting of a substance begins (first drop of liquid), but the substance is not necessarily melted completely, i.e., the solidus is not necessarily a melting point ($T_{Liquidus}$), as the case of molten ash.[181] For this distinction, the solidus may be contrasted to the liquidus. The $T_{Solidus}$ is always less than or equal to the $T_{Liquidus}$, but they do not need to coincide. If a gap exists between $T_{Solidus}$ and $T_{Liquidus}$, it is called the freezing range, and within that gap, the substance consists of a mixture of solid and liquid phases (like a slurry). Therefore, even when ash element contents are relevant for the corrosion process, also to reach $T_{Solidus}$ is crucial to the aggressiveness of the mechanism. [189,190] Further analysis will be performed on this subject.

IV.3.2 Modeling: Multiple Linear Regression

The three families of materials: Fe-based alloys, Austenitic-SS and Fe/Ni-based alloys and Ni-based alloys were analyzed by MLR, in order to assess an equation that allows representing the corrosion rates with high accuracy.

IV.3.2.1 Model 1: Austenitic stainless steels and Fe/Ni-based alloys

Model 1 was generated, from the Austenitic-SS + Fe/Ni-based alloys original data set (260 data). Approximately 50% of the original data set was randomly selected to create the model and the remaining 50% of the data set was used to verify the predictive ability of the model. The validation data set was within the model validity domain but not included in the data set used to determine the predictors of the model. Table IV.3 shows the model validity domain and the goodness of fit statistics. Figure IV.18 shows the relative weights of the variables on the corrosion rate, which represent the standardized coefficients of the model's predictors in equation (55). Finally, the Figure IV.19 shows the accuracy chart of the model and the standard deviation of the model's predictions (56)

Table IV.3a shows the highest and lowest limits between which the model is valid. The model can predict corrosion rates for austenitic SS and Fe/Ni based alloys in the composition range (28-50 wt.% Fe, 11-50 wt.% Ni, 17-29 wt.% Cr and 0-3.5 wt.% Mo), exposed at temperatures between 300°C and 725°C, complex atmospheres, as well as pure air (according to O_2 and H_2O gas contents) and ash compositions calculated in elemental form within the established limits.

Table IV.3b shows the goodness of fit statistics of the model. The R^2 = 0.82 means that 82% of the variation of the mass loss rates was explained by the model. The DW = 1.4 shows that the residuals are not independent from each other. The F = 52.8 and $|Pr > F| < 0.0001$ means that there is a significant linear relationship between the MTLr and the set of independent variables taken together in the model (Figure IV.18), all these indicators suggest that the model is satisfactory. The coefficient RMSE = 0.7 means the standard deviation on the model's predictions, leading to equation (56).

Table IV.3. Statistics of model 1. a) Validity domain b) Goodness of fit statistics

Variable	Minimum	Maximum
MTLr (mm/y)	0	6.8
T (°C)	300	725
O_2 (vol.%)	1	21
H_2O (vol.%)	0	24
Cr (wt.%)	17	29
S (wt.%)	0	17
Cl (wt.%)	0	13
Al+Ca+Si+Fe (wt.%)	0	51
Na+K+Zn+Pb (wt.%)	0	58

a)

Goodness of fit statistics:	
R²	0.82
Adjusted R²	0.81
DW	1.4
MSE	0.57
RMSE	0.75
Analysis of variance:	
F	39.1
Pr > F	< 0.0001

b)

The model's equation (55) shows the predictors of the model, whose standardized coefficients are represented in Figure IV.18. The equation allows reusing the model, under different conditions within the same validity domain.

$$\boldsymbol{MTLr = 6.1 + 1.7\times10^{-3}\times T_{Metal} - 3.2\times10^{-1}\times[O_2] - 6.4\times10^{-2}\times[H_2O]}$$
$$\boldsymbol{-1.5\times10^{-1}\times[Cr] - 1.1\times10^{-1}\times[S] + 1.7\times10^{-2}\times[Cl] - 5.3\times10^{-2}\times[Ca+Al+Si+Fe]}$$
$$\boldsymbol{+3.3\times10^{-2}\,[Cl\times(\,Na+K+Zn+Pb)]} \qquad \textbf{Equation 55}$$

Where, $MTLr$ is given in $\frac{mm}{y}$, temperature T_{Metal} in *Celsius (°C)*, $[O_2]$, $[H_2O]$ in *vol.%* in the gas, $[Cr]$ in *wt.%* in the alloy and $[S, Cl, Na, K, Zn, Pb, Ca, Al, Si, Fe\,]$ in *wt.%* in the ash.

Figure IV.18 shows the standardized coefficients of the model determined with 95% confidence, which are used to compare the relative weights of the variables on the corrosion rate. The higher the absolute value of a coefficient, the higher the influence of the independent variable on MTLr. In the model, the variables are placed according to the group of variables that they represent. The variables T_{Metal}, $[O_2]$ and $[H_2O]$ represent the atmosphere conditions, the $[Cr]$ represents the composition of the material, $[S]$and $[Cl]$, melting-elements $[Cl \times (\,Na + K + Zn + Pb)]$, and refractory oxides forming elements $[Ca + Al + Si + Fe]$ represent the ash composition.

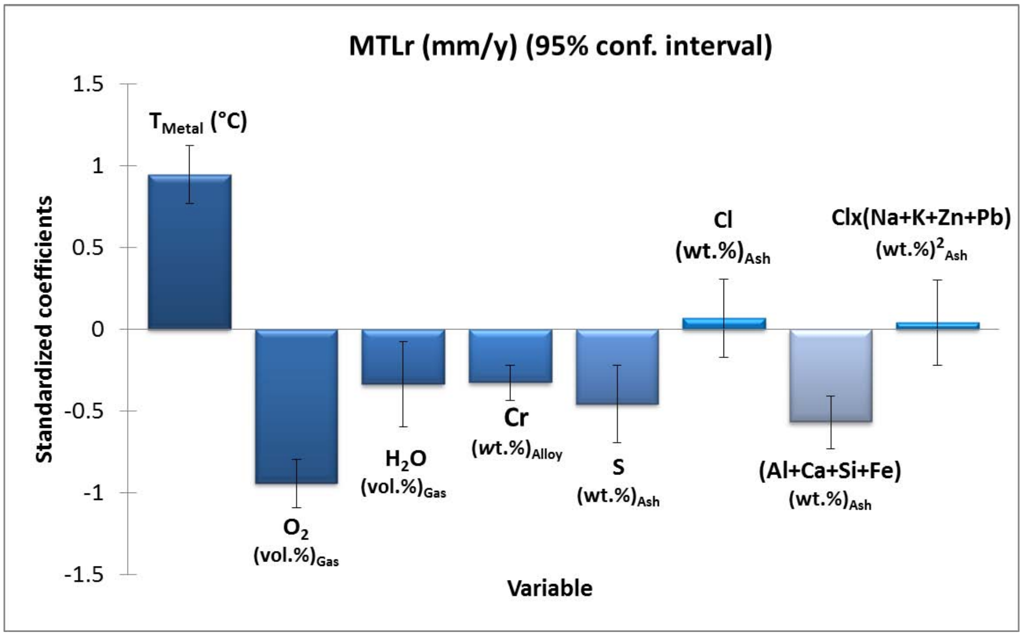

Figure IV.18. Standardized coefficients chart: relative weight of the independent variables on model 1 for austenitic stainless steels + Fe/Ni-based alloys

The effect of the variables was compare with experimental findings in literature. In the model, we can see three types of parameters according to the order of significance.

In the 1st order: T_{Metal} has a positive effect on MTLr, which indicates that T_{Metal} increases the corrosion rate.[36,53,84,91] O_2 has a negative effect on MTLr, as it contributes to form protective oxide layers and, therefore, tend to decrease the corrosion rate. [53,64]

In the 2nd order: $[H_2O]$, $[Cr]$, $[S]$ and $[Ca + Al + Si + Fe]$ have a negative effect on MTLr. H_2O also aids in the oxide formation but much less than the O_2. [53,64] Cr protects the alloy through oxide layers formation.[90,93,97,175] Higher S-content indicates higher contents of sulfates in the ash which have higher ash's melting temperature and delay the melting effect of chlorides. Finally, the refractory oxide-forming elements $[Ca + Al + Si + Fe]$ maintain relatively high the ash's melting temperature and limit the fraction of molten salts in the deposit. [45] Due to the reasons mentioned, these variables decrease the corrosion rate.

In the 3rd order: $[Cl]$ and $[Cl \times (Na + K + Zn + Pb)]$ have a positive effect on MTLr, as they promote induced deposit active oxidation and reduce the ash's melting point, accelerating corrosion rates.[62,68,73,75,110,140,185,186,188] The influence is low, a large error bar indicates that their predictors are unstable and could be eliminates from the model. However, experimental findings have shown that these are important variables on the corrosion mechanism.

In statistics, the multiple linear regression is a hyperplane formed by all the independent variables that rearrange to explain most of the corrosion rates. Collinearities between independent variables cannot exist because it generates null predictors. As observed in PCA_3, $[Cl]$ is correlated with (Na, K, Zn, Pb), and thus using both variables independently in a first-order model, it creates a biased effect and the model is not validated. In our strategy, we start from a first-order model to prioritize the variables. If the model is not validated after statistical tests, it is either completed with additional experiments, in order to improve the coefficients, or the model order has to be increased. In our case, an interaction factor was applied between $[Cl]$ and melting elements (Na+K+Zn+Pb) to counteract their collinearity, increasing the model order with [Cl,x(Na+K+Zn+Pb)]. Increasing to a second-order model showed better results, as all the assumptions of the linear regression were validated.

The interaction factor applied between chlorine and melting elements [Cl,x(Na+K+Zn+Pb)] aims to enhance the relative weight of chlorides forming elements in the model, because these elements do not act by themselves in the corrosion processes. Corrosion mechanisms as active oxidation and corrosion by molten ash are activated by the presence of alkali metal chlorides (NaCl, KCl) and heavy metal chlorides ($ZnCl_2$, $PbCl_2$), respectively. Therefore, it is the chlorine content that controls the chlorides' formation, which are detrimental to the corrosion process. [53,62,68,73,75,110,140,186]

Figure IV.19 shows the accuracy chart of the model that represents the residuals between experimental values and model's predictions. Blue data set was used to create the model, and red data is the validation data set. RMSE coefficient is the mean error of the predictions of the model, leading to equation (56). The chart shows good agreement between experimental corrosion rates and the predicted ones. However, the mean error of the model indicates that, predictions are more accurate for higher rates than lower rates. Furthermore, mean error is related with the spread of the data, similar inputs can create very different outputs. In our model design, a large population of data obtained from different experimental methods and different materials has also experimental errors associated. The sum of these errors has been brought together in the same statistical equation.

$$\boldsymbol{MTLr_{Experimental} = MTLr_{Predicted} \pm 0.75\ \frac{mm}{y}} \qquad \textbf{Equation 56}$$

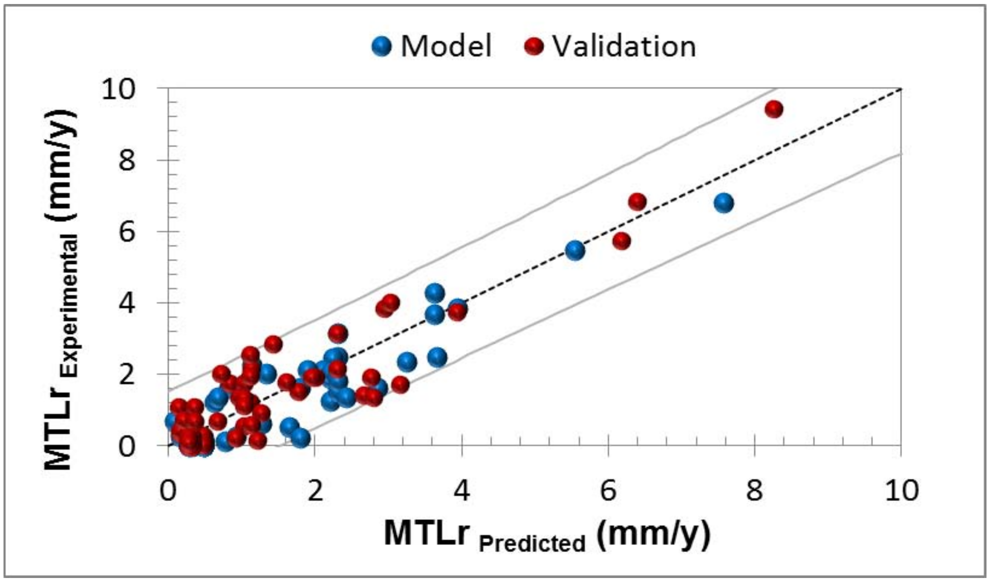

Figure IV.19. Accuracy chart with the residuals between experimental values and predicted values by model 1 for austenitic stainless steels + Fe/Ni-based alloys

The above-mentioned procedure was applied to Fe-based alloys and Ni-based alloys by using the same variables. The coefficients of determination obtained were $R^2 = 0.5$ and $R^2 = 0.4$, respectively. This means that only less than 50 % of the corrosion rates were explained by the models. Therefore, no satisfactory results were obtained. Possibly other variables that were not considered play an important role in the corrosion process or this might be also attributed to some shortcomings overlooked, such as:

- Model 1 was constructed using T_{Metal}, however 63% of the original data set belongs to temperature gradient tests and the remaining (37%) to isothermal tests. $T_{Flue\ gas}$ was excluded as an independent variable in order to avoid adding other sources of error. However, $T_{Flue\ gas}$ can affect the deposition rates and the composition of the deposit and thus increase corrosion rates. Furthermore, the temperature gradient between $T_{Flue\ gas}$ and T_{Metal} is a driving force for the condensation of vaporized species, such as metal chlorides, on the cooled surface. [191] The temperature gradient induces an alkali chloride gas phase concentration gradient in the ash deposit. This leads to a gas phase diffusion of alkali chlorides towards the steel surface. [192] Also, thermal stresses induced by the temperature gradient across the deposit and the tube wall can affect the adhesion of oxide scales on the metal surface, thereby resulting in fracture and spalling of the protective oxide layer followed by the increasing of pathways diffusion within oxide scales.[193,194]

- Model 1 was constructed base on tests performed in pure air and flue gas together. Although, the current experimental study shows no differences in corrosion rate levels (Figure IV.4), certainly there are differences between both scenarios to consider.

As a consequence, the original data set was analyzed as shown in Figure IV.20. Each block represents an analyzed scenario (18 scenarios). The number within the parentheses represents the amount of data available by each scenario. The more data population is dissected less available data remain for some scenarios. Therefore the red "X" indicates those scenarios that couldn't be modeled due to lack of data and/or lack of variability of conditions. The original data set was already processed resulting in model 1 and other two unsatisfactory models.

Subsequently, the original data set was dissected into two scenarios: T-gradient tests and isothermal tests. We can clearly see that most data (63%) belongs to T-gradient experiments and the remaining data (37%) to isothermal tests. The branch of T-gradient tests collects most of the data and the branch of isothermal tests contains the experimental results obtained in the SCAPAC project. Since no T-gradient experiments are carried out in the current experimental study, T-gradient experiments belong exclusively to literature data. The alloy family classification was maintained for both scenarios.

PCA_s and CT_s analysis were carried out for selecting the independent variables for isothermal conditions. From this level of classification, model 2 and 3 were generated under isothermal conditions in pure air + flue gas at laboratory scale. Model 2 for Fe-based alloys and model 3 for Ni-based alloys. Further modeling procedures for next classification level (pure air and flue gas) were not possible due to lack of data in the following scenarios.

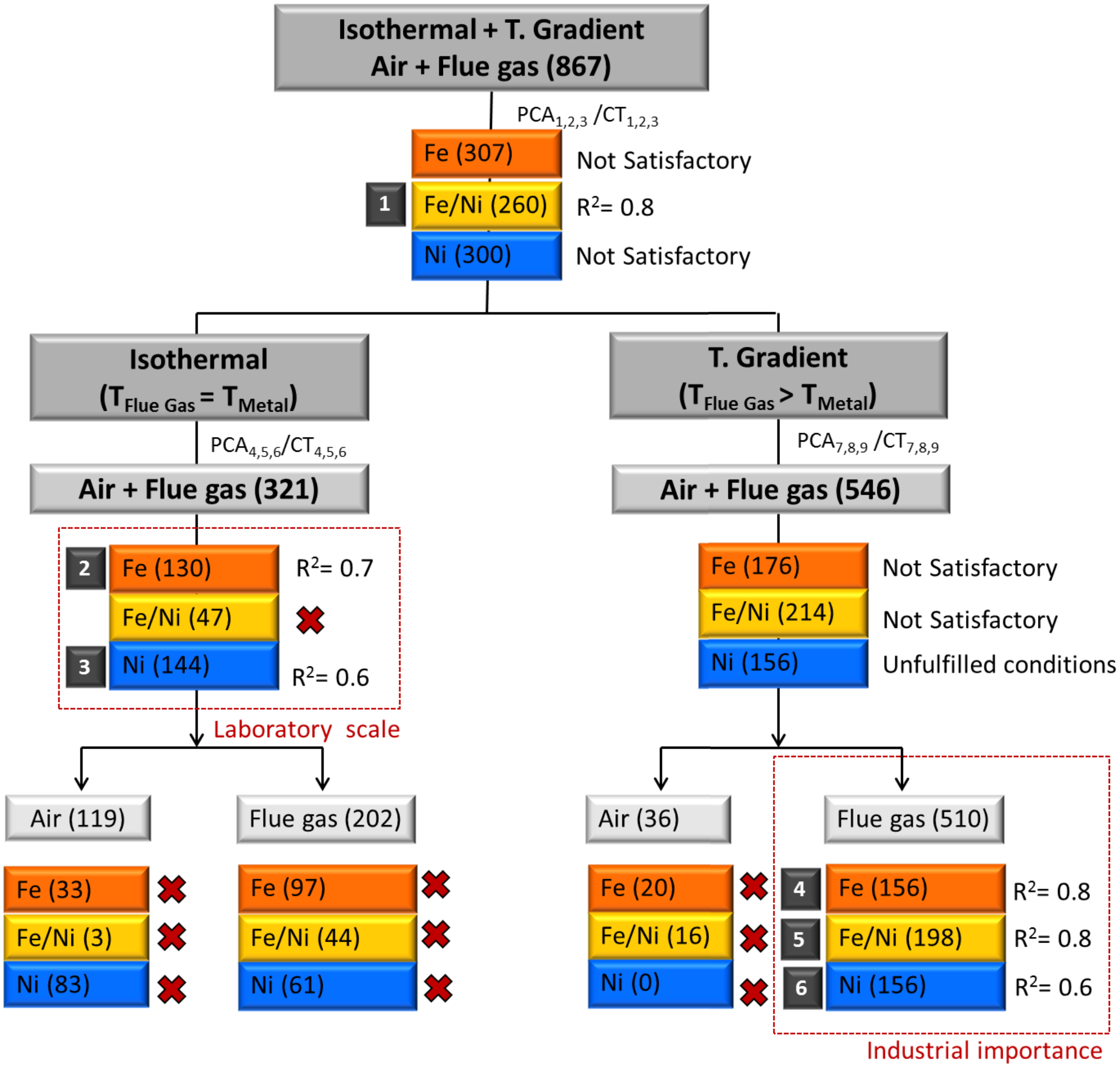

Figure IV.20. Scenarios classification from the original data set according to test conditions.

PCA_s and CT_s analysis were also performed for selecting the independent variables for T-gradient conditions. From this level of classification two models were obtained with no satisfactory results, and for Ni-based alloys the conditions were not fulfilled, as there were not air atmospheres among the test conditions. Therefore the data set was split up into pure air tests and flue gas tests. Since the amount of data for pure air was insufficient, only modeling procedures for flue gas scenarios were performed.

Models 4, 5 and 6 were generated for Fe-based alloys, austenitic-SS + Fe/Ni based alloys and Ni-based alloys, respectively under T-gradient and flue gas conditions, which happens to be the most relevant in the industry. Modeling procedures from model 2 to 6 will be explained below.

IV.3.2.1 Isothermal models

After classifying the new scenarios, PCA_s and CT_s were performed for isothermal conditions scenario for all three groups of variables: atmosphere conditions (PCA_4), materials composition (PCA_5) and ash composition (PCA_6). $PCA_{4,5,6}$ score plots are given in Appendix V and the correspond correlations matrix $CT_{4,5,6}$ are given in Appendix V.A, Appendix V.B and Appendix V.C, respectively.

PCA_4 applied on atmosphere conditions showed similar results of that on PCA_1. We can clearly see that F1 is attributed to HCl, H_2O, CO_2, F2 is attributed to T_{Metal}, SO_2, O_2 and MTLr is represented by F6 (not shown in the diagram). O_2 has the most negative correlation on MTLr and T_{Metal} has a negative but low correlation on MTLr. However, T_{Metal} is relevant for the corrosion mechanism, and hence, for modeling under isothermal conditions seems likely to add $T_{Metal,}$ and O_2 as independent variables.

PCA_5 applied on materials composition showed similar results of that on PCA_2. The analysis identified Fe, Ni, Cr and Mo with the highest effect on MTLr, but they are also highly correlated with each other. Therefore, Cr is the most viable element to be included in the models, as it forms the most protective oxide scale against high-temperature corrosion. [49] Ni and Mo will be included in the high alloyed systems where no collinearity occurs among the elements.

For PCA_6 applied on ash composition, a new variable was included, $T_{Solidus}$ which is the temperature at which melting of the ash begins. Presence of molten phases in ash mixture is known to increase the corrosion rate as they may dissolve the protective oxide layer (fluxing) on the metal surface. [189,190] The capacity of the ash melting depends on the ash's chemical composition and the temperature of the metal surface (T_{Metal}). To reach low melting point eutectics, it is necessary to have $T_{Metal} > T_{Solidus}$ and the presence of low melting point compounds.

Schaal et al. [138] analyzed by Differential Thermal Analysis (DTA), Thermo Mechanical Analyses (TMA) and thermodynamic calculations, the presence of molten phases in contact with the alloy and $T_{Solidus}$ of two different synthetic ashes: 40 wt.% chloride and 10 wt% chloride. These ash compositions correspond to Ash 1 and Ash 2, respectively (section II.2.1) but without $CaSO_4$ and keeping proportions between chlorides and sulfates.

Melt fraction estimations shown in Figure IV.21, indicates that even if chlorides content differs, $T_{Solidus}$ is the same for both salt mixtures (517°C). This means that $T_{Solidus}$ is controlled by the presence of chlorides compounds. However, the evolution of melt fraction is different above $T_{Solidus}$ for both salt mixtures. For 10 wt% chloride ash, $T_{Liquidus}$ is reached at 560°C which is 100% of NaCl-KCl-Na_2SO_4-K_2SO_4 molten phase that represents 20% of total ash (80%$CaSO_4$). For 40 wt% chloride ash, $T_{Liquidus}$ is reached at 626°C which is 100% of NaCl-KCl-Na_2SO_4-K_2SO_4 molten phase that represents 50% of total ash (50%$CaSO_4$).

$T_{Liquidus}$ of the 10 wt% chloride ash (560°C) is lower than that of the 40 wt% chloride ash (626°C). However, above $T_{Solidus}$, the fraction of molten phase of 10 wt% chloride ash is constant (20%), once the maximum fraction to be melted has been reached, while the fraction of molten phase of 40 wt% chloride ash continues increasing (50%). The higher the chloride content, the higher the molten phase fraction in contact with the oxide layer on the metal surface (fluxing). To conclude, the ash's qualitative composition controls the first appearance of molten phases ($T_{Solidus}$) and the ash's quantitative composition controls the spread of the fraction of molten phase, i.e; higher corrosion rates.

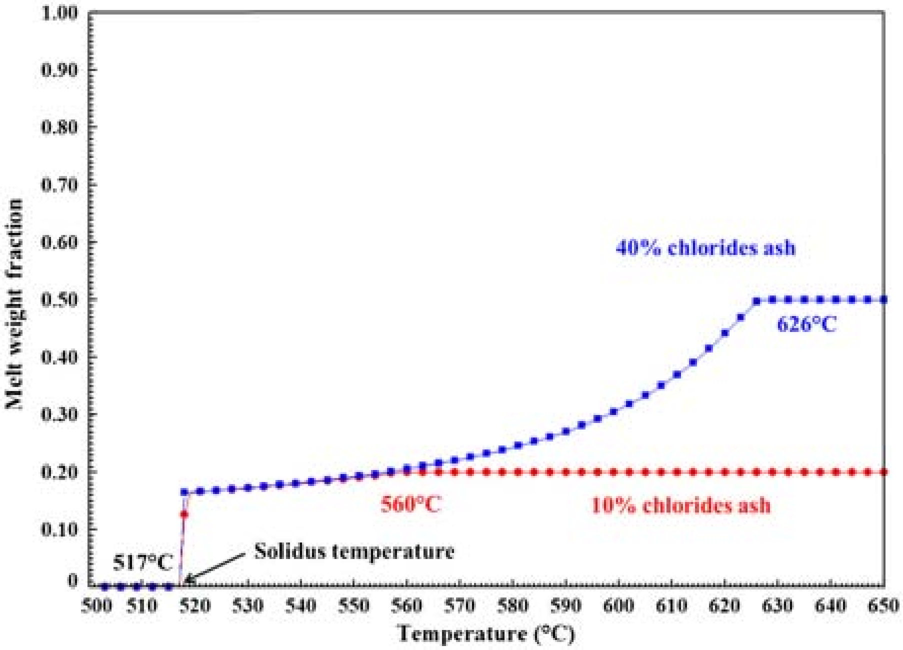

Figure IV.21. Melted weight fraction of salt mixtures calculated with the FTsalt database[195] by Schaal et al [138]

Considering that the first appearance of molten phase accelerates corrosion rates, $T_{Solidus}$ was included as independent variable in the PCA_6 analysis. Then, based on the principle that the presence of chlorides and sulfates of alkaline metals and heavy metal controls the appearance of molten phases ($T_{Solidus}$), a qualitative analysis was performed in order to estimate $T_{Solidus}$ for every ash composition present in the isothermal domain. The procedure was performed as follows:

1. $T_{Solidus}$ estimation was accomplished through a binary matrix shown in Figure IV.22, in which the presence and the absence of ash's element were indicated by 1 and 0, respectively.

2. $T_{Solidus}$ was compared to T_{Metal} and melting point of possible compounds present according to the combination of elements of the matrix.

3. $T_{Solidus}$ was estimated from phase diagrams available in literature, showing the elements present in each combination of elements of the matrix. Then $T_{Solidus}$ was assigned to each combination of elements in the matrix.

4. Once the matrix was completed, $T_{Solidus}$ was added to every ash composition of the isothermal tests that corresponds to any of 16 combination of elements of the matrix and $T_{Metal} > T_{Solidus}$. To this end, a

logical sequence (if, true, false) based on the binary code of the matrix was implemented in the database.

5. Finally, $T_{Solidus}$ was added as independent variable to PCA_6/CT_6 applied on ash composition for isothermal tests.

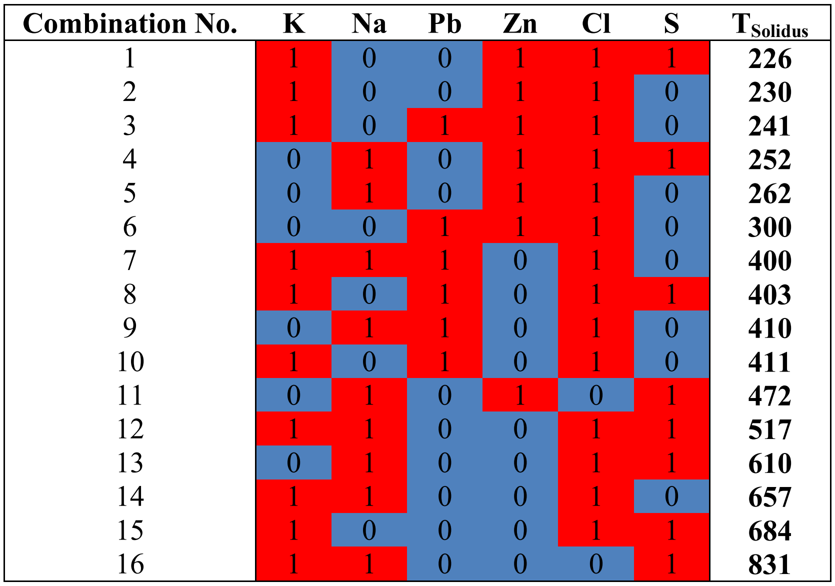

Combination No.	K	Na	Pb	Zn	Cl	S	$T_{Solidus}$
1	1	0	0	1	1	1	**226**
2	1	0	0	1	1	0	**230**
3	1	0	1	1	1	0	**241**
4	0	1	0	1	1	1	**252**
5	0	1	0	1	1	0	**262**
6	0	0	1	1	1	0	**300**
7	1	1	1	0	1	0	**400**
8	1	0	1	0	1	1	**403**
9	0	1	1	0	1	0	**410**
10	1	0	1	0	1	0	**411**
11	0	1	0	1	0	1	**472**
12	1	1	0	0	1	1	**517**
13	0	1	0	0	1	1	**610**
14	1	1	0	0	1	0	**657**
15	1	0	0	0	1	1	**684**
16	1	1	0	0	0	1	**831**

Figure IV.22. Binary matrix used to estimate $T_{Solidus}$ for each combination of ash elements in the isothermal domain.

PCA_6 applied on ash composition showed three groups of variables: $T_{Solidus}$ and chloride forming melting elements (Cl, Na, K, Pb, Zn) are placed in F1, sulfate forming elements (S and Ca) and refractory oxide-forming elements (Al, Si, Fe Ca) are placed in F2, while MTLr is in F8 (not shown in the diagram). The linear correlations with the ash's elements decrease and become no significant, while $T_{Solidus}$ shows a negative significant correlation with MTLr. This means that MTLr increases with decreasing $T_{Solidus}$, as reported in literature. [53,138] $T_{Solidus}$ is diametrically opposed (negative correlations) to Cl and melting elements (Na, K, Pb, Zn). This means that $T_{Solidus}$ decreases with increasing chlorides

The variable $T_{Solidus}$ qualitatively evaluated, has good correlation with the corrosion rate and gathers the qualitative characteristics of the ash's composition. Therefore, for modeling purposes under isothermal conditions, it seems convenient to include $T_{Solidus}$ and chloride forming melting elements in the form [Clx(Na+K+Pb+Zn] to avoid collinearity.

IV.3.2.1.1 Model 2: Fe-based alloys

Model 2 was generated from the data set of Fe-based alloys isothermal tests (130 data). Approximately 75% of the original data set was randomly selected to create the model and the remaining 25% of the data set was used to validate the model. The validation data set was within the model validity domain but not included in the data set used to determine the predictors of the model. Table IV.4 shows the model validity domain and the goodness of fit statistics. Figure IV.23 shows the relative weight of the variables in the model, which is represented by Equation (57). Figure IV.24 shows the accuracy chart of the model.

Table IV.4a shows the highest and lowest limits between which the model is valid. The model can predict corrosion rates for Fe-based alloys in the composition range (82-98 wt.%Fe, 0-3.5 wt.% Ni, 0-13 wt.%Cr 0-2 wt.% Mo), at temperatures between 400°C and 693°C, complex atmospheres, as well as pure air and ash compositions calculated in elemental form within the established limits.

Table IV.4b shows the goodness of fit statistics of the model. The $R^2 = 0.67$ means that 67% of the mass loss rates was explained by the model. The DW = 1.6 means that the residuals are independent from each other. The F = 21.7 and $|Pr > F| < 0.0001$ means that there is a significant linear relationship between the MTLr and the set of independent variables taken together in the model (Figure IV.23), from the statistical point of view the model is satisfactory.

Table IV.4. Statistics of model 2. a) Validity domain b) Goodness of fit statistics

Variable	Minimum	Maximum
MTLr (mm/y)	0,6	40.1
T_{Metal} (°C)	400	693
O_2 (vol.%)	0	21.0
Cr (wt.%)	0	13
S (wt.%)	0	14
Cl (wt.%)	0	22
$T_{Solidus}$ (°C)	226	831
Na+K+Zn+Pb (wt.%)	2.4	22

a)

Goodness of fit statistics:	
R²	0.67
Adjusted R²	0.64
DW	1.6
MSE	19.74
RMSE	4.44
Analysis of variance:	
F	21.7
Pr > F	< 0.0001

b)

The model's equation (57) shows the predictors of the model. The standardized coefficients of the model determined with 95% confidence are represented in the Figure IV.23, which are used to compare the relative weights of the variables on the corrosion rate. The higher the absolute value of a coefficient, the more important the variable on MTLr.

$$\boldsymbol{MTLr = 40.3 + 1.7 \times 10^{-2} \times T_{Metal} - 2.7 \times 10^{-1} \times [O_2] - 1.5 \times 10^{-1} \times [Cr]}$$

$$\boldsymbol{-1.2 \times [S] - 6.0 \times 10^{-2} \times T_{Solidus} + 2.0 \times 10^{-2} \times [Cl \times (Na + K + Zn + Pb)]} \quad \textbf{Equation 57}$$

Where, $MTLr$ is given in $\frac{mm}{y}$, the temperatures T_{Metal} and $T_{Solidus}$ in *Celsius (°C)*, $[O_2]$ in *vol.%* in the gas, $[Cr]$ in *wt.%* in the alloy and $[Cl, Na, K, Zn, Pb]$ in *wt.%* in the ash.

Like the previous model, the variables are placed according to the group of variables that they represent. T_{Metal}, and $[O_2]$, from the atmosphere conditions, the $[Cr]$ from the composition of the material, and $[S]$, $[Cl \times (Na + K + Zn + Pb)]$ and $T_{Solidus}$ from the ash characteristics. The effect of the variables on the MTLr was compare with experimental findings in literature. We can see in the 1st order of priority, the variables related with the ash characteristics: $T_{Solidus}$, $[S]$ and $[Cl \times (Na + K + Zn + Pb)]$. $T_{Solidus}$ has a negative effect on MTLr because the lower the $T_{Solidus}$ of the ash composition, the faster the first appearance of molten phases, and hence, the higher the corrosion rates. However, $T_{Solidus}$ only depends on the ash's qualitative composition, while $[S]$, $[Cl \times (Na + K + Zn + Pb)]$ plays a fundamental role in the extent of the molten areas, as reported by Schaal et al.[138] MTLr increases with increasing concentration of chlorides (lower melting points) and decreasing concentration of sulfates (higher melting points) in the ash. Since $T_{Solidus}$ is highly correlated with chloride forming melting elements (PCA_6), [79,138,183,185,186,190] the interaction factor between chlorine and melting elements $[Cl \times (Na + K + Zn + Pb)]$ was also applied, in order to avoid collinearity between independent variables in the MLR, as it was explained in the model 1.

In the 2nd order of importance, there are T$_{Metal}$, $[O_2]$ and $[Cr]$. MTLr increases with increasing T$_{Metal}$ as reported in literature [36,53,84,91] $[O_2]$ and $[Cr]$ has a negative effect on MTLr, as both contributes to form protective oxide layers, and therefore, tend to decrease the corrosion rate. [53,64] However, their effect is lower on the MTLr, because the Cr-content in Fe-based alloys domain is also low and insufficient to form stable oxide layers to counteract active oxidation and the fluxing effect of the ash.

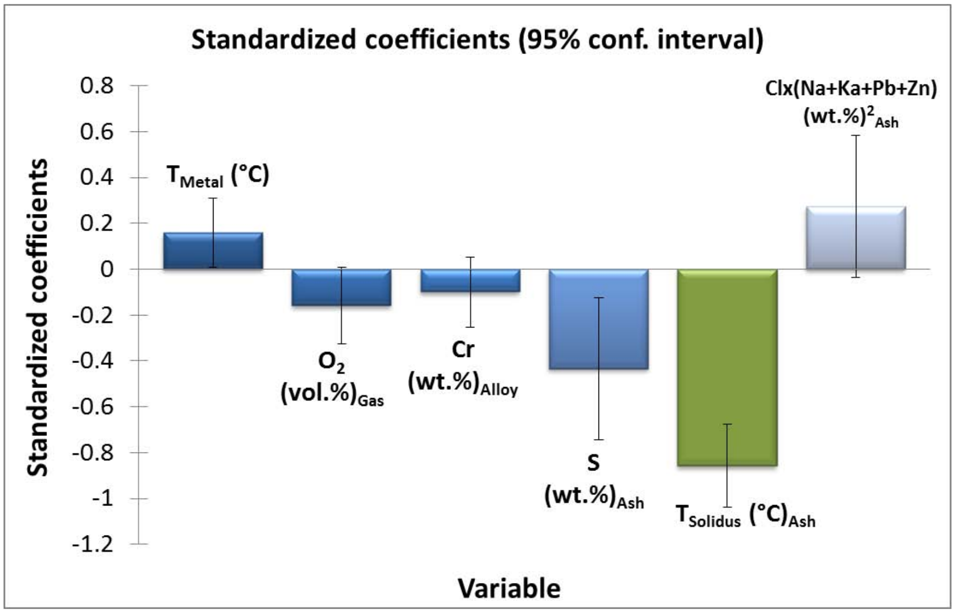

Figure IV.23. Standardized coefficients chart: relative weight of the independent variables on model 2 for Fe-based alloys

Figure IV.24 shows the accuracy chart of the model that represents the residuals between experimental values and predicted values for the model data set and the validation data set. The coefficient RMSE = 4.4 means the standard deviation (SD) of the model's predictions, leading to equation (58). The variance of MTLr for Fe-based alloys is high (0-40 mm/y), the model fits for low and high rates. This means that the mean error works well for high rates (SD < 25%) but not that much for low rates (SD > 100%). However, the accuracy of the model depends on the experimental data used for creating the model, as well as the statistic law assumed for fitting criteria. This was explained in the section IV.1 for 16Mo3 whose results are within data distribution of this model. If the corrosion rates present a SD > 50% for the same experimental condition, this error is reflected in the model, the predictions will not be better that the experimental data used for creating the model. Likewise, if the corrosion rate decreased with time for the same experimental condition with SD > 100%, this error is also reflected in the model, and hence, the assumption of a linear law instead a parabolic law also add an important source of error to the model.

$$\boldsymbol{MTLr_{Experimental} = MTLr_{Predicted} \pm 4.4\ \frac{mm}{y}} \qquad \textbf{Equation 58}$$

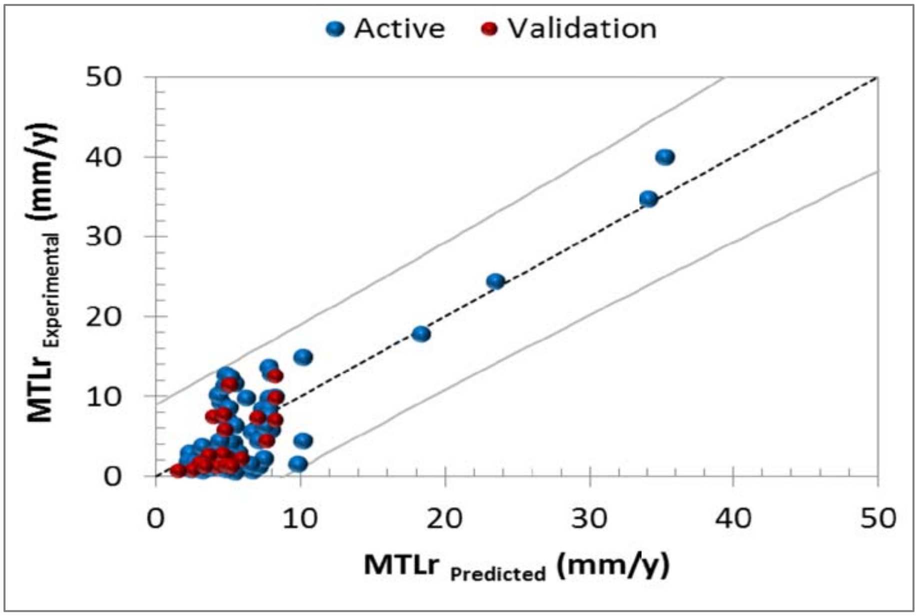

Figure IV.24. Accuracy chart with the residuals between experimental values and predicted values by model 2 for Fe-based alloys

IV.3.2.1.2 Model 3: Ni-based alloys

Model 3 was generated from the data set of Ni-based alloys for isothermal tests (144 data). Approximately 75% of the original data set was randomly selected to create the model. The residual 25% of the data set was used to verify the predictive ability of the model in the same validity domain. Table IV.5 shows the model validity domain and the goodness of fit statistics. The model is represented by Equation (59). Figure IV.25 shows the relative weights of the variables in the model and Figure IV.26 shows the accuracy chart of the model.

Table IV.5a shows the highest and lowest limits between which the model is valid. The model can predict corrosion rates for Ni-based alloys in the composition range (0-13 wt.% Fe, 53-68 wt.% Ni, 6.5-30 wt.% Cr, 0-16 wt.% Mo), at temperatures between 450°C and 750°C, complex atmospheres, as well as pure air and ash compositions calculated in elemental form within the established limits.

Table IV.5b shows the goodness of fit statistics of the model. The $R^2 = 0.57$ means that 57% of the mass loss rates was explained by the model. The DW = 1.7 shows that the residuals are independent from each other. The F = 20.6 and $|Pr > F| > 0.0001$ means that there is a significant linear relationship between the MTLr and the set of independent variables taken together in the model (Figure IV.25), and hence, the model is satisfactory from the statistical point of view.

Table IV.5. Statistics of model 3. a) Validity domain b) Goodness of fit statistics

Variable	Minimum	Maximum
MTLr (mm/y)	0	7.5
T_{Metal} (°C)	450	700
O_2 (vol.%)	8	20
Ni (wt.%)	53	68
Cr (wt.%)	6.5	30
Mo (wt.%)	0	16
Cl (wt.%)	0	53.5
Na+K+Zn+Pb (wt.%)	8.5	58.6
$T_{Solidus}$ (°C)	226	831

a)

Goodness of fit statistics:	
R^2	0.57
Adjusted R^2	0.54
DW	1.7
MSE	1.4
RMSE	1.2
Analysis of variance:	
F	20.6
Pr > F	< 0.0001

b)

The model's equation (59) shows the predictors of the model, whose standardized coefficients are represented in the Figure IV.25. The standardized coefficients are used to compare the relative weights of the variables on the corrosion rate. The higher the absolute value of a coefficient, the more important the variable on MTLr.

$$\boldsymbol{MTLr = 11.1 + 2.7 \times 10^{-3} \times (T_{Metal}) - 7.6 \times 10^{-1} \times (Ni) - 1.5 \times 10^{-1} \times (Cr) - 1.0 \times 10^{-1} \times (Mo)}$$

$$\boldsymbol{-6.4 \times 10^{-3} \times (T_{Solidus}) + 6.7 \times 10^{-3} \times [Cl \times (Na + K + Zn + Pb)]} \qquad \textbf{Equation 59}$$

Where, $MTLr$ is given in $\frac{mm}{y}$, temperatures T_{Metal} and $T_{Solidus}$ in *Celsius (°C)*, $[Ni]$, $[Cr]$, $[Mo]$ in *wt.%* in the alloy and $[Cl, Na, K, Zn, Pb\,]$ in *wt.%* in the ash.

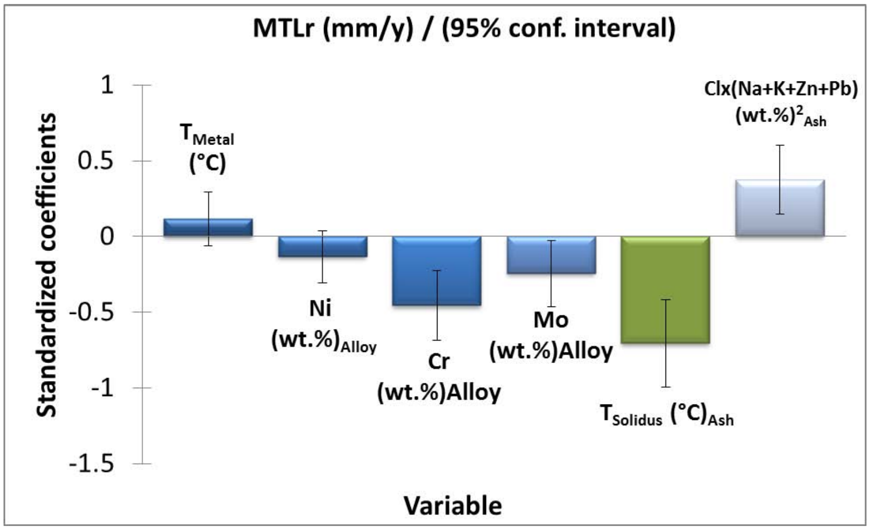

Figure IV.25. Standardized coefficients chart: relative weight of the independent variables on model 3 for Ni-based alloys

Like the previous models, the variables are placed according to the group of variables they represent. The variable T_{Metal} represents the atmosphere conditions, $[Ni]$, $[Cr]$, $[Mo]$ represent the composition of the material, $T_{Solidus}$ and $[Cl \times (\,Na + K + Zn + Pb)]$ represent the ash characteristics. As the model for Fe-based alloys (Model 2), the role of the ash variables continues standing out in the 1st order of importance in the model for Ni-based alloys. Nevertheless, the protective capacity of the high-temperature alloys becomes important; especially Cr in the 1st order, followed by Mo. In the 2nd order, there are T_{Metal} and $[Ni]$. In this domain the Cr-content is large (6.5-30 wt% Cr) as well as the Mo-content (0-16%Mo), which allows describing the protective ability of the elements in a wider range. An austenitic matrix with higher contents of Cr and Mo appear to decrease the corrosion rates, even in presence of chlorides $[Cl \times (Na + K + Zn + Pb)]$, whose influence decreases with respect to Fe-based alloys. For this model, O_2 do not improve the linear fit, and hence, it was excluded. This can be linked with the effect of combining both atmospheres (flue gas and laboratory air) in the same domain.

The model only explains 57% of the variation of the corrosion rates. This might be due to other variables also important for the corrosion process in Ni-based alloys that were not considered in the model. As the number of alloy elements increases, the corrosion mechanism also does in complexity. For example, higher Cr-contents in the temperature range of the model (450-700°C) may favor the formation of oxide layers capable to decrease the corrosion rate with time. In this case, a linear kinetics assumption would not be adequate. However, a diffusional approach must be used to confirm this theory. $T_{Solidus}$ keeps its relevance in the model, because molten phases can dissolve protective layers in the metal surface. Protective chromia layers may not perform completely well in face of chlorides $[Cl \times (Na + K + Zn + Pb)]$, due to possible reactions between chromia and potassium or zinc chlorides to form $K_2Cr_2O_4$ or $ZnCr_2O_4$, which consume the protective layers. [196]

Figure IV.27 shows the accuracy chart of the model that represents the residuals between experimental values and predicted values for the model data set (blue) and the validation data set (red). The coefficient RMSE = 1.2 means the standard deviation of the predictions of the model, leading to equation (60). In this model, even when R^2 decreases, the SD is lower than that of model 2, because the spread of the data is much less for Ni-based alloys (0-7.5 mm/y), and in most cases there is a corrosion rate for each experimental condition, which leads to lower standard deviations. However, the model still works better for higher rates.

$$MTLr_{Experimental} = MTLr_{Predicted} \pm 1.2 \frac{mm}{y} \qquad \textbf{Equation 60}$$

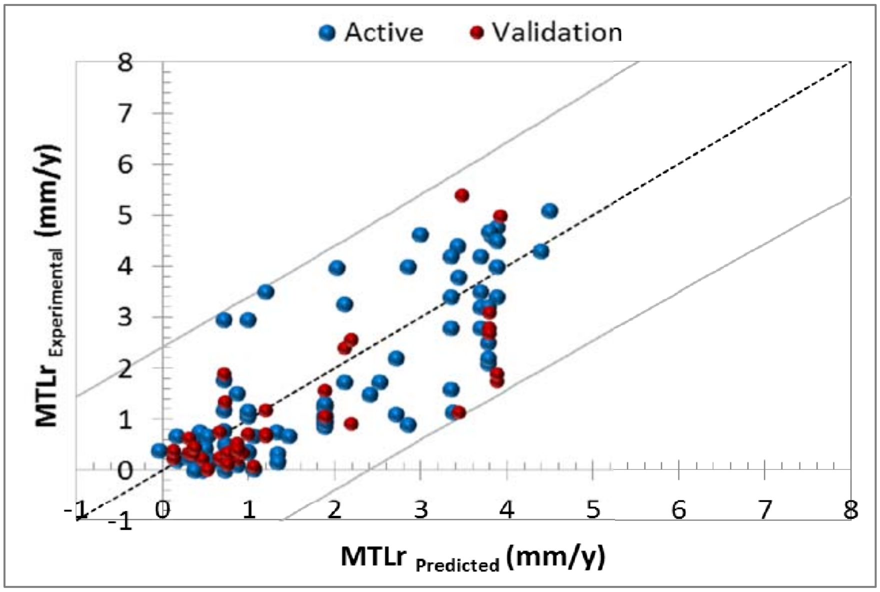

Figure IV.26. Accuracy chart with the residuals between experimental values and predicted values by model 3 for Ni-based alloys

IV.3.2.2 T-gradient models

After having classified the new scenarios, PCAs and CTs were performed for T-gradient conditions scenario for all three groups of variables: atmosphere conditions (PCA_7), material's chemical composition (PCA_8) and ash chemical composition (PCA_9). $PCA_{7,8,9}$ score plots are given in Appendix VI.A and correlations matrix $CT_{7,8,9}$ are given in Appendix VI.B, Appendix VI.C and Appendix VI.D. The Figure IV.27 shows the data distribution of the MTLr as function of $T_{Flue\ gas}$ and T_{Metal} that were included in the PCA_7 for atmosphere conditions.

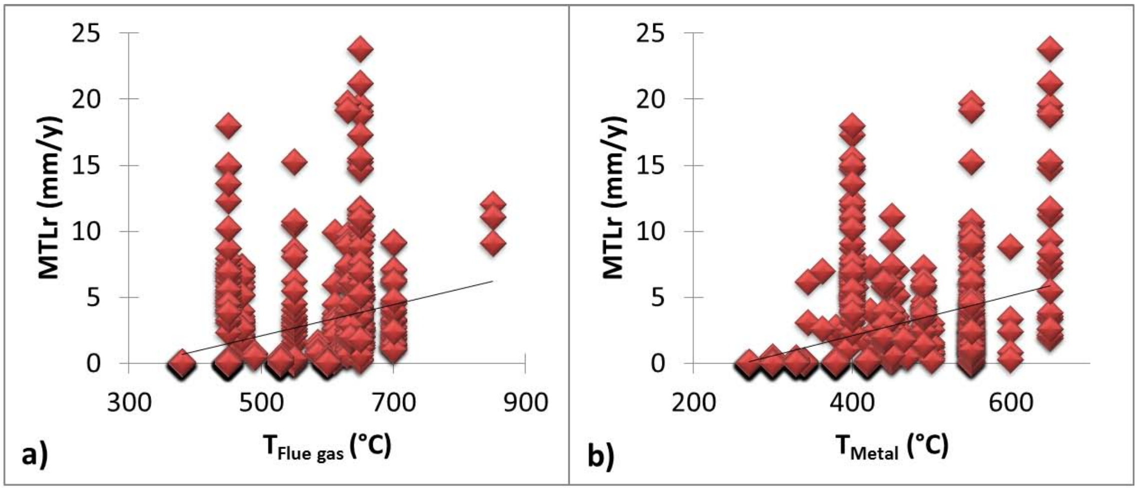

Figure IV.27. Data distribution of MTLr as a function of a) $T_{Flue\ gas}$ and T_{Metal}

In the PCA_7 score plot, we can see that F1 is attributed to HCl, H_2O, CO_2. F2 is attributed to $T_{Flue\ gas}$, SO_2 and MTLr while F3 (not shown in the digram) is attributed to T_{Metal} and O_2. The correlations among the independent variables are similar to those obtained in PCA_2. MTLr shows the highest correlations with T_{Metal} and $T_{Flue\ gas}$. Furthermore, no statistical correlation is observed between T_{Metal} and $T_{Flue\ gas}$. Therefore for modeling purposes under T-gradient conditions seems pertinent to add both temperatures: $T_{Metal,}$ and $T_{Flue\ gas.}$ The gases O_2, HCl and SO_2 show low correlations, however due to their relevance for the corrosion mechanism in complex atmospheres they will be included to improve fitting criteria.

PCA_8 for materials composition showed similar results of that on PCA_1 and PCA_4, regards the correlations among the independent variables. However, in this case MTLr shows very low correlations with regard to the alloy elements. This means that in complex atmospheres such as, T-gradient and flue gas, other variables are more relevant for the corrosion process rather than the alloy composition. Nevertheless, considering the effect in previous models, Cr and Mo will be evaluated in the linear regressions to improve fitting criteria.

PCA_9 for ash composition showed three groups of variables: chloride forming elements (Cl, Na, K, Pb, Zn), sulfate forming elements (S and Ca) and refractory oxide-forming elements (Al, Si, Fe Ca). For this data distribution, MTLr is highly correlated with S and chloride forming elements (Cl, Na, K, Pb, Zn) rather than refractory oxide forming elements (Al,Si,Fe,Ca). Therefore, for T-gradient conditions it seems suitable to add [Clx(Na+K+Pb+Zn]. The variable (Al+Si+Fe+Ca) will be added in the cases where no collinearity occurs between both variables, to improve fitting criteria.

IV.3.2.2.1 Model 4: Fe-based alloys

Model 4 was generated from the data set of Fe-based alloys in flue gas conditions (156 data). Approximately 75% of the original data set was randomly selected to determine the predictors of the model and the remaining 25% of the data set was used for the model validation. Table IV.6 shows the validity domain and the goodness of fit statistics of the model. Figure IV.28 shows the relative weights of the variables in the model and Figure IV.29 shows the accuracy chart of the model.

Table IV.6a shows the highest and lowest variable limits between which the model is valid. The model can predict corrosion rates for Fe-based alloys in the composition range (95-98 wt.% Fe, 0-2.2 wt.%Cr, 0-0.1 wt.% Ni, 0-1 wt.% Mo), at flue gas temperatures between 380°C and 850°C and metal temperatures between 270°C and 600°C, in complex atmospheres in a gas composition range (132-2000 ppm) HCl and (0-200 ppm)SO_2 and for ash compositions calculated in elemental form within the limits indicated.

Table IV.6b shows the goodness of fit statistics of the model. The $R^2 = 0.75$ means that 75% of the variation of MTLr was explained by the model. The DW = 1.0 shows that the residuals are dependent from each other. The F = 47.3 and $|Pr > F| < 0.0001$ means that there is a significant linear relationship between the MTLr and the set of independent variables taken together in the model (Figure IV.28), and hence, the model is satisfactory.

Table IV.6. Statistics of model 4. a) Validity domain b) Goodness of fit statistics

Variable	Minimum	Maximum
MTLr (mm/y)	0.001	18
$T_{Flue\ gas}$ (°C)	380	850
T_{Metal} (°C)	270	600
HCl (ppm)	132	2000
SO2 (ppm)	0	200
Cr (wt.%)	0	2.2
S (wt.%)	0	18
Cl (wt.%)	0	22
Al+Ca+Si+Fe (wt.%)	0	45
Na+K+Zn+Pb (wt.%)	0	37

a)

Goodness of fit statistics:	
R²	0.75
Adjusted R²	0.74
DW	1.0
MSE	5.08
RMSE	2.25
Analysis of variance:	
F	47.3
Pr > F	< 0.0001

b)

As previous models, the variables are placed by groups. The variables $T_{Flue\ gas}$, T_{Metal}, $[HCl]$ and $[SO_2]$ from the atmosphere conditions, the $[\boldsymbol{Cr}]$ from the composition of the material in which we can notice that the Cr-composition range is really narrow in this case and $[Cl \times (Na + K + Zn + Pb)]$ from the ash composition. The predictors of the model are presented in the Equation (61), whose standardized coefficients are shown in Figure IV.28.

$$\boldsymbol{MTLr = -17.2 + 2.2 \times 10^{-2} \times T_{Flue\ gas} + 1.8 \times 10^{-2} \times T_{Metal} + 2.6 \times 10^{-3} \times [HCl]}$$

$$\boldsymbol{-8.4 \times 10^{-3} \times [SO_2] - 1.9 \times [Cr] + 1.4 \times 10^{-2} \times [Cl \times (Na + K + Zn + Pb)]} \quad \textbf{Equation 61}$$

Where, $MTLr$ is given in $\frac{mm}{y}$, temperatures T_{Metal}, $T_{Flue\ gas}$ in *Celsius (°C)*, $[SO_2]$, $[HCl]$ in ppm in the gas, $[Cr]$ in *wt.%* in the alloy and $[Cl, Na, K, Zn, Pb]$ in *wt.%* in the ash.

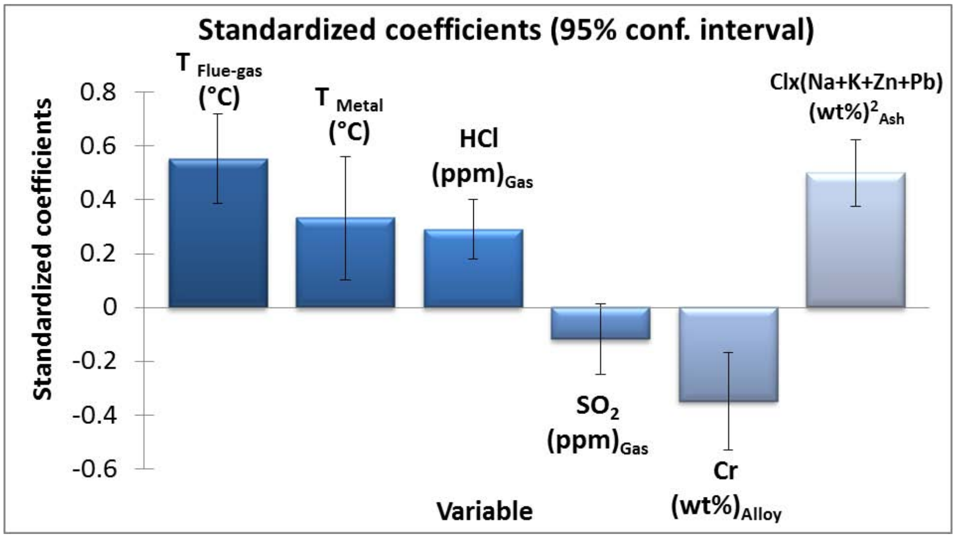

Figure IV.28. Standardized coefficients chart: relative weight of the independent variables on model 4 for Fe-based alloys

The effect of the variables on the corrosion rate has been reported by previous experimental findings in this type of atmospheres. [103,108] In the 1st order of relevance there are $T_{Flue\ gas}$ and $[Cl \times (Na + K + Zn + Pb)]$, both variables with a high positive effect on MTLr. $T_{Flue\ gas}$ controls ash and gas phase composition and thus determines the composition of the deposit and the deposition rates. At high $T_{Flue\ gas} > 650°C$-750°C, alkali and heavy metal chlorides present in the flue gas are mainly gaseous and will condense on the "cold tube". At low $T_{Flue\ gas}$, chlorides are present as solid particles. In this case alkali deposition rates is controlled by adhesion mechanism and deposit composition is different from high flue-gas temperature.[191,193,194] Chlorides concentrations increasing $[Cl \times (Na + K + Zn + Pb)]$ favors corrosion mechanisms as active oxidation and corrosion by molten ash, because the presence of alkali metal chlorides (NaCl, KCl) and heavy metal chlorides ($ZnCl_2$, $PbCl_2$), reduces the melting point of the ash. [53,62,68,73,75,110,140,186]

In the 2nd order, there are T_{Metal}, $[HCl]$ and $[Cr]$. MTLr increases with increasing T_{Metal}, because it promotes metallic chloride volatilization (limiting step of active oxidation mechanism) and ash fusion on the metal surface. [36,53,84,91] HCl increases the corrosion rates, as it promotes active oxidation through chlorine formation. [53,61,64] For Fe-based alloys, the effect is particularly high because they have low resistance to chlorinated environments compared to Ni-based alloys. This is related to the high affinity of iron for chlorine, which entails the formation of volatile iron chlorides and lowers the melting point of eutectic mixtures ($FeCl_2$, KCl).[89] Although, increasing Cr-contents in the alloy, increases corrosion resistance, in this case chromium contents are too low (0-2.2 wt.%Cr) to form stable oxide layers.[90,93,97,175] The oxidizing effect of O_2 was not included because it did not improve the fitting of the model. This may be due to the low chromium contents that are insufficient to form resistant oxide layers. In the last order there is SO_2, which slightly decreases the corrosion rates as it limits iron chloride formation and aids in the sulfation of chlorides in the deposits. [62]

The accuracy chart of the model is shown in the Figure IV.29. The chart shows good agreement between experimental corrosion rates and the predicted ones. However, the coefficient RMSE = 2.2 that is the mean error of the predictions of the model (62) is still high for low corrosion rates. In this case, the data is spread-out (0.001-18 mm/y), but also we can clearly see that this is linked to the standard deviation of the experimental data. The same experimental condition generates different corrosion rates with a high standard deviation (SD). These experimental errors or nonlinear kinetics are gathered by the model.

$$MTLr_{Experimental} = MTLr_{Predicted} \pm 2.2\ \frac{mm}{y}$$

Equation 62

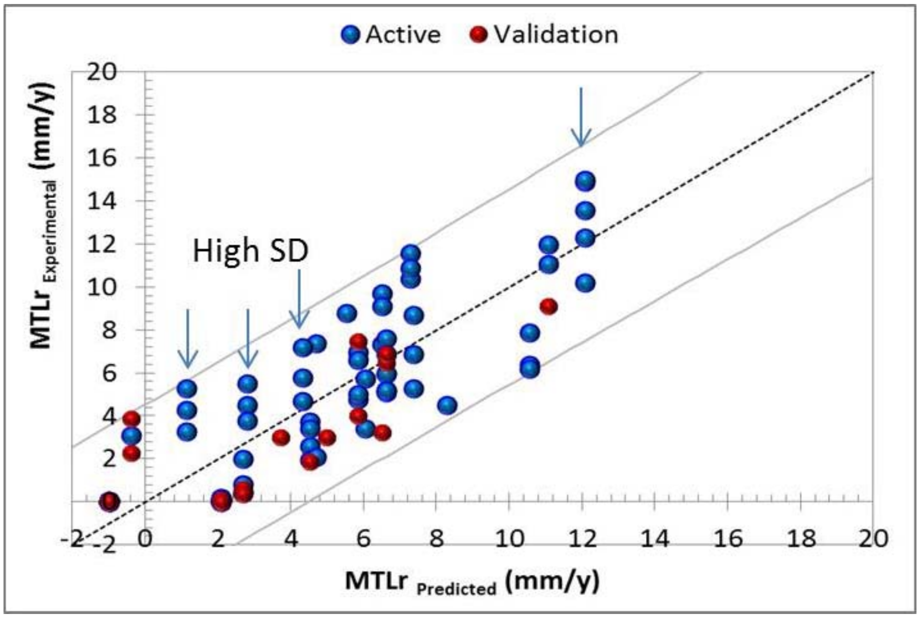

Figure IV.29. Accuracy chart with the residuals between experimental values and predicted values by model 4 for Fe-based alloys in flue gas

IV.3.2.2.2 Model 5: austenitic stainless steels and Fe/Ni-based alloys

Model 5 was proposed using the data set of austenitic stainless steels and Fe/Ni-based alloys in flue gas conditions (198 data). The dataset was randomly separated into two groups of the same size and in the same validity domain, one half was used to create the model, and the other half was used to validate the model. Table IV.7 shows the validity domain and the goodness of fit statistics of the model. Figure IV.30 shows the relative weights of the variables in the model represented by Equation (63) and Figure IV.31 shows the accuracy chart of the model.

Table IV.7a shows the highest and lowest variable limits between which the model is valid. The model can predict corrosion rates austenitic stainless steels and Fe/Ni-based alloys in the composition range (29-69 wt.% Fe, 18.2-28.9 wt.% Cr , 9-44 wt.% Ni, 0-3.3 wt.% Mo), at flue gas temperatures between 450°C and 700°C and metal temperatures between 300°C and 650°C, in complex atmospheres (within the limits established for O_2 and HCl) and for ash compositions calculated in elemental form within the limits indicated below.

Table IV.7b shows the goodness of fit statistics of the model. The $R^2 = 0.82$ means that 82% of the variation of MTLr was explained by the model. The DW = 1.8 shows that the residuals are independent from each other. The F = 58.5 and $|Pr > F|$< 0.0001 means that there is a significant linear relationship between the MTLr and the set of independent variables taken together in the model (Figure IV.30). The statistical indicators confirm that the model is satisfactory.

Table IV.7 Statistics of model 5. a) Validity domain b) Goodness of fit statistics

Variable	Minimum	Maximum
MTLr (mm/y)	0	23.8
$T_{Flue\ gas}$ (°C)	450	700
T_{Metal} (°C)	300	650
O_2 (vol.%)	5.7	10.5
HCl (ppm)	132	1500
Cr (wt.%)	18.2	28.9
Cl (wt.%)	0.1	41.4
Al+Ca+Si+Fe (wt.%)	0	44.6
Na+K+Zn+Pb (wt.%)	0	58.6

a)

Goodness of fit statistics:	
R^2	0.82
Adjusted R^2	0.80
DW	1.8
MSE	3.56
RMSE	1.89
Analysis of variance:	
F	58.5
Pr > F	< 0.0001

b)

In the equation of the model (63) as well in the diagram of standard coefficients Figure IV.30, the variables are positioned by groups: $T_{Flue\ gas}$, T_{Metal}, $[O_2]$ and $[HCl]$ from the atmosphere conditions, the $[Cr]$ represents the composition of the material, refractory oxides forming elements $[Ca + Al + Si + Fe]$ and melting elements $[Cl \times (Na + K + Zn + Pb)]$ represent the ash composition. We can notice that even when the alloy elements increase in the alloy system evaluated, the variables from external conditions (flue gas and ash) outnumber the material variables by 6 to 1. Therefore, we can realize that as the complexity of the atmosphere increases, the external conditions play a key role in the explanation of the corrosion rates rather than the material properties. On the other hand, the Cr showed low correlation coefficients in the PCA_8. However, their influence on the corrosion rate according to the model is significant, which shows the importance of the variables interaction and their weighting by linear regression.

$$\boldsymbol{MTLr = -8.2 \times E - 1 + 2.0 \times 10^{-2} \times T_{Flue\ gas} + 8.7 \times 10^{-3} \times T_{Metal} - 5.5 \times 10^{-1} \times [O_2]}$$

$$\boldsymbol{+5.5 \times 10^{-4} \times [HCl] - 2.8 \times 10^{-1} \times [Cr] - 1.2 \times 10^{-1} \times [Ca + Al + Si + Fe]}$$

$$\boldsymbol{+3.7 \times 10^{-3} \times [Cl \times (Na + K + Zn + Pb)]} \qquad \textbf{Equation 63}$$

Where, $MTLr$ is given in $\frac{mm}{y}$, temperatures $T_{Flue\ gas}$, T_{Metal} in *Celsius (°C)*,$[O_2]$ in *(vol.%)* and $[HCl]$ in *ppm* in the gas, $[Cr]$ in *wt.%* in the alloy and $[Cl, Na, K, Zn, Pb, Ca, Al, Si, Fe]$ in *wt.%* in the ash.

Figure IV.30 shows the influence of the variables on the corrosion rate. We can see that $T_{Flue\ gas}$ maintains a higher influence than T_{Metal} as observed for Fe-based alloys. According to the model, we can place $T_{Flue\ gas}$ and $[Cl \times (Na + K + Zn + Pb)]$ in the 1st order of importance, both variables increase the corrosion rates as they play an important role in the mechanism of deposit formation and molten phase corrosion. In the 2nd order, we can place T_{Metal}, $[Cr]$ and $[Ca + Al + Si + Fe]$. T_{Metal} increases the corrosion rates because it promotes the high-temperature corrosion mechanisms. The $[Cr]$ has a negative effect, as it increases the corrosion resistance, in this domain of alloys the Cr-range is also adequate for protecting through oxide layer formation [18 – 29 wt.% Cr] .Alloys with less than 15%Cr are generally very susceptible to high-temperature corrosion attacks. But austenitic stainless steels are more resistant than carbon steels. The most common is Type 304 (UNS S30400)$^{(2)}$ (18%Cr). Higher chromium austenitic stainless steels appear to be better in terms of furnace wall corrosion. For example, Type 310 (UNS S31000) (24%Cr) is more corrosion resistant than Type 304. [101]

Usually there is collinearity between $[Cl \times (Na + K + Zn + Pb)]$ and $[Ca + Al + Si + Fe]$, due to the way the ash compositions are calculated, because the higher the concentration of refractory oxides, the lower the concentration melting elements. However, this is not the case, no collinearity was found and the variable $[Ca + Al + Si + Fe]$ was included to improve the linear fit. It has a negative effect on the corrosion rate, because the higher the concentration of refractory oxides in the ash, the higher the ash's melting point, which delays the fluxing by the molten phases.

$[O_2]$ and $[HCl]$ are positioned in the last order. Unlike the Fe-based alloys model, adding the $[O_2]$ improved the linear fit with a negative effect on the corrosion rate, because higher $[O_2]$ contributes to the formation of oxide layers, which is possible on Fe/Ni based alloys, because of the higher contents of Cr in the model domain. $[HCl]$ has a slightly positive effect on the corrosion rate, the large error bar means that its effect could be neglected in the model. However, it was included due to its relevance under flue gas conditions. But its effect is certainly much lower than that of Fe-based alloys. This is linked to the higher resistance of the austenitic matrix to chlorinated environments compared to Fe-based alloys which present higher affinity to Cl_2.

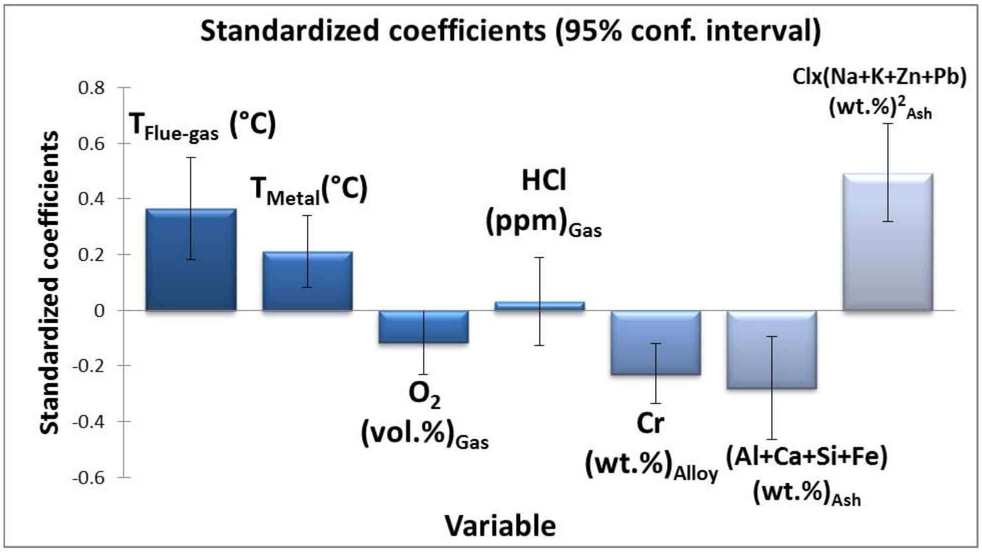

Figure IV.30. Standardized coefficients chart: relative weight of the independent variables on model 5 for austenitics-SS+Fe/Ni-based alloys in flue gas

The accuracy chart of the model in the Figure IV.31 shows good agreement between experimental corrosion rates and the predicted ones, all of them in the confidence interval. The coefficient RMSE = 1.9 means the mean error of the predictions of the model (64). Event when a good R^2 was obtained, the mean

---

(2) UNS numbers are listed in *Metals and Alloys in the Unified Numbering System*, published by the Society of Automotive Engineers (SAE International) and cosponsored by ASTM International.

error is high for low rates predictions. However, in this case the lack of reproducible rates is not an issue, but the spread of the data is still large (0-24 mm/y). In the diagram, most predictions of low corrosion rates are found very close to the bisector while the higher rates are located in the limits of the confidence interval. This difference between both cases increases the mean error of the model. Furthermore, in this domain most data comes from industrial tests, whose conditions are subjected to high variations during the dwell time considered. Also, the higher content of alloy elements in this domain favors the formation of oxide layers that may promote incubation periods. This periods are unmeasured in one-cycle tests, and thus not considered by the linear kinetics.

$$\boldsymbol{MTLr_{Experimental} = MTLr_{Predicted} \pm 1.9\ \frac{mm}{y}}$$ **Equation 64**

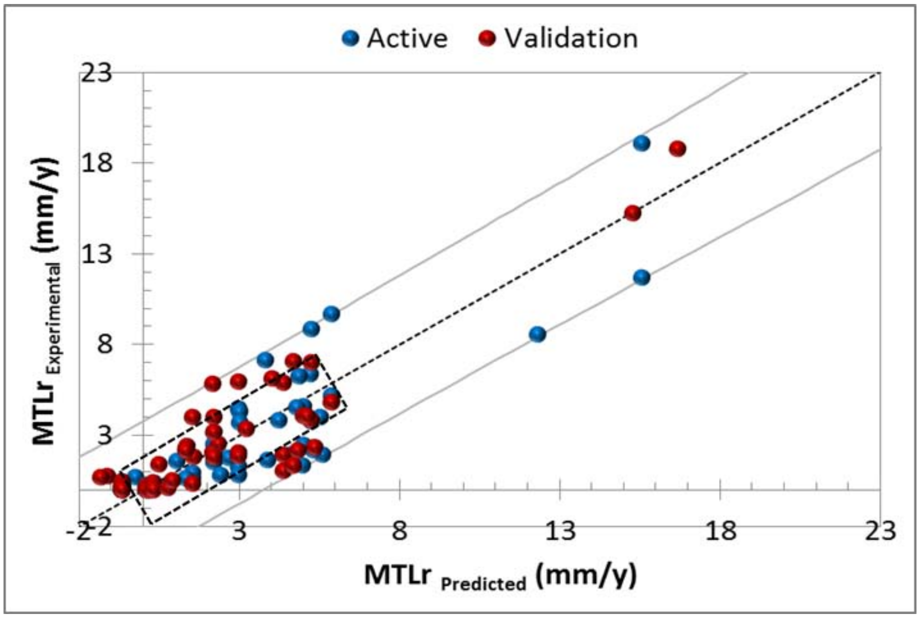

Figure IV.31. Accuracy chart with the residuals between experimental values and predicted values by model 5 for austenitics-SS+Fe/Ni-based alloys in flue gas

IV.3.2.2.3 Model 6: Ni-based alloys

The model 6 was proposed for Ni-based alloys under flue gas conditions. The original data set (156 data) was split up in two parts contained in the same validity domain: the first part consisted of 75% of the data set that was randomly selected to create the model. The other 25% of the data set was used to validate the model. Table IV.8 shows the validity domain and the goodness of fit statistics of model. Figure IV.32 shows the relative weights of the variables in the model and Figure IV.33 shows the accuracy chart of the model.

Table IV.8a shows the highest and lowest limits between which the model is valid. The model can predict corrosion rates for Ni-based alloys in the composition range (0-14.3 wt.% Fe, 52-74 wt.% Ni, 11.5-29 wt.%Cr, 0-18 wt.% Mo), at flue gas temperatures between 490° C and 700°C and metal temperatures between 440°C and 650°C, in complex atmospheres (within the limits established for O_2 and HCl) and for ash compositions calculated in elemental form within the limits indicated.

Table IV.8b shows the goodness of fit statistics of the model. The $R^2 = 0.56$ means that 56% of the variation of the MTLr was explained by the model. The DW = 1.6 shows that the residuals are independent from each other. The F = 16 and $|Pr > F| < 0.0001$ means that there is a significant linear relationship between the MTLr and the set of independent variables taken together in the model (Figure IV.32), the fulfillment of all the statistical assumptions indicates that the model is satisfactory.

Table IV.8. Statistics of model 6. a) Validity domain b) Goodness of fit statistics

Variable	Minimum	Maximum
MTLr (mm/y)	0	11.2
$T_{Flue\ gas}$ (°C)	490	700
T_{Metal} (°C)	440	650
O_2 (vol.%)	5.7	10.5
HCl (ppm)	132	1500
Cr (wt.%)	11.5	29
Mo (wt.%)	0	18.2
S (wt.%)	0	17.7
Cl (wt.%)	1	41.4
Al+Ca+Si+Fe (wt.%)	0	44.6
Na+K+Zn+Pb (wt.%)	0	58.6

a)

Goodness of fit statistics:	
R^2	0.56
Adjusted R^2	0.53
DW	1.6
MSE	2.82
RMSE	1.68
Analysis of variance:	
F	16
Pr > F	< 0.0001

b)

In the equation of the model (65) the predictors are located by groups of variables: $T_{Flue\ gas}$, T_{Metal}, $[O_2]$ and $[HCl]$ from the atmosphere conditions, the $[Cr \times Mo]$ from the material composition, $[S]$ and chlorides elements $[Cl \times (Na + K + Zn + Pb)]$ from the ash composition. In this case, we can also notice the influence of the variables from external conditions (flue gas and ash) compared to the material variables. In fact, first tests performed using Cr and Mo individually did not show good results, and therefore, a second-order variable was applied $[Cr \times Mo]$ to enhance the material properties in the model.

$$\boldsymbol{MTLr = -5.2 \times 10^{-1} + 8.5 \times 10^{-3} \times T_{Flue\ gas} + 1.2 \times 10^{-2} \times T_{Metal} - 4.8 \times 10^{-1} \times [O_2]}$$

$$\boldsymbol{+2.9 \times 10^{-4} \times [HCl] - 6.4 \times 10^{-3} \times [Cr \times Mo] + 1.1 \times 10^{-1} \times [S]}$$

$$\boldsymbol{+1.7 \times 10^{-3} \times [Cl \times (Na + K + Zn + Pb)]} \qquad \textbf{Equation 65}$$

Where, $MTLr$ is given in $\frac{mm}{y}$, temperatures $T_{Flue\ gas}$, T_{Metal} in *Celsius (°C)*, $[O_2]$ in *(vol.%)* and $[HCl]$ in *ppm* in the gas, $[Cr \times Mo]$ in *wt.%* in the alloy and $[Cl, Na, K, Zn, Pb]$ in *wt.%* in the ash.

In this model only 56% of the variation of the corrosion rate has been explained. There is still a 44% not ye explained that may be attributed to other variables not considered in the model. Also, the assumption of the linear kinetics for Ni-based alloys may not be appropriate. However, according to the diagram in the Figure IV.32, the variable $[Cl \times (Na + K + Zn + Pb)]$ is placed in the 1st order of importance in the model.

High concentration of chlorides is assumed to cause the dissolution of protectives layers, increasing the corrosion rates. In the 2nd order there are, the $[O_2]$ and $[Cr \times Mo]$ with negative effect on the corrosion rate, as both variables promote the protection of the alloy through the formation of oxides. The effect of the $[O_2]$ for Ni-based alloys increases compared to Fe/Ni-based alloys, which may be linked to the ability of Ni-based alloys with higher Cr-contents to form protective layers assisted by oxidant atmospheres. The variables from the alloy composition increase in order $[Cr \times Mo]$, because individually they did not show good results. This may be linked to the slower diffusion of Cr in the Ni-matrix compared to ferritic matrix or duplex matrix. Which is why, the effect of Cr was highlighted increasing its effect with Mo, obtaining better results. Mo has a positive effect because it is less reactive against Cl and forms Mo-oxide.

The temperatures $T_{Flue\ gas}$, T_{Metal} decrease in influence with respect Model 4 and Model 5 and $T_{Flue\ gas}$, became less important than T_{Metal}. At the same time, $[S]$ became positive in flue gas atmospheres increasing the corrosion rates, which differs from its negative effect on isothermal conditions. In this domain the T_{Metal} range also increases (440°C to 650°C) and sulfates mixtures can melt from 550°C, and hence, the higher relative influence of T_{Metal} also favors the sulfate's melting in the ash. Furthermore, Ni-based alloys form NiO and the solubility of NiO in alkali chloride/sulfate mixture can occur at 550°C while in alkali chlorides may occur at 727°C. Also at low pO_2, NiS can be formed and at high pO_2, $NiSO_4$ can be formed. Therefore, the presence of sulfur in the ash is especially detrimental for Ni-based alloys. In the last order of importance, there is HCl with a low positive effect because it increases corrosion rates but Ni is also an element comparatively stable against reaction with chlorine.

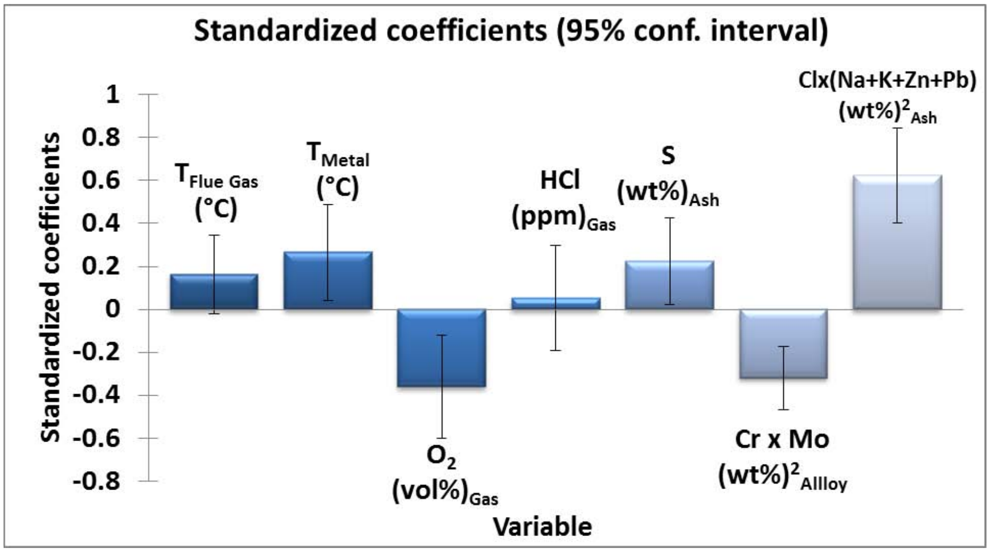

Figure IV.32. Standardized coefficients chart: relative weight of the independent variables on model 6 for Ni-based alloys

The accuracy chart of the model is shown in the Figure IV.33 with the corresponding mean error (66). The chart shows most of the predicted values close to the bisector. Although the R^2 of the model is low (0.56), the mean error RMSE slightly decreases to 1.7mm/y, as so the spread of the data (0-11 mm/y). In the diagram some variations on the experimental corrosion rates for the same prediction, also increases the mean error. However, due to the complexity of the mechanisms for Ni-based alloys, the applications of other statistical approaches rather than linear, must not be neglected.

$$MTLr_{Experimental} = MTLr_{Predicted} \pm 1.7\ \frac{mm}{y} \qquad \textbf{Equation 66}$$

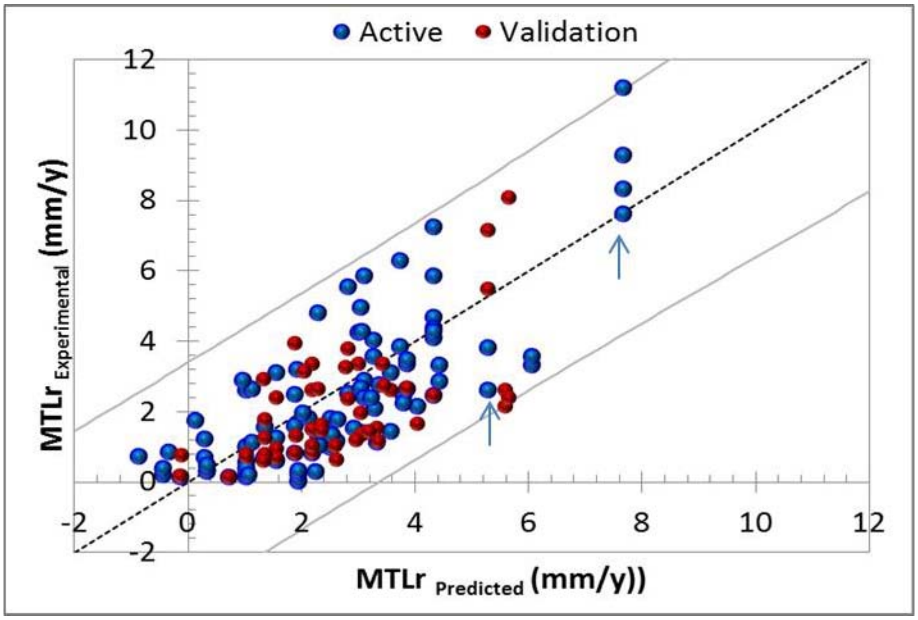

Figure IV.33. Accuracy chart with the residuals between experimental values and predicted values by model 6 for Ni-based alloys

IV.4 Conclusions

A statistical method was successfully implemented in this study to determine the most significant variables for lifetime prediction modeling of high-temperature corrosion in a wide range of conditions. The models were obtained using a large database of experiments and agree with the data previously obtained from literature.

A classification of scenarios was performed in order to avoid inconsistencies caused by the variability in the experimental procedures, the different atmospheres and the different alloy types. This procedure significantly improved the adjustments (R^2) of the linear models and highlighted the importance of using different experimental procedures for research activities aimed to understand the corrosion mechanism and to predict material's lifetime. Likewise, the different scenarios stressed the importance of taking into account industrial exposure conditions on the choice of experimental parameters, because they may have a strong influence on corrosion rates and the relative weights of the different variables that is often neglected.

For the isothermal conditions, the model for Fe-based alloys (R^2=0.7) showed better fit than the model for Ni-based alloys (R^2=0.6). However, the mean error of the model for Fe-based alloys was much higher. The different diagrams of accuracy showed that non-reproducible test results in the same condition and the fact of assuming linear rates in those cases where the kinetics may not be linear, can create large variations on the standard deviation of the models. The accuracy of the model will depend on the dataset used for creating the model.

Under T-gradient conditions, better adjustments were obtained for Fe-based alloys and Fe-Ni based alloys (R^2=0.8) followed by Ni-based alloys (R^2=0.6) and the standard deviation of the models decreases with decreasing the spread of the data. It was noticed that as the number of alloy elements increases, the corrosion mechanism also does in complexity, and hence, other kinetics approaches instead of linear laws must be evaluated.

For isothermal scenarios, the alloy elements play an important role in the explanation of the corrosion rates, unlike the temperature gradient scenarios in which the external conditions (gas composition and ash composition) explain better the variation of the corrosion kinetics. The T-gradient models reproduce better the industrial conditions. The isothermal tests are most frequently used at laboratory scale, which only consider the T_{Metal} and neglect the $T_{\text{Flue gas}}$. Modeling results show that $T_{\text{Flue gas}}$ plays a major role on the variation of the corrosion rates.

The design of the variable T_{Solidus} that depends on the ash composition showed to play a key role in the corrosion rate under isothermal conditions. Likewise, the second-order variable $[Cl \times (Na + K + Zn + Pb)]$ that was intended to avoid collinearity between chlorides and oxides in the ash, proved to be relevant in all scenarios (Isothermal and T-gradient). However, the effect of the variables varies according to the scenario and the alloy family evaluated. It was found that the variables commonly used to best describe the variation of the corrosion rates under isothermal conditions are: T_{Metal}, T_{Solidus} Cr and $[Cl \times (Na + K + Zn + Pb)]$. In T-gradient scenarios, the variables commonly used are: $T_{\text{Flue gas}}$, T_{Metal}, O_2, HCl from the atmosphere conditions, Cr from the alloy composition and the chloride concentration in the form $[Cl \times (Na + K + Zn + Pb)]$. It was observed that the effect of $T_{\text{Flue gas}}$ is usually higher than that of T_{Metal}. As the contents of the alloy elements (Ni-Cr-Mo) increase, the effect of O_2 increases and the effect of HCl decreases. Regarding the T-gradient models, the relative weight of the explanatory variables obtained is consistent with the operational response in different boiler design and operating conditions. Even if the standard deviation of the models is high, this modeling approach contributes to quantify objectively the effect of the key parameters on corrosion rates.

The goal was to show the reliability, the efficiency and the limitations of statistical methodologies to predict material's lifetime at laboratory and industrial scale. The use of such model will be the purpose of the next chapter.

Chapter 5. Modeling and lifetime assessment

Contents

V Chapter 5. Modeling and lifetime assessment

The previous four chapters have discussed the scientific review on high-temperature corrosion modeling, modeling methodology and the models obtained for different classes of materials exposed to metal dusting or fireside corrosion conditions. In this chapter, we focus on the ultimate objective of this study which is to apply the models obtained, in lifetime assessment's procedures. Here, we will discuss in detail the scope and applicability of the models.

The necessity to conduct life assessment studies grows increasingly, as it is one of the principles of preventive maintenance philosophy nowadays in industrial applications. Lifetime prediction focuses on the following question: How long will the components last? In the current study, predictive modeling was applied to forecast future behavior of materials subjected to high-temperature corrosion in WtE plants and metal dusting in steam methane reforming plants. Each model has its own strengths and weaknes and is the best fit for the particular scenarios considered in the statistical analysis performed.

V.1 Metal Dusting

For metal dusting, three models were obtained with different parameters: mass loss rate (MLr), incubation time (IT) and pit depth growth rate (PDGr) that had in common to predict the behavior of two families of alloys Fe/Ni-based and Ni-based alloys. However, there is certain discrepancies in the domain of application of the models, aspect that should be considered before establishing the settings for lifetime prediction. Table V.1 shows the highest and lowest limits, between which the models are valid. A common validity domain was established to standardized conditions for lifetime prediction.

Table V.1. Validity domain of the models to be applied for the lifetime assessment

Model/Variable	**2/MLr (mg/cm^{2}h)**		**4a/IT (h)**		**5/PDGr (µm/h)**		***Common domain***	
Alloy family	Fe/Ni-based		Fe/Ni-based + Ni-based				*Fe/Ni-based*	
Limits	**Min.**	**Max.**	**Min.**	**Max.**	**Min.**	**Max.**	***Min.***	***Max.***
Variable	0	0.46	10	5320	0.001	2.1	-	-
T_{Gas} (°C)	500	650	450	700	490	700	*450*	*700*
$P_{Internal}$ (bar)	1		1		1	30	*1*	
pCO (bar)	0.18	0.70	0.18	0.70	0.01	0.80	*0.18*	*0.70*
pH_2 (bar)	0.25	0.8	0.25	0.8	0.20	9.39	*0.25*	*0.80*
pH_2O (bar)	0.06	0.10	0.06	0.10	0.01	13.26	*0.01*	*0.10*
pCO x pH_2 (bar^2)	0.14	0.22	0.14	0.25	0.02	5.7	*0.02*	*0.22*
a_C	10	104	5.7	57.9	10	104	*5.7*	*57.9*
Ni (wt.%)	8.7	49.4	10	78	12	78	*8.66*	*49.4*
Cr (wt.%)	0	30.3	12	28	15	46	*0*	*28*
Mo (wt.%)	0	4.2	0	16	0	3.1	*0*	*3.1*
Al (wt.%)	0	1.5	0	4	0	16	*0*	*1.5*

Once the common domain was established, the settings for lifetime prediction were fixed within these limits. Conditions commonly found in industrial atmosphere cannot be reproduced for estimations, because the common domain restricts the calculations to atmospheric pressure and industrials environments deal with high pressures. Boundary conditions for estimations are shown in Figure V.1.

For the analysis, we chose to work with the experimental conditions established in the project SCAPAC in A. Fabas's thesis. [127] The gas composition was set at 47% CO – 47% H_2 – 6% H_2O at 570°C that produceS a carbon activity a_C of 32 and an oxygen partial pressure pO_2 of $2.5x10^{-27}$ bar. The wall thickness (WT) that meets mechanical requirements, such as pressure, temperature and weight of equipment was set to 2.47 mm according to specifications in standard ASME Section VIII Division 1. [197] By knowing the corrosion rate and considering a critical thickness of 0.55 mm (sensitive to failure) the time of consumption of the material thickness can be estimated using predictive models. The alloys 800HT and HR120 were selected, as they are commonly used for tubing and exchanger's applications and continuously subject of laboratory analysis. Table V.2 shows the alloy chemical composition to be considered for estimations.

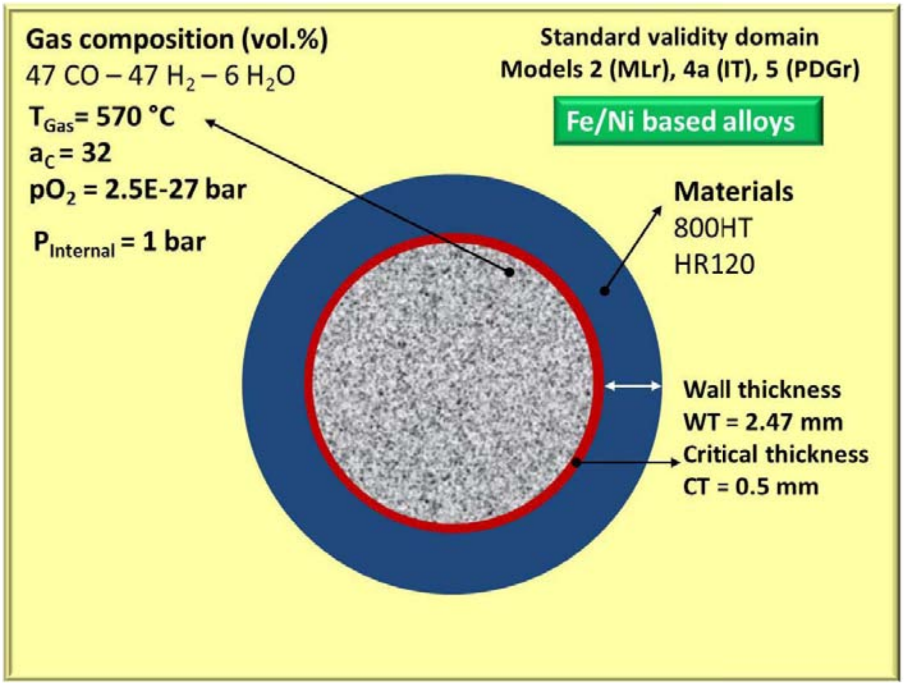

Figure V.1. Set conditions for lifetime assessment at carburizing atmospheres.

Table V.2. Nominal chemical composition for materials used for lifetime assessment

Alloy (wt.%)	Fe	Ni	Cr	Mo	Co	Cu	Al	Si	W	Ti	Mn	C	ρ (g/cm^3)
800HT	45.0	32.0	21.0				0.4	0.1		0.4	0.9	0.1	7.94
HR120	33.0	37.0	25.0	1.0	3.0	0.5	0.1	0.6	0.5		0.7	0.05	8.07

Figure V.2 and Figure V.3 shows the lifetime estimations using all three models (IT, PDgr, and MLr) under the same conditions for 800HT and HR120.

Figure V.2 shows the lifetime prediction of different materials by using the models 2 (MLr), 4a (IT) and 5 (PDGr). The MLr (mg/cm^2 h) was converted into thickness loss (mm/y) using the densities of the materials, in the diagram the curves are explained as follows:

a) In the case of alloy HR120, $MLr_{Experimental} = 1.7 \times 10^{-3}$ mg/cm^{2}h ($\approx 1.6 \times 10^{-2}$ mm/y) while $MLr_{Predicted} = 1 \times 10^{-3}$ mg/cm^{2}h ($\approx 1 \times 10^{-2}$ mm/y) resulting in 240 years lifetime (a)

b) In the case of 800HT, experiments showed that $MLr_{Experimental} = 6.7 \times 10^{-4}$ mg/cm^2 h ($\approx 6.7\times10^{-3}$ mm/y) while the model predicted negative corrosion rates (-6×10^{-3} mg/cm^2 h $\approx -6\times10^{-2}$ mm/y) which cannot be used (b). Another limitation of the model is that it is a simplified version of the real situation or concept. Therefore the model will follow trends and tendencies even when the results do not correspond with reality.

Although the model predicts well the experimental results, it is not a good reference for lifetime prediction, due to the following aspects:

- Mass loss rate (MLr) as a prediction parameter generates a significant source of error, due to the discrepancy between the mass loss measured per unit area and its equivalent to the materials thickness loss. Mass loss is an averaged over the entire surface and is not representative of the local thickness loss for lifetime prediction purposes.

- Experiments performed at 1 bar pressure and low gas velocity, are much less aggressive than real conditions, and hence, they are far from reality. The model is not a substitute for a controlled scientific experiment which generates data, but it is only as good as the information used to generate it. Therefore, more efforts in performing high pressure tests should be made, in order to improve lifetime predictions for industrial exploitation.

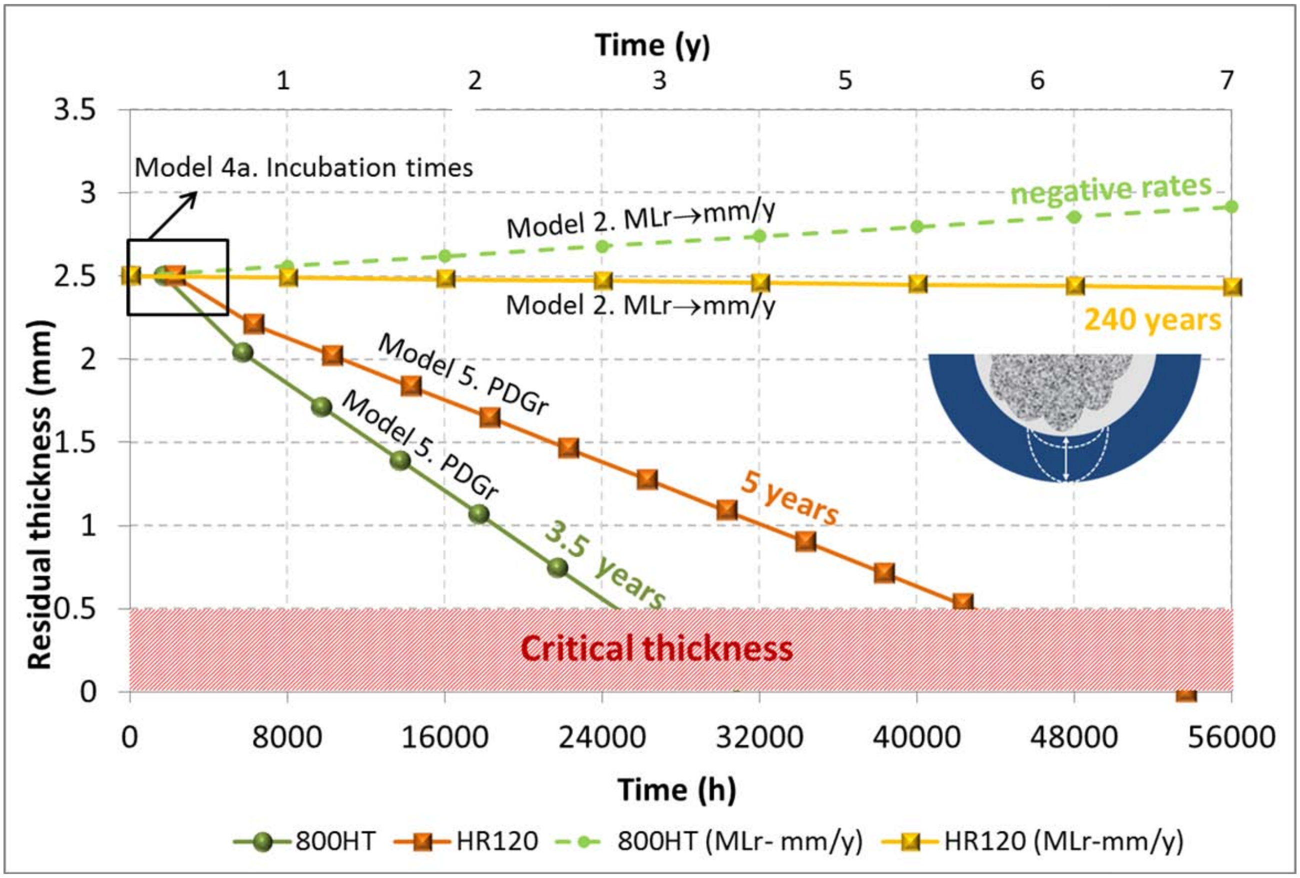

Figure V.2. Lifetime assessment for 800HT and HR120, estimated by models 2, 4a, 5

c,d) Figure V.3 shows an enlargement from Figure V.2 to visualize the incubation times predicted with model 4. Alloy HR120 presented an incubation time (2277h) slightly longer than 800HT (1733h). However, considering the standard deviation of the model (840h), both incubation times might be considered similar. Once finished the incubation period, 800HT showed faster pit depth growing rate (0.6 ± 0.7 mm/y) (c) than HR120 (0.4 ± 0.7 mm/y) (d), which results in a longer lifetime for HR120 (5 years) than 800HT (3 years). The experimental results determined at the same experimental conditions by A. Fabas's thesis, show a corrosion rate of 0.4 ± 0.2 mm/y for 800HT and a corrosion rate of 0.32 ± 0.2 mm/y for HR120, which means a good agreement with the predicted values, considering both standard deviations.

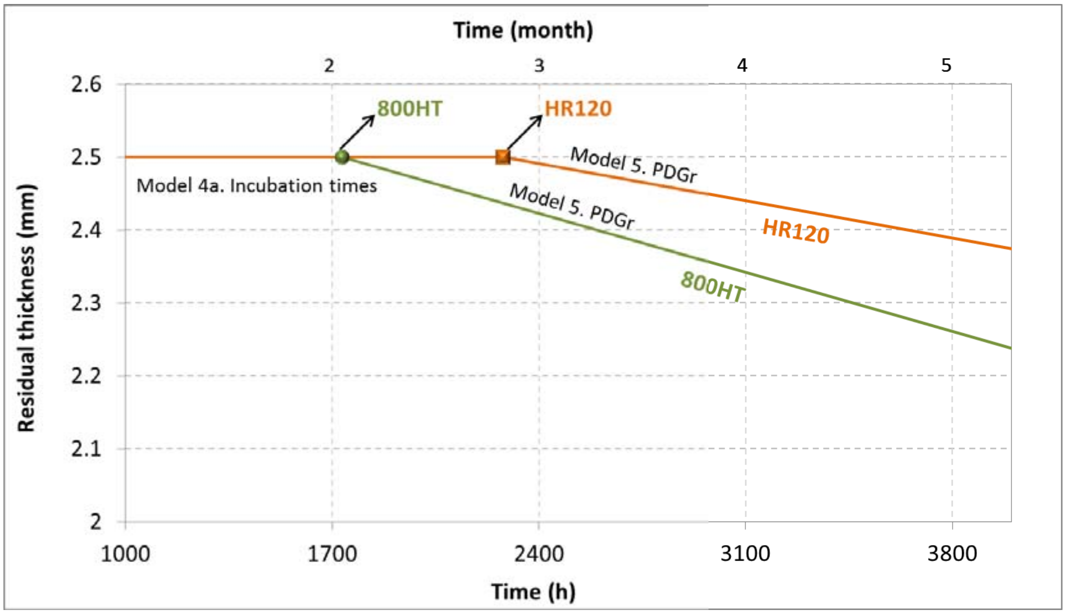

Figure V.3. Incubation times for 800HT and HR120 estimated by model 4

As mentioned above, predictions cannot be extrapolated to real conditions due to the impossibility of predicting at high pressures, in the restricted domain. However, PDGr is more representative of the materials thickness loss and shows more consistent results regarding the real conditions. According to estimations, selecting HR120 over 800HT may imply an increase of about 40% of the component lifetime. This is very useful information at the moment of conducting materials selection for industrial applications.

All the previous estimations were performed considering a stable atmosphere. Nevertheless in service this does not happen this way. In the recovery zone, fluctuations of gas temperature, pressure and gas composition produce variations in carburizing atmospheres which also generate changes in the corrosion rates during the total lifetime of the component.

An analysis of the variation of the corrosion rates as a function of T_{Gas} and $P_{Internal}$ was performed, by using the model 5 (PDGr) at the same gas composition used previously for lifetime estimations (47% CO – 47% H_2 – 6% H_2O), as shown in Table V.3. The model 6 allows working up to 30 bars at very low pCO and pH_2 ($pCOxpH_2$ up to 5.7 bar s^2) according to the validity domain. Since the variable $pCOxpH_2$ also increases with increasing $P_{Internal}$, the validity domain restricts the $P_{Internal}$ to a maximum of 5 bars in SCAPAC gas composition. In this regard, comparisons with experimental conditions at 21 bars cannot be made because the SCAPAC gas composition at 21 bars (13% CO – 49% H_2 – 3% CO_2 – 2% CH_4 - 33%

H_2O) ($pCOxpH_2 = 27$) exceeds the higher limit of the variable in the model. Figure V.4a shows the variation of PDGr as a function of $P_{Internal}$ and T_{Gas} for alloys 800HT and HR120. We can clearly see that PDGr significantly increases with $P_{Internal}$ rather than temperature. Red dashed lines indicate the corrosion rates determined previously for lifetime assessment. Predicted values of PDGr are consistent with experimental results of the SCAPAC project at the same conditions (Figure V.4a), even when these results are not included in the dataset of the model.

Once the corrosion rates were predicted for both materials, Figure V.4b shows the tube lifetime variation at constant internal pressure $P_{Internal}$ = 1 bar and varying gas temperature T_{Gas} between 570°C and 650°C. We can clearly see that the 2 years difference between HR120 lifetime (5 years) and 800HT lifetime (3 years) at low temperatures (570°C) reduces significantly at high-temperatures (650°C), where both alloys reach the same period of life (1 year). This is consistent with experimental findings of Chun et al. [10,24] who showed that materials with high content of Fe reach a maximum corrosion rate around 650°C. According to estimations, temperature variations of 30°C can reduce the component lifetime to a few years.

Table V.3. Varying conditions of T_{Gas} and $P_{Internal}$ for PDGr evaluation in the Figure V.4

Alloys	Gas composition was set at 47% CO – 47% H_2 – 6% H_2O								
800HT **HR120**	T_{Gas}	500	520	540	570	590	610	640	650
	$P_{Internal}$	1	2	3	4	5			
	$pCOxpH_2$	0.22	0.88	1.99	3.53	5.52			

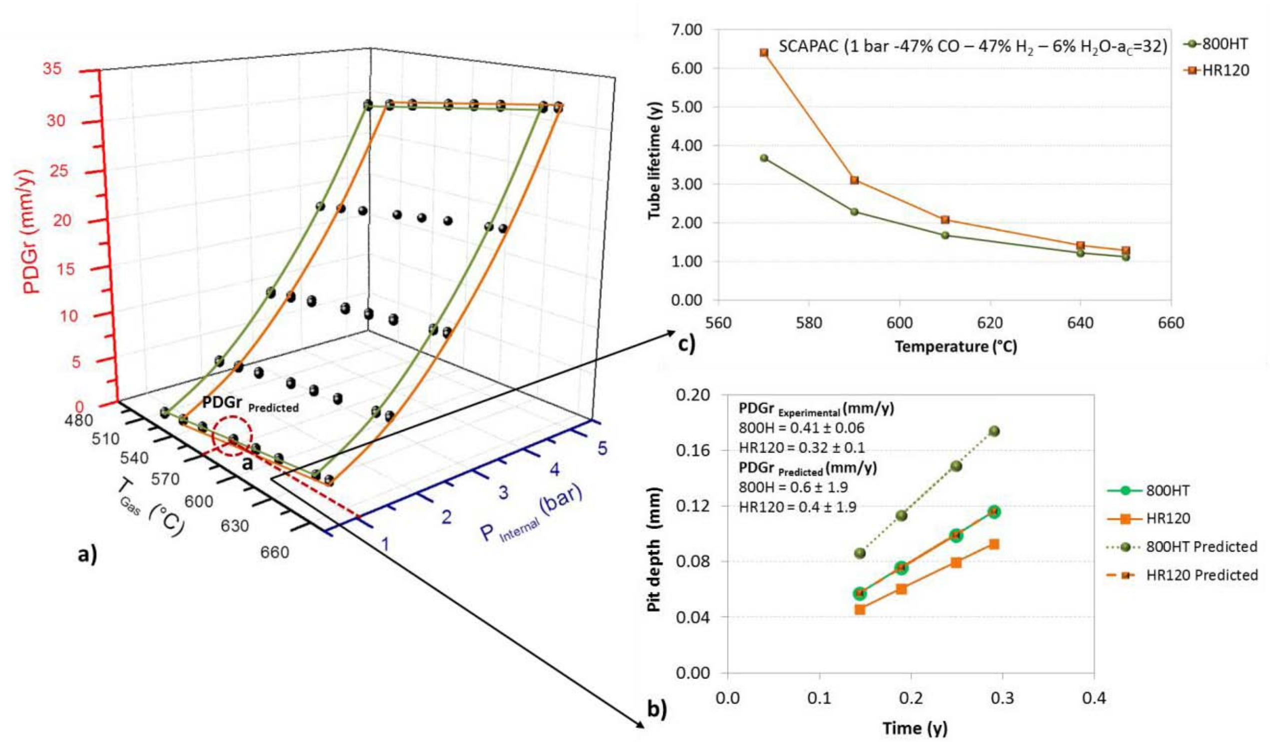

Figure V.4. a) PDGr variation as a function of $P_{Internal}$ and T_{Gas} for 800HT and HR120 steels a) Comparison with experimental results of the project SCAPAC b) Lifetime variation as a function of temperature for SCAPAC conditions.

Now, under another scenario (blue dashed lines) (b), where T_{Metal} is constant at 570°C and $P_{Internal}$ increases up to 21 bar (operational conditions), PDGr increases considerably for both alloys 800HT and HR120 which behave in a similar way. This is consistent with experimental findings of SCAPAC project (Figure V.4b) at 21bar, where different pit measurements from both materials show similar behavior with the same mean PDGr. However, if we compare $PDGr_{Predicted}$ (Figure V.4a) and $PDGr_{Experimental}$ (Figure V.4b), we can clearly see that $PDGr_{Predicted}$ is 1 order of magnitude higher than $PDGr_{Experimental}$. This means that the model overestimates ten times the experimental results. This outcome can be attributed to the fact that most data from high pressure tests were obtained for stainless steels type 316 by Levi et al. [27] Stainless steels show low resistance to metal dusting, generating higher pit depth growth rates and steeper regression lines. More test results at high pressures for Fe/Ni based alloys and Ni-based alloys are required to smooth the pressure regression line in the hyperplane of adjustment.

V.2 High-temperature corrosion

For high-temperature corrosion, three models were obtained for the three principal families of alloys: Fe-based, Fe/Ni-based and Ni-based alloys, to be applied under temperature gradient condition ($T_{Flue\ gas}$ and T_{Metal}) which is the closest to operational environments. However, there is certain discrepancy in the domain of application of the models, like metal dusting, this aspect was considered before to establish the settings for lifetime prediction. Table V.4 shows the highest and lowest limits, between which the models are valid. A common validity domain was established to standardized conditions for lifetime prediction.

Table V.4.Validity domain of the models under temperature gradient conditions

Alloy family	**Fe-based**		**Fe/Ni-based**		**Ni-based**		***Common domain***	
Variable	**Min.**	**Max.**	**Min.**	**Max.**	**Min.**	**Max.**	***Min.***	***Max.***
MTLr (mm/y)	$1x10^{-3}$	18	$1x10^{-4}$	24	$1x10^{-2}$	11	$1x10^{-4}$	*24*
$T_{Flue\ gas}$ (°C)	380	850	450	700	490	700	*490*	*700*
T_{Metal} (°C)	270	600	300	650	440	650	*440*	*600*
O_2 (vol.%)	-	-	5.7	10.5	5.7	10.5	*5.7*	*10.5*
HCl (ppm)	132	2000	132	1500	132	1500	*132*	*1500*
SO_2 (ppm)	0	200	-	-	-	-	*0*	*200*
Cr (wt.%)	0	2.2	18.0	28.9	11.5	29.0	*0*	*29*
Mo (wt.%)	-	-	-	-	0	18.2	*0*	*18.2*
S (wt.%)	0	17.9	-	-	0	17.7	*0*	*17.7*
Cl (wt.%)	0	21.5	0.1	41.4	1.0	41.4	*0*	*21.5*
Al+Ca+Si+Fe (wt.%)	0	44.6	0.0	44.6	0.0	44.6	*0*	*44.6*
Na+K+Zn+Pb (wt.%)	0	37.0	5.6	58.6	5.6	58.6	*5.6*	*37.0*

For the case study, the alloys 16Mo3 and T22 were chosen as the substrate materials because they are commonly used for boilers and exchangers applications. Sanicro 28 and Inconel 625 were selected as coatings. The calculation does not consider the coating application method.

Table V.**5** shows the alloy chemical composition to be considered for calculations.

Table V.5. Nominal chemical composition for substrate and coatings used for estimations

Alloy (wt.%)	Fe	Ni	Cr	Mo	Al	Cu	Si	Nb	Ti	Mn	C
16Mo3	97.3	0.3	0.3	0.4		0.3	0.3			0.9	0.2
T22	95.7		2.6	1.0						0.6	0.15
Sanicro 28	34.9	31.0	27.0	3.5		1	0.6			2.0	0.02
Inco 625	5.0	61.0	21.5	9.0	0.1		0.2	3.7	0.1	0.2	0.050

Once the common domain and the materials to be evaluated were established, the settings for lifetime prediction were fixed within these limits, considering the conditions commonly found in industrial atmosphere as shown in Figure V.5. The gas composition was set at 6%O_2 - 1100 ppm HCl - 110 ppm SO_2. Ash composition corresponds to Ash 5 of the current study (chemical composition is indicated in section II.2.1). The highest $T_{Flue\ gas}$ (700°C) and the lowest T_{Metal} (440°C) were selected to extend the temperature gradient.

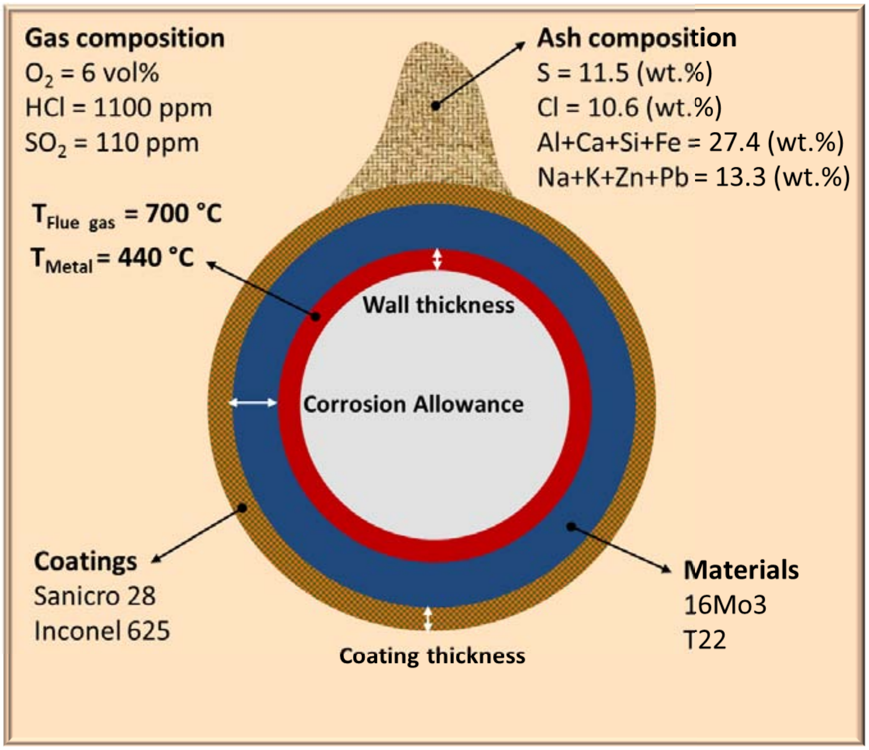

Figure V.5. Set conditions for lifetime prediction at flue gas and temperature gradient conditions

Two important tube dimensions have to be considered for components design of boilers [198] and exchangers in WtE applications: the wall thickness (WT) that meets mechanical requirements, such as pressure, temperature and weight of equipment, and an extra thickness is required for corrosion resistance of the process equipment called corrosion allowance (CA), which is added to the wall thickness to compensate the metal expected to be lost over the life of the equipment. Corrosion allowances are normally established by the end user and are somewhat based on personal preferences and industry tradition. Table 5 shows the tubes design dimensions to be considered for calculations. By knowing the expected general corrosion rate through predictive models, the time of consumption of the coating thickness and corrosion allowance can be estimated and subsequently the tube lifetime can be anticipated. The models were applied depending on the alloy family as shown in Table V.6.

Table V.6. Tube dimensions and the corresponding model according to the alloy family

Alloy	TT [a] (mm)	WT [b] (mm)	CA [b] (mm)	CT [d] (mm)	Models
16Mo3	6.3	1.62	4.68		(4)
T22	6.3	1	5.3		(4)
16Mo3 + Sanicro 28	8.3	1.62	4.68	2	(4) + (5)
16Mo3 + Inco 625	8.3	1.62	5.3	2	(4) + (6)
T22 + Sanicro 28	8.3	1	4.68	2	(4) + (5)
T22 + Inco 625	8.3	1	5.3	2	(4) + (6)

[a] Total Thickness, [b] Wall Thickness, [c] Corrosion Allowance, [d] Coating Thickness
Models: (4) Fe-based alloys , (5) Fe/Ni-based alloys and (6) Ni-based alloys

Figure V.6 shows the residual thickness over time of the alloys 16Mo3, T22, Sanicro 28 and Inconel 625 coatings and coated systems, exposed to the established conditions (Figure V.5). The lines in the figure refer to lifetime consumption in each case, 16Mo3 and T22 lifetimes were estimated by model 4 for Fe-based alloys. Sanicro 28 coating lifetime was estimated by model 5 for Fe/Ni-based alloys and Inconel 625 coating lifetime was estimated by model 6 for Ni-based alloys.

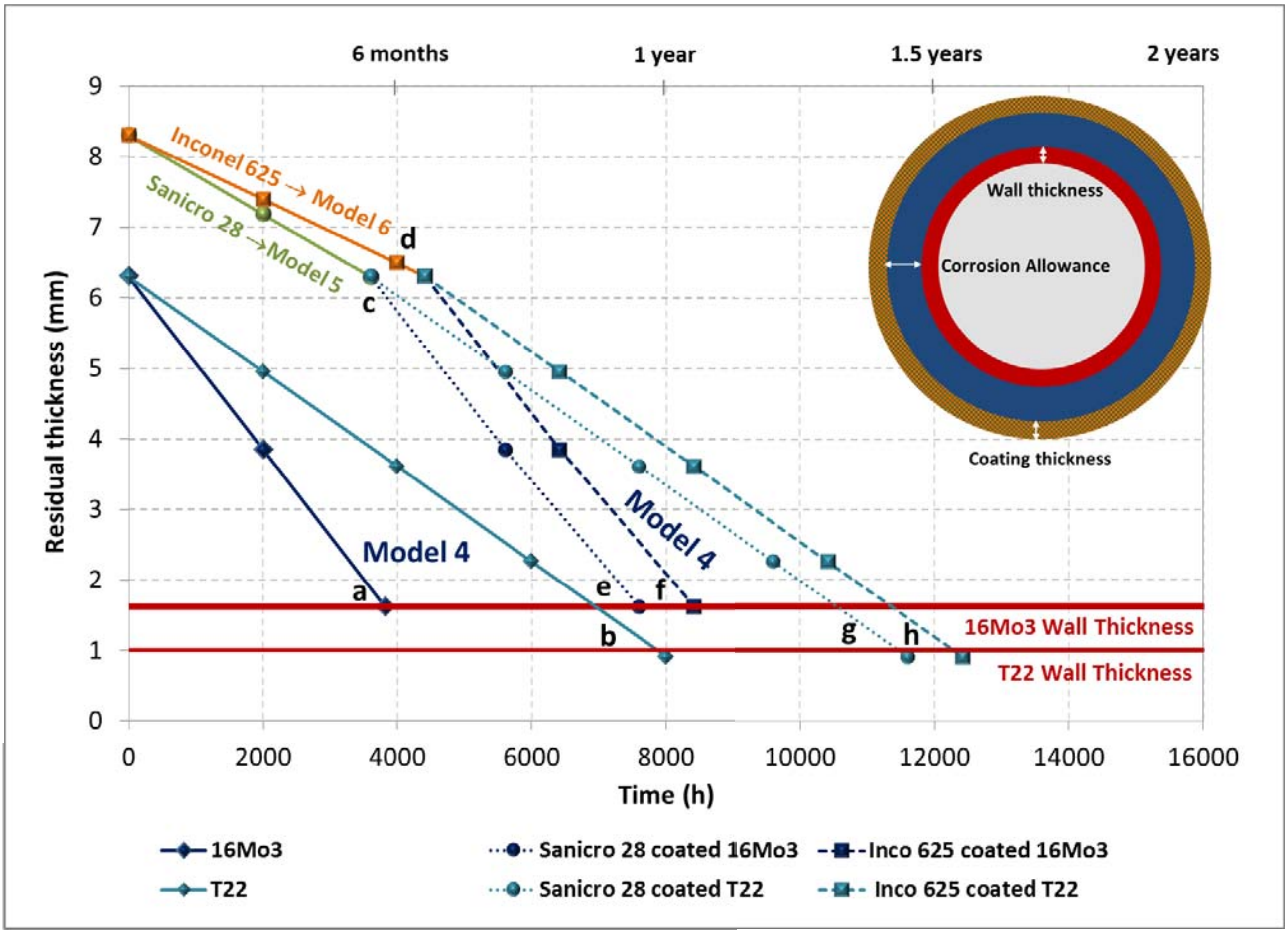

Figure V.6. Lifetime assessment for different tube configurations at established conditions, by using the models 4, 5, and 6

The alloy 16Mo3 (a) showed a wastage rate of 9.8 mm/y corresponding to a time consumption of the corrosion allowance of 6 month, while T22 (b) showed a wastage rate of 5.4 mm/y, which means a year lifetime. The estimations may be high regarding the corrosion rates commonly found in service (2 mm/y for carbon steel waterwalls and 2.5 mm/y for Cr-Mo steel superheaters tubes). [106] This is because of the high corrosion rates of laboratory tests included in the adjustment of the model. However, the model assists as reference to compare the alloy's lifetime to be installed in service. Comparison of the relative lifetime between both materials at the same conditions shows that the application of T22 over 16Mo3 would imply to double the lifetime of the steel tubes.

In the case of coatings lifetime prediction, Sanicro 28 and Inconel 625 showed wastage rates of 4.5 mm/y and 3.6 mm/y, that is a consumption time of 5.4 month (c) and 6.7 month (d) for a 2-mm coating thickness, respectively. Considering the standard deviations of the models, the estimate lifetimes are similar for both coatings. Therefore, to select between a stainless steel coating and a Ni-based coating to obtain similar results is debatable in terms of life cycle costing. Nevertheless, their application to 16Mo3 and T22 would effectively add about 6-month lifetime to the coated steels. It would imply to double the lifetime for 16Mo3 coated steel, that is around a year (e,f) and extend 50% the lifetime for T22 coated steel, that is around a year and a half (g,h).

All the previous estimations were performed considering a stable atmosphere, constant temperatures and specific ash composition, but in real service it does not occur. Fluctuations in operational conditions or differences in boilers design also generate variations in the corrosion rates that affect the total lifetime of the component. The heterogeneous physical and chemical composition of the fuel in WtE plants creates variations in heating values and volatile products, which result in changing ash composition deposits on the tubes and fluctuations of the flue gas temperature within the combustion chamber. [199] Experimental studies have shown that corrosion rates increase due to temperature fluctuations. [200]

Figure V.7 shows the variation of corrosion rate for 16Mo3 and T22 steels, at the same conditions used for lifetime evaluation (Figure V.5) as a function of $T_{\text{Flue gas}}$ and T_{Metal} variation in the temperature ranges indicated in Table V.7. Red dashed lines indicate corrosion rates at $T_{\text{Flue gas}}$= 700°C and T_{Metal} = 440°C for 16Mo3 (9.8 mm/y) and T22 (5.4 mm/y). In this scenario, at $T_{\text{Flue gas}}$= 700°C, chlorides (alkaline and heavy metals) are volatiles and can condense on the metal surface when T_{Metal}< chloride dew-point, so the corrosion rate depends on T_{Metal}. In this case corrosion rates increase with increasing T_{Metal}, because T_{Metal} > T_{Solidus} and T_{Liquidus} of the ash and "molten salt induced corrosion" takes place. [201] In another scenario (blue dashed lines) where $T_{\text{Fue gas}}$ decreases to 550°C and T_{Metal} increases to 470°C, the chemistry of the environment changes. At $T_{\text{Flue gas}}$= 550°C, the chlorides are mostly in solid state, and deposit on the metal surface by impact-adhesion. Chlorides reactivity varies depending on the deposit structure, so corrosion rates decrease for 16Mo3 (7 mm/y) and T22 (2.6 mm/y).

Table V.7. $T_{\text{Flue gas}}$ and T_{Metal} range variation for Figure V.7 and Figure V.8

Alloy	Variable	T_1	T_2	T_3	T_4	T_5	T_6	T_7	T_8
16Mo3 **T22** **Sanicro 28** **Inconel 625**	$T_{\text{Flue gas}}$	490	520	550	580	610	640	670	700
	T_{Metal}	440	470	500	530	570	600	440	470

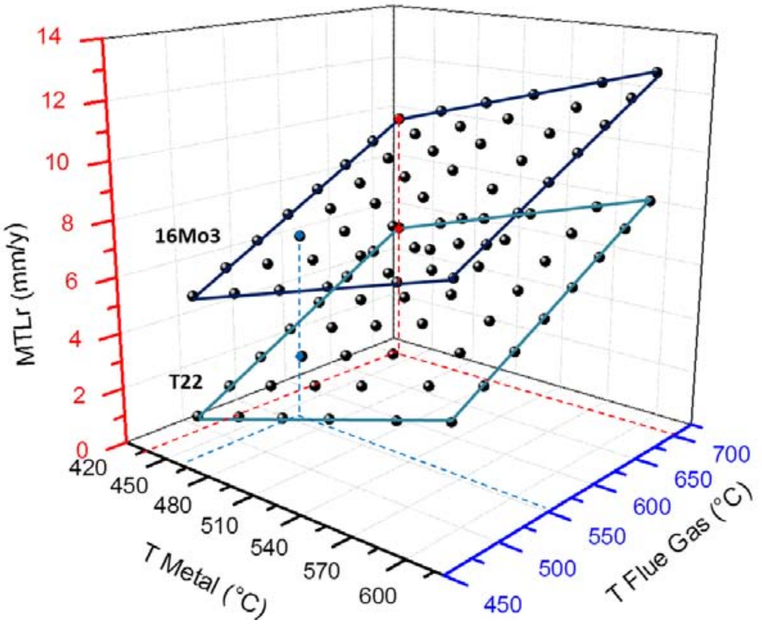

Figure V.7. Corrosion rate variation as a function of $T_{Flue\ gas}$ and T_{Metal} for 16Mo3 and T22 steels by Model 4 [1100 ppm HCl – 10.1 wt.% Cl – 13.3 wt.% (Na+K+Zn+Pb)]

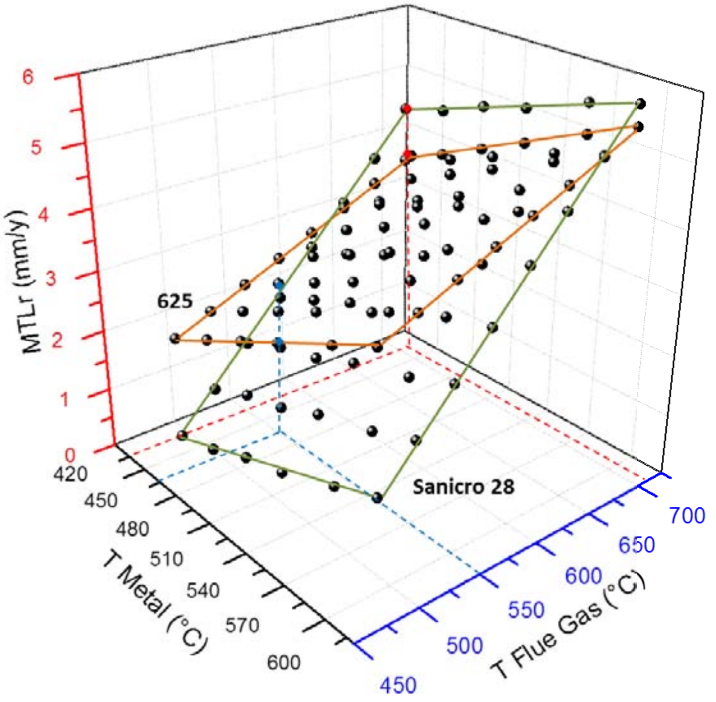

Figure V.8. Corrosion rate variation as a function of $T_{Flue\ gas}$ and T_{Metal} for Sanicro 28 and Inconel 625 coatings by using model 5 and 6 [1100 ppm HCl – 10.1 wt.% Cl – 13.3 wt.% (Na+K+Zn+Pb)]

Likewise, the Figure V.8 shows the corrosion rate variation for Sanicro 28 and Inconel 625 coatings, at the same conditions used for lifetime evaluation (Figure V.5) as a function of $T_{Flue\ gas}$ and T_{Metal} variation in the temperature ranges indicated in Table V.7. Red dashed lines indicate the corrosion rate at $T_{Flue\ gas}$= 700°C and T_{Metal} = 440°C for Sanicro 28 (4.5 mm/y) [Model 5] and Inconel 625 (3.6 mm/y) [Model 6], predictions by using different models support that Ni-based alloys are more resistant than austenitic stainless steels, and the same explanation applies regarding the environment. However, in the next scenario evaluated (blue dashed lines) where $T_{Flue\ gas}$ = 550°C and T_{Metal} = 470°C, corrosion rates for Sanicro 28 coating decreases in 65% (1.6 mm/y) and for Inconel 625 coating slightly decreases in 25% (2.7 mm/y). The new scenario places Sanicro 28 over Inconel 625 in corrosion resistance. Sanicro 28 reduces significantly the corrosion rate with temperature variations, due to the high sensitivity of austenitic steels to surrounding conditions, compared to Inconel 625 (Ni-based alloy), which shows more stability in changing environments, as it slightly decreases the corrosion rate within the standard deviation of the prediction. Furthermore, it is important to highlight that two models with different variables were applied according to the alloy family for estimations. Model 6 for Ni-base alloys (Inconel 625) favors T_{Metal} over $T_{Flue\ gas}$ and includes the protective effect of Mo and Cr as a second-order variable, while Model 5 for austenitic stainless steels has a larger influence of $T_{Flue\ gas}$ rather than T_{Metal} and only Cr as protective element.

Figure V.9 shows the corrosion rate variation as a function of HCl and [Cl x (Na+K+Zn+Pb)] for 16Mo3 and T22 steels, at the same conditions used for lifetime evaluation (Figure V.5). Ash compositions evaluated are shown in Table V.8 in increasing order for [Cl x (Na+K+Zn+Pb)] calculated values. Industrial ash composition (1) was reported by Kawahara et al. [145] from field tests for superheater tubing. Synthetic ash 5 (2) and 1 (3) corresponds to E. Schaal's thesis. Ash 5 (2) was applied for previous lifetime assessment. Finally, a hypothetical ash with the highest limits of the ash variables (common limits shown in Table 2), was considered as the most critical scenario.

Red dashed lines indicate the corrosion rate at stablished conditions for previous lifetime predictions (9.8 mm/y for 16Mo3 and 5.4 mm/y for T22). Under another scenario (blue dashed lines) where HCl decreases to 500ppm and [Cl x (Na+K+Zn+Pb)] changes to the industrial ash composition (1) [145] corrosion rates for 16Mo3 and T22 decrease to 7.1 mm/y and 2.7 mm/y, respectively. The slopes in the biplanes indicate that lower Cl-content in the ash composition reduces significantly the corrosion rate rather than any reduction in HCl concentration in the gas. Corrosion rate on T22 steel approaches to those detected in service. One possible explanation is that synthetic ash (2, 3) might be more reactive than those given in service (1), which also can explain the high wastage rates predicted by the models. Hypothetical ash is the most critical scenario considered which results in the highest wastage rates not yet reported in operational conditions.

Table V.8. Ash compositions and gas compositions evaluated in Figure V.9 and Figure V.10,

Ash		**S**	**Cl**	**(Na+K+Zn+Pb)**	**(Ca+Si+Al+Fe)**	**[Cl x (Na+K+Zn+Pb)]**	**O_2 (vol.%)**	**HCl (ppm)**
		(wt.%)						
1	Industrial Ash [145]	11.1	4.1	15.0	25.9	61	4	130
2	Ash 5	11.5	10.1	13.3	27.4	141	6	500
3	Ash 1	13.8	21.5	22.0	14.7	480	8	1100
4	Hypothetical ash	17.7	21.5	37	44.6	796	10	2000

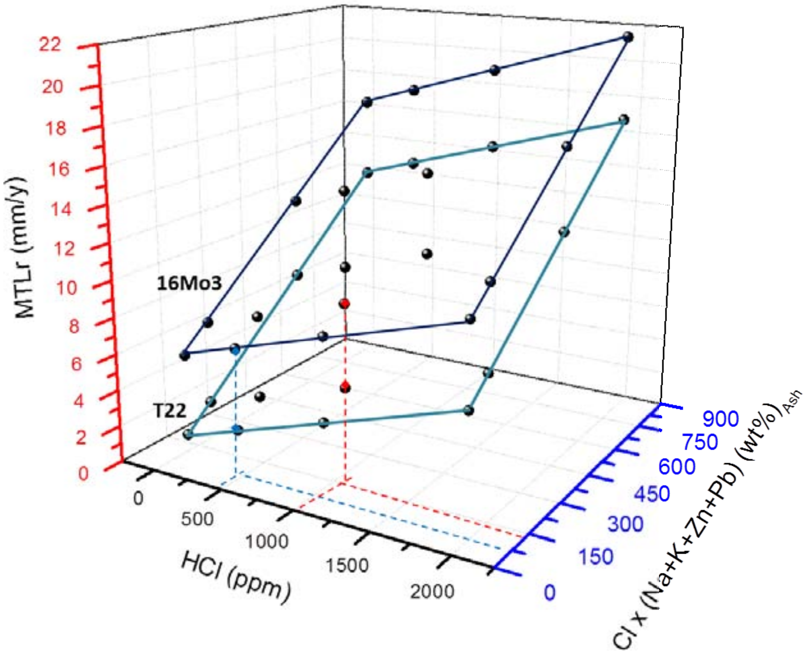

Figure V.9. Corrosion rate variation as a function of HCl and [Cl x (Na+K+Zn+Pb)] for 16Mo3 and T22 steels [$T_{Flue\ gas}$= 700°C and T_{Metal} = 440°C]

Figure V.10 shows the variation of the corrosion rate for Sanicro 28 and Inconel 625 coatings as a function of [O_2] and [Cl x (Na+K+Zn+Pb)]. Gas compositions and ash compositions evaluated are shown in Table V.8 in increasing order for [Cl x (Na+K+Zn+Pb)] calculated values. Red dashed lines point out the reference conditions used for lifetime evaluation (Figure V.5). We can clearly observe that corrosion rates for both alloys decrease significantly with increasing [O_2]. This effect is even more pronounced for Inconel 25 (Ni-based alloy). In the case of chloride concentrations [Cl x (Na+K+Zn+Pb)], corrosion rate increases linearly with increasing chlorides for Inconel 625, while for Sanicro 28, the corrosion rate increase to a peak at [Cl x (Na+K+Zn+Pb)] = 480 then decrease at higher Cl-content. Since, Cl-content favors molten phase corrosion, this is consistent with experimental findings by Kawahara, [201] who also found an increased peak (around 10% of molten phase) for austenitic stainless steel (SS 347) and more stability for Inconel 625 with increasing molten phases. This is linked with the physical properties of the deposits, because variations of the deposit permeability modify the transport of corrosive species.[46] The higher the molten phase amount, the lower the permeability by molten phase impregnation. Therefore, the penetration of corrosive gas such as HCl and oxidizing constituents such as O_2 through the deposits is much less for the maintenance of corrosion reaction. [202] Moreover, it is important to highlight that both models present different variables, the model 5 includes the maximum value of refractory oxides in the ash that also decreases the corrosion rate in the last stage of the diagram, while the model 6 for Ni-base alloys (Inconel 625) only favors the Cl-content and the corrosion rate increases linearly with increasing the chlorides composition.

Special attention should be given to coated systems estimations. The models presented estimate corrosion rates for a material composition according to a linear pattern that best fit with the equation, without taking into account the coating method or experiment type (laboratory or field tests). Regarding the coatings effectiveness, laboratory tests and field tests can present discrepancies, for example, as observed by

Otsuka et al. [203] Therefore, for more accurate estimations, the reproduction of operational conditions in the laboratory continues to be an issue.

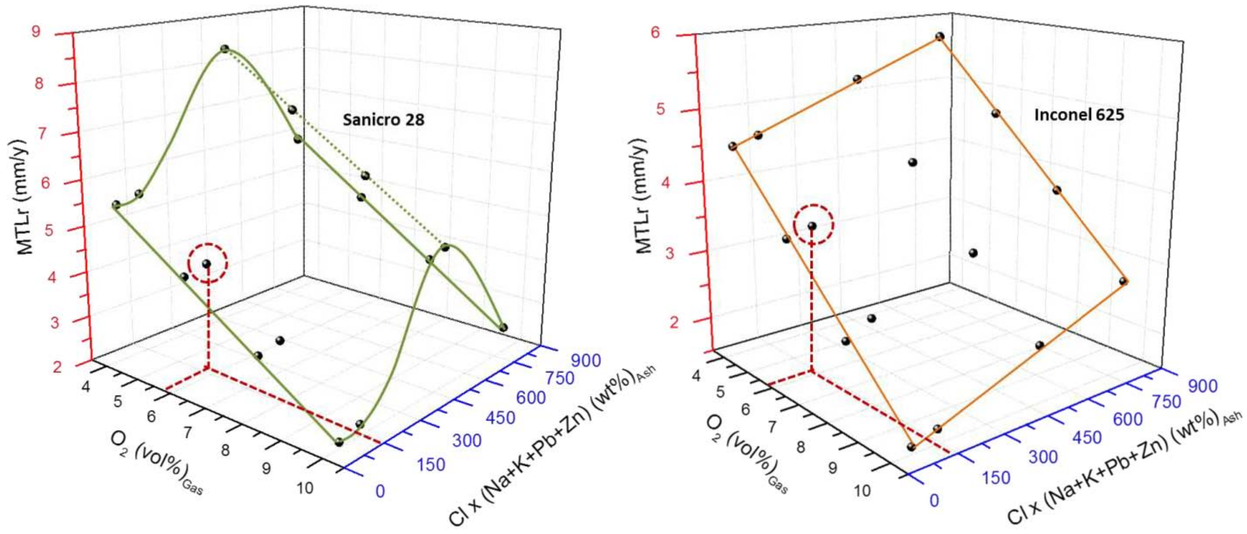

Figure V.10. Corrosion rate variation as a function of O_2 and [Cl x (Na+K+Zn+Pb)] for Sanicro 28 (Model 5) and Inconel 625 (Model 6) [$T_{Flue\ gas}$= 700°C - T_{Metal} = 440°C – 6 ppm HCl]

V.3 Conclusions

In this chapter, life assessment analyses were conducted, for both mechanisms under specific conditions. The influence of the different variables on the corrosion rate, for metal dusting and high-temperature corrosion, were quantified and illustrated through statistical models. Modeling and lifetime assessment studies allow analyzing a concept into simpler terms with a visual component.

In the case of high-temperature corrosion, three models have been proposed for T-gradient environments and flue gas conditions with encouraging results, even when corrosion rates look over estimated. These models allow us to compare material solutions, to evaluate the impact of operating conditions on the equipment and to estimate relative material's lifetime. The models offer a large range of conditions for key parameters that can be measured during the service, which suggest they can be applied for different types of boiler design and steam cycle efficiencies. Therefore, the models are useful industrial tools to improve preventive strategies, because they assist in:

- The evaluation of operating parameter's impact on fireside corrosion rates.
- Material's selection studies to compare the relative lifetime of material solutions regarding the fluctuating operating conditions.

In the case of metal dusting, the model based on mass loss rates (MLr) as dependent variable underestimates corrosion rates, which make difficult its application to real conditions, due to the lack of experimental data at high pressures and high gas velocities. The new model based on pit depth growth rates (PDGr) as dependent variable shows better results and closer to reality, as it is capable to predict corrosion rates at high pressures, within a determined validity domain.

It should be noticed that modelling of the incubation times (IT) coupled with pits growth rate after the incubation periods, appears to be the most pertinent method for equipment design and life assessment. First, because it was demonstrated that these models reproduce correctly the effects of the different variables (temperature, pressures, gas compositions and alloy composition) and second, because the pit depth and the thickness loss, are the most representative magnitudes from the mechanical point of view of component design.

The models presented limitations, as they are simplified versions of the real physical context. A model is not a substitute for scientific experimental data. However, a model may be used when it is impossible to reproduce the conditions necessary to predict a physical behavior. We have seen that the success of the models depends on the quality of data that is used to generate it. However, the methodology developed in this study is now in place to accept new data to improve the model's accuracy and to enlarge the conditions domain in order to get closer to the industrial scale.

GENERAL CONCLUSION

The overall objectives of this study were to determine the parameters that play the most significant role in metal dusting and high-temperature corrosion under deposits over a wide range of conditions, as well as, to create lifetime prediction models for materials subject to each type of corrosion under different scenarios. Both of these objectives have been attained in this study.

Statistical analyses such as Principal Component Analysis (PCA), Correlation Tests (CT) and Multiple Linear Regression (MLR) were utilized, to our knowledge, for the first time for predictive modeling of metal dusting and high-temperature corrosion. Two databases were constructed from literature data to perform the statistical treatment. It allowed us to determine, in a timely and practical manner, the most significant parameters for both corrosion processes in a large range of conditions and to highlight the interactions between these parameters and the corrosion rates.

Principal Component Analysis was conducted to have an overall view of how the different parameters of the corrosion processes are related with one another to avoid collinearities in the further Multiple Linear Regression analyses. Correlations Tests were applied in conjunction with PCA to explore all the parameter data distributions to determine the intensity of linear relations between the different parameters and the corrosion rates. The interpretations made from these analyses have led to the following conclusions:

- For metal dusting, the gas partial pressures mainly (pCO and pH_2) are strongly related with each other, due to the way the gas mixtures are conceived for experimental tests. Indeed, most experiments are done in 1 bar of CO-H_2 mixtures with little contents of H_2O and other CO_2. They are almost never diluted in Ar or He, therefore pCO and pH_2 are complementary. This leaded to increase the order of the models by the conception of a new parameter, [$pCO \times pH_2$]. Corrosion rates were evaluated by mass loss rates (MLr), incubation times (IT) and pit depth growth rate (PDGr). In all scenarios investigated, the statistical analyses showed that the temperature and the new variable [$pCO \times pH_2$] were often the most correlated with the corrosion rates, and hence, they were included in the MLr analyses. The carbon activity in the gas (a_C), calculated from the equation $a_C = K_1 \frac{pCO \times pH_2}{pH_2O}$, and the oxygen partial pressure calculated from $pO_2 = K_4 \left(\frac{pH_2O}{pH_2}\right)^2$ were often less correlated with the corrosion rate than the parameter $pCO \times pH_2$. This was surprising since a_C and pO_2 are often seen as the most important parameters to control metal dusting mechanisms and kinetics.

  In addition to these variables, other parameters were evaluated according to the scenario, such as: total pressure of the systems, water steam partial pressures and the aluminum and the molybdenum concentrations in the alloys.

  Concerning the temperature, a positive correlation was found with the corrosion rates, but only in the temperature range in which the corrosion increases with temperature, i.e. under the corrosion rate peak.

- For high-temperature-corrosion, no correlation was found between the gas temperature and the metal temperature, certain correlations were found in the combustion gases and high correlations were found between refractory oxides and chlorides in the ash composition. Consequently, it has been proposed to increase the order of the models through the conception of a new parameter, [Clx(Na+K+Pb+Zn)].

Corrosion rates were evaluated by maximum thickness loss rates (MLr) under isothermal and temperature gradient conditions. For most of the scenarios that were evaluated, the statistical results showed that, the gas temperature, the metal temperature, the O_2-content, the HCl concentration in the gas and the chloride content in the form of [Clx(Na+K+Pb+Zn)] were frequently the most correlated with the corrosion rates. Therefore, they were included in the MLR analyses. Besides, other variables were evaluated, such as the moisture and the sulfur dioxide concentrations in the gas, molybdenum content in the alloys and sulfur and refractory oxides in the ash.

- Regarding the alloy composition, it was found for both metal dusting and high-temperature corrosion that iron and nickel contents were highly correlated, due to the variation of iron and nickel concentrations along the three families of alloys contained in the domain of study. The different corrosion mechanisms that take place depending on the type of alloy, entailed to the classification of the materials contained in the database into three alloy systems: Fe-based alloys, Fe/Ni-based alloys and Ni-based alloys. Subsequent statistical analyses for most of the scenarios evaluated showed that the chromium content was the most significant parameter to increase corrosion resistance.

The conclusions drawn from the statistical analyses were compared to results obtained by experimental tests performed in the framework of the SCAPAC project and previous studies in literature, and were found to concur most of the time. In the modeling stage, according to the previous statistical analysis, several scenarios were generated to evaluate the influence of the selected variables on the corrosion rates.

In the case of metal dusting, four statistically successful models were obtained. The first two models explained the variation of the average mass loss rates for Fe-based alloys and Fe/Ni-based alloys. The other two models explained the variation of the incubation times, and the pits growth rates for Fe/Ni-based alloys in conjunction with Ni-based alloys. For most of the models that were proposed, the MLR showed that, the temperature, the internal pressure, the variable proposed [$pCO \times pH_2$] and the chromium content in the alloys were the most significant in the explanation of the corrosion rates. It has to be stressed that the results obtained from the models are restricted to the experimental range that was under investigation. However, despite the high variability of conditions, the models explained an average of 75% of the variation of the corrosion rates. There is still a 25% of variation not yet explained by the models, and this was attributed to 1/ other parameters not included in the data modeling, 2/ to the possibility of not linear relations with the parameters involved and 3/ to high standard deviation of the experimental data themselves which were used for modeling. There are important parameters for metal dusting corrosion that were not considered in the statistical analyses due to the lack of data in the literature, such as, the gas velocity, the higher pressures, the surface finish and the grain size or microstructure of the materials. Few studies have shown the important role of these variables in the corrosion process, and therefore further experimental studies are required to fill the information gap about their effect on the corrosion mechanisms in a wide range of conditions and materials.

By studding the different outputs resulting from metal dusting tests, we realized the role of the variables on each stage of the metal dusting kinetics. The modeling of the mean mass loss rates presented some difficulties due to the following two aspects:

- Mass loss measurements depend on the geometry of the samples, which add significant sources of error when different experimental protocols are brought together.
- The presence of incubation periods in the metal dusting kinetics produces lower corrosion rates than the real ones and increasing corrosion rates in the long term tests.

These two issues led to model the incubation times and the pit depth growth separately (for Fe-Ni and Ni-base alloys), showing satisfactory results. The new approach showed that the alloy composition and the frequency of thermal cycling plays an important role in the delay of the metal dusting attack, i.e. on the incubation periods, while the atmosphere conditions such as temperature, total pressure and partial pressures of the gases are the key parameters in the pits depth growth rates. Since the incubation times depend largely on the alloy composition, new approaches will be proposed for future work.

In the case of high-temperature corrosion, five successful models were obtained. Two models were obtained for isothermal conditions that explained the variation of the thickness loss rates for Fe-based alloys and Ni-based alloys. The other three models were obtained under temperature gradient conditions for Fe-based alloys, Fe/Ni-based alloys and Ni-based alloys.

Both isothermal models explained around 60% of the corrosion rates. The most significant variables were: the ash' solidus temperature and the chloride concentration in the ash. The ash' solidus temperature denoted as $T_{Solidus}$ in the models was estimated by an algorithm based on the qualitative composition of the ash. Its presence in the model significantly improved the fit of the regressions, suggesting the important influence of this variable in corrosion mechanisms. However, this data is usually not reported in the literature. More experimental measurements and thermodynamic modelling of the ash properties is required as a function of their compositions. More experimental work on the correlation between these properties and the corrosion mechanisms would be also helpful.

For all temperature gradient models, the MLR explained between 70% and 80% of the corrosion rates. The most significant variables in the explanation of the corrosion rates were the flue gas temperature, the metal temperature, the chromium content in the alloy and the chloride concentration in the ash. In addition, the modeling approach suggests a quantitative definition of the relative weight between explanatory variables which is consistent with the literature and industrial feedback. Temperature gradient models showed better percentages of explanation than isothermal models and for most cases, the flue gas temperature was more significant than metal temperature. This is an important finding, because this parameter is usually neglected in the experimental studies on heat exchangers materials performances. For all three models the chloride content in the form of [Clx(Na+K+Pb+Zn)] is also identified as one of the most important parameters. This confirms that the ash deposit chemistry related to the type of solid fuel is an important parameter to be considered for material's performance evaluations. The suppressive effect of the O_2 on the corrosion rate increases with increasing the Ni/Fe ratio in the alloy families. In operating conditions, the suppressive effect of O_2 is often neglected on the profit of combustion and energy efficiency in detriment of the material's resistance. The accelerating effect of HCl decreases with increasing the Ni/Fe ratio in the alloy families, according to the lower sensitivity of high Ni/Fe ratio material to active oxidation. On the other hand, the detrimental effect of S in deposits on Ni based alloys resistance adds also been identified. Positive Cr /Mo synergy was also identified on Ni based alloys. Nevertheless, there was about 20% to 30% of variation not yet explained by the models that can be attributed to other parameters not included in the data modeling, such as, gas velocity, ash's melting temperature, melted fraction in the deposit and viscosity of the deposit.

Despite good percentages of explanation and good agreements with theory were obtained, all metal dusting and corrosion models showed high standard deviations in the predictions regarding the experimental results. This is because two possible reasons. First, the lack of reproducibility of the experimental data that was used for modeling, in which experimental errors or not controlled tests parameter produce different corrosion rates for the same condition. Second, the assumption of linear kinetics when the processes go through a period of incubation or follow other kinetic laws, can be misleading. In consequence, the model deals with different corrosion rates for the same experimental condition. This produces high standard deviations in the predictions. The model accuracy depends on the quality of the data used for modeling. The present study attempts to make the high-temperature corrosion community be more sensitive about the importance of defining and controlling well the experimental parameters.

In the last chapter, a life assessment analysis was performed by using the models proposed in the previous chapters. This showed the applicability of the models for preventive maintenance, corrosion management, material's selection and for the impact evaluation of the operating parameters on component integrity. This type of model can be implemented in decision making tools including economic aspects to evaluate the corrosion risk of different scenarios.

Finally, the statistical approach used in this study offers dynamic models that can be improved with the addition of new data. Our main goal was to test and establish a methodology, and now the databases created are able to be supplied with new experimental information in order to create other approaches that contribute to the understanding and predictive modeling of metal dusting and high-temperature corrosion. Likewise, the statistical methodology proposed in this study to determine the most significant variables for predictive modeling of two different corrosion mechanisms, can certainly be applied to other scales and to other corrosion mechanisms. By choosing the metal dusting and the high-temperature corrosion under deposits, we have indeed chosen two of the most difficult phenomena to model. The results obtained here may be of potential use for different applications.

FUTURE WORK

The future work regarding metal dusting would involve adding and analyzing more experimental data to the database, concerning high pressure tests, different gas velocities and more information about surface finish and grain size.

Since the incubation time in metal dusting kinetics was analyzed to our knowledge, for the first time. A high influence of the alloy composition was found as well as a high correlation of the corrosion rate with the thermal cycling frequency. This suggests that the variation of the incubation times is linked to the establishment and damage of the protective oxide scale on the surface of the alloys. Therefore, several approaches can be proposed:

- Alloy composition determines the expansion coefficient of the materials. Hence, the incubation times can be related to the thermal expansion mismatch between the oxide scale and the substrate and its effect on the oxide layer resistance to thermal cycling. The alloy element concentrations (wt.%) in the model could be then replaced by the thermal expansion coefficients of the materials in order to evaluate its interaction with the corrosion rate.

- Metal dusting corrosion can be viewed as a competition between the oxide scale establishment at the surface of the alloy which is favored by the product $[Cr] \cdot D_{Cr}$, and the carbon permeability into the substrate $[C] \cdot D_C$. Therefore, for chromia forming alloys, the Cr-content (wt.%) in the model could be replaced by following variable:

$$\varphi = \frac{[Cr] \cdot D_{Cr}}{[C] \cdot D_C}$$

Where $[C]$ is the content of carbon (wt.%) in equilibrium with the gas, D_C is the diffusion coefficient of carbon in m²/s, $[Cr]$ is the atomic mass of chromium in the alloy matrix and D_{Cr} is the diffusion coefficient of Cr in m²/s. The estimation of the φ, if successful, will assist in determining if the hypothesis concerning the diffusion approach is valid or not for modeling. It should be noticed that D_C and D_{Cr} depend on the overall composition of the alloy. As a first approximation, they could depend only of the type of matrix (ferritic, austenitic). [C] depends on the composition of the alloy and the carbon activity in the gas. Its evaluation may require thermodynamic modelling, but it can also be approximated with an analytical function.

Concerning the pit growth kinetics under metal dusting conditions, nonlinear dependencies of the pit growth rate as a function of the gas partial pressure, temperature (to reproduce the temperature of the corrosion rate peak) and alloy composition can be now tested. This work is under progress.

The future work regarding high-temperature corrosion would involve adding and analyzing more experimental data to the database that come from temperature gradient tests for being the closest to operating conditions.

This work has also emphasized an information gap regarding the corrosion kinetics, which limits the statistical treatment to apply the linear kinetics law. Kinetics information would allow evaluating the use of other kinetics laws and enhance the model's accuracy. In our case, the use of a parabolic kinetic law, if successful, will determine if the hypothesis concerning reducing the standard deviation of the models is valid or not.

It was seen that the ash deposit chemistry and its behavior is a key parameter to be considered. In order to improve its influence in the model, several suggestions can be proposed on this axis:

- To use thermodynamic approaches to determine parameters related to the ash behavior ($T_{Solidus}$/$T_{Liquidus}$, melted fraction, viscosity) for every ash composition contained in the database.

- To evaluate a dynamic method or variable that represents the correlation between flue gas /metal temperature, deposit composition and deposit melting behavior (chemistry, $T_{Solidus}$/$T_{Liquidus}$, molten phase fraction).

- To introduce in modeling procedures new physical parameters related to ash deposit features such as deposit thickness and porosity in order to analyze the relative weight of these variables on the corrosion rates.

Regarding the statistical methodology, another approach, denoted as design of experience (DoE) can be employed, to determine the most significant independent variables for any of the dependent variables. The method would highlight the interaction between these variables, to determine if the current correlations concerning the variables can be optimized.

Résumé en français

Au cours des dernières décennies, le contrôle de la corrosion des alliages exposés à des conditions sévères et complexes a été un grand défi pour les applications industrielles. Les coûts de la corrosion sont élevés et les stratégies de prévention sont devenues une demande industrielle importante. Le projet SCAPAC financé par l'ANR, a proposé d'étudier la corrosion lors de deux procédés industriels: le vapo-réformage du méthane et l'incinération des déchets ménagers. Bien que les conditions de fonctionnement de ces deux procédés soient différentes, les approches de modélisation peuvent être similaires. Dans le procédé de vapo-réformage du méthane, les composants métalliques sont soumis à la corrosion par « metal dusting », qui est une forme d'endommagement catastrophique qui affecte les alliages exposés à des températures élevées (400-800 °C) et des atmosphères sursaturées en carbone. De même, les composants métalliques des incinérateurs de déchets qui sont exposés à des atmosphères de combustion sont soumis à la corrosion à haute température sous dépôts de cendres.

Le « metal dusting » est un phénomène critique qui a mené à des pertes matérielles importantes et à l'arrêt d'installations industrielles pendant les 50 dernières années. Les mécanismes de cette dégradation ont été identifiés et sont disponibles dans la littérature. Cependant, l'effet de certains paramètres des procédés ne sont pas encore bien compris et nécessitent des compléments d'études. En ce qui concerne la corrosion à haute température, les mécanismes sont bien documentés et une quantité considérable de travaux ont été publiés au cours des dernières décennies. De nombreux matériaux et revêtements ont été développés. Cependant, la performance des matériaux dans des environnements différents n'est pas assez bien comprise pour créer des modèles de prédiction de durée de vie. Une revue bibliographique de ces deux domaines a révélé qu'il existait des approches de modélisation. Néanmoins, il n'y a pas actuellement de modèles prédictifs fiables de durée de vie qui soit disponible dans la littérature pour les alliages commerciaux, et pour une gamme étendue de conditions expérimentales.

La présente étude présente une méthodologie pour développer des modèles statistiques de prévision de durée de vie. Il s'agit d'évaluer la performance de matériaux soumis au « metal dusting » et à la corrosion à haute température sous dépôt. Deux bases de données ont été construites pour intégrer les résultats expérimentaux du projet SCAPAC, aussi bien que résultats de la littérature. Ceci afin d'avoir suffisant des données pour la modélisation. Ces bases de données ont permis d'analyser plus de 4000 vitesses de corrosion à l'aide de méthodes statistiques appliquées à différents scénarios. La méthodologie de l'Analyse des Composantes Principales (ACP) a été utilisée pour identifier les paramètres clés contrôlant les cinétiques de corrosion, qui ont ensuite été utilisés pour construire des modèles de prévision de durée de vie à l'aide de la Régression Linéaire Multiple (RLM).

Pour la corrosion par « metal dusting », deux modèles ont été obtenus pour expliquer le temps d'incubation (IT) et la cinétique de croissance de profondeur de piqures (PDGr), avec des résultats satisfaisants. Il a été montré que l'IT était hautement corrélé avec la composition chimique de l'alliage et que PDGr était plutôt corrélée avec la composition du gaz et la pression totale du système. En ce qui concerne la corrosion à haute température, trois modèles ont été obtenus dans le scénario de gradient thermique pour trois familles d'alliages: des aciers ferritiques, des alliages austénitiques à base de fer et de nickel et des alliages à base de nickel, en montrant des résultats encourageants. Il a été confirmé que T_{Gas} et $T_{Métal}$ étaient des paramètres de 1er ordre dans la corrosion à haute température, et il a été montré que le poids relatif des variables varie selon la famille des alliages. Dans les deux cas, les modèles statistiques ont été comparés avec les résultats expérimentaux et théoriques. L'accord entre la modélisation et l'expérience permet de proposer des premières évaluations de durées de vie des matériaux dans un domaine de conditions d'environnement bien défini.

Bibliography

1. G.H. Koch, M. P.H. Brongers, and N. G. Thompson, Y. P.Virmani, J.H. Payer.*Corrosion Costs and Preventive Strategies in the United States*. FHWA-RD-01-156, R315-01, Final Report, (CC Technologies Laboratories, Incorporated, NACE International, Federal Highway Administration:).
2. *DOE Fundamentals Handbook. Materials Science*. (Volume 2 of 2 DOE-HDBK-1017/2-93: 1993).
3. Nace International, *Basic Corrosion Course Handbook.*
4. L. S. V. Delinder, *Corrosion Basics, An Introduction.* (NACE International:).
5. American Petroleum Institute. *Damage Mechanisms Affecting Fixed Equipment in the Refining Industry*. (Recomended Practice 571 1st Edition: 2003).
6. D. J. Young, J. Zhang, C. Geers and M. Schutze, M. Recent advances in understanding metal dusting: A review. *Materials and Corrosion* 62, (1), 7–28 (2011).
7. H.J. Grabke, R. Krajak and J.C. Nava Paz. On the mechanism of catastrophic carburization: Metal dusting. *Corrosion Science* 35, (5-8), 1141–1150 (1993).
8. J. Zhang, D. J. Young. Kinetics and mechanisms of nickel metal dusting I. Kinetics and morphology. *Corrosion Science* 49, 1496–1512 (2007).
9. R. T Jones, K. L Baumert. Metal dusting - an overview of current literature. *Corrosion 2001* Paper no. 01372, (2001).
10. C.M. Chun, T.A. Ramanarayanan and J.D. Mumford. Relationship between coking and metal dusting. *Materials and Corrosion* 50, 634–639 (1999).
11. H. J. Grabke, E. M. Müller-Lorenz, André Schneider. Carburization and Metal Dusting on Iron. *ISIJ International* 41, S1–S8 (2001).
12. H.J. Grabke. Thermodynamics, mechanisms and kinetics of metal dusting. *Materials and Corrosion* 49, 303–308 (1998).
13. H.J. Grabke, R. Krajak, E.M. Miiller-Lorenz and S. StrauB. Metal dusting of nickel-base alloys. *Materials and Corrosion* 47, 495–504 (1996).
14. E. Pippel, J. Woltersdorf and R. Schneider. Micromechanisms of metal dusting on Fe-base and Ni-base alloys. *Materials and Corrosion* 49, 309–316 (1998).
15. J.Z. Zhang and D.J. Young. Coking and Dusting of Fe–Ni Alloys in CO–H 2 –H 2 O Gas Mixtures. *Oxidation Of Metals* **70, 189**, 189–211 (2008).
16. B.A. Baker, G.D Smith. Metal dusting of nickel-containing alloys. *Corrosion 98* Paper No 445, (1998).
17. J. Klower, H.J. Grabke, E.M. Muller Lorenz. Metal dusting and carburization resistance of nickel-base alloys. *Corrosion 1997* Paper no. 139, (1997).
18. H. J. Grabke, E. M. MuÈller-Lorenz, S. Strauss, E. Pippel and J. Woltersdorf. Effects of Grain Size, Cold Working, and Surface Finish on the Metal-Dusting Resistance of Steels. *Oxidation of Metals,* 50, N° 3/4, 241–254 (1998).
19. H. J. Grabke. Corrosion by carbonaceous gases, carburization and metal dusting, and methods of prevention. *Materials at High Temperatures Volume* 17, Issue 4, 483–487 (2000).

20. J. Zhang, D.M.I. Cole, and D.J. Young. Alloying with copper to reduce metal dusting of nickel. *Materials and Corrosion* 56, No. 11, 756–763 (2005).

21. Y. Nishiyama, K. Moriguchi, N. Otsuka andT. Kudo. Improving metal dusting resistance of. transition-metals and Ni-Cu alloys. *Materials and Corrosion* 56, Issue 11, 806–813 (2005).

22. J. Zhang , D. J. Young. Effect of copper on metal dusting of austenitic stainless steels. *Corrosion Science* 49, 1450–1467 (2007).

23. E.M. Mueller-Lorenz and H.J. Grabke. Coking by metal dusting of steels. *Materials and Corrosion* 50, 614–621 (1999).

24. C. M. Chun, J. D. Mumford, and T. A. Ramanarayanan. Mechanisms of Metal Dusting Corrosion of Iron. *Journal of The Electrochemical Society,* 149, (7), B348–B355 (2002).

25. H.J. Grabke, C.B. Bracho-Troconis and E.M. Muller-Lorenz. Metal dusting of low alloy steels. *Werkstoffe und Korrosion* 45, 215–221 (1994).

26. H. Yin, D. J. Y. J. Zhang. Effect of gas composition on coking and metal dusting of 2.25Cr–1Mo steel. *Corrosion Science* 51, 2983–2993 (2009).

27. T.P.Levi, N. Briggs, I.E. Minchington and C.W. Thomas. Metal dusting of type 316 stainless steel in high pressure environments between 450° C and 650° C. *Materials and Corrosion* 53, 239–246 (2002).

28. J.Z. Albertsen, O. Grong, J.C. Walsmley, R.H. Mathiesen and W. VAN. Model for High-Temperature Pitting Corrosion in Nickel-Based Alloys Involving Internal Precipitation of Carbides, Oxides, and Graphite. *Metallurgical and Materials Transactions* 39 A, 1258–1276 (2008).

29. B. A. Baker, G. D. Smith, V. W. Hartmann, L. E. Shoemaker. Nickel-base material solutions to metal dusting problems. *Corrosion 2002* Paper no. 02394, (2002).

30. P. Hazeldine, B. Baker. Utilisation of alloy 693 in metal dusting environments. *NACE Corrosion 2007* Paper no. 07430, (2007).

31. The Babcock and Wilcox Company. *Steam its generation and use, Edition 41.*(2005)

32. A. Miltner, G. Beckmann and A. Friedl. Preventing the chlorine-induced high temperature corrosion in power boilers without loss of electrical efficiency in steam cycles,. *Applied Thermal Engineering* 26, 2005–2011 (2006).

33. J.M. Brossard. Corrosion des échangeurs de chaleurs dans les Unités de Valorisation Energétique de Déchets Ménagers. *Ecole d'Eté CNRS Porquerolles, Edition Mines ParisTech* ISBN 978-2-911256-54-7, (2010).

34. F. J. Frandsen, Utilizing biomass and waste for power production-a decade of contributing to the understanding, interpretation and analysis of deposits and corrosion products. *Fuel* 84, 1277–1294 (2005).

35. M. Montgomery, B. Carlsen, O. Biede, O.H. Larsen. Superheater corrosion in biomass-fired power plants : investigation of welds,. *NACE Corrosion 2002* Paper no. 02379, (2002).

36. P. Viklund, High temperature corrosion during waste incineration. KTH Chemical Science and Engineering (2011).

37. D. O. Albina, *Theory and experience on corrosion of waterwall and superheater tubes of Waste-To-Energy facilities. (2005).* (The Henry Krumb School of Mines and The Waste-to-Energy Research and Technology Council (WTERT): 2005).

38. I. Wright , H.H. Krause. Assessment of factors affecting boiler tube lifetime in waste-fired steam generators: new opportunities for research and technology development. *National Renewable Energy Laboratory* (1996).

39. R. Dooley, E. Wiertel. A survey of erosion and corrosion resistant materials being used on boiler tubes in waste to energy boilers. *Proceedings of the 17th Annual North American Waste-to-Energy Conference, NAWTEC17-2334, May 18-20, Chantilly, Virginia, USA* (2009).

40. A. Zahs, M.Spiegel; H.J Grabke. Chloridation and oxidation of iron, chromiun, nickel and their alloys in chloridizing and oxydizing atmospheres at 400-700°C. *Corrosion Science* 42, 1093–1122 (2000).

41. V. K. Sethi, I. G. Wright, V. Nagarajan and H.H. Krause. Solving Fireside Corrosion Problems in Incinerators. *Materials and Performances* 43–46 (1992).

42. M. Theis, B.J.Skrifvars, M.Hupa, H. Tran. Fouling tendency of ash resulting from burning mixtures of biofuels. Part 1: Deposition rates. *Fuel* 85, 1125–1130 (2006).43. M.Theis, H. T. B.-J. Skrifvars M. Zevenhoven M. Hupa Fouling tendency of ash resulting from burning mixtures of biofuels. Part 3. Influence of probe surface temperature. *Fuel* **85**, 2002–2011 (2006).

44. M. Theis, B. J. Skrifvars, M. Zevenhoven, M. Hupa, H. Tran. Fouling tendency of ash resulting from burning mixtures of biofuels. Part 3. Influence of probe surface temperature. *Fuel* 85, 2002–2011 (2006).

45. W. Spiegel, T. Herzog, G. Magel, W. Muller and W. Schmidl. Corrosion in boilers with difficult fuels. *Power Plant Chemistry* 13(5), 285–293 (2011).

46. J.M. Brossard, I. Diop, X. Chaucherie, F. Nicol, C. Rapin and M. Vilasi. Superheater fireside corrosion mechanisms in MSWI plants: Lab-scale study and on-site results. *Materials and Corrosion* 62, Issue 6, 543–548 (2011).

47. J-M. Brossard, F. Nicol, X. Chaucherie. Fireside corrosion in Energy Recovery Boilers and maintenance issues. *Materials Science Forum* 595-598, 281–288 (2008).

48. B. Waldmann, F. Haider, S. Horn, R. Warnecke. Corrosion monitoring in waste-to-energy plants. *Eurocorr 2008*

49. Y. Kawahara and Y. Kaihara. Recent trends in corrosion-resistant tube materials and improvements of corrosion environments in WtE plants. *CORROSION 2001* Nace Houston TX, Paper no. 01173 (2001).

50. H. Wiinikka. "High temperature aerosol formation and emission minimisation during combustion of wood pellets". Luleå University of Technology (2005).

51. F. Lebel. "Etude des phénomènes de corrosion à haute température en environnement type UVED: Développement d'un pilote laboratoire et quantification des paramètres clés gouvernant les mécanismes". Université de Nancy (2008).

52. P. Steinmetz and C. Rapin. Corrosion of metallic materials in waste incinerators. *Materials Sciene Forum* 251-254, 505–518 (1997).

53. G. Sorell. The role of chlorine in high temperature corrosion in waste-to-energy plants. *Materials at High Temperatures,* 137–150 (1997).

54. A.Ruh & M.Spiegel EUROCORR 2004. *Nice, France* (2004).

55. A.Ruh, & M.Spiegel. Influence of gaz composition on kinetics of chloride melt induced corrosion of pure iron. (EU-project OPTICORR. *Materials and Corrosion* 57 (3), 237–243 (2006).

56. P. Ganesan, G. D. Smith, L. E. Shoemaker, G. Y. Lai and G. Sorell. Materials Performance in Waste Incineration Systems. *CORROSION/92* NACE, Houston, TX, p. 33–1 to 33–10 (1992).

57. Y. Kawahara, & M.Kira, Corrosion Factors of Waterwall Tube and Protection by Field Metal Spraying in Municipal Refuse Incineration Plant. *CORROSION/95* NACE International, Houston, TX, Paper no. 563 (1995).

58. S. Chevalier, J. Favergeon. *French Activity on High Temperature Corrosion in Water Vapor*. (Materials Science Foundations vol. 76, Zurich, Switzerland: Trans Tech Publications).

59. Nakagawa, K. & Matunaga, Y. Effect of HCl on the corrosion of waterwall in a waste incineration plant. *Materials at high temperatures* **14(3)**, 245–250 (1997).

60. L. D. Paul, & P. L. Daniel. Corrosion Mechanisms in Oxidizing, Reducing, and Alternating Combustion Gases in Refuse-Fired Boiler Environments. *CORROSION/93* Paper no. 93216, NACE International, Houston, TX (1993).

61. J. W. Slusser, S. W.Dean, W. R.Watkins and S. P. Goff. The Effects of Gas Impurities and Salts on Metal Corrosion laboratory Studies. *CORROSION/93* NACE, Houston, TX (1993), Paper No. 217.

62. H.J. Grabke, E. Reese and M. Spiegel. The Effects of Chloride, and Sulfur Dioxide in the Oxidation of Steels Below Deposits. *Corrosion Science* 7, 1023–1043 (1995).

63. H. Krause. High Temperature Corrosion Problems in Waste Incineration Systems. *American Society for Metal* 7, (4), 322–332 (1986).

64. M. Spiegel. Influence of gas phase composition on the Hot Corrosion of steels and nickel-based alloys beneath a (Ca-Na-K)-sulfate mixture containing $PbSO_4$ and $ZnSO_4$. *Materials and Corrosion* 51, 303–312 (2000).

65. M. Bøjer, P. A. Jensena, F. Frandsen, K. Dam-Johansen, O. Hedegaard Madsen, K. Lundtorp. Alkali/Chloride release during refuse incineration on a grate: Full-scale experimental findings. *Fuel Processing Technology* 89, 528–539 (2008).

66. P. Rademakers, W. Hesseling, J. van de Wetering. Review on corrosion in waste incinerators, and possible effect of bromine,. *TNO report I02/01333/RAD* (2002).

67. H. W. Deacon. On a New Method of Obtaining Chlorine. *The Chemical News* 22 (566), 157–161 (1870).

68. J. Pyykonen and J. Jokiniemi. Modeling alkali chloride superheater deposition and its implications. *Fuel Processing Technology* 80, 225–262 (2003).

69. H. Matsuda, S, Ozawa, K. Naruse, K. Ito, Y. Kojima and T. Yanase. Kinetics of HCl emission from inorganic chlorides in simulated municipal wastes incineration conditions. *Chemical Engineering Science* 60, 545–552 (2005).

70. R. A. Rapp, Chemistry and electrochemistry of the hot corrosion of metals. *Corrosion* 42 (10), 568–577 (1986).

71. N. Otsuka and R. A. Rapp. Hot Corrosion of Preoxidized Ni by a Thin Fused Na_2SO_4 Film at 900° C. *Journal of Electrochemical Society* 137 (1), 46–52 (1990).

72. R. A. Rapp. Hot corrosion of materials: a fluxing mechanism? *Corrosion Science* 44, 209–221 (2002).

73. N. Otsuka. Chemistry and melting characteristics of fireside deposits taken from boiler tubes in wast incinerators. *Corrosion Science* 53, 2269–2276 (2011).

74. N. Otsuka, K. Nakagawa, K. Yukawa, Y. Tsukaue Y. Kawahara. A corrosion mechanism for the fireside wastage of superheater materials in waste incinerators. *CORROSION 97* Paper no. 157 (1997).

75. N.Otsuka, Y.Kawahara, Y.Fukuda and T.Hosoda. Laboratory corrosion tests for simulating fireside wastage of superheater materials in waste incinerators. *CORROSION/99* Paper 89 (1999).

76. H. P. Nielsen, F.J. Frandsen and K. Dam-Johansen. Lab-Scale Investigations of High-Temperature Corrosion Phenomena in Straw-Fired Boilers. *Energy & Fuels* 13, 1114–1121 (1999).

77. J. Sandberg, C. Karlsson, R. Bel Fdhila. A 7 year long measurement period investigating the correlation of corrosion, deposit and fuel in a biomass red circulated fluidized bed boiler. *Applied Energy* 88, 99–110 (2011).

78. P. Viklund, A. Hjörnhede, P. Henderson, A. Stålenheim, R. Pettersson. Corrosion of superheater materials in a waste-to-energy plant. *Fuel Processing Technology* 105, 106–112 (2013).

79. M. Spiegel. Salt melt induced corrosion of metallic materials in waste incineration plants. *Materials and Corrosion* 50, No. 7, 373–393 (1999).

80. L. Sorum, F.J. Frandsen and J. E Hustad. On the fate of heavy metals in municipal solid waste combustion. Part I: devolatilisation of heavy meatls on the great. *Fuel* 82, 2273–2283 (2003).

81. Daniel Lindberg, P. C. Rainer Backman Thermodynamic evaluation and optimization of the (NaCl+Na2SO4+Na2CO3+KCl+K2SO4+K2CO3) system. *J. Chem. Thermodynamics* **39**, 1001–1021 (2007).

82. D. Lindberg, R. Backman, P. Chartrand. Thermodynamic evaluation and optimization of the ($NaCl+Na_2SO_4+Na_2CO_3+KCl+K_2SO_4+K_2CO_3$) system. *J. Chem. Thermodynamics* 39, 1001–1021 (2007).

83. H.P. Nielsen, F.J. Frandsen, K. Dam-Johansen and L.L.Baxter. The implications of chlorine-associated corrosion on the operation of biomass-fired boilers. *Progress in Energy and Combustion Science* (26), 283–298 (2000).

84. G. Y. Lai, *High Temperature Corrosion of Engineering Alloys*. (Haynes International: 1990).

85. E. M. Levin, C. R. Robbing, H. F. McMurdie. *Phase diagrams for ceramists* (The American Ceramic Society Inc: 1969).

86. P. Kofstad, *High Temperature Corrosion*. (Elsevier Applied Science: 1988).

87. H. J. T. Ellingham, Reducibility of oxides and sulfides in metallurgical processes. *Journal of the Society of Chemical Industry* 63, 125–133 (1944).

88. A. S. Khanna, *Introduction to High Temperature Oxidation and Corrosion,*. (ASM International, Materials Park: 2004).

89. S. Mannan, G. Smith, S. Kiser. Performance of commercial and developmental corrosion resistant alloys in simulated waste incineration environments. *CORROSION 2002* Paper no. 02387 (2002).

90. R. Peraldi and B. A. Pint. Effect of Cr And Ni Contents on the Oxidation Behavior of Ferritic and Austenitic Model Alloys in Air with Water Vapor. *Metals and Ceramics Division Oak Ridge National Laboratory.*

91. I. G.Wright, *High Temperature Corrosion: In Metals Handbook. ASM International* 13, 9th Ed, 97–103 (1987).

92. T. Ishitsuka, K. Nosek. Stability of protective oxide films in waste incineration environment solubility measurement of oxides in molten chlorides. *Corrosion Science* 44, 247–263 (2002).

93. N. Israelson, "High Temperature Oxidation and Chlorination of FeCrAl Alloys". Chalmers University of Technology, Gothenburg, Sweden (2014).

94. R. Prescott, M. J. Graham. The formation of aluminum oxide on high temperatures alloys. *Oxidation of Metals* 38, 233–254 (1992).

95. A. Phongphiphat, C. Ryu, Y.B. Yang, K.N. Finney, A. Leyland, V.N. Sharifi, J. Swithenbank. Investigation into high-temperature corrosion in a large-scale municipal waste to energy plant. *Corrosion Science* 52, 3864–3874 (2010).

96. R. F. A. Pettersson, Characterisation of oxides formed on stainless steels at 800-1100°C. *Proc. Int. Conf. "Microscopy of Oxidation", Cambridge, UK, University of Cambridge* (1996).

97. T. Jonsson, S. Canovic, F. Liu, H. Asteman, J.-E. Svensson, L.-G. Johansson, M. Halvarsson, Microstructural investigation of the effect of water vapour on the oxidation of alloy 353 MA in oxygen at 700 and 900°C. *Materials at High Temperatures* 22(3-4), 231–243 (2005).

98. EP 1 820 875 A2 Corrosion coating for turbine blade environmental protection. *General Electric Company Schenectady, NY 12345 (US)* (2006).

99. H. E. Evans, D. A. Hilton, R. A. Holm, S. J. Webster. Influence of silicon additions on the oxidation resistance of stainless steel. *Oxidation of Metals* 19, 1–18 (1983).

100. R. Pettersson, L. Liu, J. Sund. Cyclic oxidation performance of silicon-alloyed stainless steels in dry and moist air. *Corrosion Engineering, Science and Technology* 40 (3), 211–216 (2005).

101. J.P. Bailon, J.M. Dorlot. *Des Materiaux*. (Montreal, CA : Presses Internationales Polytechnique: 2000).

102. R. A. Rapp, Hot corrosion of materials. *Pure & Appl. Chem* 1990, 113–122

103. Y. Kawahara, M. Nakamura, H. Tsuboi, K. Yukawa. Evaluation of new corrosion resistant superheater tubings in high efficiency Waste-to-Energy plants. *CORROSION 97* Paper No. 165 (1997).

104. Y. Kawahara. High temperature corrosion mechanisms and effectof alloying elements for materials used in waste incineration enviroment. *Corrosion Science* 44, 223–245 (2002).

105. R. Streiff, J. Stringer, R.C. Krutenat, M. Caillet. *High Temperature Corrosion of Materials and Coatings for Energy Systems and Turboengines*. *Essex England: Elsevier Applied Science Publishers Ltd.* (1987).

106. G. Y.Lai. Corrosion Mechanisms and Alloy Performance in Waste-To-Energy Boiler Combustion Environments. *12th North American Waste to Energy Conference* Savannah, Georgia USA, 12–2214

107. B. Waldman, Korrosion in Anlagen zur thermischen Abfallverwertung elektrochemische Korrosionserfassung und Modellbildung. *Augsburg: Thesis Augsburg University.* (2007).

108. Y. Kawahara, N. Orita, M. Nakamura, S. Ayukawa and T. Hosoda. Laboratory corrosion tests for simulating fireside wastage of superheater materials in Waste incinerators. *CORROSION/99 San Antonio, TX* Paper No.89, (1999).

109. A. Ots. Corrosive-erosive wear mechanism of boiler heat transfer surfaces. *Baltica VI VTT SYMPOSIUM 233 Life Management and Maintenance for Power Plants* Vol. 1 Helsinki, 187–208 (2004).

110. B.A. Baker, G.D. Smith, L.E. Shoemaker. Performance of commercial alloys in simulated waste incineration environments. *CORROSION 2001* Nace International, Houston, TX, Paper No. 183 (2001).

111. *API 579-1/ASME FFS-1 2007 Fitness-For-Service. (American Petroleum Institute's Recommended Practice 579, Fitness-For-Service).*

112. S. Mercier."Modèles stochastiques et méthodes numériques pour la fiabilité". Université Paris Est. (2008).

113. H. Zimmermann. *Fuzzy set theory and its applications.* (London: Kluwer Academic Publisher 4th Edition: 2001).

114. J.E. Strutt, J.R Nicholls, B. Barbier. The prediction of corrosion by statistical analysis of corrosion profiles. *Corrosion Science* 25 No. 5, 305–315 (1985).

115. J. R. Nicholls and D. J. Stephsenson. A Life prediction model for coatings based on the statistical analysis of hot salt corrosion performance. *Corrosion Science* 33, No. 8, 1313–1325 (1992).

116. C. Randy John, D. Arthur Pelton, L. Arthur Young, T. William Thompson, I. G. Wright, T. M. Besmann. Assessing Corrosion in Oil Refining and Petrochemical Processing. *Materials Research* 7, No. 1, 163–173 (2004).

117. P. Makkonen. Expert system to assist the analysis of superheater fireside corrosion. *Foster Wheeler Energia Oy, Karhula R&D Center.* (1998).

118. P. Makkonen. Neural network for prediction of superheater fireside corrosion. *Foster Wheeler Energia Oy, Karhula R&D Center* (1998).

119. A. Shanian, & O. Savadogo. A material selection model based on the concept of multiple attribute decision making. *Materials and Design* 27, 329–337 (2006).

120. R. Venkata Rao. A decision making methodology for material selection using an improved compromise ranking method. *Materials and Design* 29, 1949–1954 (2008).

121. M. J. Jiménez-Come, I. J. Turias and J. J. Ruiz-Aguilar. Pitting corrosion behaviour modelling of stainless steel with support vector machines. *Materials and Corrosion* 66, Issue 9, 915–924 (2015).

122. J. M. Gandía, P. Monzón, R. Bataller, I. Campos, J. Manuel Lloris, J. Soto. Principal component analysis applied to study of carbon steel electrochemical corrosion. *Corrosion Engineering, Science and Technology* 50, Issue 4, 320–329 (2015).

123. C. Saikaew, "Corrosion severity ranking methodology and a predictive model for corrosion growth based on environmental and corrosion growth data". University of Oklahoma (2003).

124. D. Benstock , F. Cegla. Sample selection for extreme value analysis of inspection data collected from corroded surfaces. *Corrosion Science* Available online http://dx.doi.org/10.1016/j.corsci.2015.11.020, (2015).

125. A. Fabas, "Corrosion par metal dusting d'alliages austénitiques, modélisation cinétique et mécanismes". Université de Toulouse (2015).

126. E.Schaal, "Comportement en corrosion de matériaux métalliques commerciaux et modèles dans des conditions types UVEOM". Université de Lorraine (2015).

127. A. Fabas, D. Monceau, S. Doublet, A. Rouaix-Vande Put. Doublet. Modelling of the kinetics of pitting corrosion by metal duting. *Corrosion Science* 98, 592–604 (2015).

128. J.Stewart, *Calculus*. (Cengage Learning: 2011).

129. K. Natesan, & Z. Zeng. Development of Materials Resistant to Metal Dusting Degradation. *Argonne National Laboratory* Annual Report for Calendar Year 2005, (2005).

130. Q. Wu, J. Zhang and D. J. Young. Metal dusting behaviour of several nickel- and cobalt-base alloys in CO–H2–H2O atmosphere. *Materials and Corrosion* 62, No. 9999, 1–9 (2011).

131. C. M. Chun, & T. A. Ramanarayanan. Metal Dusting Corrosion of Austenitic 304 Stainless Steel. *Journal of The Electrochemical Society* 152 (5), B169–B177 (2005).

132. Y. Nishiyama, N. Otsuka, T. Kudo. Metal dusting behaviour of Cr–Ni steels and Ni-base alloys in a simulated syngas mixture. *Corrosion Science* 48, 2064–2083 (2006).

133. C. Rosado, & M. Schutze. Protective behaviour of newly developed coatings against metal dusting. *Materials and Corrosion* 54, No. 11, 831–853 (2003).

134. C.M. Chun, T.A. Ramanarayanan. Metal dusting resistant alumina forming coatings for syngas production. *Corrosion Science* 51, 2770–2776 (2009).

135. P. Speck, D. J. Young. Influence of Hafnium Additions and Preoxidation Treatment on the Metal Dusting of Ni–Al Alloys. *Oxidation of Metals* 76, 287–305 (2011).

136. J. Zhang, D. J. Young. Contributions of carbon permeation and graphite nucleation to the austenite dusting reaction: A study of model Fe–Ni–Cu alloys. *Corrosion Science* 56, 184–193 (2012).

137. J. Zhang, D. J. Young. Philip Speck Metal Dusting of Alumina-Forming Creep-Resistant Austenitic Stainless Steels. *Oxid Met* 77, 167–187 (2012).

138. E. Schaal, N. David, P.J. Panteix, C.Rapin, J.M. Brossard, F. Maad. Effect of chloride content in ash in oxidation kinetics of Ni-Based and Fe-Based Alloys. *Oxidation of Metals* 84, 307–327 (2015).

139. *ISO/FDIS 17248 Corrosion of metals and alloys — Test method for high temperature corrosion testing of metallic materials by embedding in salt, ash, or other solids. (ISO).*

140. C. J. Davis, & L. W. Pinder. *Report No. COAL R267 DTI/Pub URN 04/1795: Fireside Corrosion of Boiler Materials – Effect of Co-Firing Biomass with Coal*. (E.ON UK: 2004).

141. B. A. Baker, & G. D. Smith, *High temperature corrosion of iron-base and nickel-base heat resistant alloys in a simulated waste incineration environment*. (INCO Alloys International, Inc).

142. K. Persson, M. Broström, J. Carlsson, A. Nordin, R. Backman. High temperature corrosion in a 65 MW waste to energy plant. *Fuel Processing Technology* 88, 1178–1182 (2007).

143. Y. Kawahara & M. Kira, Corrosion Prevention of waterwall tube by field metal spraying in municipal waste incineration plants. *Corrosion* 53 (3), 241–251 (1997).

144. R. B. Dooley, & A. K. Mehta, *Effect of chlorine on waterwall fireside corrosion*. (EPRI: 2001).

145. Y. Kawahara, N. Orita, M. Nakatmura,S. Ayukawa, T. Hosoda. Application of new corrosion resistant superheater tubing for 500 °C, 100 Kgf/cm2g high efficiency WTE plant. *Corrosion 99* Paper no. 91 (1999).

146. K. Natesan, A. Purohit, D. L. Rink. *Fireside Corrosion of Alloys for Combustion Power Plants*. (Argonne National Laboratory: 2002).

147. M. Noguchi, H. Yakuwa, M. Miyasaka, M. Yokono, A. Matsumoto, K. Miyoshi, K. Kosaka and Y. Fukuda. Experience of superheater tubes in municipal waste incineration plant. *Materials and Corrosion* 51, 774–785 (2000).

148. L. Nylof, E. Hliggblom. Corrosion of experimental superheater alloys in waste fuel combustion. *Corrosion 97 Paper no. 154* (1997).

149. M. Fukumoto, C. Tachikawame, Y. Matsuzaka, M. Hara. Formation of Si diffusion layer on stainless steels and their high temperature corrosion resistance in molten salt. *Corrosion Science* 56, 105–113 (2012).

150. S. Andersson, E. W. Blomqvist, L. Bäfver, F. Jones, K. Davidsson, J. Froitzheim, M.Karlsson, E. Larsson, J.Liske. Sulfur recirculation for increased electricity production on Waste-to-Energy plants. *Waste Management* 34, 67–78 (2014).

151. W.W. Luo, Z.D. Liu, Y.T. Wang, R.J. Yang. High Temperature corrosion behavior of the superheater materials. *Procedia Engineering* 36, 212–216 (2012).

152. Y.S. Li, M. Spiegel, S. Schimada. Corrosion behaviour of various model alloys with NaCl-KCl coatings. *Materials Chemisrty and Physics* 93, 217–233 (2005).

153. G.D. Smith, D.J. Tillack, S.J. Patel. Alloy 625 - Impressive Past/Significant presence/awesome future. *TMS (The Minerals Metals and Materials Society)* 35–46 (2001).

154. J. Sumner, A. Encinas-Oropesa, N. J. Simms, J.R. Nicholls. Type II Hot Corrosion: Kinetics Studies of CMSX-4. *Oxydation of Metals* 80, 553–563 (2013).

155. R. McGill, W. John Tukey and A.W. Larsen. Variations of Box Plots. *The American Statistician* Vol. 32, No.1, 12–16 (1978).

156. S. Dowdy & S. Wearden. *Statistics for Research*. (Wiley. ISBN 0-471-08602-9 pp 230: 1983).

157. F. Emory; C. Dudley Johnstone. *Applied General Statistics*. (Pitman. ISBN 9780273403159).

158. R. J. Harris, *A primer of multivariate statistics*. (Lawrence Erlbaum Associates, Publishers: 2001).

159. J. Cohen, *Statistical power analysis for the behavioral sciences.* (Lawrence Erlbaum Associates: 1969).

160. D. M. Hawkins. On the Investigation of Alternative Regressions by Principal Component Analysis. *Journal of the Royal Statistical Society* Series C 22 (3), 275–286 (1973).

161. A. C. Rencher, *Methods of Multivariate Analysis*. (Wiley-Interscience 2nd Edition: 2002).

162. I. T. Jolliffe, *Principal Component Analysis*. (Aberdeen UK: Springer, 2nd ed. p.80: 2002).

163. D. J. Young, Simultaneous oxidation and carburisation of chromia forming alloys. *International Journal of Hydrogen Energy* 32, 3763–3769 (2007).

164. Z. Zeng, K. Natesan, M. Grimsditch. Effect of Oxide Scale Compositions on Metal Dusting Corrosion of Fe-Based Alloys. *Corrosion* 60, No. 7, 632–642 (2004).

165. A. Aguero, M. Gutierrez , L. Korcakova, T. T. M. Nguyen, B. Hinnemann, S. Saadi. Metal Dusting Protective Coatings. A Literature Review. *Oxidation of Metals* 76, 23–42 (2011).

166. S. Kurihara, S. Matsumoto, Y. Nishiyama, H. Okada, T. Osuki and H. Anada. Excellent resistance to metal dusting of a new ni alloy (UNS N06696) in severe carbonaceous environments. *NACE Corrosion 2012* (2012).

167. Y. Nishiyama, H. Okada and T. Osuki, S. Kurihara and S. Matsumoto. A prominent Ni-Cr-Si-Cu alloy resisting in metal dusting. *NACE Corrosion 2011* Paper no. 11158 (2011).

168. J.J. Hoffman, L. Minfa, W. R. Watkins, S.W.Dean. Proposed metal dusting mechanism in lower temperature, high steam Syn gas. *NACE Corrosion 2009* Paper no. 09161, (2009).

169. R. C. Schueler, Metal Dusting. *Hydrocarbon Processing* 73–75 (1972).

170. C. Schillmoller. Solving high temperature problems in oil refineries and petrochemical plants. *Chemical Engineering* 93, 83–87 (1986).

171. R.Milner. A metallurgical approach to combat metal dusting in reduction gas production. *NACE 1997 Canadian Region Western Conference*, (1997).

172. D. Young, *High Temperature Oxidation and Corrosion of Metals, 1st Edition*. (Elsevier Corrosion Series: 2008).

173. M.P Brady, G. Muralidharan, D.N. Leonard, J.A. Haynes, R.G. Weldon, R.D. England. Long term oxidation of candidate cast iron and stainless steel exhaust system alloys from 650°-800°C in air water vapor. *Oxidation of Metals* 82, 5-6, 359–381 (2014).

174. M.P. Brady, J. Magee, Y. Yamamot, D. Helmick and L. Wang. Co-optimization of wrought alumina-forming austenitic stainless steel composition ranges for high-temperature creep and oxidation/ corrosion resistance. *Materials Science Engineering* A-590, 101–115 (2014).

175. K. Riggs. Alumina -forming austenitic alloys resist high temperature corrosion. *Materials Performance* 54, no 9, 30–34 (2015).

176. S. Chevalier, & J. Favergeon, *French Activity on High Temperature Corrosion in Water Vapor,*. (Zurich, Switzerland: rans Tech Publications Ltd).

177. B. Bordenet. Influence of novel cycle concepts on the high-temperature corrosion of power plants. *Materials and Corrosion* 59, 361–366 (2008).

178. N. J. Simms, J. Sumner, T. Hussain and J. E. Oakey. Fireside issues in advanced power generation systems. *Materials Science and Technology* 29 (7), 804–812 (2013).

179. A.U. Syed, N.J. Simms, J.E. Oakey. Fireside corrosion of superheaters: Effects of air and oxy-firing of coal and biomass. *Fuel* 101, 62–73 (2012).

180. K. Harris, J. B. Wahl. Improved Single Crystal Superalloys, CMSX-4 (SLS)[La+Y] and CMSX-486. *TMS (The Minerals, Metals & Materials Society)* 45–52 (2004).

181. L. A. Hansen, F. J. Frandsen, K. D. Johansen, H. S. Sùrensen. Quantification of fusion in ashes from solid fuel combustion. *Thermochimica Acta* 326, 105–117 (1999).

182. W. Spiegel. Analyse des Rohgases und der Kesselablagerung zur Beurteilung der Ersatzbrennstoffqualität. *Energie aus Abfall, eds. K.J. Thomé-Kozmiensky, M. Beckmann, (Neuruppin, Germany: TK Verlag)* p. 441 (2008).

183. R. Boigelot. "Gazéification de Déchets Organiques dans un Réacteur à Flux Entrainé: Impact des Inorganiques sur le Fonctionnement du Réacteur et Choix des Céramiques Réfractaires". Université d'Orleans (2012).

184. M.B. Folgueras, M. Alonso, J.R. Folgueras. Modification of lignite ash fusion temperatures by the addition of different types of sewage sludge. *Fuel Processing Technology* 131, 348–355 (2015).

185. R. Backman, F. Goile, R. A. Khalil, A. Skreiberg, D.Todorovic, L. Sørum. The effect of peat ash addition to demolition wood on the formation of alkali, lead and zinc compounds at staged combustion conditions. *Fuel Processing Technology* 105, 20–27 (2013).

186. N. Otsuka, Y. Fukuda, Y. Kawahara, T. Hosoda. Laboratory corrosion tests for simulating fireside wastage of superheater materials in waste incinerators. *Materials and Corrosion* 51, Issue 4, 236–241 (2000).

187. B. Adams et al. Seghers Boiler Prism: A Proven Primary Measure against High Temperature Boiler Corrosion. *12th North American Waste to Energy Conference.Savannah, U.S.A* (2004).

188. T. R. Miles, L. R. Baxter, R. W. Bryers, B. M. Jenkins, L.L. Oden. *Alkali Deposits Found In Biomass Power Plants, A Preliminary Investigation of their Extent and Nature*. (National Renewable Energy Laboratory: 1995).

189. M. Reinmöller, M. Klinger, M. Schreiner, H. Gutte. Relationship between ash fusion temperatures of ashes from hard coal, brown coal, and biomass and mineral phases under different atmospheres:

A combined FactSageTM computational and network theoretical approach. *Fuel* 151, 118–123 (2015).

190. S. Vargas, F.J. Frandsen, K. Dam-Johansen. Rheological properties of high-temperature melts of coal ashes and other silicates. *Progress in Energy and Combustion Science* 27, 237–429 (2001).

191. Y.Kawahara. Evaluation of high-temperature corrosion life using temperature gradient corrosion test with thermal cycle component in waste combustion enviroments. *Materials and Corrosion* 57 (1), 60–72 (2006).

192. D. Lindberg, J. N., M. Engblom, P. Yrjas, T. Laurén, M. Hupa. Effect of temperature gradient on composition and morphology of synthetic chlorine-containing biomass boiler deposits. *Fuel Processing Technology* 141, 285–298 (2016).

193. G.R. Holcomb, B.S. Covino and J.H. Russel. Oxidation in a temperature gradient. *15 Annual Conference on Fossil Energy Materials* Oak Ridge National Laboratory, (2001).

194. G.R. Holcomb. Hot corrosion in a temperature gradient. *Materials and Corrosion* 51 (8), 564–569 (2000).

195. C. W. Bale, S. A. Chartrand, G. Degterov, K.Eriksson, R. B.Hack , J. Mahfoud & S. Petersen, *Calphad 26. (2)* 189–228 (2002).

196. D. Bankiewicz, "Corrosion behaviour of boiler tube materials during combustion of fuels containing Zn and Pb". Åbo Akademi University , Turku, Finland (2012).

197. *ASME Section VIII Division 1. Boiler & Pressure Vessel Code , Rules for Construction of Pressure Vessels. (American Society of Mechanical Engineers, ASME. July 1, 2011).*

198. *NF EN 12952-3 Chaudières à tubes d’eau et installations auxiliaires - Partie 3 : conception et calcul des parties sous pression de la chaudière. (AFNOR - Février 2012).*

199. S-H Lee, N. J. Themelis and Marco J. Castaldi. High-Temperature Corrosion in Waste-to-Energy Boilers. *Journal of Thermal Spray Technology* 16(1), 1–7 (2007).

200. Y. Kawahara, K. Takahashi, Y. Nakagawa T. Hososda & T. Mizuko. Demonstration Test of New Corrosion-Resistant Superheater Tubings in a High-Eficiency Waste-To-Energy Plant. *Corrosion 2000* p 265 (2000).

201. Y. Kawahara. Application of High Temperature Corrosion-Resistant Materials and Coatings Under Severe Corrosive Environment in Waste-to-Energy Boilers. *Journal of Thermal Spray Technology* 16(2), 202–213 (2007).

202. Y. Kawahara, & M. Kira. Effect of Physical Properties of Molten Deposits on High Temperature Corrosion of Alloys in Waste Incineration Environment,. *Zairyo-to-Kankyo* 46(1), 8 (1997).

203. N.Otsuka, Y. Nishiyama, S. Hayashi, Y. Matsuda, K. Fujita, S. Taniguchi. Laboratory and field corrosion tests of Ni-Cr-No-Nb coated T22 steel in waste incinerator corrosion enviroments. *Corrosion* 2002, Paper no. 02389 (2002).

Appendix I

Metal Dusting (MLr)

A. Analyzes PCA$_1$ and CT$_1$ applied to the initial domain

Summary Statistics

Variable	**Observations**	**Minimum**	**Maximum**	**Mean**	**Std. deviation**
MLr (mg/cm^{2}h)	1389	0.0	0.7	0.0	0.1
Time (h)	1389	8.0	15958.0	3614.4	3583.7
Frequency (1/h)	1389	0.0	1.3	0.1	0.4
1/T (K^{-1})	1389	10.3	14.9	11.3	0.5
P$_{Internal}$ (bar)	1389	1.0	21.0	3.9	6.1
pH$_2$O (bar)	1389	0.0	7.0	0.8	1.8
pCO (bar)	1389	0.2	2.7	0.9	0.9
pH$_2$ (bar)	1389	0.3	10.3	2.0	3.1
pCO$_2$ (bar)	1389	0.0	0.8	0.2	0.3
a$_C$	1389	5.7	9904.0	124.5	913.6
pO$_2$ (bar)	1389	0.0	0.0	0.0	0.0

Correlation Matrix

Variables	**MLr (mg/cm2h)**	**Frequency (1/h)**	**1/T (K^{-1})**	**P$_{Internal}$ (bar)**	**pH$_2$O (bar)**	**pCO (bar)**	**pH$_2$ (bar)**	**pCO$_2$ (bar)**	**a$_C$**	**pO$_2$ (bar)**
MLr (mg/cm^{2}h)	**1.00**	**0.29**	**-0.22**	**-0.10**	**-0.09**	**-0.07**	**-0.10**	**-0.12**	-0.02	**0.16**
Frequency (1/h)	**0.29**	**1.00**	**-0.43**	**-0.15**	**-0.14**	**-0.09**	**-0.16**	**-0.18**	-0.03	**0.42**
1/T (K^{-1})	**-0.22**	**-0.43**	**1.00**	**0.34**	**0.34**	**0.24**	**0.35**	**0.28**	**0.66**	**-0.47**
P$_{Internal}$ (bar)	**-0.10**	**-0.15**	**0.34**	**1.00**	**0.98**	**0.96**	**1.00**	**0.95**	-0.05	0.03
pH$_2$O (bar)	**-0.09**	**-0.14**	**0.34**	**0.98**	**1.00**	**0.90**	**0.97**	**0.86**	-0.05	0.01
pCO (bar)	**-0.07**	**-0.09**	**0.24**	**0.96**	**0.90**	**1.00**	**0.95**	**0.98**	**-0.07**	**0.11**
pH$_2$ (bar)	**-0.10**	**-0.16**	**0.35**	**1.00**	**0.97**	**0.95**	**1.00**	**0.95**	-0.04	0.01
pCO$_2$ (bar)	**-0.12**	**-0.18**	**0.28**	**0.95**	**0.86**	**0.98**	**0.95**	**1.00**	**-0.06**	**0.11**
a$_C$	-0.02	-0.03	**0.66**	-0.05	-0.05	**-0.07**	-0.04	**-0.06**	**1.00**	**-0.07**
pO$_2$ (bar)	**0.16**	**0.42**	**-0.47**	0.03	0.01	**0.11**	0.01	**0.11**	**-0.07**	**1.00**

Values in bold are different from 0 with a significance level alpha=0.05

B. Analyzes PCA_2 and CT_2 applied to the final domain

Summary Statistics

Variable	Observations	Minimum	Maximum	Mean	Std. deviation
MLr (mg/cm^2h)	991	0.0	0.5	0.0	0.0
Time (h)	991	12.0	15958.0	3875.8	3701.9
Frequency (1/h)	991	0.0	0.1	0.0	0.0
1/T (K^{-1})	991	10.3	11.9	11.2	0.3
$P_{Internal}$ (bar)	991	0.0	0.1	0.0	0.0
pH_2O (bar)	991	0.2	0.7	0.5	0.2
pCO (bar)	991	0.3	0.8	0.5	0.2
pH_2 (bar)	991	0.0	0.1	0.0	0.0
pCO_2 (bar)	991	5.7	104.8	43.2	27.4
a_C	991	0.0	0.0	0.0	0.0
pO_2 (bar)	991	0.0	0.5	0.0	0.0

Correlation Matrix

Variables	MLr (mg/cm2h)	Frequency (1/h)	1/T (K^{-1})	pH_2O (bar)	pCO (bar)	pH_2 (bar)	pCO_2 (bar)	a_C	pO_2 (bar)
MLr (mg/cm^2h)	**1.00**	**0.17**	**-0.19**	**-0.07**	0.05	-0.02	**-0.14**	**-0.09**	0.03
Frequency (1/h)	**0.17**	**1.00**	0.02	0.05	**-0.24**	**0.24**	**-0.18**	**-0.19**	0.05
1/T (K^{-1})	**-0.19**	0.02	**1.00**	**0.42**	**-0.29**	**0.31**	**-0.40**	**0.45**	**-0.57**
pH_2O (bar)	**-0.07**	0.05	**0.42**	**1.00**	**-0.29**	**0.23**	**-0.20**	**-0.48**	**0.14**
pCO (bar)	0.05	**-0.24**	**-0.29**	**-0.29**	**1.00**	**-0.99**	**0.55**	**0.15**	**0.17**
pH_2 (bar)	-0.02	**0.24**	**0.31**	**0.23**	**-0.99**	**1.00**	**-0.65**	**-0.12**	**-0.27**
pCO_2 (bar)	**-0.14**	**-0.18**	**-0.40**	**-0.20**	**0.55**	**-0.65**	**1.00**	0.02	**0.70**
a_C	**-0.09**	**-0.19**	**0.45**	**-0.48**	**0.15**	**-0.12**	0.02	**1.00**	**-0.46**
pO_2 (bar)	0.03	0.05	**-0.57**	**0.14**	**0.17**	**-0.27**	**0.70**	**-0.46**	**1.00**

Values in bold are different from 0 with a significance level alpha=0.05

C. Analyzes PCA_3 and CT_3 applied to the initial domain

Summary Statistics

Variables (wt%)	**Observations**	**Minimum**	**Maximum**	**Mean**	**Std. deviation**
MLr (mg/cm^{2}h)	1389	0.0	0.7	0.0	0.1
Fe	1389	0.0	95.7	24.6	27.3
Ni	1389	0.0	96.0	46.1	22.8
Cr	1389	0.0	46.0	21.5	7.7
Mo	1389	0.0	16.0	1.4	3.4
Co	1389	0.0	54.0	2.7	7.8
Cu	1389	0.0	32.2	0.7	3.0
Al	1389	0.0	30.0	1.3	2.8
Si	1389	0.0	2.8	0.5	0.7
W	1389	0.0	15.0	0.1	1.2
Nb	1389	0.0	3.7	0.1	0.6
Ti	1389	0.0	2.4	0.2	0.4

Correlation Matrix

Variables (wt%)	**MLr (mg/cm^{2}h)**	**Fe**	**Ni**	**Cr**	**Mo**	**Co**	**Cu**	**Al**	**Si**	**W**	**Nb**	**Ti**
MLr (mg/cm^{2}h)	**1.00**	**0.29**	**-0.24**	**-0.34**	**-0.08**	**-0.06**	**0.38**	**-0.06**	0.01	-0.02	-0.04	**-0.11**
Fe	**0.29**	**1.00**	**-0.89**	**-0.47**	**-0.27**	**-0.28**	**0.17**	**-0.17**	**0.09**	**-0.09**	**-0.11**	**-0.11**
Ni	**-0.24**	**-0.89**	**1.00**	**0.24**	**0.15**	**-0.09**	**-0.20**	**0.23**	**-0.27**	-0.03	**0.08**	0.00
Cr	**-0.34**	**-0.47**	**0.24**	**1.00**	**-0.12**	**0.13**	**-0.25**	**-0.24**	**0.19**	-0.03	0.05	**0.10**
Mo	**-0.08**	**-0.27**	**0.15**	**-0.12**	**1.00**	**0.24**	**-0.09**	**-0.10**	**-0.18**	**0.15**	**0.28**	**0.20**
Co	**-0.06**	**-0.28**	**-0.09**	**0.13**	**0.24**	**1.00**	**-0.08**	**-0.10**	**0.40**	**0.27**	**-0.07**	**0.20**
Cu	**0.38**	**0.17**	**-0.20**	**-0.25**	**-0.09**	**-0.08**	**1.00**	**-0.10**	**0.05**	-0.03	**-0.05**	-0.03
Al	**-0.06**	**-0.17**	**0.23**	**-0.24**	**-0.10**	**-0.10**	**-0.10**	**1.00**	**-0.23**	-0.05	-0.03	-0.03
Si	0.01	**0.09**	**-0.27**	**0.19**	**-0.18**	**0.40**	**0.05**	**-0.23**	**1.00**	-0.05	**-0.10**	**-0.08**
W	-0.02	**-0.09**	-0.03	-0.03	**0.15**	**0.27**	-0.03	-0.05	-0.05	**1.00**	-0.03	-0.05
Nb	-0.04	**-0.11**	**0.08**	0.05	**0.28**	**-0.07**	**-0.05**	-0.03	**-0.10**	-0.03	**1.00**	-0.01
Ti	**-0.11**	**-0.11**	0.00	**0.10**	**0.20**	**0.20**	-0.03	-0.03	**-0.08**	-0.05	-0.01	**1.00**

Values in bold are different from 0 with a significance level alpha=0.05

D. Analyzes PCA_4 and CT_4 applied to the final domain

Summary Statistics

Variables (wt%)	Observations	Minimum	Maximum	Mean	Std. deviation
MLr (mg/cm^2h)	991	0.000	0.524	0.011	0.048
Fe	991	0.000	95.670	26.175	28.857
Ni	991	0.000	90.000	45.960	23.008
Cr	991	0.000	46.000	21.703	7.794
Mo	991	0.000	16.000	1.416	3.509
Co	991	0.000	30.000	1.905	6.185
Cu	991	0.000	10.000	0.204	1.234
Al	991	0.000	6.000	1.002	1.361
Si	991	0.000	2.800	0.437	0.701
W	991	0.000	13.970	0.113	0.925
Nb	991	0.000	3.600	0.119	0.553
Ti	991	0.000	2.400	0.243	0.418

Correlation Matrix

Variables (wt%)	MLr (mg/cm^2h)	Fe	Ni	Cr	Mo	Co	Cu	Al	Si	W	Nb	Ti
MLr (mg/cm^2h)	**1.00**	**0.30**	**-0.21**	**-0.46**	**-0.06**	-0.06	**0.55**	**-0.13**	-0.06	-0.03	-0.04	**-0.10**
Fe	**0.30**	**1.00**	**-0.93**	**-0.60**	**-0.26**	**-0.25**	**0.13**	**-0.09**	0.04	**-0.09**	**-0.13**	**-0.15**
Ni	**-0.21**	**-0.93**	**1.00**	**0.41**	**0.16**	-0.01	-0.04	0.06	**-0.18**	**0.07**	**0.10**	0.03
Cr	**-0.46**	**-0.60**	**0.41**	**1.00**	**-0.16**	**0.09**	**-0.41**	**0.18**	**0.13**	-0.05	0.04	**0.08**
Mo	**-0.06**	**-0.26**	**0.16**	**-0.16**	**1.00**	**0.23**	-0.06	**-0.16**	**-0.15**	**0.30**	**0.30**	**0.22**
Co	-0.06	**-0.25**	-0.01	**0.09**	**0.23**	**1.00**	-0.04	**-0.10**	**0.41**	-0.01	**-0.07**	**0.35**
Cu	**0.55**	**0.13**	-0.04	**-0.41**	-0.06	-0.04	**1.00**	**-0.11**	**-0.09**	-0.02	-0.04	-0.04
Al	**-0.13**	**-0.09**	0.06	**0.18**	**-0.16**	**-0.10**	**-0.11**	**1.00**	**-0.29**	**-0.07**	-0.05	0.04
Si	-0.06	0.04	**-0.18**	**0.13**	**-0.15**	**0.41**	**-0.09**	**-0.29**	**1.00**	**-0.07**	**-0.09**	-0.03
W	-0.03	**-0.09**	**0.07**	-0.05	**0.30**	-0.01	-0.02	**-0.07**	**-0.07**	**1.00**	-0.03	-0.04
Nb	-0.04	**-0.13**	**0.10**	0.04	**0.30**	**-0.07**	-0.04	-0.05	**-0.09**	-0.03	**1.00**	-0.02
Ti	**-0.10**	**-0.15**	0.03	**0.08**	**0.22**	**0.35**	-0.04	0.04	-0.03	-0.04	-0.02	**1.00**

Values in bold are different from 0 with a significance level alpha=0.05

E. CT_5: correlation test applied to atmosphere conditions for Fe-based alloys

Summary Statistics

Variables (wt%)	**Observations**	**Minimum**	**Maximum**	**Mean**	**Std. deviation**
MLr (mg/cm^{2}h)	132	0.00	0.41	0.02	0.07
Frequency (1/h)	132	0.00	0.08	0.03	0.02
1/T (K^{-1})	132	10.28	11.86	11.35	0.32
$P_{Internal}$ (bar)	132		1 bar		
pH_2O (bar)	132	0.01	0.06	0.02	0.01
pCO (bar)	132	0.24	0.70	0.37	0.19
pH_2 (bar)	132	0.25	0.74	0.60	0.21
pCO_2 (bar)	132				
a_C	132	5.68	57.90	38.78	13.07
pO_2 (bar)	132	1.2E-27	1.3E-24	7.1E-26	2.8E-25

Correlation Matrix

Variables (wt%)	**MLr (mg/cm^{2}h)**	**Frequency (1/h)**	**1/T (K^{-1})**	**pH_2O (bar)**	**pCO (bar)**	**pH_2 (bar)**	**pCO_2 (bar)**	**a_C**	**pO_2 (bar)**
MLr (mg/cm^{2}h)	**1.00**	**-0.22**	**-0.27**	-0.01	**-0.21**	**0.21**		**-0.40**	0.16
Frequency (1/h)	**-0.22**	**1.00**	**0.26**	-0.05	**-0.68**	**0.69**		-0.13	-0.14
1/T (K^{-1})	**-0.27**	**0.26**	**1.00**	**0.58**	-0.08	0.05		**0.21**	**-0.79**
pH_2O (bar)	-0.01	-0.05	**0.58**	**1.00**	**-0.19**	0.15		**-0.50**	-0.03
pCO (bar)	**-0.21**	**-0.68**	-0.08	**-0.19**	**1.00**	**-1.00**		**0.70**	-0.14
pH_2 (bar)	**0.21**	**0.69**	0.05	0.15	**-1.00**	**1.00**		**-0.69**	0.14
pCO_2 (bar)									
a_C	**-0.40**	-0.13	**0.21**	**-0.50**	**0.70**	**-0.69**		**1.00**	**-0.59**
pO_2 (bar)	0.16	-0.14	**-0.79**	-0.03	-0.14	0.14		**-0.59**	**1.00**

Values in bold are different from 0 with a significance level alpha=0.05

F. CT_6: correlation tests applied to atmosphere conditions for Fe/Ni-based alloys

Summary Statistics

Variables (wt%)	**Observations**	**Minimum**	**Maximum**	**Mean**	**Std. deviation**
MLr (mg/cm^2h)	261	0.00	0.52	0.02	0.08
Frequency (1/h)	261	0.00	0.08	0.01	0.02
1/T (K^{-1})	261	10.83	11.86	11.33	0.39
$P_{Internal}$ (bar)	261	1 bar			
pH_2O (bar)	261	0.01	0.06	0.03	0.02
pCO (bar)	261	0.18	0.70	0.44	0.19
pH_2 (bar)	261	0.25	0.80	0.51	0.21
pCO_2 (bar)	261	0.00	0.12	0.03	0.04
a_C	261	10.00	104.76	37.30	25.39
pO_2 (bar)	261	2.0E-28	6.1E-25	1.1E-25	2.2E-25

Correlation Matrix

Variables (wt%)	**MLr (mg/cm^2h)**	**Frequency (1/h)**	**1/T (K^{-1})**	**pH_2O (bar)**	**pCO (bar)**	**pH_2 (bar)**	**pCO_2 (bar)**	**a_C**	**pO_2 (bar)**
MLr (mg/cm^2h)	**1.00**	**-0.28**	**0.25**	**-0.36**	**-0.26**	**0.37**	**-0.30**	-0.08	-0.06
Frequency (1/h)	**0.25**	**-0.54**	**1.00**	**-0.17**	**-0.27**	-0.11	**0.16**	**-0.20**	-0.09
1/T (K^{-1})	**-0.36**	**0.35**	**-0.17**	**1.00**	**0.64**	**-0.39**	**0.40**	**-0.54**	**0.36**
H_2O (bar)	**-0.26**	**0.39**	**-0.27**	**0.64**	**1.00**	-0.03	-0.01	**-0.22**	**-0.35**
pCO (bar)	**0.37**	-0.11	-0.11	**-0.39**	-0.03	**1.00**	**-0.98**	**0.46**	**-0.13**
pH_2 (bar)	**-0.30**	0.06	**0.16**	**0.40**	-0.01	**-0.98**	**1.00**	**-0.59**	**0.18**
pCO_2 (bar)	-0.08	0.05	**-0.20**	**-0.54**	**-0.22**	**0.46**	**-0.59**	**1.00**	**-0.15**
a_C	-0.06	**0.13**	-0.09	**0.36**	**-0.35**	**-0.13**	**0.18**	**-0.15**	**1.00**
pO_2 (bar)	0.02	-0.02	-0.07	**-0.61**	-0.06	**0.42**	**-0.55**	**0.92**	**-0.49**

Values in bold are different from 0 with a significance level alpha=0.05

G. CT_7: correlation test applied to atmosphere conditions for Ni-based alloys

Summary Statistics

Variables (wt%)	**Observations**	**Minimum**	**Maximum**	**Mean**	**Std. deviation**
MLr (mg/cm^2h)	598	0.00	0.03	0.00	0.00
	598	72.00	15938.00	4880.35	3688.40
Frequency (1/h)	598	0.00	0.03	0.00	0.01
1/T (K^{-1})	598	10.83	11.86	11.19	0.28
$P_{Internal}$ (bar)	598	1 bar			
pH_2O (bar)	598	0.01	0.06	0.01	0.01
pCO (bar)	598	0.18	0.70	0.49	0.22
pH_2 (bar)	598	0.25	0.80	0.46	0.24
pCO_2 (bar)	598	0.00	0.12	0.04	0.03
a_C	598	10.0	104.8	46.9	30.2
pO_2 (bar)	598	2.0E-28	6.1E-25	8.4E-26	1.9E-25

Correlation Matrix

Variables (wt%)	**MLr (mg/cm^2h)**	**Frequency (1/h)**	**1/T (K^{-1})**	**pH_2O (bar)**	**pCO (bar)**	**pH_2 (bar)**	**pCO_2 (bar)**	**a_C**	**pO_2 (bar)**
MLr (mg/cm^2h)	**1.00**	-0.08	-0.02	0.02	0.00	**-0.16**	**0.17**	**-0.14**	0.04
Frequency (1/h)	-0.02	**-0.29**	**1.00**	**-0.33**	**0.32**	**0.10**	**-0.17**	**0.45**	**-0.38**
1/T (K^{-1})	0.02	0.05	**-0.33**	**1.00**	-0.02	**-0.25**	**0.28**	**-0.33**	**0.65**
H_2O (bar)	0.00	**-0.39**	**0.32**	-0.02	**1.00**	**-0.47**	**0.41**	-0.05	**-0.64**
pCO (bar)	**-0.16**	**0.37**	**0.10**	**-0.25**	**-0.47**	**1.00**	**-0.99**	**0.56**	**0.17**
pH_2 (bar)	**0.17**	**-0.33**	**-0.17**	**0.28**	**0.41**	**-0.99**	**1.00**	**-0.66**	**-0.13**
pCO_2 (bar)	**-0.14**	0.02	**0.45**	**-0.33**	-0.05	**0.56**	**-0.66**	**1.00**	0.01
a_C	0.04	**0.27**	**-0.38**	**0.65**	**-0.64**	**0.17**	**-0.13**	0.01	**1.00**
pO_2 (bar)	**-0.09**	**-0.24**	**0.63**	**-0.53**	**0.41**	**0.17**	**-0.29**	**0.82**	**-0.49**

Values in bold are different from 0 with a significance level alpha=0.05

H. CT$_8$: correlation test applied to alloy elements for Fe-based alloys

Summary Statistics

Variables (wt%)	Observations	Minimum	Maximum	Mean	Std. deviation
MLr (mg/cm^{2}h)	132.0	0.0	0.4	0.0	0.1
Fe	132.0	69.6	95.7	84.2	8.1
Ni	132.0	0.0	0.7	0.3	0.3
Cr	132.0	2.1	28.0	12.5	7.0
Mo	132.0	0.0	1.1	0.6	0.5
Co	132.0	0.0	0.0	0.0	0.0
Cu	132.0	0.0	0.3	0.0	0.1
Al	132.0	0.0	6.0	1.5	2.3
Si	132.0	0.0	2.1	0.3	0.2
W	132.0	0.0	0.0	0.0	0.0
Nb	132.0	0.0	0.2	0.0	0.0
Ti	132.0	0.0	0.5	0.1	0.2

Correlation Matrix

Variables (wt%)	MLr (mg/cm^{2}h)	Fe	Ni	Cr	Mo	Co	Cu	Al	Si	W	Nb	Ti
MLr (mg/cm^{2}h)	**1.00**	**0.41**	**-0.25**	**-0.44**	**0.31**		**0.85**	**-0.21**	**0.26**		-0.09	**-0.18**
Fe	**0.41**	**1.00**	**0.25**	**-0.99**	**0.97**		**0.44**	**-0.83**	**0.39**		0.10	**-0.62**
Ni	**-0.25**	**0.25**	**1.00**	**-0.21**	**0.45**		**-0.30**	**-0.47**	0.11		0.02	**-0.51**
Cr	**-0.44**	**-0.99**	**-0.21**	**1.00**	**-0.95**		**-0.47**	**0.76**	**-0.37**		-0.02	**0.58**
Mo	**0.31**	**0.97**	**0.45**	**-0.95**	**1.00**		**0.32**	**-0.87**	**0.41**		0.14	**-0.72**
Co												
Cu	**0.85**	**0.44**	**-0.30**	**-0.47**	**0.32**		**1.00**	**-0.21**	**0.29**		**-0.18**	**-0.17**
Al	**-0.21**	**-0.83**	**-0.47**	**0.76**	**-0.87**		**-0.21**	**1.00**	**-0.48**		**-0.36**	**0.72**
Si	**0.26**	**0.39**	0.11	**-0.37**	**0.41**		**0.29**	**-0.48**	**1.00**		-0.03	**-0.62**
W												
Nb	-0.09	0.10	0.02	-0.02	0.14		**-0.18**	**-0.36**	-0.03		**1.00**	**-0.30**
Ti	**-0.18**	**-0.62**	**-0.51**	**0.58**	**-0.72**		**-0.17**	**0.72**	**-0.62**		**-0.30**	**1.00**

Values in bold are different from 0 with a significance level alpha=0.05

I. CT_9: correlation tests applied to alloy elements for Fe/Ni-based alloys

Summary Statistics

Variables (wt%)	Observations	Minimum	Maximum	Mean	Std. deviation
MLr (mg/cm^2h)	261	0.0	0.5	0.0	0.1
Fe	261	4.0	80.0	40.2	18.5
Ni	261	8.7	49.4	32.4	9.7
Cr	261	0.0	30.3	21.4	7.9
Mo	261	0.0	4.2	0.1	0.6
Co	261	0.0	30.0	3.2	9.3
Cu	261	0.0	10.0	0.8	2.4
Al	261	0.0	1.5	0.3	0.5
Si	261	0.0	2.8	1.1	1.0
W	261	0.0	0.0	0.0	0.0
Nb	261	0.0	0.8	0.0	0.1
Ti	261	0.0	1.0	0.3	0.4

Correlation Matrix

Variables (wt%)	MLr (mg/cm^2h)	Fe	Ni	Cr	Mo	Co	Cu	Al	Si	Nb	Ti
MLr (mg/cm^2h)	**1.00**	**0.37**	**-0.14**	**-0.70**	-0.05	-0.10	**0.69**	**-0.19**	**-0.31**	-0.09	**-0.20**
Fe	**0.37**	**1.00**	**-0.69**	**-0.69**	-0.05	**-0.68**	**0.38**	0.05	**-0.78**	-0.06	0.06
Ni	**-0.14**	**-0.69**	**1.00**	**0.30**	0.03	0.07	-0.09	**-0.14**	**0.50**	0.03	-0.02
Cr	**-0.70**	**-0.69**	**0.30**	**1.00**	0.01	**0.29**	**-0.79**	0.11	**0.57**	**0.21**	0.08
Mo	-0.05	-0.05	0.03	0.01	**1.00**	-0.01	-0.06	-0.01	-0.02	-0.03	**0.13**
Co	-0.10	**-0.68**	0.07	**0.29**	-0.01	**1.00**	-0.11	-0.08	**0.57**	-0.10	**-0.25**
Cu	**0.69**	**0.38**	-0.09	**-0.79**	-0.06	-0.11	**1.00**	**-0.16**	**-0.35**	-0.09	**-0.15**
Al	**-0.19**	0.05	**-0.14**	0.11	-0.01	-0.08	**-0.16**	**1.00**	-0.06	**-0.15**	**0.88**
Si	**-0.31**	**-0.78**	**0.50**	**0.57**	-0.02	**0.57**	**-0.35**	-0.06	**1.00**	-0.09	**-0.15**
Nb	-0.09	-0.06	0.03	**0.21**	-0.03	-0.10	-0.09	**-0.15**	-0.09	**1.00**	**-0.20**
Ti	**-0.20**	0.06	-0.02	0.08	**0.13**	**-0.25**	**-0.15**	**0.88**	**-0.15**	**-0.20**	**1.00**

Values in bold are different from 0 with a significance level alpha=0.05

J. CT_{10}: correlation test applied to alloy elements for Ni-based alloys

Summary Statistics

Variables (wt%)	Observations	Minimum	Maximum	Mean	Std. deviation
MLr (mg/cm^2h)	598	0.0	0.0	0.0	0.0
Fe	598	0.0	35.0	7.3	5.7
Ni	598	52.0	90.0	61.9	6.3
Cr	598	0.0	46.0	23.8	6.4
Mo	598	0.0	16.0	2.2	4.4
Co	598	0.0	20.0	1.8	5.0
Cu	598	0.0	10.0	0.1	0.9
Al	598	0.0	3.7	1.1	1.1
Si	598	0.0	1.4	0.2	0.2
W	598	0.0	14.0	0.2	1.2
Nb	598	0.0	3.6	0.2	0.7
Ti	598	0.0	2.4	0.3	0.5

Correlation Matrix

Variables (wt%)	MLr (mg/cm^2h)	Fe	Ni	Cr	Mo	Co	Cu	Al	Si	W	Nb	Ti
MLr (mg/cm^2h)	**1.00**	0.05	**0.30**	**-0.27**	-0.06	-0.05	0.06	0.00	0.01	-0.04	-0.01	-0.04
Fe	0.05	**1.00**	-0.01	**-0.19**	**-0.46**	**-0.40**	**0.18**	-0.06	0.03	**-0.10**	**-0.17**	**-0.35**
Ni	**0.30**	-0.01	**1.00**	**-0.42**	**-0.26**	**-0.49**	**0.12**	**0.09**	**0.19**	**-0.09**	-0.04	**-0.37**
Cr	**-0.27**	**-0.19**	**-0.42**	**1.00**	**-0.37**	**-0.18**	**-0.34**	**0.11**	**-0.20**	**-0.13**	-0.04	-0.05
Mo	-0.06	**-0.46**	**-0.26**	**-0.37**	**1.00**	**0.42**	-0.04	**-0.28**	-0.01	**0.29**	**0.29**	**0.25**
Co	-0.05	**-0.40**	**-0.49**	**-0.18**	**0.42**	**1.00**	0.00	**-0.08**	**0.12**	-0.01	**-0.09**	**0.78**
Cu	0.06	**0.18**	**0.12**	**-0.34**	-0.04	0.00	**1.00**	**-0.09**	-0.05	-0.02	-0.03	-0.01
Al	0.00	-0.06	**0.09**	**0.11**	**-0.28**	**-0.08**	**-0.09**	**1.00**	**-0.33**	**-0.13**	-0.08	**-0.15**
Si	0.01	0.03	**0.19**	**-0.20**	-0.01	**0.12**	-0.05	**-0.33**	**1.00**	-0.08	**-0.08**	**0.12**
W	-0.04	**-0.10**	**-0.09**	**-0.13**	**0.29**	-0.01	-0.02	**-0.13**	-0.08	**1.00**	-0.04	-0.05
Nb	-0.01	**-0.17**	-0.04	-0.04	**0.29**	**-0.09**	-0.03	-0.08	**-0.08**	-0.04	**1.00**	-0.02
Ti	-0.04	**-0.35**	**-0.37**	-0.05	**0.25**	**0.78**	-0.01	**-0.15**	**0.12**	-0.05	-0.02	**1.00**

Values in bold are different from 0 with a significance level alpha=0.05

Appendix II

Metal Dusting (IT) and (AIMLr)

A. PCA_5 and PCA_6 applied on IT and AIMLr data distribution.
a) PCA_5 applied on atmosphere conditions b) PCA_6 applied on alloy composition

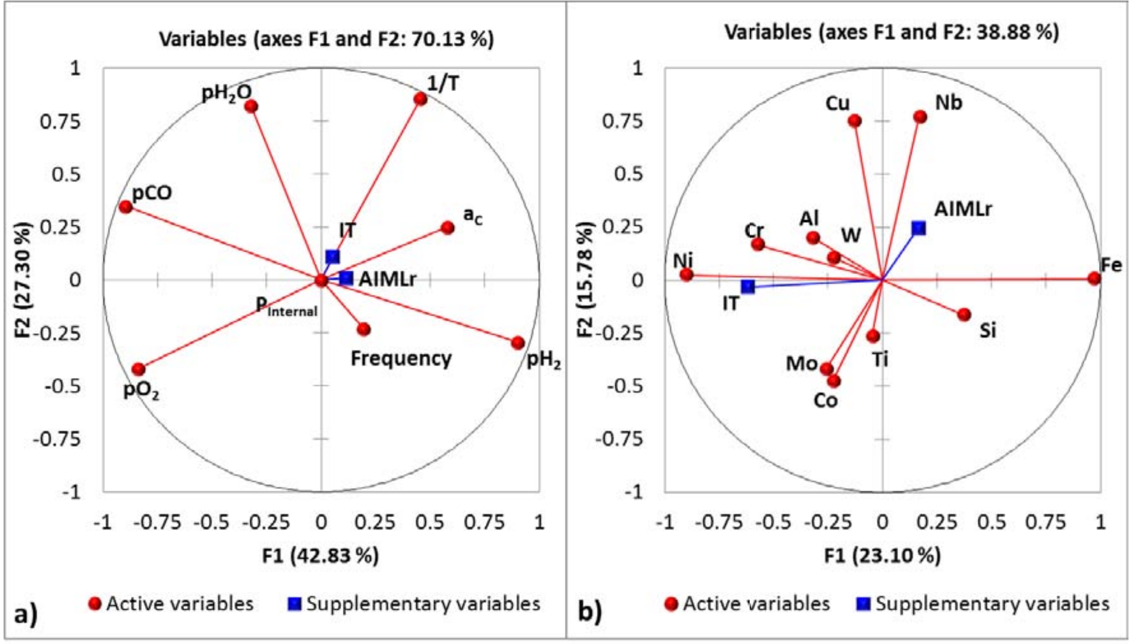

PCA5 Summary Statistics

Variables (wt%)	Observations	Minimum	Maximum	Mean	Std. deviation
AIMLr (mg/cm^{2}h)	58	0.0	0.1	0.0	0.0
IT (h)	58	12.0	7159.2	2242.1	1818.0
Frequency (1/h)	58	0.001	0.081	0.010	0.017
1/T (K^{-1})	58	10.277	11.860	11.286	0.426
$P_{Internal}$ (bar)	58		1 bar		
pH_2O (bar)	58	0.009	0.060	0.028	0.017
pCO (bar)	58	0.182	0.600	0.357	0.150
pH_2 (bar)	58	0.260	0.795	0.589	0.193
a_C	58	5.680	104.758	32.885	29.893
pO_2 (bar)	58	2.0E-28	1.1E-24	1.5E-25	2.7E-25

PCA5 Correlation Matrix

Variables (wt%)	Frequency (1/h)	1/T (K^{-1})	pH_2O (bar)	pCO (bar)	pH_2 (bar)	pCO_2 (bar)	a_C	pO_2 (bar)
AIMLr (mg/cm^{2}h)	-0.09	0.01	-0.02	-0.11	0.12	0.01	-0.17	-0.02
IT (h)	-0.49	0.04	-0.02	-0.02	0.01	0.19	-0.11	-0.02
Frequency (1/h)	**1.00**	0.03	-0.18	-0.17	0.16	-0.03	-0.05	**1.00**
1/T (K^{-1})	0.03	**1.00**	0.53	-0.09	0.13	0.52	-0.69	0.03
H_2O (bar)	-0.18	0.53	**1.00**	0.46	-0.40	-0.29	-0.12	-0.18
pCO (bar)	-0.17	-0.09	0.46	**1.00**	-1.00	-0.27	0.61	-0.17
pH_2 (bar)	0.16	0.13	-0.40	-1.00	**1.00**	0.26	-0.65	0.16
a_C	-0.03	0.52	-0.29	-0.27	0.26	**1.00**	-0.43	-0.03
pO_2 (bar)	-0.05	-0.69	-0.12	0.61	-0.65	-0.43	**1.00**	-0.05

Values in bold are different from 0 with a significance level alpha=0.05

PCA6 Summary Statistics

Variables (wt%)	Observations	Minimum	Maximum	Mean	Std. deviation
MLr (mg/cm^{2}h)	58	0.0	0.1	0.0	0.0
IT (h)	58	12.0	7159.2	2242.1	1818.0
Fe	58	0.9	89.2	33.0	28.9
Ni	58	0.0	77.1	43.4	25.8
Cr	58	8.6	29.0	20.1	5.2
Mo	58	0.0	15.7	0.7	2.6
Co	58	0.0	12.5	0.3	1.8
Cu	58	0.0	0.7	0.0	0.2
Al	58	0.0	6.0	0.8	1.2
Si	58	0.0	2.8	0.4	0.6
W	58	0.0	14.0	0.3	2.0
Nb	58	0.0	0.2	0.0	0.0
Ti	58	0.0	1.0	0.2	0.2

PCA6 Correlation Matrix

Variables (wt%)	Fe	Ni	Cr	Mo	Co	Cu	Al	Si	W	Nb	Ti
AIMLr (mg/cm^{2}h)	0.11	-0.05	-0.30	-0.10	-0.08	0.26	0.03	0.09	-0.06	0.25	-0.09
IT (h)	-0.61	0.51	0.64	0.20	0.29	0.14	0.05	0.04	0.01	-0.05	0.09
Fe	**1.00**	-0.97	-0.50	-0.18	-0.17	-0.11	-0.19	0.25	-0.17	0.17	-0.04
Ni	-0.97	**1.00**	0.35	0.10	0.06	0.09	0.15	-0.28	0.11	-0.16	-0.02
Cr	-0.50	0.35	**1.00**	-0.16	0.04	0.16	0.20	0.03	0.09	-0.06	0.21
Mo	-0.18	0.10	-0.16	**1.00**	0.50	-0.07	-0.07	-0.15	0.02	-0.07	0.08
Co	-0.17	0.06	0.04	0.50	**1.00**	-0.04	0.04	-0.09	-0.02	-0.06	0.09
Cu	-0.11	0.09	0.16	-0.07	-0.04	**1.00**	0.11	0.01	0.04	0.60	0.06
Al	-0.19	0.15	0.20	-0.07	0.04	0.11	**1.00**	-0.16	-0.04	-0.02	-0.01
Si	0.25	-0.28	0.03	-0.15	-0.09	0.01	-0.16	**1.00**	-0.12	-0.15	0.30
W	-0.17	0.11	0.09	0.02	-0.02	0.04	-0.04	-0.12	**1.00**	-0.01	-0.11
Nb	0.17	-0.16	-0.06	-0.07	-0.06	0.60	-0.02	-0.15	-0.01	**1.00**	-0.17
Ti	-0.04	-0.02	0.21	0.08	0.09	0.06	-0.01	0.30	-0.11	-0.17	**1.00**

Values in bold are different from 0 with a significance level alpha=0.05

Appendix III

Metal Dusting (PDGr)

A. PCA_7 and PCA_8 applied on PDGr data distribution.
a) PCA_7 applied on atmosphere conditions b) PCA_8 applied on alloy composition.

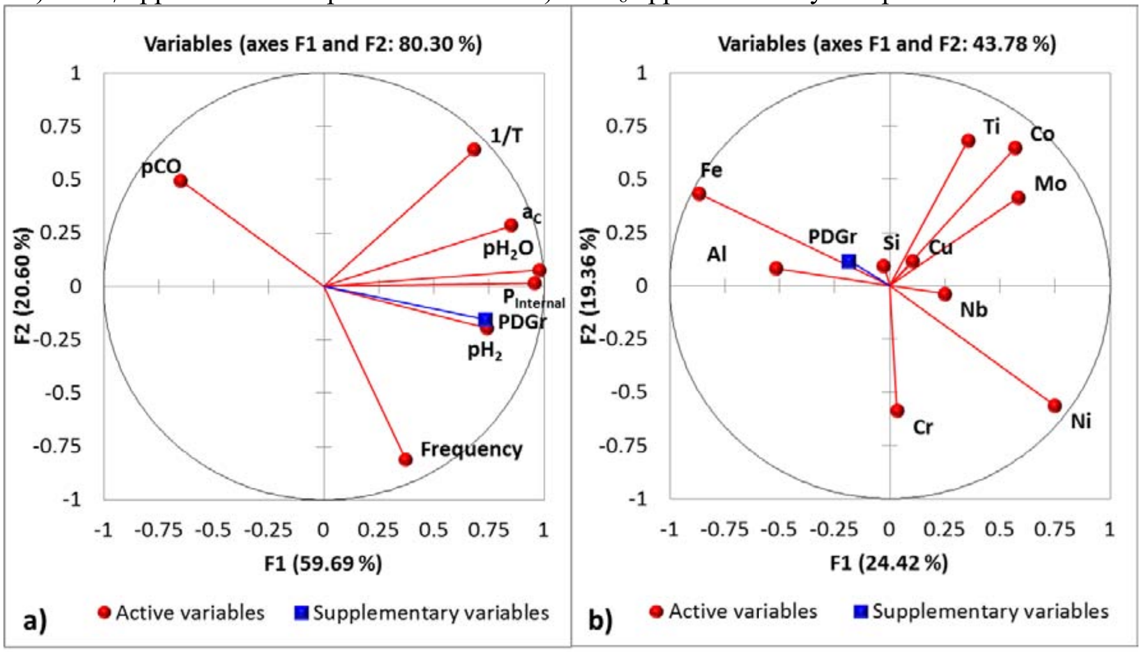

PCA_7 Summary Statistics

Variables (wt%)	Observations	Minimum	Maximum	Mean	Std. deviation
PDGr (µm/h)	385	0.000	6.335	0.086	0.397
Frequency (1/h)	385	0.0	0.0	0.0	0.0
1/T (K^{-1})	385	10.8	13.8	11.1	0.3
$P_{Internal}$ (bar)	385	1.0	30.0	1.3	2.8
pH_2O (bar)	385	0.0	13.3	0.1	1.1
pCO (bar)	385	0.0	0.8	0.7	0.1
pH_2 (bar)	385	0.2	9.4	0.3	0.6
a_C	385	10.0	7689.3	94.7	526.5
pO_2 (bar)					

PCA_7 Correlation Matrix

Variables (wt%)	Frequency (1/h)	1/T (K^{-1})	pH_2O (bar)	pCO (bar)	pH_2 (bar)	a_C	pO_2 (bar)
PDGr (µm/h)	**0.25**	**0.25**	**0.86**	**0.75**	**-0.33**	**0.97**	**0.37**
Frequency (1/h)	**1.00**	**-0.17**	**0.29**	**0.29**	**-0.57**	**0.27**	
1/T (K^{-1})	**-0.17**	**1.00**	**0.59**	**0.67**	**-0.21**	**0.25**	
H_2O (bar)	**0.29**	**0.59**	**1.00**	**0.98**	**-0.50**	**0.86**	
pCO (bar)	**0.29**	**0.67**	**0.98**	**1.00**	**-0.54**	**0.74**	
pH_2 (bar)	**-0.57**	**-0.21**	**-0.50**	**-0.54**	**1.00**	**-0.39**	
a_C	**0.27**	**0.25**	**0.86**	**0.74**	**-0.39**	**1.00**	
pO_2 (bar)							

Values in bold are different from 0 with a significance level alpha=0.05

PCA_8 Summary Statistics

Variables (wt%)	**Observations**	**Minimum**	**Maximum**	**Mean**	**Std. deviation**
PDGr (µm/h)	385	0.000	6.335	0.086	0.397
Fe	385	0.9	89.2	33.0	28.9
Ni	385	0.0	77.1	43.4	25.8
Cr	385	8.6	29.0	20.1	5.2
Mo	385	0.0	15.7	0.7	2.6
Co	385	0.0	12.5	0.3	1.8
Cu	385	0.0	0.7	0.0	0.2
Al	385	0.0	6.0	0.8	1.2
Si	385	0.0	2.8	0.4	0.6
W	385	0.0	14.0	0.3	2.0
Nb	385	0.0	0.2	0.0	0.0
Ti	385	0.0	1.0	0.2	0.2

PCA_8 Correlation Matrix

Variables (wt%)	**Fe**	**Ni**	**Cr**	**Mo**	**Co**	**Cu**	**Al**	**Si**	**W**	**Nb**	**Ti**
PDGr (µm/h)	**1.00**	**0.27**	**-0.25**	**-0.13**	-0.02	-0.07	-0.01	**-0.14**	**0.18**	-0.03	-0.08
Fe	**0.27**	**1.00**	**-0.93**	**-0.33**	**-0.28**	**-0.29**	-0.03	**0.30**	**0.13**	**-0.12**	-0.06
Ni	**-0.25**	**-0.93**	**1.00**	**0.16**	**0.13**	0.06	-0.01	**-0.35**	-0.04	0.09	**-0.12**
Cr	**-0.13**	**-0.33**	**0.16**	**1.00**	**-0.36**	**-0.19**	0.10	0.03	**-0.22**	-0.07	-0.06
Mo	-0.02	**-0.28**	**0.13**	**-0.36**	**1.00**	**0.45**	-0.10	**-0.24**	-0.06	**0.31**	**0.19**
Co	-0.07	**-0.29**	0.06	**-0.19**	**0.45**	**1.00**	0.00	-0.06	-0.06	-0.07	**0.70**
Cu	-0.01	-0.03	-0.01	0.10	-0.10	0.00	**1.00**	**-0.16**	0.04	-0.05	**0.33**
Al	**-0.14**	**0.30**	**-0.35**	0.03	**-0.24**	-0.06	**-0.16**	**1.00**	**-0.41**	**-0.12**	-0.05
Si	**0.18**	**0.13**	-0.04	**-0.22**	-0.06	-0.06	0.04	**-0.41**	**1.00**	-0.08	-0.04
W	-0.03	**-0.12**	0.09	-0.07	**0.31**	-0.07	-0.05	**-0.12**	-0.08	**1.00**	-0.05
Nb	-0.08	-0.06	**-0.12**	-0.06	**0.19**	**0.70**	**0.33**	-0.05	-0.04	-0.05	**1.00**
Ti	**1.00**	**0.27**	**-0.25**	**-0.13**	-0.02	-0.07	-0.01	**-0.14**	**0.18**	-0.03	-0.08

Values in bold are different from 0 with a significance level alpha=0.05

Appendix IV

High-temperature corrosion (Full domain)

A. PCA_1, and CT_1 applied on atmosphere conditions

PCA_1 and CT_1 Summary Statistics

Variable	Observations	Minimum	Maximum	Mean	Std. deviation
MTLr (mm/y)	867	0	40.1	3.3	4.5
T_{Metal} (°C)	867	230	725.0	491.8	110.3
O_2 (vol.%)	867	0	21.0	10.3	5.9
H_2O (vol.%)	867	0	23.8	12.1	9.9
CO_2 (vol.%)	867	0	13.7	6.4	5.2
HCl (ppm)	867	0	2000.0	619.3	549.1
SO_2 (ppm)	867	0	10000.0	372.4	1731.0

PCA_1 and CT_1 Correlation matrix

Variables	MTLr (mm/y)	T_{Metal} (°C)	O_2 (vol.%)	H_2O (vol.%)	CO_2 (vol.%)	HCl (ppm)	SO2 (ppm)
MTLr (mm/y)	**1**	**0.24**	**-0.21**	-0.03	**-0.09**	**0.13**	**-0.08**
T_{Metal} (°C)	**0.24**	**1**	**0.20**	**-0.34**	**-0.39**	**-0.13**	**0.30**
O_2 (vol.%)	**-0.21**	**0.20**	**1**	**-0.21**	**-0.27**	**-0.18**	**0.32**
H_2O (vol.%)	-0.03	**-0.34**	**-0.21**	**1**	**0.76**	**0.84**	**-0.20**
CO_2 (vol.%)	**-0.09**	**-0.39**	**-0.27**	**0.76**	**1**	**0.66**	**-0.20**
HCl (ppm)	**0.13**	**-0.13**	**-0.18**	**0.84**	**0.66**	**1**	**-0.17**
SO_2 (ppm)	**-0.08**	**0.30**	**0.32**	**-0.20**	**-0.20**	**-0.17**	**1**

Values in bold are different from 0 with a significance level alpha=0.05

B. PCA$_2$, and CT$_2$ applied on atmosphere conditions on alloy chemical composition

PCA$_2$ and CT$_2$ Summary Statistics

Variables (wt.)	Observations	Minimum	Maximum	Mean	Std. deviation
MTLr (mm/y)	867	0	40.1	3.3	4.5
Fe	867	0	99.2	50.3	39.0
Ni	867	0	74.0	27.6	26.5
Cr	867	0	48.0	14.9	10.4
Mo	867	0	18.2	3.6	5.0
Co	867	0	9.0	0.3	1.3
Cu	867	0	3.0	0.1	0.4
Al	867	0	5.6	0.2	0.8
Si	867	0	1.5	0.4	0.4
W	867	0	6.0	0.4	1.1
Nb	867	0	8.6	0.7	1.5
Ti	867	0	1.0	0.1	0.2

PCA$_2$ and CT$_2$ Correlation matrix

Variables (wt.%)	MTLr (mm/y)	Fe	Ni	Cr	Mo	Co	Cu	Al	Si	W	Nb	Ti
MTLr (mm/y)	**1**	**0.22**	**-0.18**	**-0.25**	**-0.15**	-0.04	**0.09**	-0.03	-0.05	0.00	**-0.12**	0.03
Fe	**0.22**	**1**	**-0.97**	**-0.78**	**-0.74**	**-0.31**	**-0.17**	**-0.27**	**-0.14**	**-0.26**	**-0.46**	**-0.49**
Ni	**-0.18**	**-0.97**	**1**	**0.65**	**0.74**	**0.31**	**0.17**	**0.27**	**-0.09**	**0.23**	**0.49**	**0.52**
Cr	**-0.25**	**-0.78**	**0.65**	**1**	**0.40**	-0.01	**0.11**	-0.06	**0.23**	-0.02	**0.29**	**0.17**
Mo	**-0.15**	**-0.74**	**0.74**	**0.40**	**1**	**0.07**	**0.17**	0.00	**-0.09**	**0.21**	**0.40**	**0.20**
Co	-0.04	**-0.31**	**0.31**	-0.01	**0.07**	**1**	0.03	**0.93**	-0.03	**0.73**	-0.06	**0.66**
Cu	**0.09**	**-0.17**	**0.17**	**0.11**	**0.17**	0.03	**1**	-0.03	-0.04	-0.03	**-0.12**	**0.29**
Al	-0.03	**-0.27**	**0.27**	-0.06	0.00	**0.93**	-0.03	**1**	-0.03	**0.67**	-0.03	**0.71**
Si	**-0.14**	-0.06	**-0.09**	**0.23**	**-0.09**	-0.03	-0.04	-0.03	**1**	-0.05	-0.06	-0.05
W	0.00	**-0.26**	**0.23**	-0.02	**0.21**	**0.73**	-0.03	**0.67**	-0.05	**1**	**-0.14**	**0.40**
Nb	**-0.12**	**-0.46**	**0.49**	**0.29**	**0.40**	-0.06	**-0.12**	-0.03	-0.06	**-0.14**	**1**	**0.09**
Ti	0.03	**-0.49**	**0.52**	**0.17**	**0.20**	**0.66**	**0.29**	**0.71**	-0.05	**0.40**	**0.09**	**1**

Values in bold are different from 0 with a significance level alpha=0.05

C. PCA$_3$, and CT$_3$ applied on ash chemical composition

PCA$_3$ and CT$_3$ Summary Statistics

Variables (wt.%)	**Observations**	**Minimum**	**Maximum**	**Mean**	**Std. deviation**
MTLr (mm/y)	867	0	40.1	3.3	4.5
S	867	0	21.6	8.1	7.0
Cl	867	0	53.5	9.8	13.2
Na	867	0	24.8	6.3	5.5
K	867	0	18.2	7.1	5.0
Pb	867	0	30.6	2.6	7.6
Zn	867	0	9.6	1.5	2.5
P	867	0	0.7	0.1	0.1
Ca	867	0	29.7	9.8	8.0
Si	867	0	25.8	6.4	7.7
Al	867	0	37.1	5.2	6.8
Fe	867	0	21.0	2.2	4.0

PCA$_3$ and CT$_3$ Correlation matrix

Variables	**MTLr (mm/y)**	**S**	**Cl**	**Na**	**K**	**Pb**	**Zn**	**P**	**Ca**	**Si**	**Al**	**Fe**
MTLr (mm/y)	**1**	**-0.31**	**0.18**	**-0.16**	**-0.13**	**0.17**	**0.16**	**0.07**	0.03	**0.20**	0.04	**0.10**
S	**-0.31**	**1**	**-0.29**	**0.45**	**0.37**	**-0.31**	**-0.25**	**-0.18**	**0.42**	**-0.49**	**-0.45**	**-0.38**
Cl	**0.18**	**-0.29**	**1**	**0.34**	**0.47**	**0.67**	**0.70**	**-0.07**	**-0.13**	**-0.41**	**-0.34**	**-0.28**
Na	**-0.16**	**0.45**	**0.34**	**1**	**0.81**	**0.10**	**0.20**	**-0.26**	**-0.24**	**-0.50**	**-0.48**	**-0.38**
K	**-0.13**	**0.37**	**0.47**	**0.81**	**1**	**0.30**	**0.33**	**-0.29**	**-0.19**	**-0.52**	**-0.52**	**-0.42**
Pb	**0.17**	**-0.31**	**0.67**	**0.10**	**0.30**	**1**	**0.92**	**-0.12**	**-0.39**	**-0.27**	**-0.16**	**-0.18**
Zn	**0.16**	**-0.25**	**0.70**	**0.20**	**0.33**	**0.92**	**1**	**-0.14**	**-0.32**	**-0.34**	**-0.24**	**-0.26**
P	**0.07**	**-0.18**	**-0.07**	**-0.26**	**-0.29**	**-0.12**	**-0.14**	**1**	**0.21**	**0.26**	**0.16**	**0.08**
Ca	0.03	**0.42**	**-0.13**	**-0.24**	**-0.19**	**-0.39**	**-0.32**	**0.21**	**1**	**-0.11**	**-0.17**	**-0.20**
Si	**0.20**	**-0.49**	**-0.41**	**-0.50**	**-0.52**	**-0.27**	**-0.34**	**0.26**	**-0.11**	**1**	**0.63**	**0.68**
Al	0.04	**-0.45**	**-0.34**	**-0.48**	**-0.52**	**-0.16**	**-0.24**	**0.16**	**-0.17**	**0.63**	**1**	**0.55**
Fe	**0.10**	**-0.38**	**-0.28**	**-0.38**	**-0.42**	**-0.18**	**-0.26**	**0.08**	**-0.20**	**0.68**	**0.55**	**1**

Values in bold are different from 0 with a significance level alpha=0.05

D. $CT_{1.1}$ applied on atmosphere conditions for Fe-based alloys

$CT_{1.1}$ Summary Statistics

Variable	Observations	Minimum	Maximum	Mean	Std. deviation
MTLr (mm/y)	307	0	24.5	4.6	4.8
T_{Metal} (°C)	307	230	693.0	453.0	108.4
O_2 (vol.%)	307	0	21.0	8.5	6.8
H_2O (vol.%)	307	0	23.8	9.1	10.0
CO_2 (vol.%)	307	0	13.7	4.0	4.8
HCl (ppm)	307	0	2000.0	432.6	556.7
SO_2 (ppm)	307	0	10000.0	134.5	986.8

$CT_{1.1}$ Correlation matrix

Variables	MTLr (mm/y)	T_{Metal} (°C)	O_2 (vol.%)	H_2O (vol.%)	CO_2 (vol.%)	HCl (ppm)	SO2 (ppm)
MTLr (mm/y)	**1.00**	**0.30**	**-0.14**	-0.08	**-0.21**	0.11	-0.07
T_{Metal} (°C)	**0.30**	**1.00**	-0.05	**-0.51**	**-0.56**	**-0.38**	**0.17**
O_2 (vol.%)	**-0.14**	-0.05	**1.00**	**0.14**	0.11	**0.14**	**0.17**
H_2O (vol.%)	-0.08	**-0.51**	**0.14**	**1.00**	**0.90**	**0.83**	-0.07
CO_2 (vol.%)	**-0.21**	**-0.56**	0.11	**0.90**	**1.00**	**0.68**	-0.08
HCl (ppm)	0.11	**-0.38**	**0.14**	**0.83**	**0.68**	**1.00**	-0.06
SO_2 (ppm)	-0.07	**0.17**	**0.17**	-0.07	-0.08	-0.06	**1.00**

E. $CT_{2.1}$ applied on alloy chemical composition for Fe-based alloys

$CT_{2.1}$ Summary Statistics

Variables (wt.)	Observations	Minimum	Maximum	Mean	Std. deviation
MTLr (mm/y)	307	0	24.5	4.6	4.8
Fe	307	83	99.2	95.7	4.7
Ni	307	0	0.5	0.1	0.1
Cr	307	0	48.0	3.0	7.4
Mo	307	0	1.2	0.4	0.5
Co	307	0	0.0	0.0	0.0
Cu	307	0	0.9	0.1	0.1
Al	307	0	0.0	0.0	0.0
Si	307	0	52.0	1.3	7.2
W	307	0	2.0	0.2	0.5
Nb	307	0	0.6	0.0	0.1
Ti	307	0	0.1	0.0	0.0

$CT_{2.1}$ Correlation matrix

Variables (wt.%)	MTLr (mm/y)	Fe	Ni	Cr	Mo	Cu	Al	Si	W	Nb	Ti
MTLr (mm/y)	**1.00**	-0.05	0.00	-0.09	**0.16**	**0.13**	**0.14**	0.00	0.07	0.00	**0.16**
Fe	-0.05	**1.00**	**-0.33**	**-0.45**	**-0.80**	0.09	**-0.34**	0.04	**-0.68**	**-0.57**	**-0.13**
Ni	0.00	**-0.33**	**1.00**	**0.37**	**0.20**	**0.38**	**0.12**	**0.22**	0.09	-0.02	**-0.13**
Cr	-0.09	**-0.45**	**0.37**	**1.00**	**0.33**	**0.12**	0.10	**0.86**	**0.27**	**0.25**	-0.01
Mo	**0.16**	**-0.80**	**0.20**	**0.33**	**1.00**	**-0.28**	**0.46**	-0.01	**0.55**	**0.44**	**0.34**
Cu	**0.13**	0.09	**0.38**	**0.12**	**-0.28**	**1.00**	**-0.19**	**0.20**	-0.03	**-0.16**	**-0.14**
Al	**0.14**	**-0.34**	**0.12**	0.10	**0.46**	**-0.19**	**1.00**	-0.04	**0.77**	**0.32**	**0.81**
Si	0.00	0.04	**0.22**	**0.86**	-0.01	**0.20**	-0.04	**1.00**	-0.05	-0.04	-0.03
W	0.07	**-0.68**	0.09	**0.27**	**0.55**	-0.03	**0.77**	-0.05	**1.00**	**0.57**	**0.69**
Nb	0.00	**-0.57**	-0.02	**0.25**	**0.44**	**-0.16**	**0.32**	-0.04	**0.57**	**1.00**	**0.22**
Ti	**0.16**	**-0.13**	**-0.13**	-0.01	**0.34**	**-0.14**	**0.81**	-0.03	**0.69**	**0.22**	**1.00**

F. CT$_{3.1}$ applied on ash chemical composition for Fe-based alloys

CT$_{3.1}$ Summary Statistics

Variables (wt.%)	Observations	Minimum	Maximum	Mean	Std. deviation
MTLr (mm/y)	307	0	24.5	4.6	4.8
S	307	0	20.9	7.7	7.5
Cl	307	0	21.5	4.9	7.2
Na	307	0	14.1	4.9	5.1
K	307	0	18.2	6.6	6.3
Pb	307	0	2.7	0.5	1.0
Zn	307	0	4.8	0.5	1.0
P	307	0	0.7	0.1	0.1
Ca	307	0	29.7	8.9	8.3
Si	307	0	25.8	10.4	10.0
Al	307	0	15.9	6.6	6.2
Fe	307	0	21.0	3.3	3.4

CT$_{3.1}$ Correlation matrix

Variables	MTLr (mm/y)	S	Cl	Na	K	Pb	Zn	P	Ca	Si	Al	Fe
MTLr (mm/y)	**1.00**	**-0.28**	**0.18**	**-0.32**	**-0.31**	**-0.45**	**-0.18**	0.09	**0.26**	**0.22**	**0.20**	**0.22**
S	**-0.28**	**1.00**	**0.23**	**0.75**	**0.71**	**0.56**	**0.53**	**-0.58**	**0.38**	**-0.74**	**-0.73**	**-0.64**
Cl	**0.18**	**0.23**	**1.00**	**0.33**	**0.34**	**-0.21**	-0.06	**-0.33**	**0.51**	**-0.45**	**-0.46**	**-0.35**
Na	**-0.32**	**0.75**	**0.33**	**1.00**	**0.99**	**0.81**	**0.55**	**-0.49**	-0.02	**-0.62**	**-0.65**	**-0.58**
K	**-0.31**	**0.71**	**0.34**	**0.99**	**1.00**	**0.79**	**0.51**	**-0.46**	-0.04	**-0.58**	**-0.62**	**-0.55**
Pb	**-0.45**	**0.56**	**-0.21**	**0.81**	**0.79**	**1.00**	**0.60**	**-0.30**	**-0.42**	**-0.43**	**-0.46**	**-0.45**
Zn	**-0.18**	**0.53**	-0.06	**0.55**	**0.51**	**0.60**	**1.00**	**-0.30**	-0.10	**-0.43**	**-0.41**	**-0.42**
P	0.09	**-0.58**	**-0.33**	**-0.49**	**-0.46**	**-0.30**	**-0.30**	**1.00**	**-0.20**	**0.71**	**0.68**	**0.52**
Ca	**0.26**	**0.38**	**0.51**	-0.02	-0.04	**-0.42**	-0.10	**-0.20**	**1.00**	**-0.24**	**-0.20**	**-0.14**
Si	**0.22**	**-0.74**	**-0.45**	**-0.62**	**-0.58**	**-0.43**	**-0.43**	**0.71**	**-0.24**	**1.00**	**0.97**	**0.86**
Al	**0.20**	**-0.73**	**-0.46**	**-0.65**	**-0.62**	**-0.46**	**-0.41**	**0.68**	**-0.20**	**0.97**	**1.00**	**0.88**
Fe	**0.22**	**-0.64**	**-0.35**	**-0.58**	**-0.55**	**-0.45**	**-0.42**	**0.52**	**-0.14**	**0.86**	**0.88**	**1.00**

G. CT$_{1.2}$ applied on atmosphere conditions for Fe/Ni-based alloys

CT$_{1.2}$ Summary Statistics

Variable	Observations	Minimum	Maximum	Mean	Std. deviation
MTLr (mm/y)	260	0	3.8	0.3	0.6
T$_{Metal}$ (°C)	260	300	725.0	470.3	122.6
O_2 (vol.%)	260	1	21.0	10.6	4.8
H_2O (vol.%)	260	0	23.8	15.9	8.7
CO_2 (vol.%)	260	0	13.7	8.4	4.5
HCl (ppm)	260	0	1500.0	675.9	420.9
SO_2 (ppm)	260	0	10000.0	955.9	2885.3

CT$_{1.2}$ Correlation matrix

Variables	MTLr (mm/y)	T$_{Metal}$ (°C)	O_2 (vol.%)	H_2O (vol.%)	CO_2 (vol.%)	HCl (ppm)	SO2 (ppm)
MTLr (mm/y)	**1**	**-0.516**	**0.479**	**-0.178**	-0.058	-0.101	**0.237**
T$_{Metal}$ (°C)	**0.479**	**-0.805**	**1**	**0.259**	**-0.582**	**-0.591**	**-0.296**
O_2 (vol.%)	**-0.178**	**-0.292**	**0.259**	**1**	**-0.562**	**-0.594**	**-0.466**
H_2O (vol.%)	-0.058	**0.587**	**-0.582**	**-0.562**	**1**	**0.906**	**0.847**
CO_2 (vol.%)	-0.101	**0.583**	**-0.591**	**-0.594**	**0.906**	**1**	**0.759**
HCl (ppm)	**0.237**	**0.270**	**-0.296**	**-0.466**	**0.847**	**0.759**	**1**
SO_2 (ppm)	-0.096	**-0.288**	**0.542**	**0.688**	**-0.578**	**-0.588**	**-0.499**

H. CT2.2 applied on alloy chemical composition for Fe/Ni-based alloys

CT$_{2.2}$ Summary Statistics

Variables (wt.)	Observations	Minimum	Maximum	Mean	Std. deviation
MTLr (mm/y)	260	0	3.8	0.3	0.6
Fe	260	27	70.2	51.4	12.7
Ni	260	9	44.0	21.3	10.1
Cr	260	15	28.9	22.8	3.7
Mo	260	0	3.5	1.0	1.1
Co	260	0	3.0	0.1	0.5
Cu	260	0	3.0	0.2	0.6
Al	260	0	0.4	0.0	0.1
Si	260	0	1.5	0.8	0.5
W	260	0	2.5	0.1	0.5
Nb	260	0	4.0	0.2	0.5
Ti	260	0	0.7	0.1	0.2

CT$_{2.2}$ Correlation matrix

Variables (wt.%)	MTLr (mm/y)	Fe	Ni	Cr	Mo	Co	Cu	Al	Si	W	Nb	Ti
MTLr (mm/y)	**1.00**	-0.08	**0.18**	**-0.20**	**0.13**	0.04	**0.21**	**0.21**	**-0.27**	0.03	**0.30**	**0.33**
Fe	-0.08	**1.00**	**-0.97**	**-0.73**	**-0.39**	**-0.36**	**-0.37**	**-0.30**	-0.01	**-0.34**	**0.12**	**-0.44**
Ni	**0.18**	**-0.97**	**1.00**	**0.60**	**0.37**	**0.30**	**0.41**	**0.36**	**-0.14**	**0.27**	-0.05	**0.59**
Cr	**-0.20**	**-0.73**	**0.60**	**1.00**	-0.04	0.11	-0.01	**0.14**	**0.47**	0.11	**-0.27**	-0.10
Mo	**0.13**	**-0.39**	**0.37**	-0.04	**1.00**	**0.27**	**0.42**	-0.08	**-0.30**	**0.22**	**-0.18**	**0.33**
Co	0.04	**-0.36**	**0.30**	0.11	**0.27**	**1.00**	0.00	**0.19**	-0.10	**0.94**	**0.20**	-0.06
Cu	**0.21**	**-0.37**	**0.41**	-0.01	**0.42**	0.00	**1.00**	-0.07	**-0.36**	**0.18**	-0.06	**0.52**
Al	**0.21**	**-0.30**	**0.36**	**0.14**	-0.08	**0.19**	-0.07	**1.00**	-0.08	**0.17**	**0.20**	**0.35**
Si	**-0.27**	-0.01	**-0.14**	**0.47**	**-0.30**	-0.10	**-0.36**	-0.08	**1.00**	**-0.12**	**-0.17**	**-0.33**
W	0.03	**-0.34**	**0.27**	0.11	**0.22**	**0.94**	**0.18**	**0.17**	**-0.12**	**1.00**	**0.21**	-0.07
Nb	**0.30**	**0.12**	-0.05	**-0.27**	**-0.18**	**0.20**	-0.06	**0.20**	**-0.17**	**0.21**	**1.00**	-0.02
Ti	**0.33**	**-0.44**	**0.59**	-0.10	**0.33**	-0.06	**0.52**	**0.35**	**-0.33**	-0.07	-0.02	**1.00**

I. CT$_{3.2}$ applied on ash chemical composition for Fe/Ni-based alloys

CT$_{3.2}$ Summary Statistics

Variables (wt.%)	Observations	Minimum	Maximum	Mean	Std. deviation
MTLr (mm/y)	260	0	30.0	2.5	4.6
S	260	0	18.0	7.4	6.1
Cl	260	0	53.5	6.7	10.3
Na	260	0	21.9	6.2	4.5
K	260	0	14.5	6.5	3.8
Pb	260	0	30.6	1.9	6.4
Zn	260	0	9.6	1.3	2.0
P	260	0	0.7	0.0	0.1
Ca	260	0	29.7	9.1	6.7
Si	260	0	23.0	6.1	5.4
Al	260	0	37.1	5.4	6.3
Fe	260	0	21.0	2.6	5.9

CT$_{3.2}$ Correlation matrix

Variables	MTLr (mm/y)	S	Cl	Na	K	Pb	Zn	P	Ca	Si	Al	Fe
MTLr (mm/y)	**1.00**	**-0.34**	**0.53**	-0.09	0.07	**0.50**	**0.50**	0.12	-0.06	0.05	-0.05	-0.03
S	**-0.34**	**1.00**	**-0.45**	**0.67**	**0.45**	**-0.23**	**-0.17**	-0.11	**0.27**	**-0.43**	**-0.42**	**-0.36**
Cl	**0.53**	**-0.45**	**1.00**	0.06	**0.35**	**0.74**	**0.77**	-0.01	-0.09	**-0.27**	**-0.18**	**-0.20**
Na	-0.09	**0.67**	0.06	**1.00**	**0.84**	0.11	**0.17**	**-0.18**	-0.10	**-0.45**	**-0.45**	**-0.37**
K	0.07	**0.45**	**0.35**	**0.84**	**1.00**	**0.33**	**0.38**	**-0.19**	0.00	**-0.44**	**-0.47**	**-0.44**
Pb	**0.50**	**-0.23**	**0.74**	0.11	**0.33**	**1.00**	**0.94**	-0.06	**-0.34**	**-0.31**	**-0.14**	**-0.13**
Zn	**0.50**	**-0.17**	**0.77**	**0.17**	**0.38**	**0.94**	**1.00**	-0.08	**-0.15**	**-0.36**	**-0.23**	**-0.25**
P	0.12	-0.11	-0.01	**-0.18**	**-0.19**	-0.06	-0.08	**1.00**	**0.13**	**0.25**	0.11	0.02
Ca	-0.06	**0.27**	-0.09	-0.10	0.00	**-0.34**	**-0.15**	**0.13**	**1.00**	-0.02	**-0.20**	**-0.39**
Si	0.05	**-0.43**	**-0.27**	**-0.45**	**-0.44**	**-0.31**	**-0.36**	**0.25**	-0.02	**1.00**	**0.61**	**0.63**
Al	-0.05	**-0.42**	**-0.18**	**-0.45**	**-0.47**	**-0.14**	**-0.23**	0.11	**-0.20**	**0.61**	**1.00**	**0.61**
Fe	-0.03	**-0.36**	**-0.20**	**-0.37**	**-0.44**	**-0.13**	**-0.25**	0.02	**-0.39**	**0.63**	**0.61**	**1.00**

J. $CT_{1.3}$ applied on atmosphere conditions for Ni-based alloys

$CT_{1.3}$ Summary Statistics

Variable	Observations	Minimum	Maximum	Mean	Std. deviation
MTLr (mm/y)	300	0	1.9	0.3	0.3
T_{Metal} (°C)	300	440	700.0	550.5	69.3
O_2 (vol.%)	300	6	20.0	11.9	5.2
H_2O (vol.%)	300	0	23.8	11.9	9.5
CO_2 (vol.%)	300	0	13.7	6.9	5.3
HCl (ppm)	300	0	1500.0	763.4	586.6
SO_2 (ppm)	300	0	650.0	107.1	129.5

$CT_{1.3}$ Correlation matrix

Variables	MTLr (mm/y)	T_{Metal} (°C)	O_2 (vol.%)	H_2O (vol.%)	CO_2 (vol.%)	HCl (ppm)	SO2 (ppm)
MTLr (mm/y)	**1.00**	**-0.20**	0.08	**-0.29**	**0.23**	**0.37**	**0.37**
T_{Metal} (°C)	0.08	**-0.27**	**1.00**	**0.33**	-0.01	**-0.42**	-0.01
O_2 (vol.%)	**-0.29**	**-0.30**	**0.33**	**1.00**	**-0.61**	**-0.81**	**-0.67**
H_2O (vol.%)	**0.23**	**0.23**	-0.01	**-0.61**	**1.00**	**0.48**	**0.89**
CO_2 (vol.%)	**0.37**	**0.35**	**-0.42**	**-0.81**	**0.48**	**1.00**	**0.56**
HCl (ppm)	**0.37**	0.01	-0.01	**-0.67**	**0.89**	**0.56**	**1.00**
SO_2 (ppm)	**0.37**	**-0.26**	0.00	**-0.42**	**0.55**	**0.40**	**0.76**

K. $CT_{2.3}$ applied on alloy chemical composition for Ni-based alloys

$CT_{2.3}$ Summary Statistics

Variables (wt.)	Observations	Minimum	Maximum	Mean	Std. deviation
MTLr (mm/y)	300	0	1.9	0.3	0.3
Fe	300	0	14.3	4.2	2.7
Ni	300	52	74.0	61.1	3.7
Cr	300	7	43.0	20.8	4.6
Mo	300	0	18.2	9.1	4.9
Co	300	0	9.0	0.9	2.0
Cu	300	0	1.6	0.2	0.3
Al	300	0	5.6	0.5	1.2
Si	300	0	0.5	0.2	0.2
W	300	0	6.0	0.8	1.7
Nb	300	0	8.6	1.7	2.1
Ti	300	0	1.0	0.2	0.2

$CT_{2.3}$ Correlation matrix

Variables (wt.%)	MTLr (mm/y)	Fe	Ni	Cr	Mo	Co	Cu	Al	Si	W	Nb	Ti
MTLr (mm/y)	**1.00**	**0.17**	**0.17**	0.04	**-0.22**	0.01	0.05	0.02	0.08	0.04	**-0.22**	0.09
Fe	**0.17**	**1.00**	**0.12**	**0.23**	**-0.32**	**-0.37**	**-0.13**	**-0.35**	**0.32**	**-0.50**	**0.15**	-0.11
Ni	**0.17**	**0.12**	**1.00**	**-0.26**	**-0.58**	-0.02	-0.07	0.05	**0.18**	**-0.23**	0.05	**0.12**
Cr	0.04	**0.23**	**-0.26**	**1.00**	**0.15**	**-0.72**	0.10	**-0.75**	**0.13**	**-0.60**	**0.17**	**-0.52**
Mo	**-0.22**	**-0.32**	**-0.58**	**0.15**	**1.00**	**-0.35**	**0.23**	**-0.42**	-0.09	-0.03	-0.03	**-0.48**
Co	0.01	**-0.37**	-0.02	**-0.72**	**-0.35**	**1.00**	0.01	**0.95**	-0.07	**0.73**	**-0.30**	**0.78**
Cu	0.05	**-0.13**	-0.07	0.10	**0.23**	0.01	**1.00**	-0.10	**0.39**	**-0.16**	**-0.39**	0.08
Al	0.02	**-0.35**	0.05	**-0.75**	**-0.42**	**0.95**	-0.10	**1.00**	**-0.13**	**0.69**	**-0.22**	**0.82**
Si	0.08	**0.32**	**0.18**	**0.13**	-0.09	-0.07	**0.39**	**-0.13**	**1.00**	**-0.42**	**-0.13**	**0.36**
W	0.04	**-0.50**	**-0.23**	**-0.60**	-0.03	**0.73**	**-0.16**	**0.69**	**-0.42**	**1.00**	**-0.38**	**0.43**
Nb	**-0.22**	**0.15**	0.05	**0.17**	-0.03	**-0.30**	**-0.39**	**-0.22**	**-0.13**	**-0.38**	**1.00**	**-0.25**
Ti	0.09	-0.11	**0.12**	**-0.52**	**-0.48**	**0.78**	0.08	**0.82**	**0.36**	**0.43**	**-0.25**	**1.00**

L. CT$_{3.3}$ applied on ash chemical composition for Ni-based alloys

CT$_{3.3}$ Summary Statistics

Variables (wt.%)	Observations	Minimum	Maximum	Mean	Std. deviation
MTLr (mm/y)	300	0	15.2	2.3	2.5
S	300	0	21.6	9.2	7.0
Cl	300	0	53.5	17.7	16.3
Na	300	0.7	24.8	7.8	6.2
K	300	2.0	14.5	8.2	4.4
Pb	300	0	30.6	5.4	10.9
Zn	300	0	9.6	2.5	3.4
P	300	0	0.7	0.1	0.2
Ca	300	0	29.7	12.4	9.3
Si	300	0	12.8	2.5	3.1
Al	300	0	37.1	3.7	7.4
Fe	300	0	4.3	0.6	1.0

CT$_{3.3}$ Correlation matrix

Variables	MTLr (mm/y)	S	Cl	Na	K	Pb	Zn	P	Ca	Si	Al	Fe
MTLr (mm/y)	**1.00**	**-0.38**	**0.35**	0.09	0.07	**0.45**	**0.51**	**0.12**	**-0.33**	-0.02	**-0.19**	-0.09
S	**-0.38**	**1.00**	**-0.68**	0.07	**-0.23**	**-0.64**	**-0.71**	-0.11	**0.49**	-0.07	**-0.20**	-0.04
Cl	**0.35**	**-0.68**	**1.00**	**0.37**	**0.72**	**0.67**	**0.72**	**-0.12**	**-0.48**	**-0.45**	**-0.32**	**-0.34**
Na	0.09	0.07	**0.37**	**1.00**	**0.66**	-0.02	0.03	**-0.27**	**-0.42**	**-0.38**	**-0.34**	**-0.31**
K	0.07	**-0.23**	**0.72**	**0.66**	**1.00**	**0.35**	**0.29**	**-0.39**	**-0.32**	**-0.50**	**-0.46**	**-0.38**
Pb	**0.45**	**-0.64**	**0.67**	-0.02	**0.35**	**1.00**	**0.93**	**-0.17**	**-0.65**	**-0.38**	-0.11	**-0.32**
Zn	**0.51**	**-0.71**	**0.72**	0.03	**0.29**	**0.93**	**1.00**	**-0.18**	**-0.68**	**-0.27**	**-0.13**	**-0.19**
P	**0.12**	-0.11	**-0.12**	**-0.27**	**-0.39**	**-0.17**	**-0.18**	**1.00**	**0.33**	**0.29**	0.04	0.07
Ca	**-0.33**	**0.49**	**-0.48**	**-0.42**	**-0.32**	**-0.65**	**-0.68**	**0.33**	**1.00**	**0.28**	**-0.13**	**0.17**
Si	-0.02	-0.07	**-0.45**	**-0.38**	**-0.50**	**-0.38**	**-0.27**	**0.29**	**0.28**	**1.00**	**0.19**	**0.88**
Al	**-0.19**	**-0.20**	**-0.32**	**-0.34**	**-0.46**	-0.11	**-0.13**	0.04	**-0.13**	**0.19**	**1.00**	**0.16**
Fe	-0.09	-0.04	**-0.34**	**-0.31**	**-0.38**	**-0.32**	**-0.19**	0.07	**0.17**	**0.88**	**0.16**	**1.00**

Appendix V

High-temperature corrosion (Isothermal domain)

A. PCA$_s$ applied on isothermal tests data distribution. a) PCA$_4$ applied on alloy composition b) PCA$_5$ applied on atmosphere conditions c) PCA$_6$ applied on ash composition.

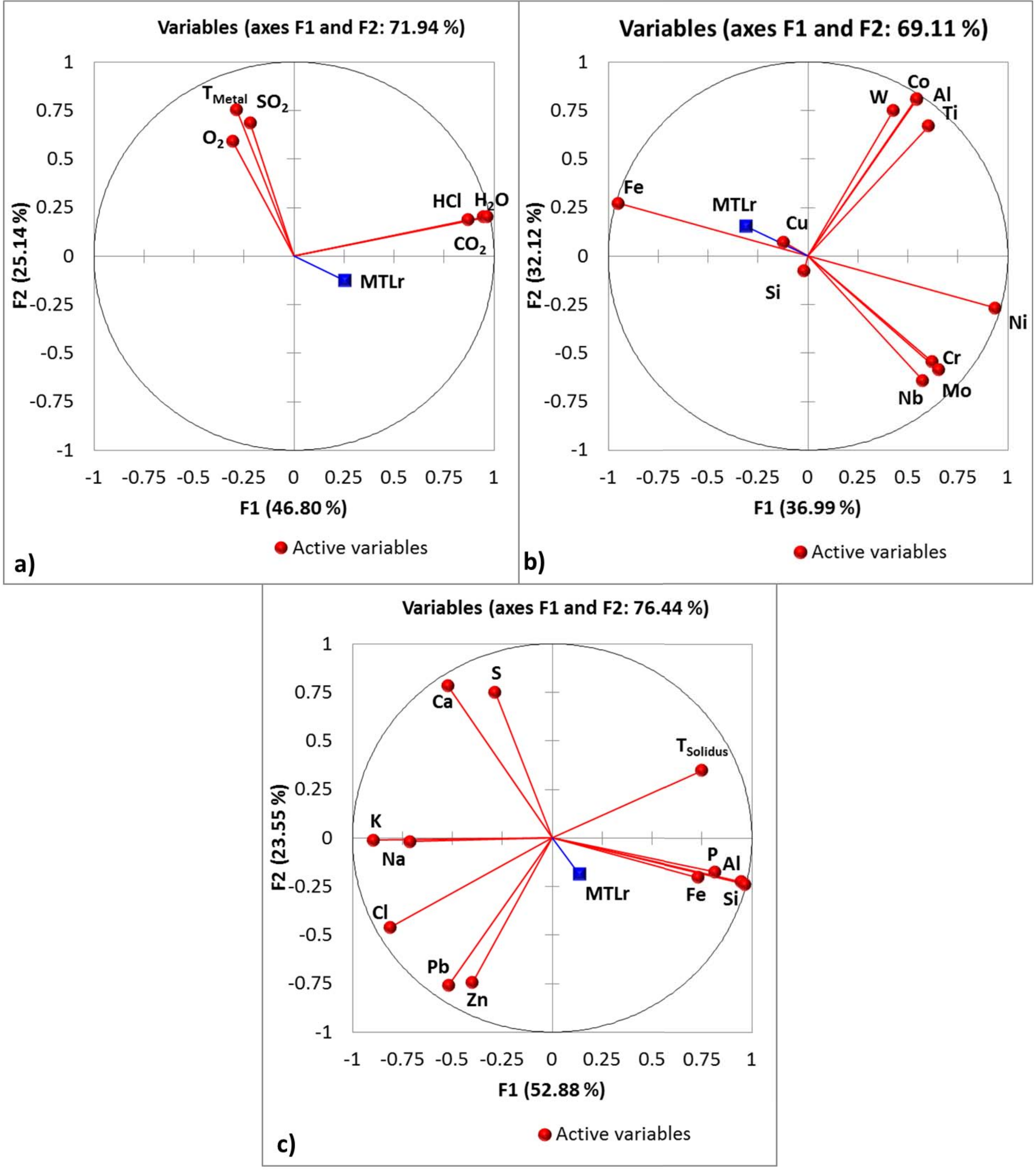

B. PCA_4 and CT_4 applied on atmosphere conditions

PCA_4 and CT_4 Summary Statistics

Variable	Observations	Minimum	Maximum	Mean	Std. deviation
MTLr (mm/y)	321	0	40.1	3.8	5.5
T_{Metal} (°C)	321	400	725.0	570.1	82.9
O_2 (vol.%)	321	0	21.0	11.8	8.2
H_2O (vol.%)	321	0	20.0	4.6	8.2
CO_2 (vol.%)	321	0	10.0	1.4	3.5
HCl (ppm)	321	0	1500.0	315.4	568.1
SO_2 (ppm)	321	0	10000.0	900.1	2778.0

PCA_4 and CT_4 Correlation matrix

Variables	MTLr (mm/y)	T_{Metal} (°C)	O_2 (vol.%)	H_2O (vol.%)	CO_2 (vol.%)	HCl (ppm)	SO2 (ppm)
MTLr (mm/y)	**1.00**	0.05	**-0.38**	**0.21**	**0.23**	**0.17**	**-0.16**
T_{Metal} (°C)	0.05	**1.00**	**0.20**	-0.04	**-0.15**	-0.07	**0.37**
O_2 (vol.%)	**-0.38**	**0.20**	**1.00**	**-0.18**	-0.09	**-0.17**	**0.34**
H_2O (vol.%)	**0.21**	-0.04	**-0.18**	**1.00**	**0.75**	**0.99**	**-0.14**
CO_2 (vol.%)	**0.23**	**-0.15**	-0.09	**0.75**	**1.00**	**0.80**	-0.09
HCl (ppm)	**0.17**	-0.07	**-0.17**	**0.99**	**0.80**	**1.00**	**-0.14**
SO_2 (ppm)	**-0.16**	**0.37**	**0.34**	**-0.14**	-0.09	**-0.14**	**1.00**

Values in bold are different from 0 with a significance level alpha=0.05

C. PCA$_5$ and CT$_5$ applied on alloy chemical composition

PCA$_5$ and CT$_5$ Summary Statistics

Variables (wt.)	**Observations**	**Minimum**	**Maximum**	**Mean**	**Std. deviation**
MTLr (mm/y)	321	0	40.1	3.8	5.5
Fe	321	0	98.1	45.9	41.5
Ni	321	0	67.5	31.2	28.6
Cr	321	0	30.0	13.8	9.5
Mo	321	0	16.0	4.3	4.6
Co	321	0	9.0	0.6	2.0
Cu	321	0	3.0	0.1	0.4
Al	321	0	5.6	0.3	1.2
Si	321	0	1.5	0.3	0.3
W	321	0	6.0	0.8	1.5
Nb	321	0	4.2	1.2	1.7
Ti	321	0	1.0	0.1	0.2

PCA$_5$ and CT$_5$ Correlation matrix

Variables (wt.%)	**MTLr (mm/y)**	**Fe**	**Ni**	**Cr**	**Mo**	**Co**	**Cu**	**Al**	**Si**	**W**	**Nb**	**Ti**
MTLr (mm/y)	**1.00**	**0.34**	**-0.34**	**-0.26**	**-0.25**	-0.06	0.03	-0.07	**0.27**	-0.01	**-0.33**	-0.06
Fe	**0.34**	**1.00**	**-0.99**	**-0.80**	**-0.77**	**-0.30**	0.08	**-0.29**	**0.41**	**-0.22**	**-0.68**	**-0.39**
Ni	**-0.34**	**-0.99**	**1.00**	**0.75**	**0.77**	**0.28**	-0.09	**0.28**	**-0.47**	**0.17**	**0.71**	**0.39**
Cr	**-0.26**	**-0.80**	**0.75**	**1.00**	**0.66**	-0.09	0.03	**-0.14**	-0.06	-0.08	**0.61**	0.02
Mo	**-0.25**	**-0.77**	**0.77**	**0.66**	**1.00**	**-0.16**	**-0.14**	**-0.15**	**-0.37**	-0.08	**0.68**	-0.02
Co	-0.06	**-0.30**	**0.28**	-0.09	**-0.16**	**1.00**	-0.05	**0.97**	**-0.18**	**0.81**	**-0.16**	**0.83**
Cu	0.03	0.08	-0.09	0.03	**-0.14**	-0.05	**1.00**	-0.07	0.08	-0.02	**-0.20**	0.07
Al	-0.07	**-0.29**	**0.28**	**-0.14**	**-0.15**	**0.97**	-0.07	**1.00**	**-0.25**	**0.79**	**-0.15**	**0.86**
Si	**0.27**	**0.41**	**-0.47**	-0.06	**-0.37**	**-0.18**	0.08	**-0.25**	**1.00**	**-0.22**	**-0.34**	**-0.16**
W	-0.01	**-0.22**	**0.17**	-0.08	-0.08	**0.81**	-0.02	**0.79**	**-0.22**	**1.00**	**-0.34**	**0.61**
Nb	**-0.33**	**-0.68**	**0.71**	**0.61**	**0.68**	**-0.16**	**-0.20**	**-0.15**	**-0.34**	**-0.34**	**1.00**	-0.08
Ti	-0.06	**-0.39**	**0.39**	0.02	-0.02	**0.83**	0.07	**0.86**	**-0.16**	**0.61**	-0.08	**1.00**

Values in bold are different from 0 with a significance level alpha=0.05

D. PCA$_6$ and CT$_6$ applied on ash chemical composition

PCA$_6$ and CT$_6$ Summary Statistics

Variables (wt.%)	Observations	Minimum	Maximum	Mean	Std. deviation
MTLr (mm/y)	321	0	40.1	3.8	5.5
S	321	0	21.6	7.5	8.2
Cl	321	0	53.5	13.0	16.1
Na	321	0.7	24.8	6.7	7.0
K	321	1.7	14.5	7.1	5.1
Pb	321	0	30.6	2.1	7.1
Zn	321	0	9.6	1.2	2.6
P	321	0	0.2	0.0	0.1
Ca	321	0	23.5	8.7	7.6
Si	321	0	23.0	8.8	10.3
Al	321	0	15.9	6.0	6.9
Fe	321	0	21.0	4.0	5.8
$T_{Solidus}$ (°C)	321	226	831	553	189

PCA$_6$ and CT$_6$ Correlation matrix

Variables (wt.%)	MTLr (mm/y)	S	Cl	Na	K	Pb	Zn	P	Ca	Si	Al	Fe	$T_{Solidus}$
MTLr (mm/y)	**1.00**	**-0.30**	-0.05	**-0.12**	**-0.17**	0.02	0.09	**0.24**	-0.09	**0.21**	**0.15**	-0.02	**-0.11**
S	**-0.30**	**1.00**	-0.04	**0.34**	**0.38**	**-0.27**	**-0.24**	**-0.61**	**0.71**	**-0.70**	**-0.70**	**-0.50**	-0.07
Cl	-0.05	-0.04	**1.00**	**0.61**	**0.82**	**0.55**	**0.69**	**-0.54**	-0.11	**-0.64**	**-0.65**	**-0.49**	**-0.79**
Na	**-0.12**	**0.34**	**0.61**	**1.00**	**0.79**	**0.11**	**0.25**	**-0.57**	**-0.19**	**-0.67**	**-0.67**	**-0.48**	**-0.30**
K	**-0.17**	**0.38**	**0.82**	**0.79**	**1.00**	**0.28**	**0.33**	**-0.71**	0.10	**-0.83**	**-0.84**	**-0.64**	**-0.55**
Pb	0.02	**-0.27**	**0.55**	**0.11**	**0.28**	**1.00**	**0.86**	**-0.20**	**-0.34**	**-0.25**	**-0.26**	**-0.20**	**-0.50**
Zn	0.09	**-0.24**	**0.69**	**0.25**	**0.33**	**0.86**	**1.00**	**-0.30**	**-0.30**	**-0.33**	**-0.35**	**-0.26**	**-0.76**
P	**0.24**	**-0.61**	**-0.54**	**-0.57**	**-0.71**	**-0.20**	**-0.30**	**1.00**	**-0.27**	**0.92**	**0.79**	**0.28**	**0.53**
Ca	-0.09	**0.71**	-0.11	**-0.19**	0.10	**-0.34**	**-0.30**	**-0.27**	**1.00**	**-0.41**	**-0.47**	**-0.48**	**-0.20**
Si	**0.21**	**-0.70**	**-0.64**	**-0.67**	**-0.83**	**-0.25**	**-0.33**	**0.92**	**-0.41**	**1.00**	**0.96**	**0.61**	**0.60**
Al	**0.15**	**-0.70**	**-0.65**	**-0.67**	**-0.84**	**-0.26**	**-0.35**	**0.79**	**-0.47**	**0.96**	**1.00**	**0.81**	**0.63**
Fe	-0.02	**-0.50**	**-0.49**	**-0.48**	**-0.64**	**-0.20**	**-0.26**	**0.28**	**-0.48**	**0.61**	**0.81**	**1.00**	**0.51**
$T_{Solidus}$	**-0.11**	-0.07	**-0.79**	**-0.30**	**-0.55**	**-0.50**	**-0.76**	**0.53**	**-0.20**	**0.60**	**0.63**	**0.51**	**1.00**

Values in bold are different from 0 with a significance level alpha=0.05

Appendix VI

High-temperature corrosion (temperature gradient domain)

A. PCA$_s$ applied on temperature gradient tests data distribution. a) PCA7 applied on alloy composition b) PCA8 applied on atmosphere conditions c) PCA9 applied on ash composition.

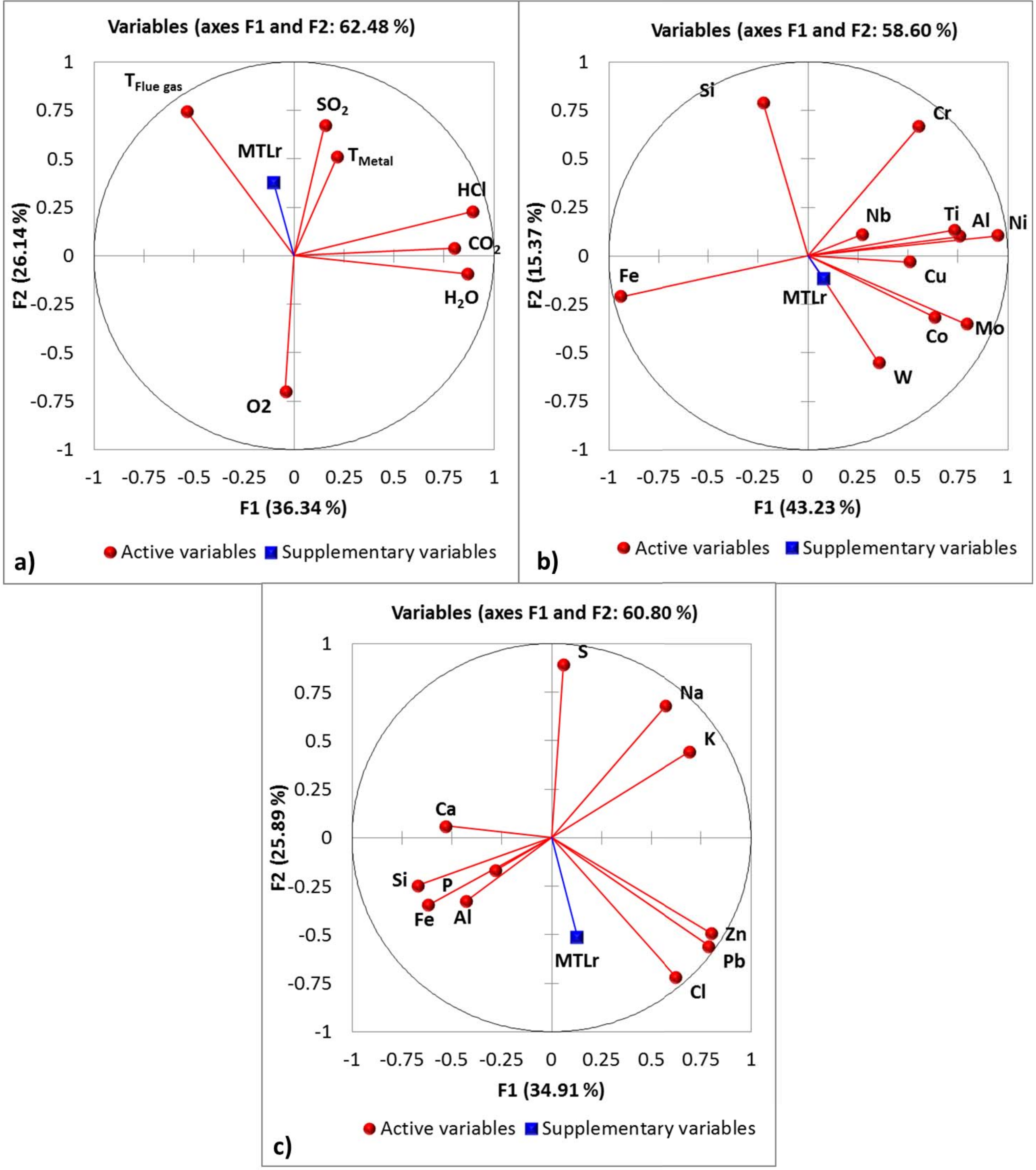

B. PCA_7 and CT_7 applied on atmosphere conditions

PCA_7 and CT_7 Summary Statistics

Variable	Observations	Minimum	Maximum	Mean	Std. deviation
MTLr (mm/y)	546	0	23.8	2.5	3.5
$T_{\text{Flue gas}}$ (°C)	546	380	700	569	90
T_{Metal} (°C)	546	270	650	454	102
O_2 (vol.%)	546	0	20.0	9.3	3.7
H_2O (vol.%)	546	0	23.8	16.3	8.2
CO_2 (vol.%)	546	0	13.7	9.6	3.7
HCl (ppm)	546	0	1500.0	765.3	406.6
SO_2 (ppm)	546	0	650.0	64.0	128.3

PCA_7 and CT_7 Correlation matrix

Variables	MTLr (mm/y)	$T_{\text{Flue gas}}$ (°C)	T_{Metal} (°C)	O_2 (vol.%)	H_2O (vol.%)	CO_2 (vol.%)	HCl (ppm)	SO2 (ppm)
MTLr (mm/y)	**1.00**	**0.38**	**0.54**	0.08	**-0.16**	**-0.11**	**0.15**	**0.33**
$T_{\text{Flue gas}}$ (°C)	**0.38**	**1.00**	**0.70**	**-0.36**	-0.05	**0.29**	**0.20**	**0.24**
T_{Metal} (°C)	**0.54**	**0.70**	**1.00**	-0.03	**-0.11**	-0.03	**0.33**	**0.45**
O_2 (vol.%)	0.08	**-0.36**	-0.03	**1.00**	**-0.40**	**-0.98**	**-0.38**	**-0.15**
H_2O (vol.%)	**-0.16**	-0.05	**-0.11**	**-0.40**	**1.00**	**0.43**	**0.68**	0.08
CO_2 (vol.%)	**-0.11**	**0.29**	-0.03	**-0.98**	**0.43**	**1.00**	**0.44**	0.05
HCl (ppm)	**0.15**	**0.20**	**0.33**	**-0.38**	**0.68**	**0.44**	**1.00**	**0.46**
SO_2 (ppm)	**0.33**	**0.24**	**0.45**	**-0.15**	0.08	0.05	**0.46**	**1.00**

C. PCA_8 and CT_8 applied on alloy chemical composition

PCA_8 and CT_8 Summary Statistics

Variables (wt.)	Observations	Minimum	Maximum	Mean	Std. deviation
MTLr (mm/y)	546	0	23.8	2.5	3.5
Fe	546	0	99.2	48.8	36.1
Ni	546	0	74.0	28.1	24.8
Cr	546	0	43.0	16.9	9.9
Mo	546	0	18.2	3.5	5.2
Co	546	0	2.5	0.2	0.5
Cu	546	0	3.0	0.2	0.4
Al	546	0	0.4	0.1	0.1
Si	546	0	1.5	0.5	0.5
W	546	0	3.8	0.2	0.8
Nb	546	0	8.6	0.4	1.3
Ti	546	0	0.7	0.1	0.2

PCA_8, and CT_8 Correlation matrix

Variables (wt.%)	MTLr (mm/y)	Fe	Ni	Cr	Mo	Co	Cu	Al	Si	W	Nb	Ti
MTLr (mm/y)	**1.00**	-0.03	0.09	-0.08	-0.04	-0.03	**0.15**	0.07	**-0.31**	-0.04	**0.09**	**0.20**
Fe	-0.03	**1.00**	**-0.97**	**-0.75**	**-0.72**	**-0.50**	**-0.39**	**-0.63**	0.04	**-0.31**	**-0.25**	**-0.58**
Ni	0.09	**-0.97**	**1.00**	**0.61**	**0.72**	**0.51**	**0.40**	**0.70**	**-0.18**	**0.28**	**0.27**	**0.65**
Cr	-0.08	**-0.75**	**0.61**	**1.00**	**0.26**	**0.17**	**0.21**	**0.27**	**0.44**	0.06	**0.13**	**0.28**
Mo	-0.04	**-0.72**	**0.72**	**0.26**	**1.00**	**0.53**	**0.36**	**0.52**	**-0.37**	**0.51**	**0.17**	**0.34**
Co	-0.03	**-0.50**	**0.51**	**0.17**	**0.53**	**1.00**	**0.28**	**0.43**	**-0.18**	**0.44**	0.01	**0.33**
Cu	**0.15**	**-0.39**	**0.40**	**0.21**	**0.36**	**0.28**	**1.00**	**0.22**	**-0.19**	0.02	-0.03	**0.52**
Al	0.07	**-0.63**	**0.70**	**0.27**	**0.52**	**0.43**	**0.22**	**1.00**	**-0.14**	0.00	**0.20**	**0.77**
Si	**-0.31**	0.04	**-0.18**	**0.44**	**-0.37**	**-0.18**	**-0.19**	**-0.14**	**1.00**	**-0.25**	**-0.15**	**-0.18**
W	-0.04	**-0.31**	**0.28**	0.06	**0.51**	**0.44**	0.02	0.00	**-0.25**	**1.00**	-0.07	0.01
Nb	**0.09**	**-0.25**	**0.27**	**0.13**	**0.17**	0.01	-0.03	**0.20**	**-0.15**	-0.07	**1.00**	**0.23**
Ti	**0.20**	**-0.58**	**0.65**	**0.28**	**0.34**	**0.33**	**0.52**	**0.77**	**-0.18**	0.01	**0.23**	**1.00**

D. PCA$_9$ and CT$_9$ applied on ash chemical composition

PCA$_9$ and CT$_9$ Summary Statistics

Variables (wt.%)	Observations	Minimum	Maximum	Mean	Std. deviation
MTLr (mm/y)	546	0	23.8	2.5	3.5
S	546	0	18.0	8.3	6.2
Cl	546	0	41.4	7.8	11.0
Na	546	0	15.1	6.1	4.4
K	546	0	18.2	7.2	5.1
Pb	546	0	30.6	3.2	8.2
Zn	546	0	9.6	1.8	2.4
P	546	0	0.7	0.1	0.2
Ca	546	0	29.7	9.5	7.7
Si	546	0	25.8	4.8	5.3
Al	546	0	37.1	4.9	6.9
Fe	546	0	8.1	0.9	1.7

PCA9 and CT9Correlation matrix

Variables	MTLr (mm/y)	S	Cl	Na	K	Pb	Zn	P	Ca	Si	Al	Fe
MTLr (mm/y)	**1.00**	**-0.40**	**0.48**	**-0.27**	**-0.13**	**0.40**	**0.39**	0.08	-0.03	**0.10**	-0.07	**0.21**
S	**-0.40**	**1.00**	**-0.59**	**0.66**	**0.42**	**-0.36**	**-0.27**	-0.09	**0.15**	**-0.23**	**-0.26**	**-0.26**
Cl	**0.48**	**-0.59**	**1.00**	**-0.11**	**0.14**	**0.88**	**0.86**	**0.09**	**-0.20**	**-0.23**	**-0.13**	**-0.16**
Na	**-0.27**	**0.66**	**-0.11**	**1.00**	**0.86**	**0.11**	**0.16**	**-0.23**	**-0.33**	**-0.31**	**-0.37**	**-0.38**
K	**-0.13**	**0.42**	**0.14**	**0.86**	**1.00**	**0.32**	**0.34**	**-0.24**	**-0.44**	**-0.28**	**-0.35**	**-0.33**
Pb	**0.40**	**-0.36**	**0.88**	**0.11**	**0.32**	**1.00**	**0.97**	**-0.12**	**-0.44**	**-0.33**	**-0.11**	**-0.20**
Zn	**0.39**	**-0.27**	**0.86**	**0.16**	**0.34**	**0.97**	**1.00**	**-0.14**	**-0.32**	**-0.35**	**-0.17**	**-0.24**
P	0.08	-0.09	**0.09**	**-0.23**	**-0.24**	**-0.12**	**-0.14**	**1.00**	**0.40**	**0.11**	0.02	**0.09**
Ca	-0.03	**0.15**	**-0.20**	**-0.33**	**-0.44**	**-0.44**	**-0.32**	**0.40**	**1.00**	**0.18**	0.01	0.08
Si	**0.10**	**-0.23**	**-0.23**	**-0.31**	**-0.28**	**-0.33**	**-0.35**	**0.11**	**0.18**	**1.00**	**0.32**	**0.91**
Al	-0.07	**-0.26**	**-0.13**	**-0.37**	**-0.35**	**-0.11**	**-0.17**	0.02	0.01	**0.32**	**1.00**	**0.36**
Fe	**0.21**	**-0.26**	**-0.16**	**-0.38**	**-0.33**	**-0.20**	**-0.24**	**0.09**	0.08	**0.91**	**0.36**	**1.00**